UNIVERSITY OF SOUTHAMPTON

FACULTY OF ENGINEERING, SCIENCE AND MATHEMATICS

Institute of Sound and Vibration Research

VIBRATION OF RAILWAY BRIDGES IN THE AUDIBLE FREQUENCY RANGE

by

David Herron

Thesis submitted for the degree of Engineering Doctorate

October 2009

UNIVERSITY OF SOUTHAMPTON

ABSTRACT

FACULTY OF ENGINEERING, SCIENCE AND MATHEMATICS

INSTITUTE OF SOUND AND VIBRATION RESEARCH

Engineering Doctorate

VIBRATION OF RAILWAY BRIDGES IN THE AUDIBLE FREQUENCY RANGE

by David Herron

The noise level associated with a train travelling on a bridge is normally greater than that for a train travelling on plain track. It is sometimes the bridge noise that causes the highest levels of disturbance to people in the vicinity or triggers action under regulations such as the Environmental Noise Directive. Consequently, there is a need to study means of predicting noise levels from proposed bridges, noise control measures for existing structures and principles of low-noise bridge design.

This thesis describes a programme of work in which an existing calculation model for bridge noise and vibration has been tested and alternative calculation methods have been developed where required. The existing model is based on analytical models for wheel-rail interaction and the calculation of the power input to the bridge. The response of the various component parts of the bridge for this power input is found using a simplified SEA scheme.

In this work, the existing model has been tested against measurements made on railway bridges and the results of an advanced method of structural analysis, the Waveguide Finite Element (WFE) method. This method is well-suited to modelling

some important types of railway bridge. Specifically, it allows a numerical modelling approach to be used up to higher frequency than conventional Finite Element methods. It has been found to offer some significant advantages over the existing bridge noise model, particularly for concrete-steel composite bridges and concrete box-section viaducts.

The track support structure has an important influence on bridge noise and vibration, through its role in the transmission of vibration from the rail to the bridge. Laboratory measurements have been made in this work to characterise the vibration transmission properties of two important types of track support structure on bridges; ballasted track and two-stage resilient baseplate track. Improved methods of modelling the dynamic behaviour of these track forms have been developed from the measurements, which can be used in calculation models for both bridge noise and also for rolling noise.

Keywords: Railway, Bridge, Wavenumber Finite Element, Noise, Vibration, Ballast.

CONTENTS

Academic Thesis: Declaration Of Authorship

I, …… [please print name]

declare that this thesis and the work presented in it are my own and has been generated by me as the result of my own original research.

[title of thesis]

……..

I confirm that:

1. This work was done wholly or mainly while in candidature for a research degree at this University;
2. Where any part of this thesis has previously been submitted for a degree or any other qualification at this University or any other institution, this has been clearly stated;
3. Where I have consulted the published work of others, this is always clearly attributed;
4. Where I have quoted from the work of others, the source is always given. With the exception of such quotations, this thesis is entirely my own work;
5. I have acknowledged all main sources of help;
6. Where the thesis is based on work done by myself jointly with others, I have made clear exactly what was done by others and what I have contributed myself;
7. Either none of this work has been published before submission, or parts of this work have been published as: [please list references below]:

Signed:

……

Date: ……

ACKNOWLEDGEMENTS

I would like to thank Doctor Chris Jones, Professor David Thompson and Doctor David Rhodes for their patient supervision during the course of this EngD project. I am also grateful for the support of Pandrol Limited; the guidance of their staff and use of their specialist equipment and laboratories. Further, I must thank both EPSRC and Pandrol Limited for funding this project.

LIST OF SYMBOLS

A	area
A_p	point accelerance in Chapter 6
A_t	transfer accelerance in Chapter 6
A_{Norm}	normalised accelerance in Chapter 6
c_o	speed of sound in air
c_L	longitudinal wave speed
D	flexural rigidity
f	frequency
E	Young's modulus
F	force
$\mathbf{F}$	force matrix
G	shear modulus
h	thickness
k	stiffness
$\mathbf{K}$	stiffness matrix
L	length
m	mass
$\mathbf{M}$	mass matrix
N_w	number of train wheels
n	modal density

P	power
r	combined wheel-rail roughness
S	stiffness per unit length
T_f	force transmissibility
v	vibration velocity
W	vertical displacement of bridge or rail
$\mathbf{W}$	displacement matrix
Y	mobility
Z	impedance
z	displacement across the track support
x	displacement in the laboratory stiffness tests, Chapters 4 and 5
$< >$	spatially-averaged response
Ω	ratio of forcing frequency to undamped natural frequency
η	damping loss factor
θ	phase angle
κ	wavenumber
λ	wavelength
ρ	density
σ	radiation efficiency
υ	Poisson's ratio
ω	circular frequency

1. INTRODUCTION

1.1. THE ENVIRONMENTAL NOISE PROBLEM

1.1.1. Environmental noise from the railway

Environmental noise is a growing concern throughout the industrialised world. In the European Union, it is estimated that 20% of the population are exposed to noise levels that scientists and health professionals believe to be unacceptable (Future Noise Policy, 1996). The primary effect of this noise on humans is typically 'annoyance' during the day-time and sleep disturbance at night.

Transportation noise is the main component of environmental noise. The EU has estimated that road traffic is the major source of noise with a long-term average sound level greater than 65dB(A). Of the locations with noise levels higher than this, it is estimated that around 1.7% are due to noise from railways (Future Noise Policy, 1996). Relative to road and aircraft noise, it is also found that rail noise is less annoying for a given noise level (Fields and Walker, 1981) and (Miedema, 1998).

Nonetheless, excessive noise is the main concern expressed by the public regarding the effect of railways on the environment (Future Noise Policy, 1996). On this basis, there has been considerable opposition to the expansion of railway infrastructure and capacity in some areas. Large public protests have taken place in response to the introduction of high-speed trains between Paris and Marseille for example (European Environment Agency, 2009). It is therefore necessary to reduce railway noise if the role of rail transport is to be increased, an important objective of transport policy in Europe and elsewhere.

1.1.2. Noise reduction programmes

There has been legislation enforcing maximum at-source sound levels for road vehicles and aircraft since the 1970s. For railway noise, the difficulty in separating the noise produced by the track and that from the rolling stock delayed the introduction of such legislation. There are now limits for the noise produced by the rolling stock when measured on a reference track, within the so-called Technical Standards for Interoperability (Directive 2001/16/EC, 2001), but not for noise from the track or from support structures, such as bridges and viaducts.

An important mechanism by which public concerns regarding railway noise are addressed is the environmental impact assessment that is required in order to gain approval for a new railway infrastructure project. In England and Wales, this normally takes the form of a public enquiry for major projects, following the Transport and Works Act (1992). This leads to undertakings being given concerning noise and its control by which the project must abide. Similar processes are used in other parts of the world. It is therefore necessary to demonstrate that the environmental impact of a railway infrastructure project is acceptable in advance of its construction.

The Directive on Environmental Noise (Directive 2002/49/EC) is an important legislative control for environmental noise from existing infrastructure in the European Union. Member states are required to produce noise maps, that is to predict the noise levels around major urban areas using simple and largely empirical calculation methods. Locations where an unacceptable noise level is expected are identified from these noise maps. Actions plans are required to reduce the noise levels at these locations and for railways may include a range of noise control measures, such as changes to the track or rolling stock, limits on the number of train movements or maximum train speed. This is therefore a further driver for railway noise research and is notable because it is the first regarding noise control measures for existing infrastructure.

1.2. THE GENERATION OF RAILWAY NOISE

1.2.1. Noise from a train travelling on plain track at -grade

The noise associated with a train travelling on plain track at grade consists of three major components: rolling noise, traction noise and aerodynamic noise. Of these, rolling noise is normally the major source (Thompson and Jones, 2000). Unevenness in the running surfaces of the wheels and rails, normally referred to as wheel-rail roughness, causes relative vertical motion between the rail and wheel (Thompson, 1993). These components therefore radiate sound.

Rolling noise has been studied extensively and a predictive model for this noise has been developed, Track-Wheel Interaction Noise Software, TWINS. This model is based on a description of the rolling stock and track, together with appropriate

roughness spectra for the wheel and rail. TWINS has been shown to predict rolling noise for typical track and wheel designs to within about 2dB. A summary of this work is given by (Thompson et al. 1996a), (Thompson et al. 1996b) and (Jones and Thompson, 2003).

The relevant wavelengths of the wheel and rail roughness typically lie in the range from 5 to 500mm, with amplitudes of up to 50μm (Remington, 1987). For a wheel or rail roughness of wavelength λ and a train travelling at speed V, a sinusoidal vibration will be produced with frequency f,

$$f = \frac{v}{\lambda} \tag{1.1}$$

The contact zone between the rail and wheel has a length of the order of 10mm, and there is therefore a contact filter effect for wavelengths shorter than this (Remington, 1987). The maximum frequency of interest in rolling noise is typically about 5kHz, due to this contact filter effect.

The relative contributions made by the wheel and rail to the overall rolling noise differ through the frequency range, according to their relative mobilities, vibration transmission and sound radiation. For frequencies between about 100Hz and those in which the wheel exhibits a modal response, typically above 1 to 2kHz, the rail normally has a higher mobility than the wheel. In this frequency range, the vibration of the rail is therefore greater than that of the wheel. The rolling noise is then dominated by either the noise radiated by the rail or by components of the track structure, such as the sleepers. Sleeper noise is normally important only up to frequencies of about 500Hz, dependent on the rail fastener stiffness (Thompson et al. 1996b). In the frequency range in which the wheel exhibits a modal response, the wheel vibration is normally large relative to that of the rail, such that the wheel noise component dominates the rolling noise in this range.

1.2.2. Noise from a train travelling on a bridge

When a train is travelling on a bridge, the vibration generated by the combined wheel-rail roughness is transmitted from the rail to the bridge, via the track support structure. This vibrational energy propagates through the bridge, causing the whole bridge to radiate noise (Janssens and Thompson, 1996). The noise radiated by this

large structure normally constitutes a significant addition to the wheel-rail rolling noise and other noise sources. In some cases, the different type of track structure used on bridges than on plain track at-grade also causes a significant increase in the rolling noise (Poisson and Margiocchi, 2006). Measurements show that the overall noise level associated with a train travelling on a bridge may be up to 20dB greater than that for a train on plain track at grade (Hardy, 1999).

Urban railways are heavily dependent on bridges and viaducts: Kurzweil (1977) estimates that 30% of route miles on urban light rail systems in the US are on elevated track. Mainlines are also more reliant on bridges in heavily populated areas, as the need to cross roads and other railway lines is encountered more frequently than in rural areas.

Due to the prevalence of bridges and viaducts in urban areas, combined with the higher noise levels expected for these cases than for trains travelling at-grade, the noise from elevated structures is an important part of the noise impact of the railway. Elevated sections of a proposed new railway line may therefore receive particular attention in an environmental impact assessment. For existing lines, it is likely that bridges and viaducts will be identified in action plans produced from the noise mapping exercise required by the Directive on Environmental Noise (Directive 2002/49/EC, 2002). The standard used for noise mapping in the UK, Calculation of Railway Noise (1995), requires a correction of up to +9dB(A) for a train travelling on a bridge rather than on plain track at-grade. Consequently, there is a need to study means of predicting noise levels from proposed bridges and viaducts, noise control measures for existing structures and principles of low-noise bridge and viaduct design.

1.3. RAILWAY BRIDGE AND TRACK STRUCTURES

1.3.1. Introduction

A wide range of bridge and track structures are in use on railways and previous work has shown that their associated noise levels vary considerably. It is therefore appropriate to introduce the reader to common bridge and track structures at this stage.

1.3.2. Railway bridge structures

Bridges and viaducts are required on the railway in order to cross valleys, water (rivers, river estuaries and flood plains for example), roads and other railway lines. The term viaduct will be used here to refer to a longer elevated structure, composed of many consecutive spans. The majority of modern bridges and viaducts can be divided into three groups: concrete box-section, concrete-steel composite and all-steel. Examples of these are shown in Figure 1.1 below.

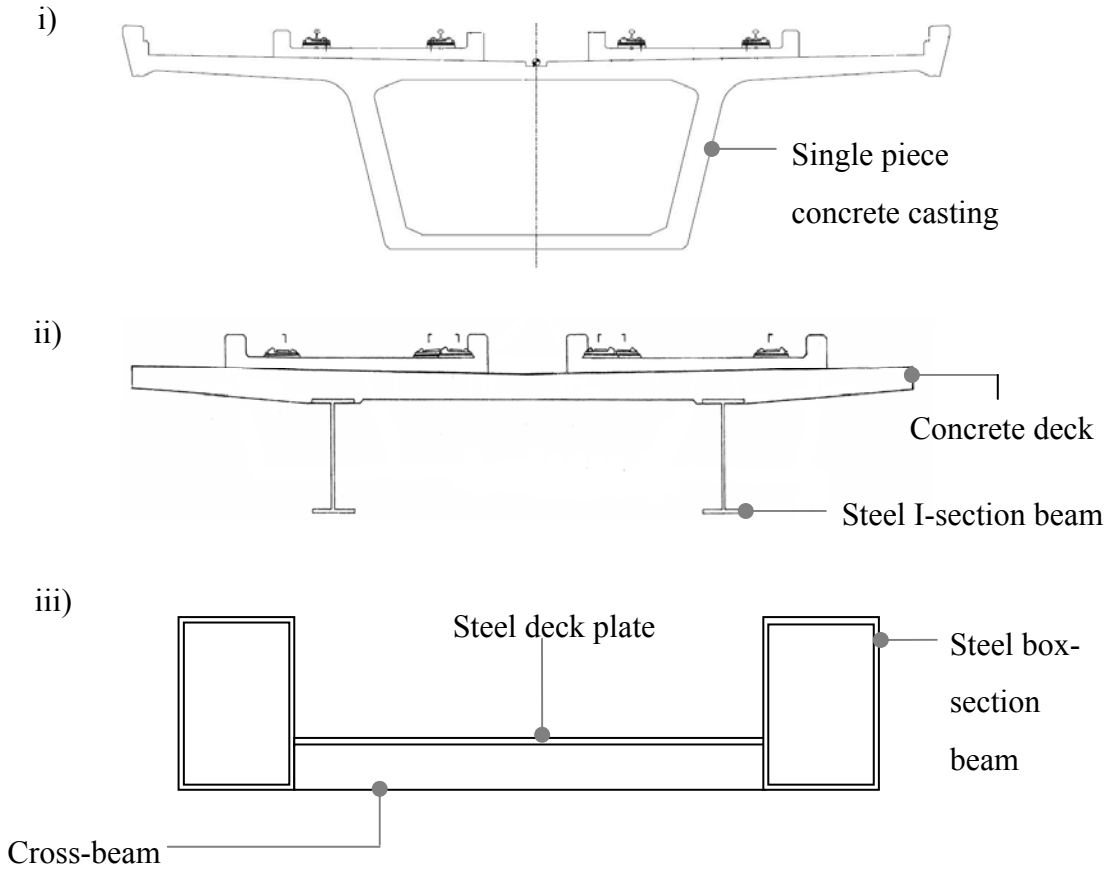

Figure 1.1. Examples of modern bridge structures i) concrete box-section ,ii) concrete-steel composite (taken from Bewes, 2006)), iii) all-steel.

In the past, masonry, iron and steel bridges were built for the railway. Masonry bridges are normally regarded as very low-noise elevated structures (Shield et al., 1989), such that they have required little attention with regard to noise. However, such structures have not been built in recent years because of their high cost.

Iron and steel bridges have been built in various different configurations. Some of these do not have a deck plate, rather they are constructed only from beams and these

will be referred to here as open bridges. In addition to beams running parallel to the axis of the bridge, some bridges include beams that lie perpendicular to the axis of the bridge, referred to here as cross-beams. Some of the most common configurations for historical iron and steel bridges are shown in Figure 1.2 below.

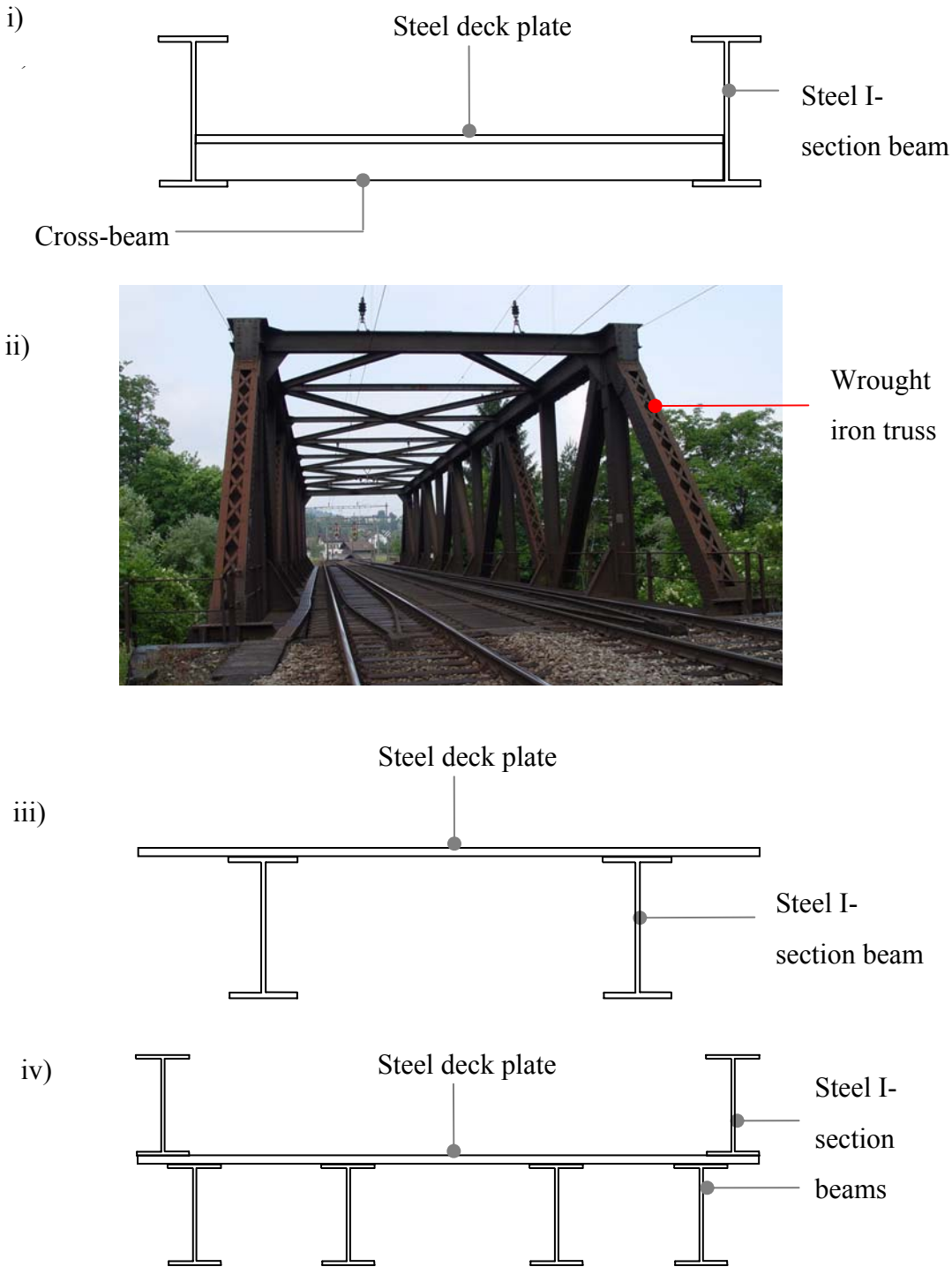

Figure 1.2. Four historical designs for iron and steel railway bridges: i) side-deck I-beam, ii) truss, iii) under-deck I-beam, iv) side and under-deck I-beam.

1.3.3. Track structures with a ballast layer

Most railway track is ballasted, which means that the rails are fastened to sleepers, which are supported by a layer of ballast. A cross-sectional view of a typical ballasted track arrangement on a bridge is shown in Figure 1.3 below.

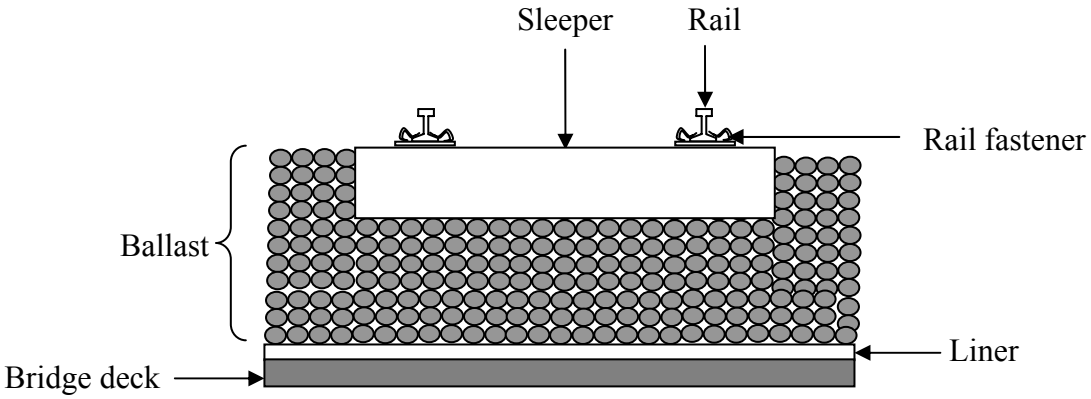

Figure 1.3. Typical ballasted track arrangement on a bridge.

Ballast is usually crushed natural rock, such as granite. Specifications for railway ballast, such as British Standard BS EN 13450 (2002), require a carefully controlled range of ballast grain sizes and an angular grain shape, in order to promote interlocking between the grains and high internal friction. The ballast layer is typically 250mm to 500mm deep, measured from the underside of the sleeper.

The ballast is packed under the sleeper only in the areas beneath the rails, during track construction and maintenance operations, in order to promote track stability (Esveld, 1989). The sleeper should be fully embedded in the ballast, as shown in Figure 1.3, to prevent lateral and longitudinal motion of the sleeper under the moving load of the train. Wooden sleepers were widely used in the first half of the 20th century, but concrete sleepers are now the most usually used. The sleepers are normally set at a distance of between 0.6 and 0.75m apart, measured parallel to the axis of the bridge (Esveld, 1989).

Some form of liner is normally placed between the ballast and the bridge deck. In the past, wood has been used for this purpose to protect the deck from impact damage. Specialist liners are used on modern bridges, which may also prevent rainwater reaching the bridge deck in order to guard against corrosion of the structure.

Rail fasteners are used to connect the rails to the sleepers. The fastener normally consists of a clip to provide the required clamping load to the rail-foot and an elastomeric railpad, fitted between the rail and sleeper. This resilient connection protects the sleeper from high-frequency excitation (Esveld, 1989), which prevents crack formation in concrete sleepers and extends the service life of sleepers in general.

1.3.4. Track structures without a ballast layer

Some railway track structures, both at grade and on bridges, do not include a ballast layer or sleepers. These will be referred to as directly-fastened track here. The main reason for using this type of track is that it requires less maintenance than ballasted track. The cost associated with maintenance of ballasted track may be a significant part of the running costs of a railway (Zhai et al., 2004). However, construction costs for directly-fastened track are greater than those for ballasted track (Esveld, 1989). For bridges, the use of directly-fastened track in preference to ballasted track also brings a significant reduction in the weight that the bridge must support and therefore the bearing strength requirements. Further, use of directly-fastened track can lead to a reduction in the overall depth of the bridge below rail height, which may be of value in some cases.

Modern rail fasteners on directly-fastened track are referred to as baseplate-type rail fasteners, or ‘baseplates’ here. A range of different baseplates are used; an example of a relatively simple design is shown in Figure 1.4 below.

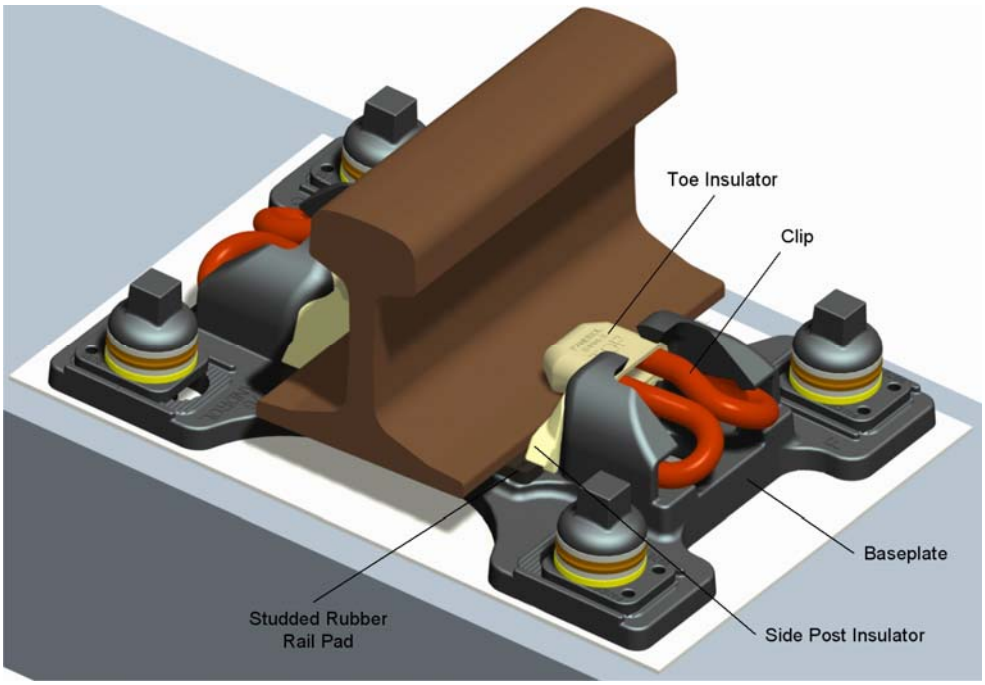

Figure 1.4. Example of a baseplate-type rail fastener (drawing courtesy of Pandrol , used with permission).

The baseplate shown above consists of a railpad fitted between the rail and a cast-iron plate that is fixed to the bridge structure using bolts. The stiffness of the railpad used in baseplate rail fasteners may be much lower than that in ballasted track, because the railpad is normally the only source of resilience in directly-fastened track. More complex baseplate designs are used where relatively low levels of vertical stiffness are required. Two-stage resilient baseplates are an example of this, in which there is a resilient pad between the plate and the rail and another between the plate and the track-slab or bridge.

In the past, directly-fastened track structures on bridges were built from wooden beams. A typical arrangement is shown in Figure 1.5 below.

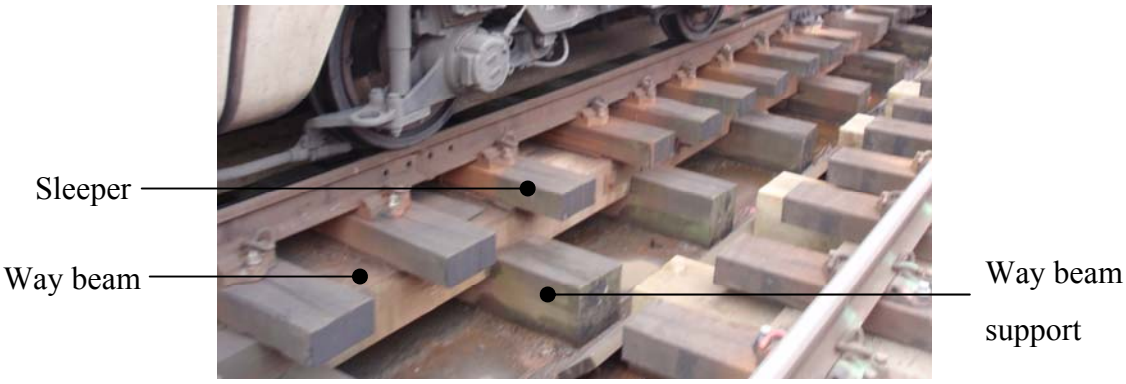

Figure 1.5. Directly-fastened track structure built from wooden beams.

The assembly of beams shown above is normally used to transmit the load from the rail to positions on the bridge deck that are located directly above cross-beams in the bridge. On this type of track, the rail fastener usually consists of a clip to hold the rail foot in position and a screw or spike connection to the sleeper. There is often no railpad in this type of track, the resilience coming from the beams themselves.

1.3.5. Influence of the track structure on noise

The transmission of vibration from the wheel-rail contact zone to the bridge, via the track structure, was identified as the means by which the bridge is caused to vibrate and radiate sound in Section 1.2.2. The track structure, in its various forms, was described as a resilient connection between the rails and the bridge in Sections 1.3.3 and 1.3.4. Vibration isolation, that is, dynamic decoupling of two connecting systems (Brennan and Ferguson, 2004), therefore occurs between the rail and the bridge in some frequency range. This behaviour is an important factor in bridge noise and it is introduced here using the single degree-of-freedom system shown in Figure 1.6 below,

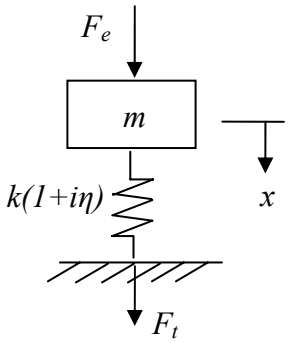

Figure 1.6. Single degree-of-freedom mass-spring system.

where F_e represents a harmonic excitation force applied to the mass m and x is the displacement of the mass. The term $k(1+i\eta)$ describes the stiffness of a mass-less spring with hysteretic damping. F_t is the force transmitted to the rigid foundation, and it is related to the excitation force in the frequency domain by the force transmissibility, T_f, as follows (Mead, 1998),

$$T_f = \frac{F_t}{F_e} = \frac{1+i\eta}{1-\Omega^2+i\eta} \qquad (1.2)$$

where $\Omega = \omega/\omega_n$ is the ratio of the forcing frequency to the undamped natural frequency of the system, $\omega_n = \sqrt{k/m}$. The force transmissibility is a measure of the effectiveness of the vibration isolation provided by the damped spring. This is shown in Figure 1.7 as a function of the normalised frequency Ω, for two different levels of damping in the spring.

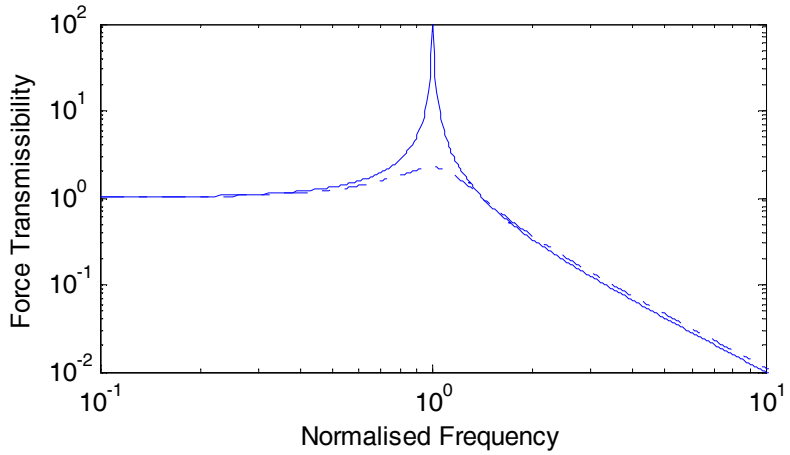

Figure 1.7. Force transmissibility of the mass-spring system shown versus non-dimensional frequency: ———, $\eta = 0.01$; – · – · –, $\eta = 0.5$.

For values of Ω much less than unity, the transmitted force is approximately equal to the excitation force, for both damping levels. There is therefore no significant vibration isolation effect in this frequency range. For values of Ω close to unity, the transmitted force is greater than the excitation force. This vibration amplification effect is larger for the low damping case. It is only when Ω is greater than $\sqrt{2}$ that the transmitted force is smaller than the excitation force, such that there is effective vibration isolation. In this frequency range, the effect of the hysteretic damping level is small. However, a viscous damping model would indicate a larger effect.

The complexity of a system that consists of a rail, track support and bridge means that it is not possible to evaluate the vibration isolation effect precisely using a simple expression such as that for the simple system of Figure 1.6. However, as a first approximation the effect of different track structures on the behaviour of the rail, track support and bridge system can be predicted using a simple lumped parameter approach. A two degree-of-freedom system can be proposed where the rail and the bridge are represented by masses and the track support by a damped spring between them. The natural frequency of the mode in which the rail and bridge move in anti-phase on the stiffness of the track support can then be estimated from,

$$\omega_n = \sqrt{\frac{S_t}{m_r} + \frac{S_t}{m_b}} \tag{1.3}$$

where S_t is the track stiffness per unit length, m_r is the mass per unit length of the rail and m_b is the mass per unit length of the bridge. The frequency given by equation (1.3) will be referred to hereafter as the decoupling frequency. In simple terms, the motion of the rail and bridge are well-coupled up to this frequency, and decoupled for higher frequencies. Effective vibration isolation can be expected for frequencies greater than about $\sqrt{2}$ times the decoupling frequency. The form of equation (1.3) shows that there will be isolation between the rail and bridge down to lower frequencies when a relatively soft track support is used. Control of this frequency range through changes to the mass per unit length of the rail and bridge is also possible, but these changes are normally more difficult to achieve practically.

In addition to its role in bridge noise, the track structure also has an important influence on rolling noise, or more specifically on the noise from the rail and track support structure. This is largely due to the effect of the dynamic properties of the track on the rate at which vibration is attenuated as it travels along the rail, normally called the decay rate (Jones et al., 2006). The decay rate controls the length of rail that is effective in radiating noise, such that it is a key factor in the noise radiated by the rail. Janssens and Thompson (1996) compare decay rate and rail vibration measurements between directly-fastened track on a bridge and ballasted track at-grade: the decay rates are generally much lower and the rail vibration level higher for the directly-fastened track on a bridge. The stiffness of a direct-fastening system is

also important to the decay rates in the rail. The frequency range over which the motion of the rail and bridge are well-coupled is associated with a high rate of decay of vibration in the rail and therefore low rail noise. Relatively soft direct-fasteners are therefore associated with higher rolling noise levels (Wang et al., 2000).

There are secondary effects of the track stiffness on rolling noise, such as an increase in sleeper noise for a relatively stiff rail fastener on ballasted track (Vincent et al., 1996), or an increase in noise radiated by the baseplates in directly-fastened track (Wang et al., 2000). However, the track stiffness required to give minimum rolling noise is normally much greater than that for minimum noise from the bridge. The track stiffness level required for minimum overall noise from a train travelling a bridge is therefore dependent on the relative levels of rolling noise and bridge noise. This needs to be addressed on a case-by-case basis.

1.4. LITERATURE REVIEW

1.4.1. Surveys of bridge noise

The problem of noise from railway bridges and viaducts has been studied extensively since the 1960's. Early published work took the form of noise measurements for existing bridges in Europe (ORE, 1966), (ORE, 1971) and in Japan (Japanese National Railways, 1973), (Japanese National Railways, 1975). Kurzweil (1977) presents a compilation of results from these measurement programmes in Europe and in Japan. A total of 11 different classifications of bridge are identified from this data, such that all bridges within each classification have similar construction and noise characteristics. Mean A-weighted noise levels are given for each of these bridge classifications at a distance of 25m from the track. The lowest noise levels are for concrete bridges with ballasted track, and for a given train speed these levels are comparable to those for at-grade track. The highest noise levels are those for steel bridges with directly-fastened track, typically 15dB higher than those for at-grade track. Kurzweil (1977) attributes the lower noise levels found for bridges with ballasted track than those with directly-fastened track to the added mass on the bridge deck, vibration damping in the ballast and the sound absorption properties of the ballast.

Ban and Miyamoto (1975) present the results of a thorough noise survey for bridges and viaducts on high-speed Shinkansen lines in Japan. The findings reported are broadly similar to those from Kurzweil (1977) with regard to the relative noise levels for different types of bridge and track structure. Notably, it was found that concrete bridges produce noise mainly in the frequency range up to about 500Hz, while steel bridges produce significant noise over a much larger range, up to about 2kHz.

Later, Hardy (1999) presents the results of a noise measurement survey that show considerable overlap between the noise levels for different classes of bridge, including those with ballasted track and directly-fastened track. This indicates that an empirical scheme is not a suitable means to predict the noise from a proposed bridge, even in cases where measurement data is available for bridges of similar design.

As described in Section 1.3.2, bridges with a concrete deck and steel support beams have been built in recent years, mainly on the basis of relatively low construction costs. These bridges are referred to here as composite bridges and are common on urban light railways. Composite bridges have been linked to high noise levels, particularly compared with all-concrete structures (Shield et al., 1989) and (Walker et al., 1996). Noise from composite bridges on urban light railways have been the cause of complaints from local residents. Shield et al. (1989) present an example case on the Docklands Light Railway in London (DLR). These complaints were linked to very high noise levels at low frequencies, particularly for the 63Hz one-third octave band, often described as bridge 'rumbling' noise. This case demonstrates that overall A-weighted noise levels, which emphasise the higher-frequency noise components, may not correlate well with the disturbance caused by railway bridge noise to local residents.

1.4.2. Noise control measures for railway bridges

Kurzweil (1977) identifies seven different approaches to noise control for railway bridges: i) source reduction, ii) vibration isolation, iii) vibration damping, iv) mass addition, v) acoustic isolation, vi) acoustic absorption, vii) reduction of radiating area. This will be used here as a structure for reviewing the previous work on noise control measures for railway bridges.

Source reduction for railway bridge noise refers to improving the quality of the wheel and rail running surfaces. With the exception of trains with cast-iron block brakes, or the removal of rail corrugation, there is normally very limited scope for such improvements (Thompson, 2009).

The vibration isolation principle and its application to railway bridges was described in Section 1.3.5. Numerous publications describe the use of this approach to achieve significant reductions in the noise radiated by the bridge, such as Ban and Miyamoto (1975), Kurzweil (1977), Oderbrant (1996), Hardy (1999), Wang et al. (2000) and Wang et al. (2007). A particularly clear example of the use of resilient baseplates to reduce noise from a steel bridge is given by Wang et al. (2000). Originally, the track structure was of the directly-fastened wooden type. This was replaced by modern resilient baseplates, with a stiffness of approximately 30kN/mm. Vibration velocity measurements made on the bridge girders before and after the change to the track structure show a reduction of typically 5dB in the frequency range from 100Hz to 400Hz and of about 20 dB for higher frequencies. Wayside noise measurements show a reduction of 6dB(A).

Vibration isolation using resilient baseplates has been found to be one of the most effective noise control measures for railway bridges (Kurzweil, 1977) and Oderbrant (1996). However, it was noted by Wang et al. (2007) that the noise reduction achieved by using resilient fasteners is dependent on the relative levels of rolling noise and bridge-radiated noise. The reduction in overall noise achieved by changing to a more resilient track structure is often smaller than expected, because of the greater rolling noise for more resilient track supports (see Section 1.3.5).

There are means of achieving effective vibration isolation between the rail and the bridge other than resilient rail fasteners. For ballasted track, resilient mats can be laid between the ballast and the bridge deck. It may be expected that this approach would not have as great an effect on the decay rates in the rail as resilient fasteners, because the coupling between the rail and the relatively heavily-damped ballast would not be affected. For directly-fastened track, resilient material may be added between a concrete slab that supports the track and the bridge deck, so-called floating slab track. The modelling study presented by Crockett and Pyke (2000) shows that the use of

floating slab track, together with very soft baseplates, may be an effective measure for reducing bridge noise. This is a very high cost approach, but as for ballast mats, effective vibration isolation can be achieved down to very low frequencies by this means, because of the large sprung mass above the resilient layer combined with low overall stiffness.

It may be possible to treat bridge noise by increasing the damping in the bridge, using constrained layer treatments or by adding ballast to the bridge deck. The effectiveness of these measures seems to vary significantly from one case to another. This may be related to the wide range of damping levels reported for bridge structures in previous work. Hanel and Seeger (1978) report large noise reductions on fitting constrained layer damping treatments to an all-steel bridge that initially had very low damping, with an estimated damping loss factor of 0.0015. Other work indicates that the damping loss factor for an all-steel bridge may be as high as 0.05, without the use of special damping treatments (Kurzweil, 1977). This may explain the lesser effects of constrained layer damping treatments on other all-steel bridges, such those reported by Oderbrant (1996). Remington and Wittig (1985) report a similar finding for a concrete-steel composite bridge on which damping treatments were tested.

Poisson and Margiocchi (2006) used rail dampers, in the form of a tuned absorber system attached to the rails, to reduce the noise associated with the passage of a train over a bridge by about 3dB. This was achieved by reducing the rolling noise level, which was the dominant source for this steel bridge with direct fasteners. Adding damping to the rail is not expected to reduce the noise radiated by the bridge significantly, because it is only the rail vibration close to the forcing point that is related to the transmission of power to the bridge (Thompson, 1992). Tuned absorbers have also been tested on a steel bridge deck. The vibration levels were reduced at low frequencies, but there was no effect on the overall A-weighted level (Poisson and Margiocchi, 2006).

Practically, the addition of mass to an existing bridge is normally achieved by laying ballast on the bridge as a replacement for directly-fastened track. The noise surveys described in Section 1.4.1 indicate that the effects of this change may include

vibration damping, sound absorption and added mass. It is therefore difficult to identify the effect of any one of these on bridge noise.

Acoustic measures for reducing bridge noise normally involve blocking noise paths and providing a means to absorb the acoustic energy. Rolling noise is more readily treated by this means than the noise radiated by the bridge, because of its more local nature. Sound barriers beside the track are used for this purpose, such as in the case reported by Fitzgerald (1996). However, it is also possible to shield the noise radiated by the bridge structure. Kurzweil (1977) reports that a noise reduction of 27dB was achieved by fitting a complete enclosure around a bridge. However, this is clearly an extremely high cost approach.

A lesser effect can be achieved at a lower cost by using a closed bridge design, such as the concrete box-section structure shown in Figure 1.1i). The noise radiated by the underside of the bridge deck is shielded by the main box beneath the deck. A closed-section steel bridge design has also been shown to bring a noise benefit over open-girder bridges (Thompson, 2009).

As a final note, large reductions in noise from existing bridges can often be achieved by using several of the noise control measures described above for a single case. Fitzgerald (1996) presents an example of using two complementary noise control measures, resilient baseplates for the noise radiated by the bridge and noise barriers for the rolling noise. This approach was shown to reduce the overall noise level for a composite bridge by about 15dB(A).

1.4.3. Predictive models for bridge noise

A predictive model for bridge noise is sought for use in making environmental impact assessments of new railway infrastructure projects, to guide noise control programmes for existing bridges and also low-noise design of new bridges and track structures. The work of Hardy (1999) indicates that an empirical scheme is not a reliable means to predict the noise from a new bridge. Further, such an approach is clearly not an ideal basis for the development of novel noise control measures and low-noise bridge and track designs. A theoretical model for bridge noise is therefore required, based on the physical processes by which bridge noise is produced. The literature shows a range of different approaches for the development of such a model.

Ouelaa et al. (2005) present a model for bridge noise and vibration that is based on the modal superposition method. The bridge is modelled as an equivalent simply-supported beam coupled to a moving train, represented by a series of two degree-of-freedom systems for the bogies. Excitation of the bridge due to both the moving load and wheel-rail roughness is considered. However, neither the rail nor the track support structure are defined explicitly in this model. Given the important influence of the track structure on both the noise radiated by the bridge and the rolling noise, it is clear that this model does not satisfy the requirements of a predictive model for bridge noise described above.

Finite Element (FE) models have been used to study bridge noise, such as those described by (Walker et al, 1996) and (Crocket and Pyke, 2000). The main difficulty in using an FE model to predict bridge vibration and noise is the enormous number of modes expected in the frequency range of interest for bridge noise, up to approximately 1500Hz (Janssens and Thompson, 1996). Consequently, the computational demand involved in solving such a model over this frequency range is too great for it to be used for repeated design calculations. FE models for bridge noise and vibration are therefore normally used for only some lower part of the frequency range of interest. Crocket and Pyke (2000) present an FE model of a concrete box-section viaduct, track and rolling stock (for the primary and secondary suspension systems, bogie and coach masses) that has approximately 60,000 degrees of freedom. Despite this level of complexity, the model is valid only up to a frequency of about 630Hz.

The Statistical Energy Analysis (SEA) method seems to address the difficulty of using the FE method for railway bridges. The input power to each major component of the structure, or in SEA terms, each 'subsystem' of the 'SEA network', is equated to the power dissipated within it and the power flow to other subsystems (the coupling power). Individual modes are not accounted for, rather the average response of all the modes in a given frequency band is found. The fluctuations in the response of the physical system due to the effects of individual modes become smaller as the number of modes in the structure increases. Unlike the FE method, SEA therefore becomes more attractive for complex systems at high frequencies, where the number of effective modes is large. For this reason and due to its very low

computational cost, SEA has been widely used to predict bridge noise and vibration. A comprehensive account of the SEA method is given by Lyon and DeJong (1995). The development of SEA-based models for bridge noise and vibration is described here, with a more detailed account of one particular model given in Section 1.5 to follow.

Kurzweil (1977) presents an early example of an SEA-based model for bridge noise and vibration, which provides a relatively simple introduction to this type of model. The rail vibration energy is found from measurements of the rail vibration velocity and a beam on elastic foundation model for the rail and the track structure. The transmission of vibrational energy to the bridge, via the track structure, is found using an SEA model. The power flow between subsystems was found using the coupling loss factor approach, see (Lyon and DeJong, 1995) for details. The coupling loss factors were obtained from analytical expressions for idealised structural components, beams and plates.

The output of the SEA calculation is the energy of each major component of the structure (or subsystem of the SEA network). These energies can be used to find spatially-averaged velocities for each major component of the bridge, as frequency band averages. The sound power radiated by each of the bridge components is then calculated using a radiation efficiency approach. The sound pressure at a given location is found from the sound power by treating each component of the bridge as a line of incoherent point sources.

Remington and Wittig (1985) used a similar approach to model an open (no deck plate) steel bridge, with wooden sleepers. A wheel-rail interaction calculation was used for the excitation of the wheel and rail due to the roughness on the rolling surfaces. The combined roughness spectrum was calculated from rail velocity measurements, rather than being found by direct measurement. This approach was chosen in preference to using rail velocity measurements directly as an input to the bridge noise and vibration calculation, so that the effects of changes to the track structure can be evaluated using the model. Then an SEA calculation was used to predict both the vibration transmission from the rail to the bridge and also the

vibration response of the bridge, with coupling loss factors found from analytical expressions for idealised structural components.

Both Kurzweil (1977) and Remington and Wittig (1985) compared the results of the models to bridge noise measurements and showed that reasonable agreement could be obtained from this relatively simple and computationally-light approach.

Janssens and Thompson (1996) present a model for the noise and vibration from all-steel bridges with directly-fastened track, in which an SEA-based method is used to predict the response of the bridge structure, although not the vibrational power transmitted from the rail to the bridge. This, hereafter referred to as the power input to the bridge, is found from the product of the real part of the bridge input point mobility and the excitation force applied by the rail fasteners to the bridge. Note that this is valid only for the frequency range in which the motion of the rail is decoupled from that of the bridge. Simple mobility models for I-section beams are proposed and shown to compare well with FE predictions and measurements made on a bridge.

The power input to the bridge is used in an SEA-based calculation for the bridge vibration response. The rail and track structure are not included in this calculation. The bridge is divided into a number of subystems, which take the form of plates; typically one plate is used for each beam web, two for the beam flanges and one plate for the bridge deck. It is assumed that the bridge structure is *strongly-coupled* in SEA terms and that the structure is reasonably homogeneous, which is reasonable for a steel bridge unless local damping treatments are used (Janssens and Thompson, 1996). Under these conditions, it is possible to calculate the response of each plate in the system without the use of coupling loss factors. This approach to calculation of the bridge response is referred to here as a simplified SEA scheme. It is an attractive one, because finding suitable coupling loss factors may be the most difficult part of an SEA model (Harrison et al., 2000).

The model originally proposed by Janssens and Thompson (1996) has been developed further, (Harrison et al., 2000), (Bewes et al., 2006) and (Bewes, 2006). In its present form it is called NORBERT and a more detailed description is given in Section 1.5.

The development of the models for bridge noise and vibration described above has yielded a greater understanding of low-noise bridge design. An important example of this is the identification of the direct relationship between the input point mobility of the bridge and the vibrational power input to the bridge, by both Janssens and Thompson (1996) and Walker et al. (1996).

1.5. THE NORBERT BRIDGE NOISE MODEL

1.5.1. Overview

The NORBERT model calculates the vibration response of the bridge, the noise radiated by the bridge and the rolling noise during the passage of a train. The inputs to the model are sets of data that describe the rolling stock, the track structure, the bridge structure and the roughness of the wheel and rail rolling surfaces. A brief account of the calculation methodology is given here, based mainly on the description given in the manual for the NORBERT program (Thompson et al, 2005). A structure for the calculation of bridge noise is shown in Figure 1.8 below.

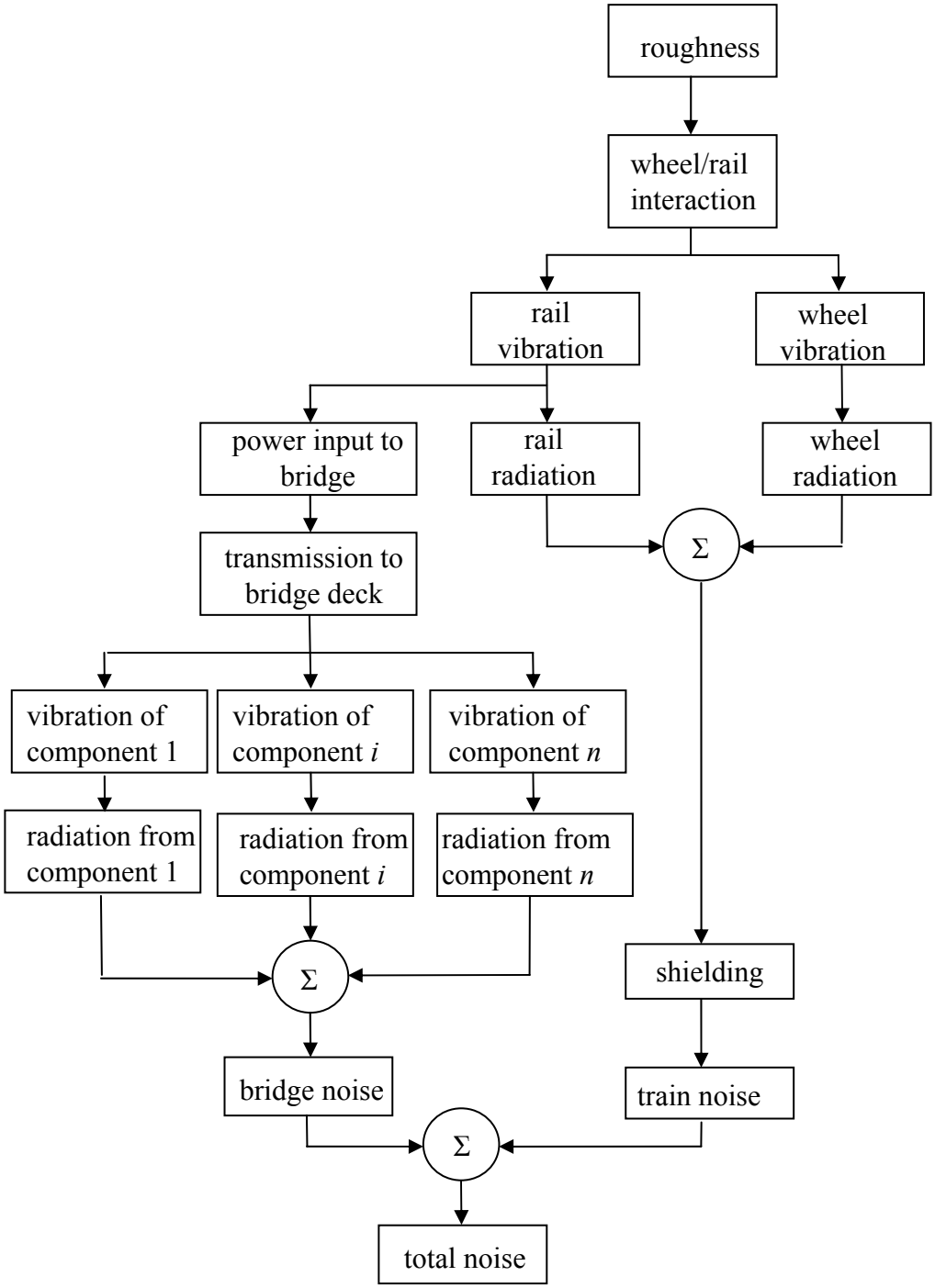

Figure 1.8. Flowchart of a model for railway bridge noise, based on (Janssens and Thompson, 1996).

The methods used to calculate bridge noise and vibration in NORBERT are described in Sections 1.5.2 to 1.5.6.

1.5.2. Excitation at the wheel-rail interface

The component velocities at the contact point and the excitation force applied to the rail can be found from the following wheel-rail interaction calculation at each frequency (Thompson, 2009),

$$v_{r,o} = \left| \frac{i\omega r Y_r}{Y_r + Y_w + Y_c} \right| \tag{1.4}$$

$$v_{w,o} = \left| \frac{i\omega r Y_w}{Y_r + Y_w + Y_c} \right| \tag{1.5}$$

$$F_{rail} = \left| \frac{i\omega r}{Y_r + Y_w + Y_c} \right| \tag{1.6}$$

where $v_{r,o}$ is the r.m.s. vibration velocity of the rail at the contact point, $v_{w,o}$ is the r.m.s vibration velocity of the wheel at the contact point and F_{rail} is the r.m.s. input force to the rail. Y_r denotes the mobility of the rail, Y_w that of the wheel and Y_c that of a linearised Hertzian contact spring between them (Grassie et al., 1982). r is the r.m.s. combined wheel-rail roughness. Note that only vertical motion is considered in the model, which is expected to be adequate for the case for straight track. However, lateral excitation forces may be significant for curved track (Bewes, 2006).

The wheel mobility is found from a two degree-of-freedom model for each wheel, shown in Figure 1.9.

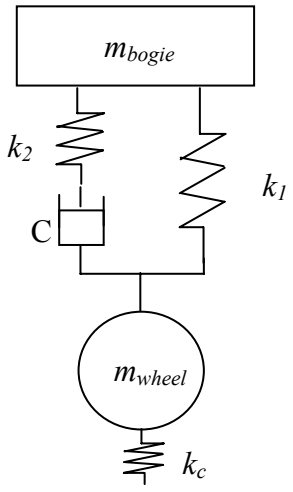

Figure 1.9. Two degree-of-freedom model for each wheel of the train.

m_{bogie} represents the bogie mass per wheel and m_{wheel} the unsprung mass per wheel. The use of a mass to represent the wheel is normally adequate in the frequency range of interest for bridge noise. Two springs, k_1 and k_2, and a viscous damper, C, represent the primary suspension. Physically, spring k_2 represents bushes and/or the 'blow/off' characteristics of the damper. k_c represents the stiffness of the linearised Hertzian contact spring between the wheel and rail, which has been set to 1.3GN/m in this work. A notional damping loss factor of 0.1 is applied to the contact spring, required to prevent excessive vibration at the contact resonance (around 80Hz).

The rail mobility is found from a model of the rail as a Timoshenko beam continuously connected to another Timoshenko beam, for the bridge, by up to three continuous resilient layers and up to two continuous mass layers. This will be referred to as the coupled beam model hereafter and it is described further in Section 1.5.3.

The r.m.s. roughness amplitude is found from roughness measurements made on wheel and rail running surfaces. The wheel and rail roughness spectra are added in the frequency domain, assuming that they are uncorrelated (Thompson et al. 1996a). No account is taken of the low-frequency excitation associated with the moving axle load, which is expected to be significant only for frequencies lower than about 25Hz (Bewes, 2006).

The measurement of wheel and rail roughness is a specialised activity, such that measurements for wheel and rail roughness levels are not normally made on a case-by-case basis. Average roughness spectra have been produced from measurement programmes such as those reported by (Dings and Dittrich, 1996), (Thompson et al., 1996a), (Thompson et al., 1996b) and (Hardy, 1997). These roughness measurements have been extended to longer wavelengths using track geometry data from (Esveld, 1989) and are available for use in the NORBERT program.

1.5.3. Power input to the bridge

In the frequency range over which the bridge is expected to behave as a Timoshenko beam, the coupled beam model introduced in Section 1.5.2 is used to calculate the power input to the bridge. Either a coupled infinite Timoshenko beam model or a coupled finite Timoshenko beam model may be used. For the finite length model,

the beams are simply supported at their ends and are assigned a length equal to that of the bridge spans. The layers of resilience and mass between the two beams are specified to represent the track structure. While the track supports are normally periodic, no account is taken of this in the coupled beam model; the support is treated as continuous. It is expected that some error will be introduced by this simplified treatment of the track support structure in the frequency range around 1kHz, due to the so-called 'pinned-pinned' mode of the rail between the discrete supports.

A ballast layer can be modelled using a resilient layer in which distributed mass and stiffness effects are accounted for, such that the expected internal modes of the ballast layer can be included in the analysis. However, there is currently a lack of evidence in the literature to support the approach taken in this part of the calculation. Further, when NORBERT has been used for bridges with ballasted track, the predicted noise and vibration levels have generally shown less agreement with measurement data than is normally the case for bridges with directly-fastened track.

For some resilient baseplates of relatively complex design, internal modes are expected within the frequency range of interest for bridge noise. In previous work, these have been modelled using two resilient layers and one mass layer. However, the suitability of this modelling approach is unclear because measurement data for the high-frequency dynamic stiffness of these baseplates is not available.

The power input to the bridge per wheel, per unit force applied to the rail is found from the coupled beam model as follows,

$$P_{in} = \frac{1}{2} Re \int_{-L/2}^{L/2} F^*(x) \dot{W}_{bridge}(x) dx \qquad (1.7)$$

where F^* is the complex conjugate of the force applied by the track structure to the bridge, found from the product of the displacement across the resilient layer adjacent to the bridge and its transfer stiffness. $\dot{W}_{bridge}(x)$ represents the velocity of the bridge at the base of the track and L the length of the bridge.

The power input to the bridge for the idealised excitation (equation (1.7)) is then corrected for the number of wheels on the bridge and the roughness excitation force as follows,

$$P_{bridge} = N_w F_{rail}^2 P_{in} \tag{1.8}$$

where N_w is the number of wheels on the bridge.

In the frequency range in which the bridge is not expected to behave as a Timoshenko beam and it is decoupled from the rail, an alternative method is used to calculate the power input to the bridge,

$$P_{bridge} = Re\{Y_{br}\} F_{brid}^2 \tag{1.9}$$

where Y_{br} is the input point mobility of the bridge. F_{brid} is the r.m.s. force applied by the track support to the bridge, found from the velocity of the rail at the contact point between a single wheel and the rail, the number of wheels on the bridge and a modified track transfer stiffness, k_{eq}, as follows,

$$F_{brid}^2 = \left(\frac{|k_{eq}| v_{r,o}}{\omega} \right)^2 N_w \tag{1.10}$$

where,

$$k_{eq} = \frac{0.45 \lambda_{min}}{L_{spacing}} \tag{1.11}$$

The use of a modified track transfer stiffness follows from the work of Thompson (1992), which shows that for two continuously-coupled beams with excitation at the upper beam, only vibration within about half a wavelength of the excitation force transmits net power to the lower beam. λ_{min} is the smaller of either the wavelength in rail or in the bridge beam and $L_{spacing}$ is the distance between track supports.

The input point mobility of the bridge is calculated using expressions for the mobility of an I-section beam, from Bewes (2006) and a thick plate, from (Cremer et al., 1988). For bridges that have support beams and a deck, the lateral distance between the input point and the support beam is expected to control the relative influence of the support beam and the deck on the mobility of the bridge. In NORBERT, the mobility of the beam is used up to the frequency at which the lateral distance between the input point (the base of the track support) and the centre-line of the support beam is equal to one-quarter of a bending wavelength in the bridge deck. At higher frequencies, i.e. when the distance between the input point and the centre-line of the

support beam is greater than one quarter of a bending wavelength in the deck plate, the mobility of the bridge is set to that of the deck.

For bridges in which the mobility of the beams and the deck are substantially different, such as all-steel bridges, this switch between the beam mobility model and plate mobility model may introduce a large step-change to the input mobility of the bridge and therefore also to the input power to the bridge. Physically, however, a transition would be expected between beam and plate-dominated behaviour, over some range of frequencies. This is a part of the model that requires further study.

1.5.4. Vibration response of the bridge

The vibration response of the bridge is found by application of the simplified SEA scheme introduced in Section 1.4.3. In the steady state, the input power to the bridge must equal to the power dissipated within it plus that radiated as sound,

$$P_{bridge} = P_{diss} + P_{rad} \approx P_{diss} \tag{1.12}$$

where it can normally be assumed that the radiated power, P_{rad}, is small relative to the dissipated power P_{diss}. The power dissipated within each plate subsystem is related to its mean-square velocity as follows (Cremer and Heckl, 1988),

$$P_{diss,i} = 2\pi f \eta_i \rho_i h_i A_i \left\langle v_i^{\,2} \right\rangle \tag{1.13}$$

where η_i is the damping loss factor of plate i, ρ_i its density, h_i its thickness and A_i its surface area. $\left\langle v_i^{\,2} \right\rangle$ is the spatially averaged mean square velocity.

If the bridge can be assumed to be *strongly-coupled* in SEA terms and reasonably homogeneous, the vibrational energy per mode in each subsystem will tend to equalise across the system (Lyon and DeJong, 1995). This is commonly referred to as the *equipartition of modal energy*. The ratio of the mean-square velocities in two subsystems is then equal to the ratio of their mobilities (Cremer and Heckl, 1988),

$$\frac{\left\langle v_i^{\,2} \right\rangle}{\left\langle v_j^{\,2} \right\rangle} = \frac{Re\left(Y_i\right)}{Re\left(Y_j\right)} \tag{1.14}$$

and for the plate subsystems used here with identical material properties, this can be related to their thickness,

$$\frac{Re(Y_i)}{Re(Y_j)} = \frac{h_j^2}{h_i^2} \tag{1.15}$$

If all the subsystems of the bridge have the same material properties and damping loss factor, the spatially-averaged mean-square velocity of subsystem *j* can be obtained from (Janssens and Thompson, 1996),

$$\left\langle v_j^2 \right\rangle = \frac{P_{bridge}}{2\pi f \eta \rho h_j^2 \sum_i \frac{A_i}{h_i}} \tag{1.16}$$

Equipartition of modal energy is not expected to apply for concrete-steel composite bridges, in which a thick concrete deck is connected to relatively thin-walled steel beams (Thompson et al., 2005). As an alternative to the use of a relatively complex SEA scheme, in which coupling loss factors are required as inputs to the calculation, Bewes (2006) proposed that concrete-steel composite bridges could be modelled using two SEA networks; one for the steel beams and one for the concrete deck. Equipartition of modal energy is expected to apply within each of these networks, such that the simplified SEA scheme described above can be applied to each network separately. One of the SEA networks must be chosen as the primary SEA network, which receives vibrational energy from the track supports. Intuitively, this would be the network for the relatively thick concrete deck, which would impose its velocity as an edge excitation to the steel beam. The power flow, P_{edge}, between the two networks is then given by (Beranek and Ver, 1992),

$$P_{edge} = L_{ex} v_1^2 \, Re(Z') \tag{1.17}$$

where L_{ex} is the excitation length, v_1 is the r.m.s. velocity of the primary component and Z' is the impedance of the secondary component per unit width. The vibration response of the plates in the secondary SEA network is found by application of equation (1.16) for the power input given by equation (1.17).

Bewes (2006) trialled this two SEA network approach for modelling concrete-steel composite bridges, with the deck as the primary network and also with the steel beam as the primary network, together with several options for the input point mobility calculation. Reasonable agreement with measurements was obtained for frequencies between 60Hz and 630Hz using the deck as the primary SEA system together with

the mobility calculation based on the switch between the beam and plate models. Large differences between the measured and predicted vibration levels were found outside this frequency range.

1.5.5. Sound power radiated by the bridge

The spatially averaged velocity of the plates can be used to calculate the sound power radiated by the bridge from,

$$P_{rad} = \rho_o c_o \sum_i \sigma_i A_i \left\langle v_i^2 \right\rangle \tag{1.18}$$

where ρ_o and c_o are the density of air and the speed of sound in air respectively and σ_i is the radiation efficiency of plate i, obtained from standard formulae for beams at low frequencies and simply supported baffled plates at higher frequencies.

1.5.6. Rolling noise

NORBERT contains a database of transfer functions for rolling noise spectra from wheel-rail roughness spectra. These transfer functions have been calculated using the separate predictive model for rolling noise, TWINS, for three different wheel designs and three different track structures. Corrections are applied to account for the differences between these reference cases and that under consideration, with regard to the effect of the track stiffness on the wheel and rail vibration, and also the effect of the decay rate in the rail on the noise radiated by the rail. The overall noise associated with the passage of a train on a bridge can be estimated by this means together with the calculation of the noise radiated by the bridge, with minimal additional user input or computational cost. More reliable rolling noise estimates can be obtained from a TWINS model for the specific rolling stock and track combination, if required.

1.6. PROJECT SPONSOR

This research has been carried out as an EngD project, the principles of which are to conduct industrially relevant work with a sponsor in such a way that the knowledge and know-how is transferred to industry. Pandrol is a UK-based company specialising in the design and manufacture of rail fasteners and associated installation equipment. Pandrol supplies over 200 railway systems in 91 countries worldwide

and has the largest share of the rail fastener market. This has been achieved through the development of a wide range of rail fastener products, from relatively simple low-cost fasteners, such as those described in Section 1.3.3, to sophisticated resilient baseplates.

Railway bridges are an important application for resilient baseplates, due to the noise impact of bridges and the influence of the track structure on this noise impact. Pandrol therefore has a commercial interest in the development of a predictive model for bridge noise, inclusive of the role of the track structure. Such a model can be used to guide the design of new products and to select the most appropriate fastener for a given application. Perhaps the most important reason for Pandrol to develop a bridge noise model is to demonstrate to its customers that it understands the nature and solution of the engineering problems that their products are required to address.

The NORBERT model has been used for these purposes prior to this project (Wang et al. 2007) and also during the present work (Herron, 2008). The work outlined in Section 1.7 below is intended to improve Pandrol's ability to predict the vibration response and noise for types of bridge that represent important applications for resilient baseplates.

1.7. PROJECT OBJECTIVES AND THESIS STRUCTURE

The NORBERT model was evaluated against noise and vibration measurement data for three different types of bridge in a previous EngD project, (Bewes, 2006). Several areas of the model that require further development were identified from this evaluation. In addition, the limited use of NORBERT for bridges with ballasted track in previous work indicates that its predictive ability is poorer than that for bridges with directly-fastened track.

The overall objective of this work is to test the NORBERT model further, particularly with regard to the issues identified by Bewes (2006) and the treatment of bridges with ballasted track, and to develop alternative calculation methods where required. This has been pursued using an advanced method of structural analysis, together with laboratory tests and measurements on a railway bridge.

There are five specific objectives within this overall project objective, each relating to an aspect of the NORBERT model in which there is a need for further work. A single chapter of the thesis has been dedicated to each of these five objectives.

In Chapter 2, the approach taken to calculation of the input point mobility of an all-steel railway bridge in NORBERT is studied using a range of analysis methods. The objective of this work is to assess the NORBERT mobility model, particularly with regard to the switch made between the mobility of the support beam and that of the deck at some discrete frequency (see section 1.5.3), and to develop an alternative mobility calculation where necessary. One of the analysis methods used here, an advanced FE approach called the Waveguide Finite Element (WFE) method, is found to be particularly appropriate for studying the response of some important types of bridge.

Chapters 3 and 6 describe the use of the WFE method to model the vibration response of a concrete-steel composite bridge and a concrete box-section viaduct. The objective of this work is to evaluate further the approaches proposed by Bewes (2006) for application of NORBERT to these types of bridge and, again, to propose alternative methods where required.

The objective of the work described in Chapter 4 is to find a means to model the dynamic behaviour of the ballast layer in NORBERT that is supported by suitable measurement data. A programme of laboratory measurements is described, together with the assessment of three simple models against this data. Chapter 5 describes similar work for resilient baseplates, again with the aim of developing a proven means to model this type of track structure in NORBERT.

Chapter 7 presents a set of conclusions for the work described in Chapters 2 to 6 and recommendations for future work.

1.8. ORIGINAL CONTRIBUTION

The application of the WFE method to railway bridges is a major part of the work presented in this thesis. To the author's knowledge, this is the first time WFE has been used for this purpose and it has provided new knowledge with regard to the vibration response characteristics of three different types of bridge. For all-steel bridges with a plate-like deck and I-section beams beneath the deck, an improved

simple model for calculating the input point mobility was developed from the results of the WFE analysis. For concrete-steel composite bridges and concrete box-section bridges, the WFE analysis shows that their vibration response is complex and requires a more detailed modelling approach than that available in NORBERT.

The WFE method has also been used to calculate the transmission of power from the rail to the bridge via the track structure and the vibration response of the bridge during the passage of a train. This is of particular value for concrete-steel composite and concrete box-section bridges, which are not amenable to the use of simple structural models such as those contained in NORBERT. Further, the WFE-based modelling approach developed in this work is more attractive than one based on conventional FE methods, mainly due to its calculation efficiency.

The second major topic of the work presented in this thesis is the development of improved means to model the track support structure on railway bridges for use in predicting bridge noise and vibration. Measurements have been made for the high-frequency dynamic transfer stiffness of a layer of railway ballast between two concrete blocks. These measurements provide evidence to support the approach taken to modelling ballast in NORBERT, which was previously unavailable for the case of ballast on a stiff foundation such as a concrete bridge deck.

A combined FE and experimental study of the high-frequency dynamic behaviour of a typical commercial two-stage resilient baseplate rail fastener has also been conducted. It is found that bending modes of the cast-iron top plate need to be considered in modelling bridges with this type of track structure. This has an important effect on the dynamic stiffness of the baseplate and it may be particularly significant in rolling noise. Means of accounting for this behaviour in modelling the track have been developed in this work.

2. MODELS FOR THE INPUT POINT MOBILITY OF A RAILWAY BRIDGE

2.1. THE MOBILITY MODEL IN NORBERT

2.1.1. Introduction

The need to calculate the input point mobility of the bridge, in order to find the input power to the bridge in NORBERT, was described in Section 1.5.3. The mobility model in NORBERT is based on expressions for the mobility of idealised bridge components; a beam and a plate. The beam represents the primary support beams that are normally orientated parallel to the axis of the bridge and the plate represents the bridge deck. The approach taken to the calculation of the beam and plate mobilities in NORBERT is described in Sections 2.1.2 and 2.1.3. The means by which these are used to find the input point mobility of the bridge is described in Section 2.1.4.

2.1.2. Mobility of the support beam

I-section girders are commonly used as the primary support beams in a railway bridge, (Janssens and Thompson, 1996). NORBERT contains a set of expressions for the mobility of an I-section beam, divided into three different frequency ranges. At low frequency, it is modelled as a finite simply-supported Timoshenko beam, with a length equal to the bridge span (Thompson et al., 2005). The modes of the support beam are therefore accounted for in this frequency range.

At high frequencies, there is longitudinal or 'in-plane motion' in the beam's web and bending motion in the beam's flanges. In this frequency range, the mobility of the support beam is found from the combination of the mobility of the beam flange, treated as a normally-excited flat plate, and that of the beam web treated as an edge-excited flat plate (Thompson et al., 2005). In an intermediate frequency range, an empirical transition is made between the results of the low and high frequency models.

This set of equations will be referred to here as the Bewes equations for the mobility of an I-section beam, described in (Bewes, 2006). Note that an infinite structure model of the beam is used in the high frequency range, such that the result represents a spatial and frequency average input mobility of an equivalent finite structure with a

high modal density (Skudrzyk, 1980). It is expected that this condition will be met for the frequency range in which there is in-plane motion in the beam web, so that it is also reasonable to neglect the modes of the beam in the intermediate frequency range, where the empirical calculation for the mobility of the beam is used.

In some bridges there are beams orientated perpendicular to the axis of the bridge, called cross-beams here, in addition to the primary beams. These cross beams have smaller cross-section dimensions than the primary beams, such that they usually have a lesser effect on the input point mobility of the bridge, but there are exceptions to this. In some cases, particularly those with wooden directly-fastened track, the track supports are connected to the cross-beams. The cross-beams may then have an important influence on the input point mobility of the bridge in some higher frequency range. The work of Behr (2005) also suggests that the effect of local reinforcements to the deck (such as cross-beams) on the input point mobility of the bridge may be greater for bridges with ballasted track. Modelling a bridge with cross-beams is therefore particularly challenging and relies greatly on the judgement of the user. Bridges with cross-beams are not considered further in this thesis.

2.1.3. Mobility of the bridge deck

The mobility of the bridge deck is normally used in NORBERT only for relatively high frequencies. It is assumed that the modal density of the deck is large in this range, such that an infinite plate model can be used to represent the deck.

The point mobility of an infinite plate, in the frequency range in which the effects of transverse shear motion and rotational inertia are small, is given by,

$$Y_{11}(\omega) = \frac{1}{8\sqrt{\rho h D}} \tag{2.1}$$

where,

$$D = \frac{Eh^3}{12\left(1-\upsilon^2\right)} \tag{2.2}$$

is the flexural rigidity, E is the Young's modulus, h is the plate thickness, υ is the Poisson's ratio and ρ is the density. This will be referred to as the thin plate model here.

In NORBERT, the mobility of the deck plate is calculated from the so-called thick plate equation. This is equivalent to equation (2.1) for low frequencies, but accounts

for the effects of transverse shear deformation and rotational inertia at high frequencies. The point mobility of the thick plate is given by (Cremer et al, 1988),

$$Y_{11}(\omega) = \frac{1}{8\sqrt{\rho h D}} \frac{1 + \frac{\rho h^2}{24 G^*} \left[\frac{12D}{G^* h^3} - 1 \right] \omega^2}{\sqrt{1 + \frac{\rho h^5}{576 D} \left[\frac{12D}{G^* h^3} - 1 \right]^2 \omega^2}} \tag{2.3}$$

where G is the shear modulus and $G^* = 0.85G$ is a reduced shear modulus.

2.1.4. Application of beam and plate models to a railway bridge

Sometimes a bridge is designed so that the rails and therefore the track supports are located directly above the longitudinal support beams in the bridge. With regard to bridge noise, this is an attractive approach because the input point mobility and therefore the input power to the bridge at these positions are smaller than for other rail positions on a given bridge structure. For bridges where the track supports are positioned at some lateral distance d from the centre-line of the support beam, this distance is expected to control the relative influence of the support beam and the deck on the point mobility. The NORBERT mobility model calculates the point mobility of the bridge based on the following 'switch' between the mobility of the support beam and that of the deck plate (Bewes, 2006).

$$\text{For } d < \frac{\lambda}{4}, \text{ then } Y_{bridge} = Y_{beam} \tag{2.4}$$

$$\text{For } d > \frac{\lambda}{4}, \text{ then } Y_{bridge} = Y_{plate} \tag{2.5}$$

where λ is the bending wavelength in the deck. Physically, this means that the influence of the beam dominates the point mobility at positions that are within a lateral distance of one-quarter of a bending wavelength in the deck from the support beam. For positions on the deck that are further from the support beam, the influence of the deck controls the point mobility.

The switch in mobility models described by equations (2.4) and (2.5) means that for a bridge in which the track supports are at some lateral distance from the longitudinal beams, the input power to the bridge is found from the mobility of the primary support beam in some lower frequency range and from the mobility of the deck in some higher frequency range. In a steel bridge, the mobility of the I-section beam is

normally small relative to that of the bridge deck in the frequency range up to that in which in-plane motion in the web of the I-section beam becomes important. For these bridges, the switch in mobility model therefore introduces a large step-change to the input mobility of the bridge and therefore also to the input power to the bridge. Physically, it is expected that the input mobility of the bridge would show a transition between the mobility of the beam and that of the plate over some range of frequencies, rather than a step-change at some particular frequency. The switch in mobility models described by equations (2.4) and (2.5) may therefore cause significant error in some part of the frequency range of interest, for bridges in which the track supports are offset from the centre-line of the support beams.

The aims of this chapter are to assess the suitability of the NORBERT mobility model and to develop an alternative model if this is found to be necessary. Three progressively more detailed analyses have been made for the mobility of a coupled beam and plate structure. Model 1 is based on the mobility of a beam at a point some distance from a supporting spring, presented in Section 2.2. Model 2 is based on the mobility of a plate at some distance from a supporting beam obtained using an analytical approach, described in Section 2.3. Model 3 is for the same structure but obtained using a finite element approach, see Section 2.4.

2.2. MODEL 1: ONE DIMENSIONAL MODEL OF A BRIDGE

2.2.1. Description of model 1

As a simple example of the behaviour to be investigated, *i.e.* that of a bridge which consists of a deck plate and a support beam, a model was constructed of an infinite beam and a spring. This is shown in Figure 2.1 below.

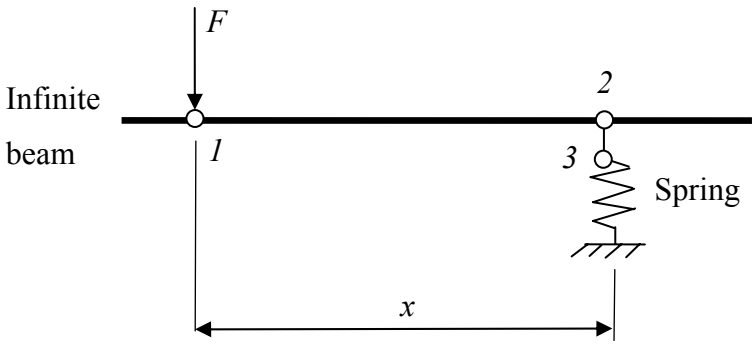

Figure 2.1. One dimensional model of a railway bridge cross-section.

The one dimensional model shown in Figure 2.1 consists of an infinite beam that represents the bridge deck and a spring that represents the support beam. A rigid link connects positions 2 and 3.

The point and transfer mobility terms at frequency ω relate the velocity amplitude at positions 1 and 2 on the beam to the applied force amplitude at position 1,

$$v_1 = Y_{11}F_1 + Y_{21}F_2 \tag{2.6}$$

$$v_2 = Y_{12}F_1 + Y_{22}F_2 \tag{2.7}$$

where v_n is the velocity at position n and F_n is the applied force. For the mobility terms, Y_{nm} , the left-hand index indicates the force position and the right-hand index refers to the velocity position. For a linear system, the two transfer mobility terms are identical.

At position 2, the spring force is related to the velocity by,

$$v_2 = Y_{33}F_2 \tag{2.8}$$

where Y_{33} is the mobility of the spring. Substituting equation (2.8) into (2.7),

$$Y_{33}F_2 = Y_{12}F_1 + Y_{22}F_2 \tag{2.9}$$

$$\therefore F_2 = \frac{Y_{12}F_1}{Y_{33} - Y_{22}} \tag{2.10}$$

Now substituting for F_2 in equation (2.6) gives the mobility of the combined system,

$$Y_{system} = \frac{v_1}{F_1} = Y_{11} + \left(\frac{{Y_{12}}^2}{Y_{33} - Y_{22}} \right) \tag{2.11}$$

For this simple analysis, it is appropriate to use Euler beam theory to calculate the point and transfer mobility of the infinite beam, neglecting transverse shear and rotational inertia effects. The point mobility of an infinite beam without the spring is the same at all positions along the beam. The point mobility is given by,

$$Y_{11}(\omega) = Y_{22}(\omega) = \frac{\omega(1 - i)}{4EI{\kappa_b}^3} \tag{2.12}$$

and for $x \geq 0$, the transfer mobility to a point x is given by,

$$Y_{12}(\omega) = Y_{21}(\omega) = \frac{\omega}{4EI\kappa_b^{\,3}}\left(e^{-i\kappa_b x} - ie^{-\kappa_b x}\right) \tag{2.13}$$

where the bending wavenumber κ_b is given by,

$$\kappa_b = \sqrt[4]{\frac{\rho A}{EI}\omega^2} \tag{2.14}$$

Equation (2.14) gives four solutions: a near-field wave for each direction along the beam, with wavenumbers of $\kappa = \pm i\kappa_b$, and a propagating wave for each direction, with wavenumbers of $\kappa = \pm\kappa_b$.

The results of equations (2.12) and (2.13) can be used in equation (2.11) to calculate the mobility of the combined beam and spring system.

2.2.2. Results of model 1

Mobilities calculated from the model described in Section 2.2.1 are given here to demonstrate the behaviour of the system. These are presented in terms of a normalised mobility and a normalised distance between the input point and spring, defined as follows,

$$\tilde{Y}_{Norm} = \left|\frac{Y_{system}}{Y_{spring}}\right| \tag{2.15}$$

and,

$$x_{Norm} = \frac{x}{real(\lambda_{beam})} \tag{2.16}$$

Two different cases are considered here: one in which the beam has a magnitude of point mobility that is ten times larger than that of spring, and one in which the beam has a magnitude of point mobility that is twice as large as that of spring A damping loss factor of 0.1 has been assigned to the beam in each case.

Figures 2.2 i) and 2.2 ii) show the point mobility as a function of distance between the input point and the spring for these two systems.

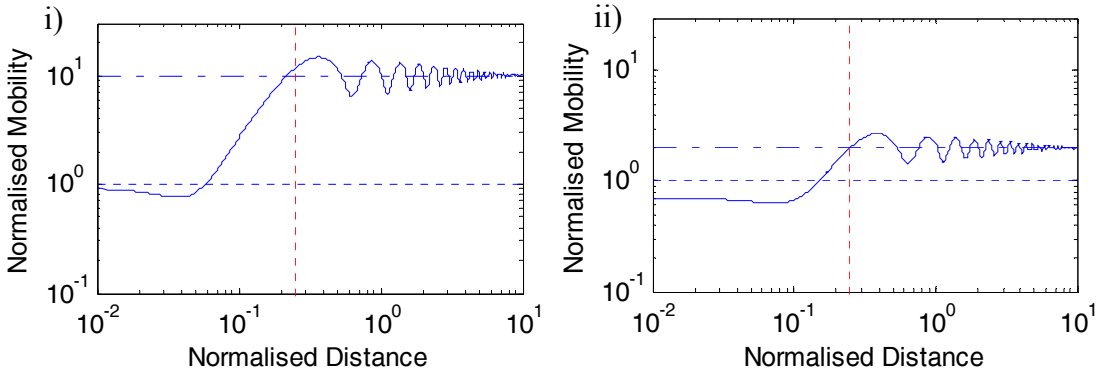

Figure 2.2. Normalised point mobility shown against normalised distance between the input point and spring, i) beam mobility (magnitude) ten times larger than that of spring, ii) beam mobility (magnitude) twice as large as that of spring: ——— *, beam and spring model;* – · – · – · *, uncoupled beam;* – – – – *, uncoupled spring;* – – – – *, indicates one-quarter of a bending wavelength in beam.*

Figure 2.2 i) shows the expected behaviour: the point mobility of the system is similar to that of the spring for input points that are located close to the spring and makes a transition to that of the beam (in a spatially-averaged sense) as the input point is moved toward one-quarter of a bending wavelength away from the spring.

Figure 2.2 ii) shows that when the mobility of the spring is not small relative to that of the beam, the input point mobility of the system is significantly lower than that of either the beam or spring for positions close to the spring. This would be expected, since the beam and spring are combined in parallel and this combination would be characterised by the sum of their impedances. As the input point is moved away from the beam, the system mobility again tends toward that of the beam in a spatially-averaged sense. This simple model thus indicates the type of transition that the point mobility makes as the forcing point moves away from the support.

Further results from this model will be presented in Section 2.5, together with those from the more complex models described in Sections 2.3 and 2.4 below. The next model is of a plate supported by a beam and therefore is a much fuller representation of the transition made by the point mobility of a plate-beam bridge as the forcing point moves away from the location of the support beam.

2.3. MODEL 2: TWO-DIMENSIONAL MODEL OF A BRIDGE

Yoo et al. (2004) developed an analytical model for the response of an infinite beam coupled to a thin plate of infinite length, but finite width. A very similar approach has been used here to model a plate that is of infinite width and length, coupled to an infinite beam. A detailed description of this model is given in Appendix A. Some results from this model are presented here for a structure intended to represent a steel railway bridge. A rectangular-section beam has been considered, because the Euler beam model used in the analysis is applicable to this type of beam over a larger frequency range than it is for an I-section beam. This system is shown in Figure 2.3 below.

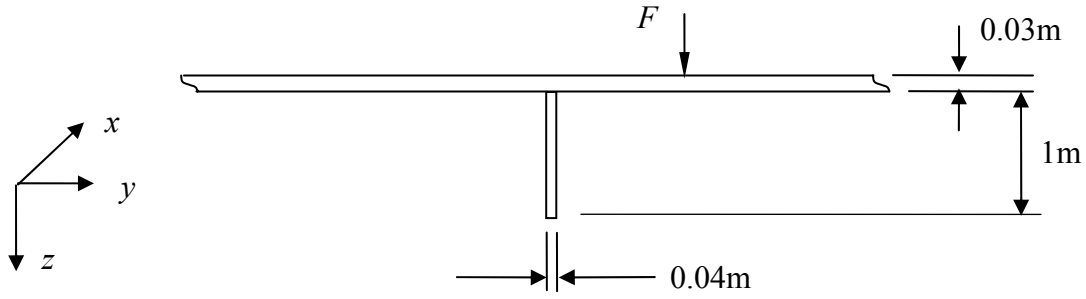

Figure 2.3. Infinite plate and infinite beam structure.

It has been assumed in this analysis that the beam does not rotate. This is a reasonable simplifying assumption, given the large torsional stiffness of the beam relative to the bending stiffness of the thin plate. A damping loss factor of 0.01 and the material properties for steel given in Table 2.1 have been used for both the beam and the deck.

Property	Value
Dynamic Young's Modulus (GPa)	207
Density (kg/m^3)	7800
Poisson's ratio	0.3

Table 2.1. Material properties for the steel beam and deck.

The input point mobility of this structure in the wavenumber domain is shown in Figure 2.4 below, as a function of the wavenumber in the *x* directon, for three different distances between the input point and the support beam, *d*, at a frequency of 100Hz. The real part the input point mobility is shown here because this relates directly to the power input to the structure.

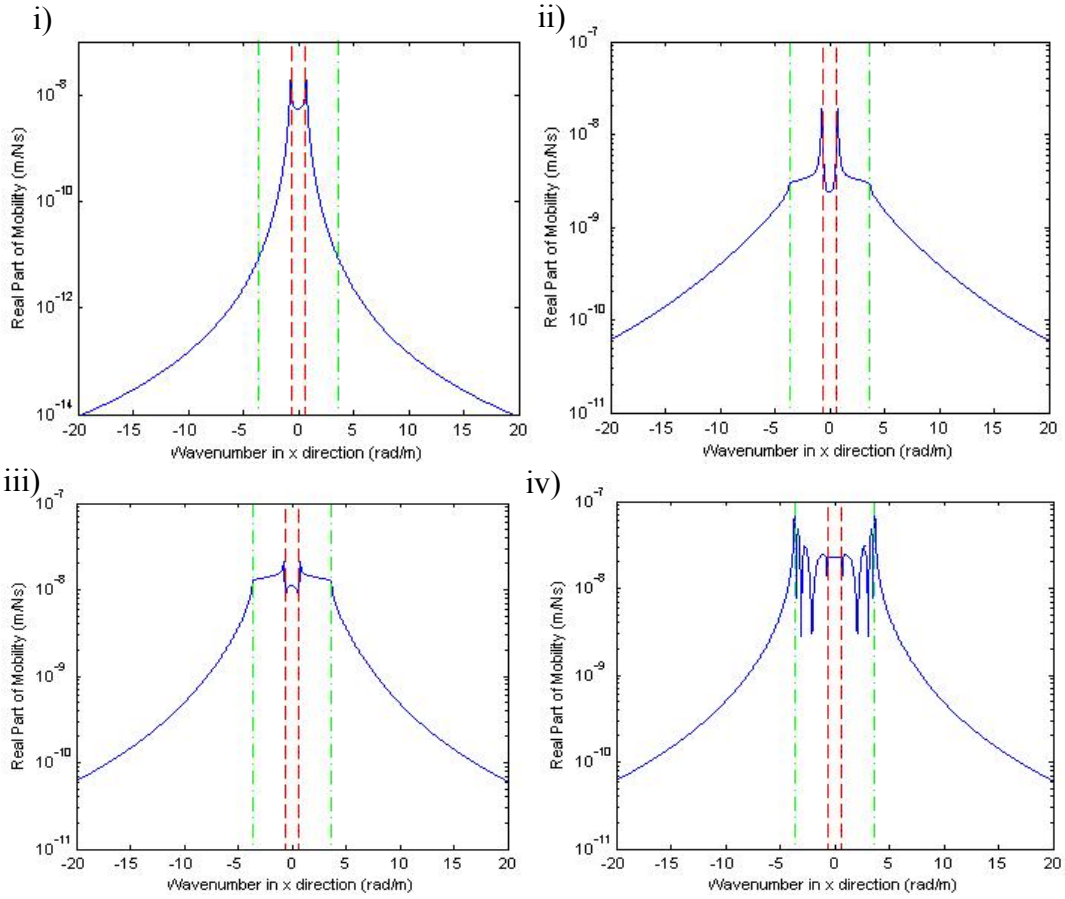

Figure 2.4. Real part of input point mobility of the coupled plate and beam system shown versus wavenumber in the x direction, at a frequency of 100Hz. i) for $d = 0$, ii) $d = \lambda / 8$, iii) $d = \lambda / 4$, iv) $d = 2\lambda$, _____, analytical solution; _ _ _ _, free plate wavenumber; _ _ _ _, free beam wavenumber.

For a position directly over the beam, Figure 2.4 i) shows that the point mobility of the structure in the wavenumber domain has large peaks centred on the free beam wavenumbers. The point response of the structure at this position is therefore dominated by the behaviour of the beam.

At a lateral distance of *λ/8* and *λ/4* from the support beam, Figures 2.4 ii) and iii) show significant response around both the free plate wavenumber and the free beam wavenumber. Figure 2.4 iv) shows that for a position two wavelengths away from the support beam, the point mobility is dominated by large peaks centred on the free plate wavenumber.

In summary, the results of the two dimensional beam and plate model presented here in the wavenumber domain serve to confirm the conclusions drawn from the one-

dimensional system analysis given in Section 2.2. Spatial-domain results from this two dimensional model are presented in Section 2.5.

2.4. MODEL 3: WAVEGUIDE FINITE ELEMENT MODEL OF A BRIDGE

2.4.1. The Waveguide Finite Element method

If a structure can be idealised for vibration modelling purposes to be infinitely long and have a constant cross-section, special modelling methods can be used to analyse its vibration with much better efficiency than conventional three-dimensional numerical techniques such as the finite element method. The individual spans of many railway bridges are suitable for this kind of idealisation. A novel finite element (FE) approach to modelling this class of structure has been developed, (Gavric, 1992), (Karassalo, 1994), (Nilsson, 2004). This will be referred to here as the Waveguide Finite Element (WFE) method. Since the cross-section properties are constant in one direction, it is sufficient to use finite elements to represent only the cross-section of the structure. The deformation of the structure in the direction of wave propagation, along its length, is described using an analytical form; complex exponential terms representing waves propagating along the axis of the waveguide.

The advantage of using WFE rather than conventional FE for 'waveguide structures' is the much lower computational cost, due to the relatively limited use of finite elements in WFE. It can therefore be expected that WFE, unlike conventional FE, can be used to predict the response of a railway bridge over the frequency range of interest to bridge noise in a reasonable time scale.

2.4.2. Basis of the WFE method

The basis of the WFE approach is briefly described here, in order to provide a background for the description of how WFE has been used in this work to study the vibration response of railway bridge structures. Software developed by Nilsson (2004) has been used to produce mass and stiffness matrices from an element description of the structure. The focus of the work presented here is therefore the use of these matrices to calculate the free and forced vibration response, rather than the element or matrix formulations. This is described below, based on the more comprehensive accounts of the WFE method given by (Gavric, 1992), (Karassalo, 1994) and (Nilsson, 2004).

The structure under analysis is defined in three-dimensional space, using *x, y* and *z* coordinates. The cross-section lies in the *y-z* plane and the wave propagation is in the *x* direction, in which the structure is of infinite extent. The structure undergoes steady state harmonic motion at circular frequency ω, such that the deformation is elastic. The displacement at any node in the cross-section, for a single wave of wavenumber κ, can be described by,

$$\mathbf{W}_i(x,y,z,t) = \bar{\mathbf{W}}(y,z)e^{-i\kappa x}e^{i\omega t} \tag{2.17}$$

where $\mathbf{W}$ is the displacement, a function of the coordinates in three perpendicular directions and time *t*. $\bar{\mathbf{W}}$ is the displacement of the cross-section, a function of coordinates in two perpendicular directions (*y* and *z*) that define the plane of the cross-section. The virtual work principle is the basis for the development of the equations used to describe the behaviour of the structure. For details of this development procedure, see (Petyt, 1990). This leads to a set of linear algebraic equations of the following form (Nilsson, 2004).

$$\left(\sum_{j=0}^{4} \mathbf{K}_j \left(\frac{\partial^j}{\partial x^j} \right) - \omega^2 \mathbf{M} \right) \bar{\mathbf{W}}(x) = \bar{\mathbf{F}}(x) \tag{2.18}$$

where $\mathbf{K}_j$ are a set of stiffness matrices, *j* takes the values 0, 1, 2 and 4 for the plate elements used in this work, $\mathbf{M}$ is the mass matrix and $\bar{\mathbf{F}}$ is the force vector for the cross-section. Equation (2.18) can be written in the following form, by referring to equation (2.17) for the partial derivative terms.

$$\left(\sum_{j=0}^{4} \mathbf{K}_j (-i\kappa)^j - \omega^2 \mathbf{M} \right) \bar{\mathbf{W}}(x) = \bar{\mathbf{F}}(x) \tag{2.19}$$

The dispersion relations are obtained by solving the eigenvalue problem given by equation (2.19) for the case of free vibration,

$$\left(\sum_{j=0}^{4} \mathbf{K}_j (-i\kappa)^j - \omega^2 \mathbf{M} \right) \bar{\mathbf{W}}(x) = 0 \tag{2.20}$$

The simple eigenvalue problem in ω^2 can be solved for known values of κ, or alternatively, a solution for the polynomial eigenvalue problem in $(-i\kappa)$ can be found

for known values of ω . For each eigenvalue there exists a corresponding eigenvector, which describes the mode shape of the cross-section for this wave. Solutions to equation (2.20) in its polynomial form in κ can be found using standard computing routines. Alternatively, the eigenvalue problem given by equation (2.20) can be transformed to a simple linear eigenvalue problem in κ (Gavric, 1994). The more widely-available standard solution routines for linear eigenvalue problems can then be used to obtain the dispersion characteristics of the structure. This has been found to be a more stable method of solution for some problems than the polynomial eigensolution routine and has therefore been used in all the WFE modelling work reported here.

The response of the structure to a concentrated load can be described in the spatial domain using a delta function, as follows.

$$\left(\sum_{j=0}^{4} \mathbf{K}_j (-i\kappa)^j - \omega^2 \mathbf{M} \right) \bar{\mathbf{W}}(x) = \bar{\mathbf{F}}\, \delta(x) \tag{2.21}$$

Use can be made of the following Fourier transforms in order to transform equation (2.21) from the spatial domain into the wavenumber domain.

$$\tilde{\mathbf{W}}(\kappa) = \int_{-\infty}^{\infty} \bar{\mathbf{W}}(x) e^{i\kappa x} dx \tag{2.22}$$

$$\tilde{\mathbf{F}}(\kappa) = \int_{-\infty}^{\infty} \bar{\mathbf{F}}(x) e^{i\kappa x} dx = \int_{-\infty}^{\infty} \bar{\mathbf{F}}\, \delta(x) e^{i\kappa x} dx = \bar{\mathbf{F}} \tag{2.23}$$

where $\tilde{\mathbf{W}}$ indicates displacement of the cross-section in the wavenumber domain and $\tilde{\mathbf{F}}$ is the force vector for the cross-section in the wavenumber domain. Equation (2.21) can therefore be written in the wavenumber domain as,

$$\left(\sum_{j=0}^{4} \mathbf{K}_j (-i\kappa)^j - \omega^2 \mathbf{M} \right) \tilde{\mathbf{W}}(\kappa) = \tilde{\mathbf{F}}(\kappa) \tag{2.24}$$

The cross-section displacements in the wavenumber domain can be found using matrix inversion,

$$\tilde{\mathbf{W}}(\kappa) = \left(\sum_{j=0}^{4} \mathbf{K}_j (-i\kappa)^j - \omega^2 \mathbf{M} \right)^{-1} \tilde{\mathbf{F}}(\kappa) \tag{2.25}$$

The following inverse Fourier transform returns the cross-section displacement vector to the spatial domain,

$$\bar{\mathbf{W}}(x) = \frac{1}{2\pi} \int_{-\infty}^{\infty} \tilde{\mathbf{W}}(\kappa) e^{-i\kappa x} d\kappa \tag{2.26}$$

A method of evaluating this integral based on the method of residues was presented by Karassalo (1994).

$$\lim_{\kappa \to \kappa_p} \bar{\mathbf{W}}(x) = i \sum_n \frac{\tilde{\mathbf{W}}_{n,L}^T \tilde{\mathbf{F}}}{\tilde{\mathbf{W}}_{n,L}^T \left(\frac{\partial \left(\Sigma \mathbf{K}_j (-i\kappa)^j \right)}{\partial \kappa} \right)_n \tilde{\mathbf{W}}_{n,R}} \tilde{\mathbf{W}}_{DOF,n,R} \tag{2.27}$$

where n is the number of waves in the structure at a given frequency, over which a sum is taken to find the overall response of the structure. κ_p is the wave number at the pole under consideration, at which all the wavenumber-dependent terms in equation (2.27) are evaluated. The 'L' and 'R' indices indicate the left and right-eigenvectors respectively. The 'DOF' subscript is an index that refers to the degree-of-freedom at which the displacement is required. The derivative term in equation (2.27) can be expanded as follows,

$$\frac{\partial \left(\Sigma \mathbf{K}_j (-i\kappa)^j \right)}{\partial \kappa} = -i \left(4\mathbf{K}_4 (-i\kappa)^3 + 2\mathbf{K}_2 (-i\kappa) + \mathbf{K}_1 \right) \tag{2.28}$$

MATLAB computer programs have been used to calculate the free and forced response of a waveguide structure from the WFE matrices, following the approach described above.

2.4.3. WFE model of a coupled beam and plate

Having introduced the WFE approach, the focus is now returned to the point mobility of a plate near to a supporting beam. The WFE models described in this work are for structures of infinite extent in the length direction, but finite cross-section dimensions. A WFE model was created of a coupled beam and plate structure, in which the plate has a width of 4m. With this exception, the geometric and material properties of the coupled beam and plate in the WFE model are the same as those defined in Section 2.3 above. The 'beam' is represented as a vertically-orientated plate.

Figure 2.5 shows the nodes of the WFE model for this structure.

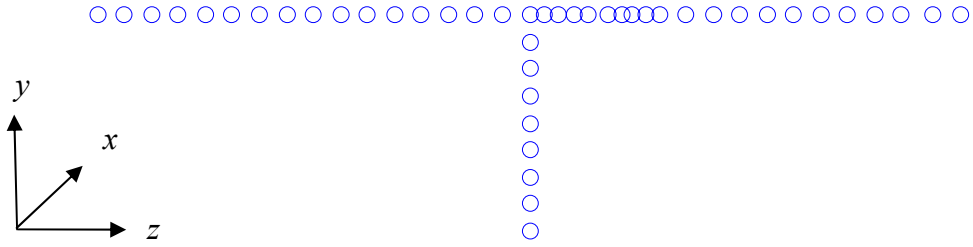

Figure 2.5. Node positions in the WFE model of the 4m wide plate coupled to a 1m deep rectangular-section beam.

The elements used in the WFE model are two-noded plate elements, in which each node has four degrees of freedom: translation in the three coordinate directions shown in Figure 2.5 and rotation about the *x* axis. These elements can be thought of as thin strips of material, of finite width and infinite length. The plate elements are defined in terms of two node positions, the thickness of the element and the material properties.

Testing has shown that 3 elements per wavelength are sufficient to obtain satisfactory results when using these plate elements, which have cubic interpolation functions. Simple analytical models were used to predict the wavelength in the plate and in the beam at the maximum frequency considered in this work, 2kHz. For a thin plate, the bending wavenumber is given by,

$$\kappa_{plate} = \left(\frac{\rho h \omega^2}{D_{plate}} \right)^{1/4} \tag{2.29}$$

where the flexural rigidity of the plate is given by,

$$D_{plate} = \frac{Eh^3}{12\left(1-\nu^2\right)} \tag{2.30}$$

and the wavelength is related to the wavenumber by,

$$\lambda_{plate} = \frac{2\pi}{\kappa_{plate}} \tag{2.31}$$

A bending wavelength of approximately 0.38m is expected in the 30mm thickness steel plate at a frequency of 2kHz. An element width of 0.125m is therefore appropriate and has been used to model most of the plate. Smaller elements have been used in part of the plate, in order to provide the required spatial resolution for the

point mobility calculations as a function of position on the deck presented in Section 2.5.

The vertical and lateral beam bending waves were not considered in the selection of the element size for the beam in the WFE model. These waves cause displacements that vary as a function of position along the length of the structure and these are dealt with using the analytical wave functions. Rather, plate bending and in-plane wave motions were considered in selecting an appropriate element size for modelling the beam using WFE. Equations (2.29) to (2.31) show that the plate bending wavelength in the 'beam' is approximately 0.44m at a frequency of 2kHz. For the in-plane wave, a wavelength of 2.5m was found at this frequency from the longitudinal wave speed in steel. It is therefore sufficient and convenient to use an element width of 0.125m in modelling the beam using WFE.

Note that the WFE method has also been used to study the response of rectangular and I-section beams, see Appendix B.

2.4.4. Results of model 3

To develop the understanding from the mobilties presented in Sections 2.2.2 (results from the beam and spring model) and 2.3 (results from the analytical plate and beam model) calculations are presented in this section from the WFE model described above in Section 2.4.3. Firstly, results of a free vibration response WFE analysis are presented here, in the form of dispersion relations and mode shapes. The eigenvalue problem of equation (2.20) has been solved for ω^2, given a set of known and purely-real values of κ. It is therefore only the propagating waves that are considered here. This limits the number of waves to be included in the dispersion diagram in a given frequency range, such that these may shown reasonably clearly. The dispersion diagram obtained from the WFE analysis for the coupled beam and plate is shown in Figure 2.6 below, for the case of zero damping, together with the results of simple analytical models for the waves in the structure.

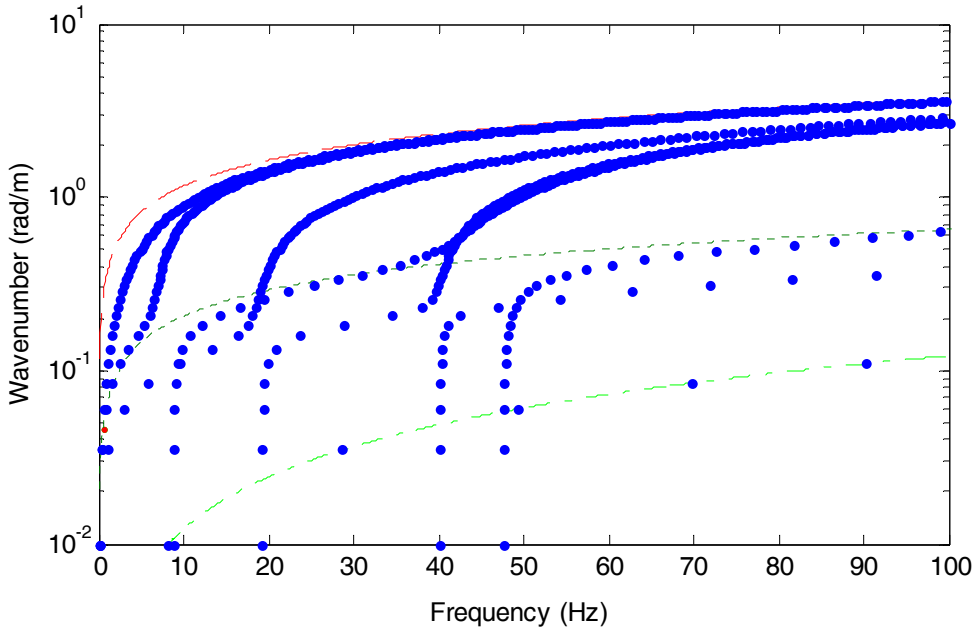

Figure 2.6. Purely-real wavenumber shown versus frequency for the coupled beam and plate structure, with no damping: ● ,WFE; _ _ _ _ _ , vertical bending wave in deck (thin plate model for 30mm thickness plate);_ _ _ _ _ _ _ _ , vertical bending wave in beam (Euler beam model); _ . _ . _ . _ , longitudinal wave in steel.

The WFE solution consists of a set of discrete points, or wavenumber-frequency pairs. Each of these points is a solution to the eigenvalue problem of equation (2.20). Loci can be identified from these discrete solutions and many of these loci will not pass through the origin (at zero wavenumber and zero frequency). These are propagating waves only above some minimum frequency, known as the wave cut-on frequency.

Comparing the WFE solutions with the curves obtained from the analytical models, a longitudinal wave can be identified in the WFE solution, a vertical beam-bending wave up to a frequency of approximately 5Hz and a plate-bending wave in the upper part of the frequency range shown.

The mode shapes can also be found from the solution of equation (2.20). These provide further information for identification of the wave types in the coupled beam and plate and are shown in Figure 2.7 for frequencies of 1Hz and 50Hz.

Frequency of 1Hz

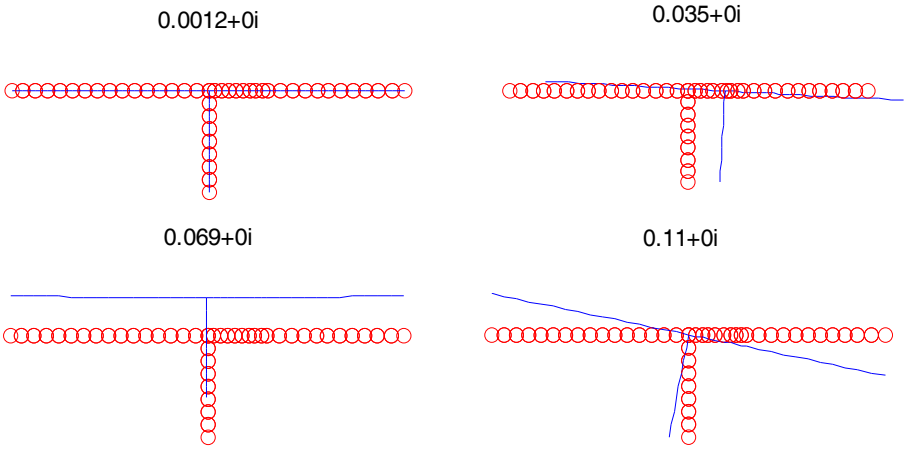

Frequency of 50Hz

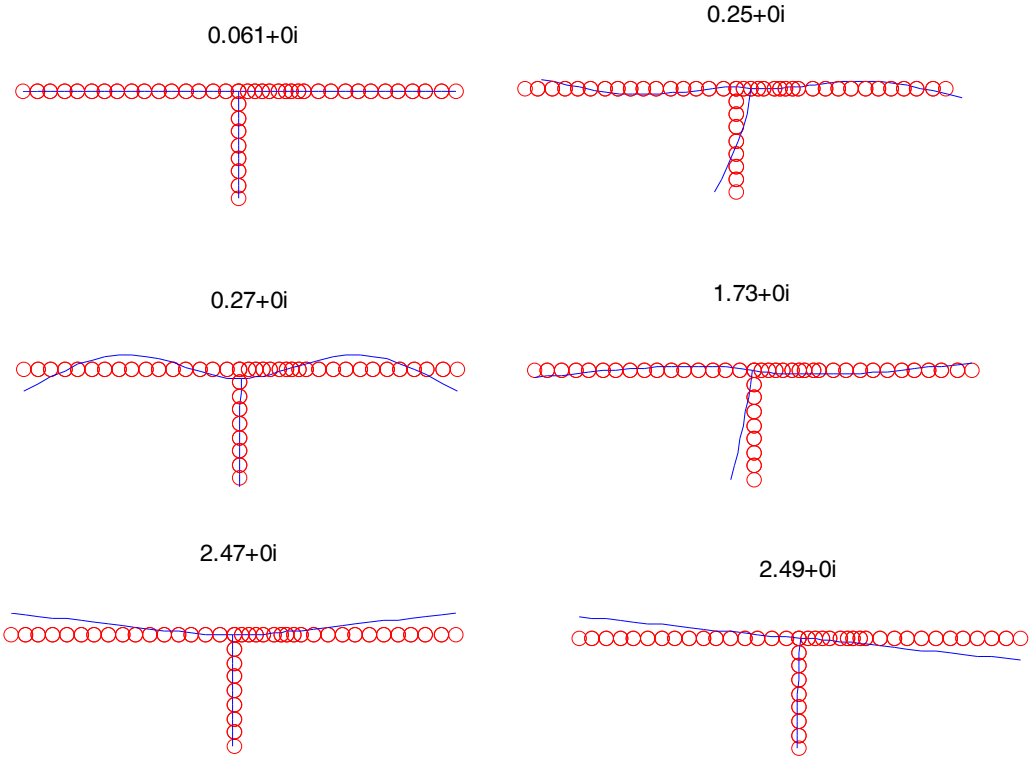

Figure 2.7. Mode shape plots and corresponding wavenumbers for the couple beam and plate structure. Caption above each plot shows wavenumber (rad/m): o *, original node position;* ——— *, deformed shape.*

At 1Hz, Figure 2.7 shows the expected waves with a zero cut-on frequency: a longitudinal mode, a lateral bending mode, a vertical bending mode and a torsional mode. There is very little deformation of the cross-section at this frequency.

The modes that show deformation of the cross-section at a frequency of 50Hz are for various combinations of either vertical bending or torsional motion of the beam and/or the plate. For all but very low frequencies, modes of these types are expected to control the response of the structure to vertical excitation. With increasing frequency, there is a progression toward higher-order versions of these modes, that is to modes of the same basic form but with shorter wavelengths. To illustrate this, two modes that are important in the response of the structure to vertical excitation at a frequency of 250Hz are shown in Figure 2.8 below.

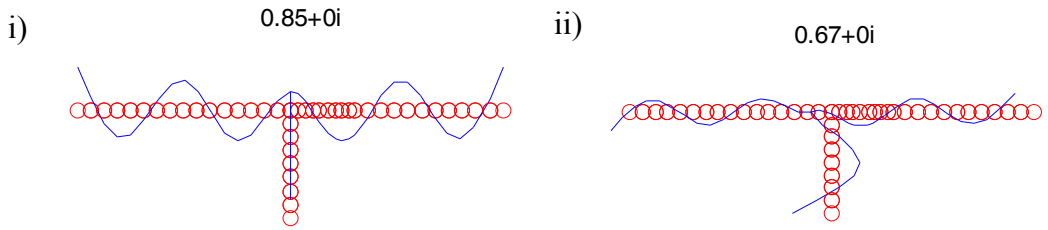

Figure 2.8. Mode shape plots and corresponding wavenumbers for two important modes of the couple beam and plate structure at 250Hz. Caption above each plot shows wavenumber (rad/m): o , original node position; _____ ,deformed shape.

Comparing the modes shown in Figure 2.8 at a frequency of 250Hz with those of similar basic form in Figure 2.7 at 50Hz shows the expected change in the wavelengths. This comparison also illustrates how the influence of the beam on the point mobility at some lateral distance from the beam would become smaller as the frequency is increased.

2.5. EVALUATION OF THE THREE MOBILITY MODELS

2.5.1. Introduction

The three models presented in Sections 2.2 to 2.4 have been used to predict the input point mobility of the coupled beam and plate structure described above, first as a function of input point position and then as a function of frequency. In this section, the results given by these three different models are compared with each other and with those of the NORBERT mobility model.

2.5.2. Point mobility as a function of position

The normalised point mobility of the coupled beam and plate structure is shown as a function of the normalised distance between the input point and the beam centre-line

in Figure 2.9 below. Note that these quantities are as defined in Section 2.2 above (equations (2.15) and (2.16)), except that the system mobility is normalised by the mobility of the beam for the models described in Sections 2.3 and 2.4, rather than that of the spring as for the model in Section 2.2. Note also that these results have been obtained at a single frequency, 100Hz.

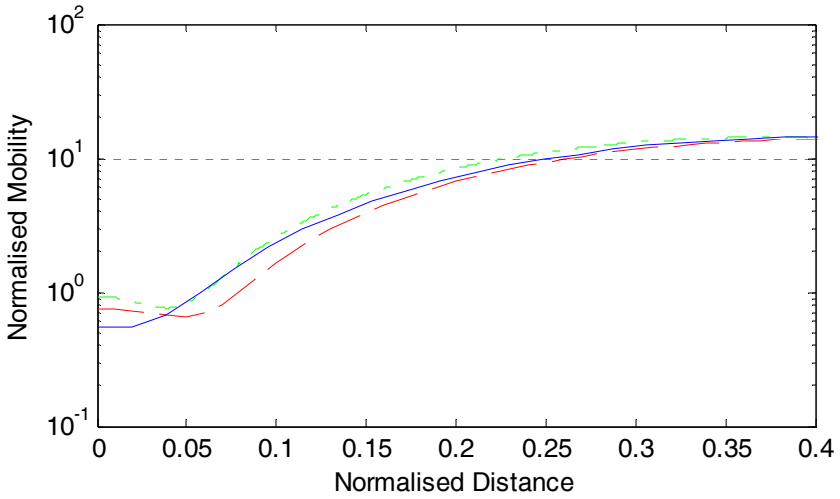

Figure 2.9. Normalised point mobility of the coupled beam and plate structure shown against normalised distance between the input point and the beam centre-line: ——— , WFE; – – – – – , two dimensional analytical model; – . – . – , one dimensional analytical model; - - - - - - - , uncoupled plate mobility.

The three models give results that are similar; each shows a transition from close to the mobility of the support beam to that of the plate as the input point is moved from the beam to a distance equal to approximately one-quarter of a wavelength from the beam. For a normalised distance of between about 0.05 and 0.2, the two dimensional analytical model gives a lower mobility than either the WFE model or the one dimensional model. It is likely that this is due to the assumption that the beam does not rotate in the two dimensional analytical model.

It is expected that of these three different models, the WFE model is based on the best representation of the coupled beam and plate structure. The one dimensional model gives the expected behaviour in terms of the magnitude of the point mobility, but not the real part of point mobility: the mobility of the one dimensional system at a normalised distance of zero is purely imaginary. It is therefore not a suitable means to predict the vibration input power to railway bridge structures. The WFE model also has advantages over the two dimensional model, principally that the motion of the

beam is not limited to that given by an Euler beam model. The one dimensional model and the two dimensional analytical model will therefore not be used further in this section. This makes it possible to present results in the form of the real part of point mobility, which is again preferred because of its relation to power input.

A simple empirical model has been fitted to the WFE result for the real part of point mobility that can be used to predict the transition between the mobility of the beam and that of the plate in a coupled beam and plate structure. This is given by,

$$\mathrm{Re}\{Y_{bridge}\} = \mathrm{Re}\{Y_{beam}\} + d_N{}^3 \times \left(\frac{\mathrm{Re}\{Y_{deck}\} - \mathrm{Re}\{Y_{beam}\}}{0.25^3} \right) \qquad (2.32)$$

where 'd_N' is the normalised distance between the input point and the beam. Here, the beam mobility is calculated using the Euler beam model and the deck mobility is calculated using the thin plate model. Since it is now the real part of the point mobility that is of concern, the normalised system mobility is re-defined as,

$$Y_{Norm} = \frac{real(Y_{system})}{real(Y_{Beam})} \qquad (2.33)$$

A comparison between this normalised mobility given by the simple empirical model, the WFE model and the NORBERT mobility model is shown in Figure 2.10 below, for the coupled beam and plate structure defined above, at a frequency of 100Hz.

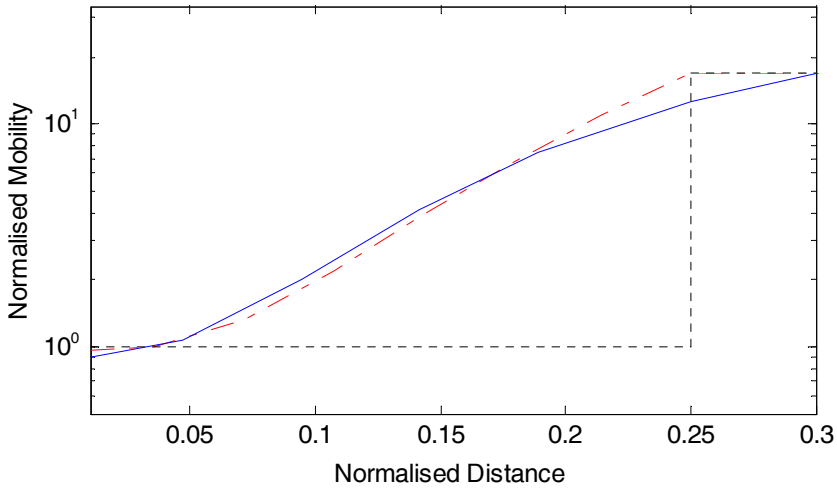

Figure 2.10. Normalised point mobility (as given by equation 2.33) of the coupled beam and plate structure shown against normalised distance between the input point and the beam centre-line: ——— , WFE; – · – · – , empirical transition; - - - - - - - - , NORBERT mobility model.

In order to test further the proposed empirical transition, an alternative coupled beam and plate structure has been studied here using the WFE method, the empirical transition and the NORBERT mobility model. The plate remains as before, but for this case it is coupled to the I-section beam shown in Figure 2.11 below.

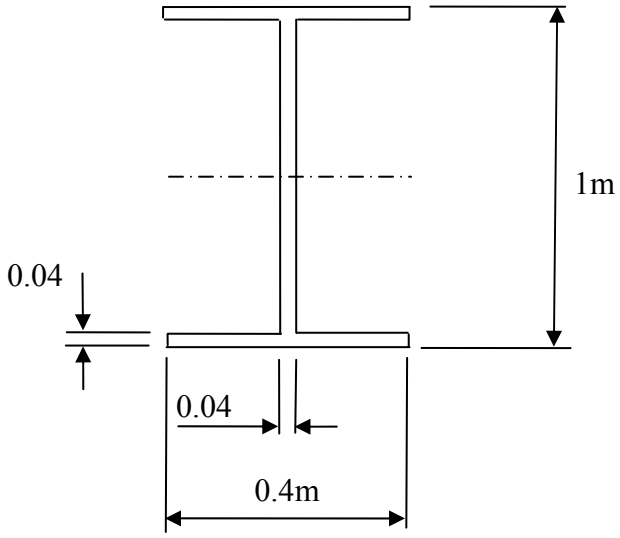

Figure 2.11. Cross-section geometry of the I-section support beam in the alternative coupled beam and plate structure.

The nodes of the top flange of the I-section beam shown in Figure 2.11 are common to those in the deck. The top flange elements therefore over-lay those in the deck, over the width of the top flange. The nodes of the WFE model for this structure are shown in Figure 2.12 below.

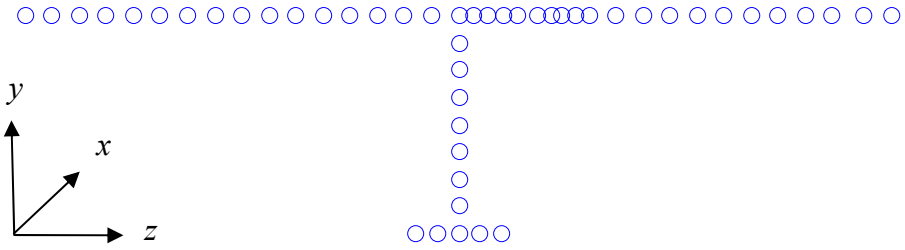

Figure 2.12. Node positions in the WFE model of the coupled I-section beam and plate structure.

The input point mobility of the coupled I-section beam and plate structure at a frequency of 100Hz is shown as a function of the distance between the input point and the centre-line of the support beam web in Figure 2.13.

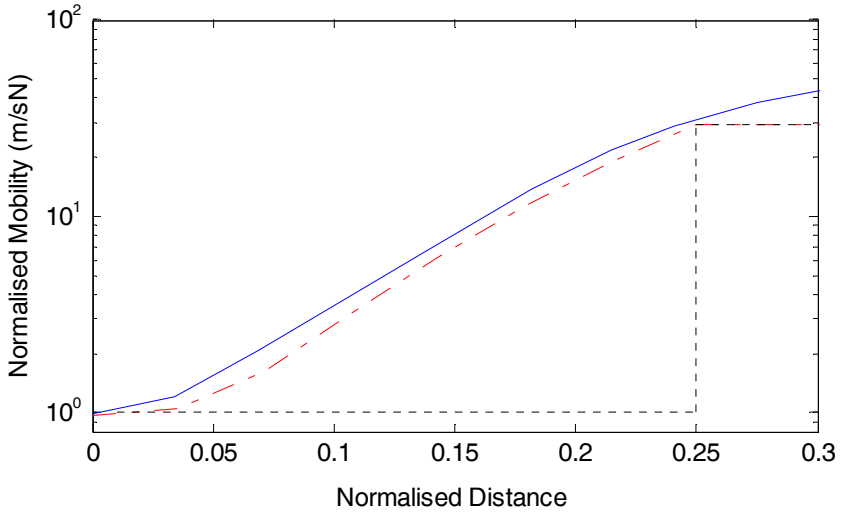

Figure 2.13. Normalised point mobility (as given by equation 2.33) of the coupled I-section beam and plate structure shown against normalised distance between the input point and the beam centre-line:_____ , WFE; _ . _ . _ . _ , empirical transition;_ _ _ _ _ _ _ _ , NORBERT mobility model.

Figure 2.13 shows that the empirical transition model is in satisfactory agreement with the WFE result for this case and again seems to offer an advantage over the NORBERT mobility model.

2.5.3. Point mobility as a function of frequency

In NORBERT, the point mobility is required at a single position on the bridge deck over the frequency range of interest in bridge noise. It is therefore of interest to compare the point mobility given by the WFE, empirical transition and NORBERT mobility models as a function of frequency. This allows an assessment to be made of any benefit there may be in using the empirical transition to predict the mobility of the bridge in preference to the NORBERT mobility model.

Figure 2.14 shows the input point mobility of the coupled I-section beam and plate structure as a function of frequency, for an input point located at a lateral distance of 0.2m from the centre-line of the support beam.

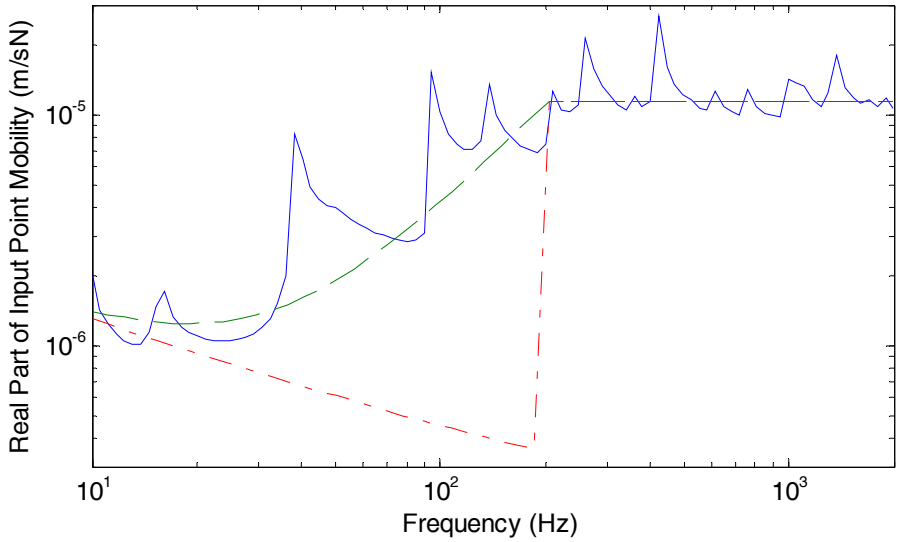

Figure 2.14. Real part of the input point mobility of the coupled I-section beam and plate structure, at a lateral distance of 0.2m from the centre-line of the beam: ——— , WFE; – – – – , empirical transition; –·–·– , NORBERT mobility model.

The input point mobility obtained from the WFE analysis shows the expected transition from the mobility of the beam to that of the plate over the frequency range up to approximately 200Hz. It is seen that the empirical transition is an approximate frequency-average to the WFE result in this range. There are peaks in the WFE result due to the cut-on of waves over the frequency range shown. The NORBERT mobility model underestimates the mobility of the structure for frequencies between about 40Hz and 200Hz, by up to an order of magnitude.

2.6. CONCLUSIONS

The work presented in this chapter is concerned with the calculation of the input point mobility of a railway bridge, required in order to predict the power input to the bridge. The NORBERT mobility model is based on a switch between the mobility of the support beam and that of the deck plate. It was expected that this switch may introduce some error to the calculation, for bridges in which the track supports are not positioned directly over the support beams. This was confirmed by using three different approaches to modelling a coupled beam and plate, intended to represent a typical all-steel railway bridge. All three models show that a transition is required between the mobility of the beam and that of the plate as the input force is moved away from the support beam, rather than the switch between them used in the NORBERT mobility model.

An empirical means to predict the transition between the mobility of the beam and that of the plate was found by fitting to the results of the WFE analysis described here. This empirical transition represents an alternative to the NORBERT mobility model and requires no additional computation or user input. It is shown that the empirical transition is in much closer agreement with the results of the WFE analysis than the NORBERT mobility model. On this basis, it is recommended here that the transition model is added to NORBERT and used to calculate the input point mobility for all-steel bridges in which the track supports are not positioned directly over the support beams. Further, it is preferable to use the result of an infinite beam model as input to the transition model. This is because this type of structure has been shown to behave as a beam only for very low frequencies, up to about 20Hz here, such that a finite beam model would predict the modes of the structure incorrectly at higher frequencies.

The second major outcome of the work presented in this chapter is the demonstration of the WFE method as a suitable tool for the analysis of those railway bridge structures that have a constant cross-section along their span length. WFE addresses the difficulty found in using conventional FE for bridges, related to the number of modes at high frequencies and the consequent computational cost. The WFE analysis of the coupled I-section beam and plate presented in Section 2.5 required approximately one hour using a laptop computer. There are also advantages in using WFE for the analysis of bridge structures rather than the analytical models described in Sections 2.2 and 2.3, related to its flexibility and the frequency range over which valid results can be expected. The WFE method has therefore been used to study the vibration response of concrete-steel composite bridges and concrete box-section bridges in Chapters 3 and 6 to follow.

3. APPLICATION OF THE MODELS TO CONCRETE-STEEL COMPOSITE RAILWAY BRIDGES

3.1. INTRODUCTION

3.1.1. Concrete-steel composite bridges

In this chapter, concrete-steel composite bridges are studied using both the WFE method and the NORBERT model. Bewes (2006) found that the behaviour of concrete-steel composite bridges, referred to here as 'composite bridges', is quite different from that of all-steel bridges. In a composite bridge, the point mobility of the concrete deck may be in the same order of magnitude as that of the steel support beam over much of the frequency range of interest. For this reason, the procedure that has been developed for calculating the mobility of all-steel bridges in NORBERT, as either the mobility of the deck or that of the beam, or as a transition between them, may not be applicable to composite bridges.

Moreover, the simplified SEA scheme used in NORBERT, which is based on the assumption of equipartition of energy between the subsystems, is valid only for reasonably homogeneous structures (Janssens and Thompson, 1996). An all-steel or an all-concrete bridge satisfies this criterion; the plate subsystems in a NORBERT SEA model of these bridges normally have similar thickness and impedance. However, this is not the case for a composite bridge, in which a thick concrete deck is connected to relatively thin-walled steel beams (Thompson et al., 2005).

3.1.2. Use of NORBERT for concrete-steel composite bridges

Bewes (2006) proposed three different models for the input point mobility of a composite bridge in NORBERT: a beam model, a plate model and the switch between them described in the previous chapter. Two different approaches to the use of a simplified SEA calculation for composite bridges were also tested. In both of these, the support beams and the deck were treated as separate SEA networks, such that equipartition of modal energy can be applied to each network separately. One of these networks was set as the primary SEA network, which receives the power input from the base of the track. The secondary SEA system is then driven by the primary system. While this approach avoids the need to determine coupling loss factors, a particularly difficult part of an SEA analysis, there is a lack of physical basis for the

selection of either the deck or the support beam as the primary system into which the vibrational power from the track is injected.

A further concern in using two SEA networks to model a composite bridge in NORBERT is the smaller number of modes in each of these networks over a given frequency band than would be the case if only a single network had been used. The minimum frequency for which the use of a statistical method can be justified for a composite bridge is therefore likely to be greater than that for a single material bridge. This minimum frequency can be estimated from the modal densities, n (modes per rad/s), of each plate in the SEA network, given by (Cremer et al., 1988),

$$n = \frac{\kappa_B^2 A}{4\pi\omega} \tag{3.1}$$

where A is the surface area of the plate and κ_B is the bending wavenumber in the plate. Application of equation (3.1) to the SEA networks used by Bewes (2006) to model a composite bridge on the Docklands Light Railway (DLR) in London gives the following frequency-independent modal densities,

	Deck (concrete)	**Side-deck (concrete)**	**Beam flanges (steel)**	**Beam webs (steel)**
n (modes per rad/s)	0.008	0.004	0.004	0.03

Table 3.1. Modal density of each plate in the SEA model of a composite bridge on the DLR used by Bewes (2006).

Based on the modal densities shown in Table 3.1, the total number of modes expected in the one-third octave frequency band centred on 315Hz is just five for the concrete component SEA network (deck and side-deck) and 15 for the steel component network (beam flanges and beam webs). It may therefore be inappropriate to use a statistical method such as SEA for this composite bridge below the 315Hz one-third octave frequency band.

Bewes evaluated the proposed NORBERT mobility and SEA calculations for composite bridges by comparison with measurements made for vibration under-traffic on the DLR composite bridge. The best agreement was achieved by using the switch between beam and plate models for the mobility calculation and setting the deck as the primary SEA network. However, that work could not be regarded as an ideal

basis for assessment of the proposed mobility and SEA models, as there is significant uncertainty in other parts of the NORBERT calculation for vibration under traffic, such as the roughness excitation at the wheel-rail interface and the behaviour of the track structure. Further, the comparison with measurement data does not easily lead to a physical explanation for the observed behaviour.

3.1.3. Modelling concrete-steel composite bridges using WFE

In the work described in this chapter, the WFE method has been used to investigate the issues relating to the application of NORBERT to composite bridges. It is expected that the WFE method is a suitable approach to the prediction of both the input point mobility of the bridge and the response of the main components of the bridge during a train pass-by. The results of this analysis have been compared with those obtained from NORBERT, using the mobility and SEA models proposed by Bewes, for the same composite bridge on the DLR. Bewes's measurement data has also been referred to, where available.

3.2. CHARACTERISING THE VIBRATION REPSONSE OF THE COMPOSITE BRIDGE ON THE DOCKLANDS LIGHT RAILWAY

3.2.1. The composite bridge on the DLR

Measurements were made in previous work for noise and vibration on a composite bridge on the DLR in London, located between Tower Gateway and Shadwell stations (Bewes, 2006). The cross-section geometry of this twin-track bridge is shown in Figure 3.1 below.

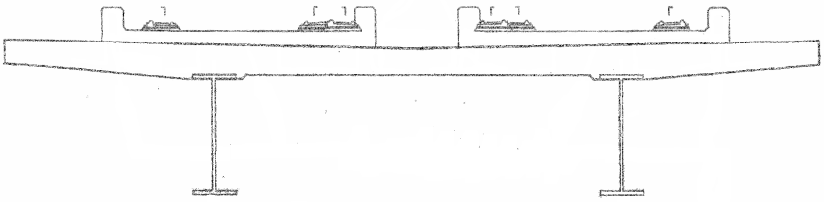

Figure 3.1. A sketch of the composite bridge on the DLR, taken from Bewes (2006).

Figure 3.1 shows a concrete deck supported by two steel I-section beams. The deck has a typical thickness of 0.39m where it is reinforced by the track slab, 0.23m elsewhere and an overall width of 8m. The I-section beams are 1m deep, with a web thickness of 0.03m, flange thickness of 0.04m and flange width of 0.4m. This bridge consists of 16m length spans, with support from concrete columns at the span ends.

The material properties for steel defined in Chapter 2 (Table 2.1) were used here to model the I-section support beams. For the concrete deck, the Young's modulus is subject to significant uncertainty because it is dependent on the precise composition of the concrete. Following consultation with a company responsible for building concrete bridges on the DLR and reference to Kong and Evans (1982), the following set of material properties have been assumed for the concrete deck.

Property	**Value**
Dynamic Young's Modulus	40GPa
Density	2400kg/m^3
Poisson's ratio	0.2

Table 3.1. Material properties for the concrete deck.

3.2.2. WFE model for the composite bridge on the DLR

The concrete deck in this bridge is expected to show thick-plate behaviour in the frequency range of interest for bridge noise. This behaviour cannot be accounted for using the WFE plate elements, which are based on thin plate theory. Rather, a solid element model would be required. However, a plate element model is preferred here because it is simple and computationally light relative to a solid element model.

In order to assess the need to account for thick-plate effects in this modelling work, a comparison was made between the mobility of the concrete deck given by both thick and thin infinite plate theory. It was found that these differ by less than 15% in the frequency range up to 1.5kHz for the concrete deck in this bridge. On this basis, thick-plate effects have been neglected in the modelling work presented here and plate elements are used to model both the bridge deck and the support beams.

A WFE model for half of the bridge cross-section was run separately for boundary conditions at the bridge centre-line appropriate to symmetric and anti-symmetric motion about the centre-line. A significant reduction in the overall solution time is achieved by this approach, relative to that for a model of the full bridge cross-section, due to the reduction in the number of degrees-of-freedom in the model.

Figure 3.2 shows the nodes of the WFE model for half of the DLR composite bridge.

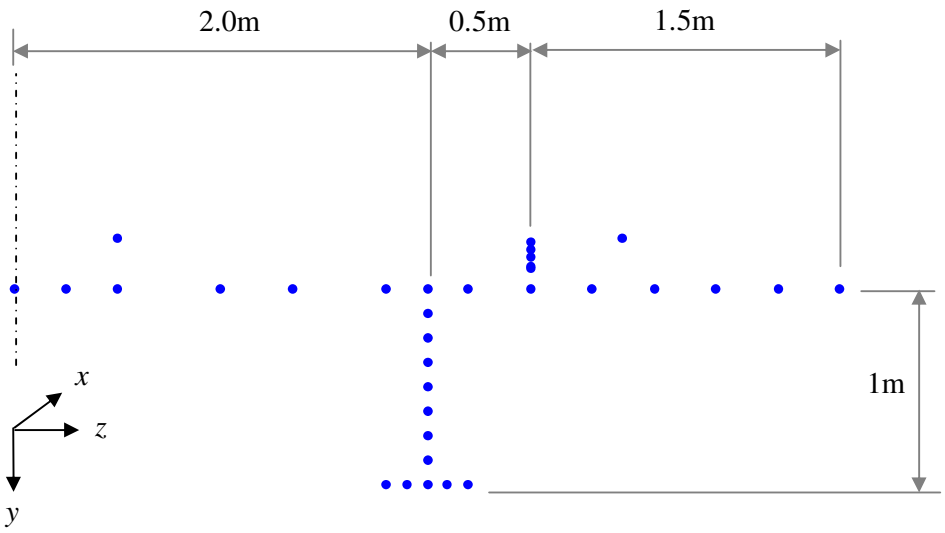

Figure 3.2. Node positions in the WFE model for half of the composite bridge on the DLR.

The lengths of the elements shown in Figure 3.2 were chosen with reference to the requirement for at least three elements per wavelength described in Chapter 2. Thin infinite plate theory was applied to the bridge deck, the flanges and the web of the I-section beam, in order to estimate the minimum wavelength in each of these components in the frequency range up to 1.5kHz.

Bewes (2006) used a frequency-dependent loss factor to model this bridge in NORBERT. However, this cannot be included in the WFE analysis easily. In the absence of suitable measurement data for the damping in this structure, a frequency-independent structural damping loss factor has been used in both the WFE and NORBERT modelling work presented here. A structural damping loss factor of 0.02 has been chosen for this composite bridge, following Harrison et al. (2000). The term structural damping loss factor is used here for a loss factor that describes the overall level of damping in a structure, inclusive of the damping in the material and at the joints in the bridge and track structure.

Note that the modelling of the rail and track supports will be described in Section 3.2.5 to follow.

3.2.3. Free vibration response analysis

The dispersion relations obtained from solution of the eigenvalue problem for a prescribed set of purely real wavenumbers are identified for the case of zero damping in Figure 3.3 below. A number of dispersion curves calculated from simple analytical models are also shown to aid interpretation of the waveforms in the bridge.

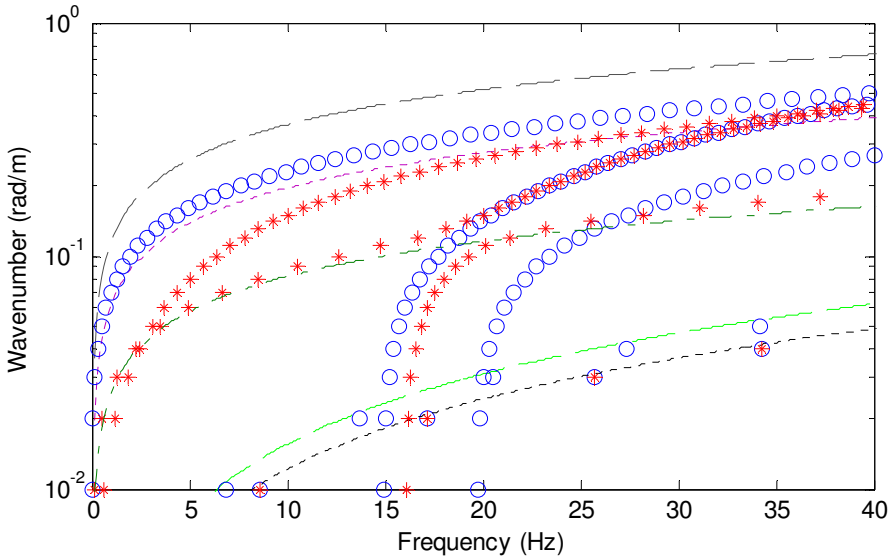

*Figure 3.3. Purely-real wavenumber shown versus frequency for the composite bridge on the DLR, with no damping: ○ ,WFE for symmetric case; * , WFE for anti-symmetric case; _ _ _ _ _ _ , longitudinal wave in steel; _ _ _ _ _ , longitudinal wave in concrete;_ . _ . _ . , lateral beam-bending wave in deck (Euler beam model; _ _ _ _ _ _ , vertical bending wave in I-section beam (Euler beam model); _ _ _ _ _ , vertical bending wave in deck (thin plate model).*

The waves in the structure with a zero cut-on frequency can be identified from a comparison of the discrete WFE solution points to the curves obtained from the analytical models. The symmetric case WFE solution in Figure 3.3 shows waves with dispersion properties that approximately follow those for a vertical bending wave in the I-section beam at very low frequencies, a longitudinal wave in the concrete deck and a longitudinal wave in the I-section beam. For the anti-symmetric case, the WFE solution shows waves with dispersion properties that approximately follow those for a lateral beam-bending wave in the concrete deck at low frequencies and a longitudinal wave in the I-section beam. There is an additional set of WFE solution points for the anti-symmetric case with a zero cut-on frequency. These are for the torsional wave.

For frequencies greater than approximately 10Hz, it can be seen that the WFE solution points depart from the analytical models for the vertical bending wave in the I-section beam and the lateral beam-bending wave in the deck. Further, three waves cut on in the frequency range up to 20Hz. It is necessary to study the mode shapes associated with these waves in order to identify the wave type in each case. These are shown for the symmetric waves in Figure 3.4 below, at frequencies of 1Hz and 25Hz.

Frequency of 1Hz

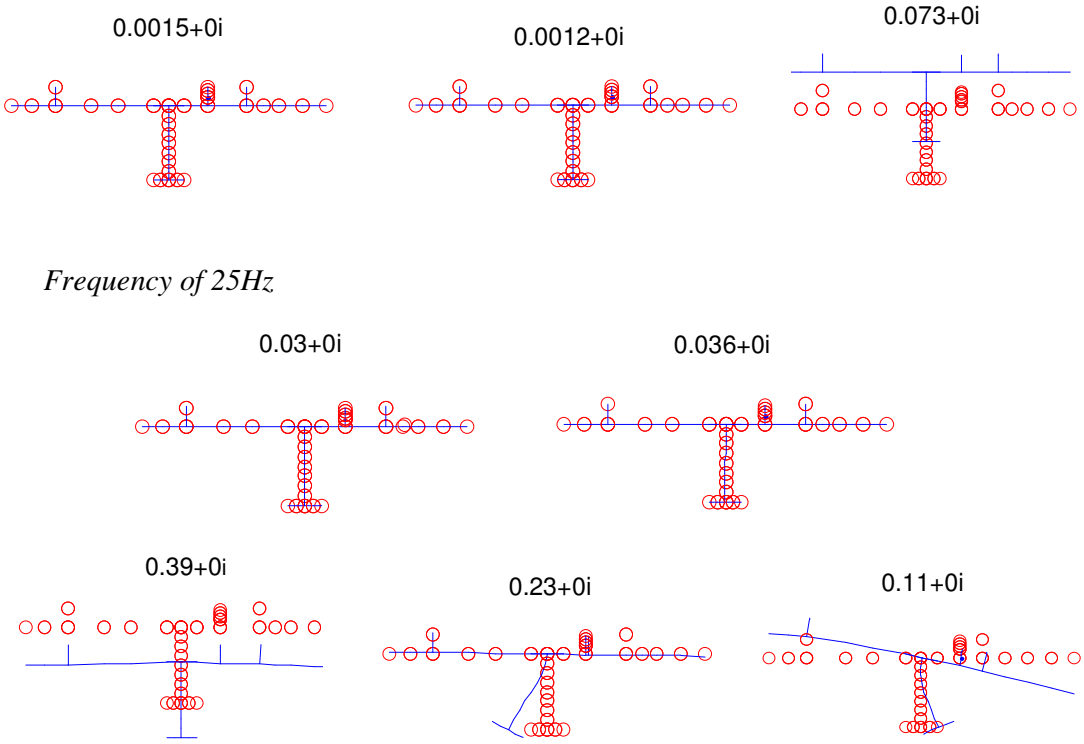

Figure 3.4. Mode shape plots and corresponding wavenumbers for the symmetric modes of the composite bridge on the DLR. Caption above each plot shows wavenumber (rad/m): ○ , original node position; ——— , deformed shape.

For a frequency of 1Hz, Figure 3.4 shows a mode in which the bridge performs beam-bending motion in the vertical direction, with no cross-sectional deformation, in addition to the longitudinal waves in the I-section beam and the deck. At the higher frequency shown in Figure 3.4, the two longitudinal modes remain unchanged and the beam-bending mode of the bridge is also present. Two additional modes are shown, one which has a cut-on frequency of 15Hz and another with a cut-on at 20Hz. The

former shows primarily torsional motion of the I-section beam and the latter is the first plate-bending mode in the bridge deck.

Figure 3.5 shows the mode shapes for the anti-symmetric waves in the bridge for frequencies of 1Hz and 25Hz.

Frequency of 1Hz

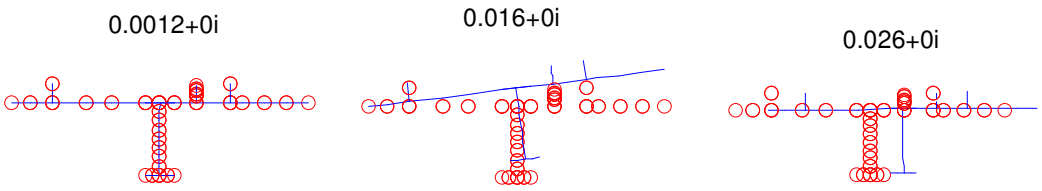

Frequency of 25Hz

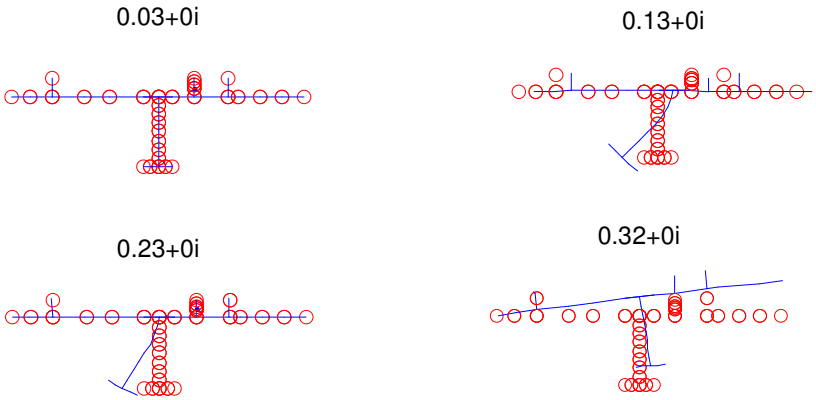

Figure 3.5. Mode shape plots and corresponding wavenumbers for the anti-symmetric modes of the composite bridge on the DLR. Caption above each plot shows wavenumber (rad/m): o , original node position; _____ , deformed shape.

At 1Hz there is a longitudinal mode of the steel beams, a torsional mode of the bridge and a lateral beam-bending mode of the bridge. At 25Hz the longitudinal, torsional and lateral beam-bending modes persist and they are joined by a mode in which the I-section beam performs torsional motion. This is the anti-symmetric counterpart to the mode with similar appearance shown in Figure 3.4 for a frequency of 25Hz.

The dispersion and mode shape diagrams presented in Figures 3.3 to 3.5 describe the low-frequency behaviour of the viaduct. Presentation of the free vibration response analysis results for higher frequencies is made difficult by the large number of waves in the viaduct. In order to present dispersion results clearly over a larger frequency range, it is necessary to select only some of the waves from the full WFE solution for plotting. This has been done by plotting the dispersion results only for the waves with relatively large wave amplitudes at the excitation position (where the force from the track support is input to the bridge). The majority of the total power input to the structure is transmitted to these waves. It is then only a small fraction of the total number of waves in the WFE solution that need to be considered in characterising the response of the bridge.

To implement this, a wave with a displacement amplitude (magnitude of the complex amplitude) greater than 75% of the largest wave amplitude at a given frequency is labelled as a 'very high power wave', a wave with an amplitude of between 50% and 75% of the maximum wave amplitude as a 'high power wave' and a wave with between 25% and 50% of the maximum wave amplitude as a 'medium power wave'. Note that the term 'power' is used loosely here as the relative wave amplitudes are only an approximate indicator of the relative powers transmitted to the waves.

Figure 3.6 shows the dispersion relations for these waves when the viaduct is excited at the outer rail position on the deck, for the symmetric case only, together with the results of appropriate analytical models. A relatively large frequency range of 1Hz to 3kHz has been chosen for this analysis, so that the high-frequency asymptotic behaviour may be shown.

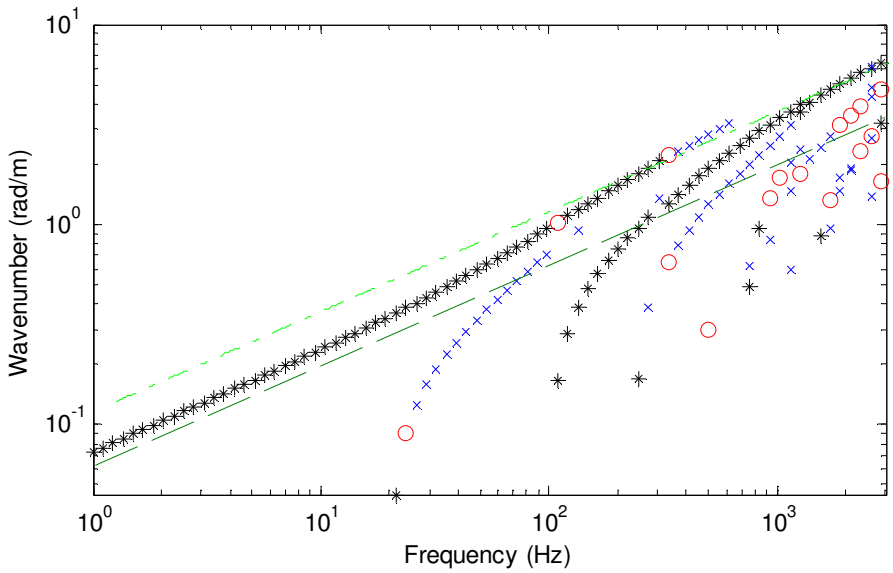

*Figure 3.6. Purely-real wavenumber shown versus frequency for the composite bridge on the DLR, with no damping, for symmetric motion about the centre-line and excitation at the outer rail position: *, WFE result for very high power waves; ×, WFE result for high power waves; ○, WFE result for medium power waves; _ _ _ _ _ _, vertical bending wave in deck (thin plate model); _ _ _ _ _, vertical bending wave in I-section beam (Euler beam model).*

Figure 3.6 shows that for frequencies up to about 20Hz and the symmetric waves only, the vibration power input to the bridge is transmitted to waves with dispersion properties similar to those given by the Euler beam model for the I-section support beam. At a frequency of 20Hz the first plate-bending mode within the width of the deck cuts-on and as expected, a significant part of the power input to the bridge is transmitted to these waves. However, very high power waves in the frequency range from 20Hz to about 300Hz have dispersion properties that lie between those of the Euler beam model and the thin plate equation.

For frequencies greater than 300Hz, the power is transmitted to waves which are predominantly bending waves in the deck. This is a significantly lower frequency than that at which the distance between the excitation position and the web of the support beam becomes equal to one-quarter of a bending wavelength in the deck, which is about 730Hz. There are no WFE solutions shown in Figure 3.6 that closely approximate to the results of analytical models for the I-section beam or the component parts of the beam for frequencies greater than 300Hz. This is supporting

evidence for nomination of the deck as the primary SEA system in NORBERT, which receives the power input from the base of the track.

Figure 3.7 shows the dispersion relations for the important anti-symmetric waves in the bridge, again for excitation at the outer rail position.

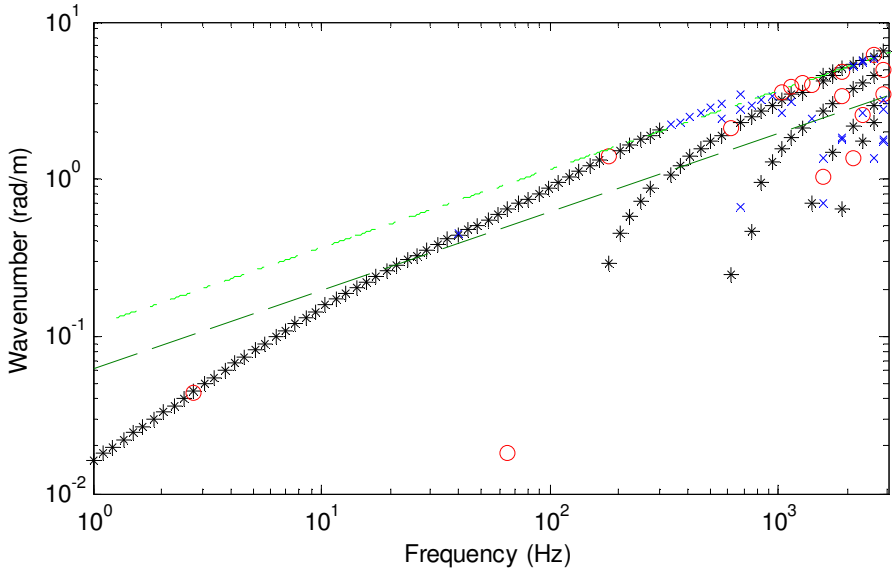

*Figure 3.7. Purely-real wavenumber shown versus frequency for the composite bridge on the DLR, with no damping, for anti-symmetric motion about the centre-line and excitation at the outer rail position: *, WFE result for very high power waves; ×, WFE result for high power waves; ○, WFE result for medium power waves; _ _ _ _ _ , vertical bending wave in deck (thin plate model); _ _ _ _ _ , vertical bending wave in I-section beam (Euler beam model).*

It can be seen that the power input to the bridge is transmitted predominantly to plate bending waves in the deck, for frequencies greater than about 300Hz in the anti-symmetric case solution, as for the symmetric case solution. For lower frequencies and excitation at the outer rail position, torsional waves of the bridge section dominate the power transmission to the anti-symmetric waves.

3.2.4. Input point mobility

The point mobility on the bridge deck at the outer rail position has been calculated from the WFE model of the bridge and also from the NORBERT model, shown in Figure 3.8 below. The real part of mobility, rather than the magnitude, has been shown here because this is directly related to the vibrational power input to the bridge.

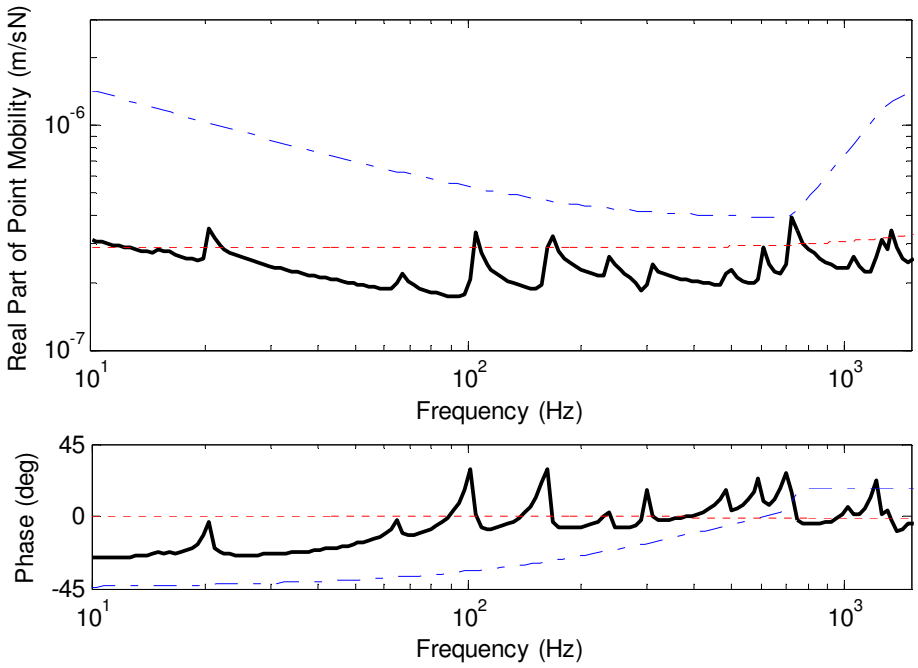

Figure 3.8. Real part and phase of point mobility on the deck of the composite bridge on the DLR, at the outer rail position, shown versus frequency: ——— , from WFE model; - - - - - - - - , from thick infinite plate model applied to bridge deck; — · — · — , from Bewes equations for mobility of an I-section beam.

Figure 3.8 shows that the point mobility at the outer rail position given by the WFE model has plate-like characteristics for frequencies greater than about 100Hz: the real part of mobility is close to frequency-independent and the phase is approximately zero, when a frequency-average of the mobility is considered. For lower frequencies, the WFE mobility spectrum shows some influence of the bending waves in the support beam: the real part of the mobility becomes smaller with increasing frequency over this range and the phase angle is closer to that expected for a beam (-45^{o}). The peaks and troughs in the WFE mobility spectrum are due to the modes of the cross-section, and correspond to the wave cut-on frequencies.

In NORBERT, the thick-plate approximation for the bridge mobility would be used for the outer rail position in the frequency range above 730Hz, based on the switch between beam and plate mobility models described in Section 2.1.4. This leads to an overestimate for the real part of point mobility relative to the frequency-average WFE result in this range, but only by about 30%.

For frequencies lower than 730Hz, the bridge would be modelled as a beam in NORBERT. This approach would lead to an overestimate for the real part of point mobility relative to the WFE result by a factor of between three and four in the frequency range up to 100Hz and by a factor of about two for frequencies between 100Hz and 730Hz. This comparison with the WFE mobility shows that it is necessary to account for the influence of both the steel I-section beam and the concrete deck of this bridge. This is because the I-section beam and the concrete deck have similar mobilities. The WFE method is expected to capture the behaviour of the composite bridge more reliably, because the combined behaviour of the deck and the support beam can be accounted for.

If an appropriate representation of the rail and track support is included in the WFE model, the power input to the bridge may be found from the WFE matrices. This is the subject of Section 3.2.5 below.

3.2.5. Calculation of the power input to the bridge using a WFE model of the bridge and track

In this section, the track is added to the WFE model of the bridge in order to allow computation of the power transfer from the track into the bridge structure. The rail behaves as a beam in the frequency range of interest, with transverse shear and rotational inertia effects in the upper part of this range. In the absence of Timoshenko beam elements in WFE, four vertically-orientated plate elements were used to model the rail: one for the rail head, one for the rail foot and two for the web. The rail on the DLR is of BS80A rail section, the geometry for which was taken from (Esveld, 1989).

The WFE representation of the rail was checked by finding the point mobility from a WFE model of only the rail and comparing it with that given by Timoshenko beam theory for the properties of the BS80A rail. This is shown in Figure 3.9 below.

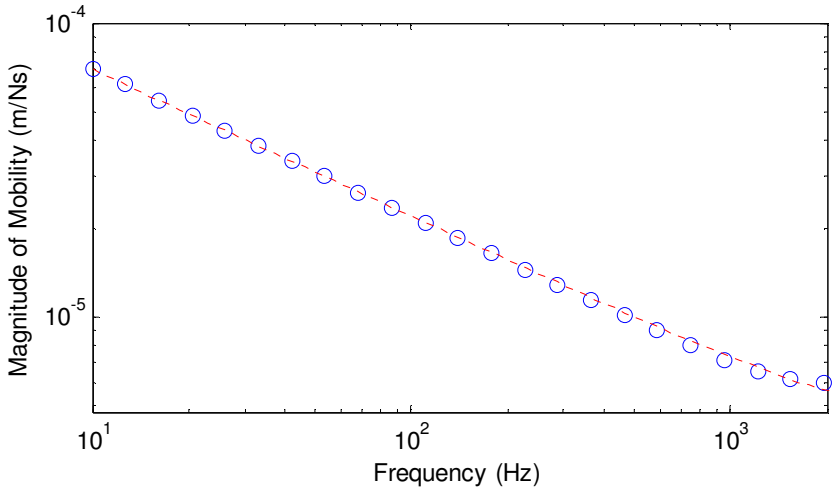

Figure 3.9. Magnitude of point mobility on the BS80A rail: ○, from a WFE model of only the rail; - - - - - - - - , from Timoshenko beam theory.

Figure 3.9 shows that the WFE representation of the rail is suitable for prediction of the rail response over the frequency of interest. A damping loss factor of 0.02 was used for the rail in all the modelling work described here.

The rails are directly-fastened to the concrete bridge deck with Pandrol type 4479 baseplates, set at 0.6m intervals along the rail. There is a single rubber pad in these baseplates. Bewes (2006) used a point accelerance measurement on the unloaded rail together with the coupled beam model to determine a dynamic stiffness of 84MN/m and a damping loss factor of 0.17 for these rail fasteners.

A single vertically-orientated plate element was used to represent the track support as an equivalent continuous resilient layer in the WFE model. The Young's modulus of the resilient layer in the vertical direction was specified by considering the stiffness of a strip of material subject to a distributed load,

$$k = \frac{ELt}{h} \tag{3.2}$$

where L is the length of the strip, t is its thickness and h is its height. In the WFE model, the thickness and height dimensions were set to 0.1m, such that the stiffness per unit length of the resilient layer is equal to the Young's modulus for the plate element in the vertical direction. For these fasteners with a dynamic stiffness of 84MN/m, set at 0.6m intervals, a vertical Young's modulus of 140MPa is appropriate.

Orthotropic material properties were assigned to the plate element used to represent the resilient layer in the WFE model, in order to minimise the effects of shear waves along its length. Physically, such shear waves do not exist because the track support consists of spatially discrete rail fasteners rather than a continuous resilient connection between the rail and bridge. The Young's modulus in the axial direction and the shear modulus were therefore set to very small values.

The power input to the bridge is found from an appropriate model of the rail, track support structure and the bridge as follows,

$$P_{bridge} = \frac{1}{2} Re \int_{-L/2}^{L/2} (s.z(x))^* \dot{W}_{bridge}(x) dx \tag{3.3}$$

where s is the stiffness of the track support per unit length, $z(x)$ is the displacement across the track support and * indicates the complex conjugate. $\dot{W}_{bridge}(x)$ is the velocity of the bridge directly below the track and L is the length of the bridge.

Other power quantities can be found from the WFE model and these provide further understanding of the behaviour of the combined rail, track support and bridge system. For excitation at the rail, the power input to the rail is given by,

$$P_{in\_rail} = Re\{Y_{rail}\} F_{rail}^2 \tag{3.4}$$

where Y_{rail} is the point mobility at the rail head and F_{rail} is the r.m.s. force input to the rail. The power dissipated in the resilient layer is found from (by the definition of loss factor),

$$P_{resilient} = \frac{1}{2} \omega \eta_{resilient} \int_{-L/2}^{L/2} s |z(x)|^2 dx \tag{3.5}$$

where $\eta_{resilient}$ is the damping loss factor of the resilient layer.

Equations (3.3) and (3.5) require that the response of the structure is calculated as a function of the axial distance along the bridge span, followed by integration along the axis. Simple trapezoidal integration has been used to evaluate these integrals over the span length of the bridge.

The power quantities defined by equations (3.3) to (3.5) are shown below in Figure 3.10 for excitation at the outer rail of the DLR composite bridge, for a single input force at the rail of unit amplitude (peak).

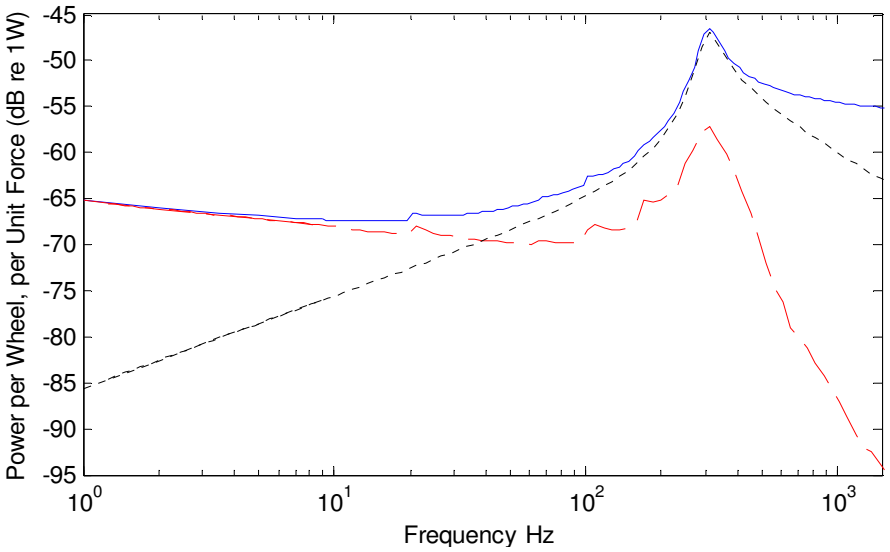

Figure 3.10. Power shown versus frequency, for a single excitation force of unit amplitude (peak) at the outer rail of the composite bridge on the DLR: ——— , input power to the rail; – – – – , input power to the bridge; - - - - - - - - , power dissipated in the resilient layer.

At low frequencies, almost all of the power input to the rail is transmitted across the track support structure to the bridge. The motion of the rail and bridge are well-coupled in this frequency range and, due to the relative impedances of the bridge and rail, the power is transmitted to the bridge in preference to the rail.

The power input to the rail is proportional to the point mobility at the rail head for this idealised excitation case (constant input force for all frequencies) and is therefore greatest at the resonance frequency, approximately 315Hz in this case. Here, the bridge and the rail move in anti-phase on the track stiffness. This frequency can therefore be called the decoupling frequency. At this frequency, the majority of the power input to the system is dissipated in the resilient layer, due to the large displacements across it. However, the maximum power input to the bridge is also found at this frequency, because the force applied to the bridge is dependent on the displacement across the resilient layer (equation (3.3)).

The rail becomes decoupled from the bridge at high frequencies and the power input to the bridge is therefore relatively small in this range. This is the effect of the

vibration isolation provided by the resilient layer, introduced in Section 1.3.5. In this frequency range, the majority of the power input to the system is dissipated in the rail.

It is of interest to compare the power input to the bridge obtained from the WFE and NORBERT models. The infinite length coupled beam model in NORBERT has been used here, rather than the finite length coupled beam model, mainly because this can be compared directly with the WFE model (also an infinite length model). However, it is also expected that the finite length coupled beam model in NORBERT would predict the modes of the structure incorrectly, because it was shown in Sections 3.2.3 and 3.2.4 that this bridge behaves as a beam only for frequencies up to about 20Hz.

Figure 3.11 compares the power input to the bridge obtained from the WFE and NORBERT models.

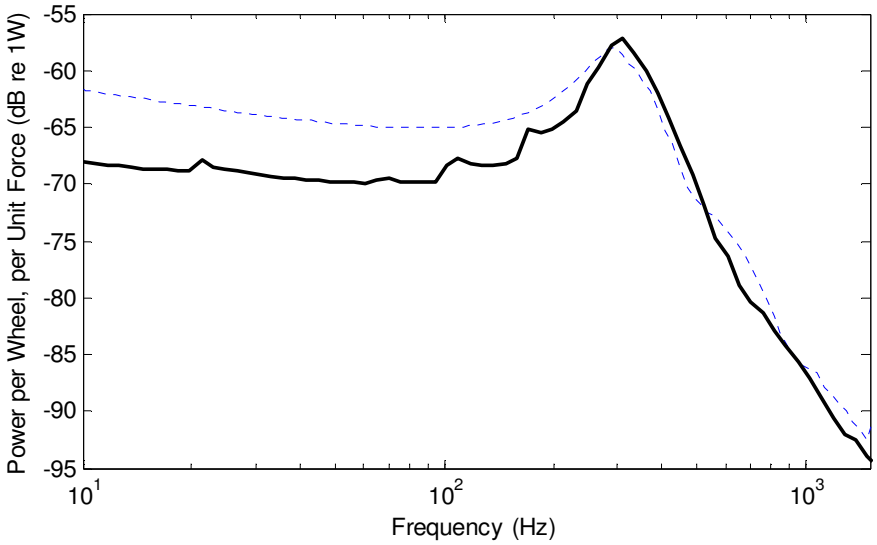

Figure 3.11. Power input to the bridge shown versus frequency, for a single excitation force of unit amplitude (peak) at the outer rail of the composite bridge on the DLR: ——— , from WFE; - - - - - - - - , from NORBERT.

The power input to the bridge obtained from the WFE model is lower than that given by NORBERT in the frequency range up to about 250Hz; by between 4 and 6dB up to 100Hz and by about 3dB in the range between 100Hz and 250Hz. This is consistent with the comparison shown between the NORBERT and WFE results for the input point mobility of the bridge in Section 3.2.4.

The peaks in the power input spectra given by the two models occur at slightly different frequencies: about 295Hz for the NORBERT model and 315Hz for the WFE model. That is, the coupling between the rail and the bridge occurs differently in the

two models. Since, it is expected that the representation of the rail and the track support structure in the two models is the same, this difference can be attributed to the representation of the bridge structure in the two models.

In the frequency range above 300Hz, the two models give similar results for power input to the bridge. From the comparison made between the input point mobilities of the bridge in these two models in Section 3.2.4, it was expected that the power input to the bridge given by NORBERT would be significantly greater than that from the WFE model up to about 730Hz. The difference in the coupling between the rail and the bridge in these models largely offsets the effect of the different bridge mobilities on the power input calculation.

3.3. VIBRATION OF THE COMPOSITE BRIDGE UNDER-TRAFFIC

3.3.1. Prediction of the bridge velocity during a train pass-by

In this section, the vibration response of the composite bridge during the passage of a train is calculated using the WFE model. This is compared with the vibration under traffic found using NORBERT and from the measurements made by Bewes (2006).

The bridge velocity has been calculated from the WFE model in response to a single unit force acting at the outer rail head, which was then adjusted for the excitation expected during the passage of a train as follows,

$$< V^2 >= N_w F_{rail}^2 < v^2 > \tag{3.6}$$

where $< V^2 >$ is the spatially-averaged mean-square velocity in response to the passage of the train, F_{rail} is the r.m.s. amplitude of the input force to the rail, N_w is the number of wheels within the span length of the viaduct and $< v^2 >$ is the spatially-averaged mean-square velocity in response to a unit force. The number of wheels on the bridge can be found by comparing the length of the train and the axle positions to the span length of the bridge. The force input to the bridge at each wheel-rail interface was calculated using the appropriate NORBERT modules, described in Section 1.5.2. The rail mobility obtained from a preliminary run of the WFE model was used in this calculation.

A different approach has been taken to modelling the B90/B92 rolling stock used on the DLR in this work than in the previous work by Bewes (2006). These vehicles are

fitted with Bochum 54 or Bochum 84 resilient wheels. The motion of the bogie and that of the wheel are expected to decouple at a frequency of about 10Hz. Since bridge vibration data is not available for such low frequencies, it is sufficient to calculate the force input to the bridge at each wheel-rail interface using a vehicle model that is limited to a description of the resilient wheel, shown in Figure 3.12 below.

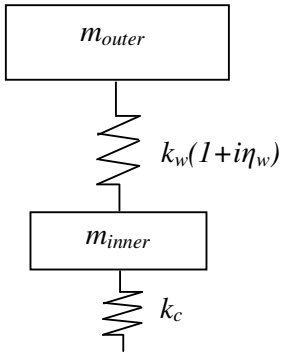

Figure 3.12. Two degree-of-freedom model for the resilient wheel on B90/B92 rolling stock.

m_{outer} is the mass of the outer part of the wheel and m_{inner} is that of the inner part of the wheel. k_w represents the stiffness of the rubber elements fitted between the inner and outer parts of the wheel. The damping in these rubber elements has been modelled using a damping loss factor η_w. k_c represents the stiffness of the linearised Hertzian contact spring between the wheel and rail, which has been set to 1.3GN/m in this work.

The parameter values used to model the resilient wheels have been taken from the specifications for Bochum 54 and Bochum 84 wheels. These are shown in Table 3.2, together with the other input data to the NORBERT vehicle model appropriate for the B90/B92 rolling stock on the DLR. Note that the train speed given here is the average train speed found by Bewes (2006) using the measured acceleration time histories and knowledge of the axle spacing.

Stiffness of rubber elements in wheel, k_w (N/m)	300×10^6
Damping loss factor for rubber elements in wheel, η_w (N/m)	0.2
Contact stiffness, k_c (N/m)	1.3×10^9
Mass of inner part of wheel (kg)	350
Mass of outer part of wheel (kg)	120
Length of one vehicle (m)	14
Length of train (m)	56
Number of wheels per vehicle	6
Train speed (km/h)	54

Table 3.2. Input data to the NORBERT vehicle model for the B90/B92 rolling stock on the DLR.

The wheel roughness spectrum was taken from (Dings and Dittrich, 1996) and represents an average of measurements made on 37 disc-braked wheels. For the rail, an 'average UK roughness' was used, from (Hardy, 1997).

Bewes (2006) measured the vibration on the bridge deck at four positions where the deck thickness is 0.39m and four positions where the deck thickness is 0.23m. The former will be described as the deck and the latter as the side-deck hereafter. These measurements have been spatially-averaged for both the deck and the side-deck (*i.e.* averaged over four transducer positions for the deck and four for the side-deck), and averaged over the 48 train pass-bys for which measurements were made.

The spatially-averaged velocities found from the measurements are directly comparable to the output of the simplified SEA calculation in NORBERT. The assembly of plates proposed by Bewes (2006) as the basis of this calculation has been adopted in the NORBERT modelling work reported here. This consists of plates for the deck, side-deck, beam flanges and beam webs.

In order to obtain corresponding results from the WFE model, the velocity at each node in the cross-section was calculated at regular sampling points away from the excitation position, in a direction parallel to the axis of the bridge.

$$< v_p^2 >= \frac{\sum_{n=1}^{N} v_p^2(x_n)}{N_{span}} \tag{3.7}$$

where $< v_p^2 >$ is the spatially-averaged mean-square velocity along the length of the structure at node 'p' in the cross-section, $v_p^2(x_n)$ is the mean-square velocity at each sampling position along the length of the bridge for this node and the series x_n defines the sampling positions.

Physically, wave reflection at the ends of the bridge span would be expected to make a significant contribution to the energy in the bridge span, at least for low frequencies. Since the WFE model used here is for an infinite structure, it cannot account for wave reflection at the span ends directly. Two different approaches were considered for the calculation of the spatially-averaged velocity along the length of the bridge: one based on the assumption of strong wave reflection at the span ends of the bridge and one based on weak wave reflection at the span ends. In the former, the sum of the squared velocities in equation (3.7) was made over a length that includes all points at which there is a significant response. This sum was then divided by the number of sampling points in the span length of the bridge, N_{span}. For the weak reflection case, the sum of the squared velocities in equation (3.7) was made only over the span length of the bridge.

The difference between the results of these two calculations is large at low frequencies, approximately 13dB at a frequency of 50Hz, but small at higher frequencies. It is expected that the calculation based on the assumption of strong reflection at the span ends represents a closer approximation to the physical behaviour of the bridge, due to the large impedance change at the span ends. This approach has therefore been taken to the calculation of the spatially-averaged velocity along the length of the bridge at each node in the WFE model, using equation (3.7). These results were then averaged over all the nodes in each of the major components of the bridge, such that they represent spatially-averaged velocities for these components that can be compared with the results of the simplified SEA calculations proposed for this bridge by Bewes (2006) and with the measurement data.

The spatially-averaged velocity on the deck of the composite bridge is shown below in Figure 3.13.

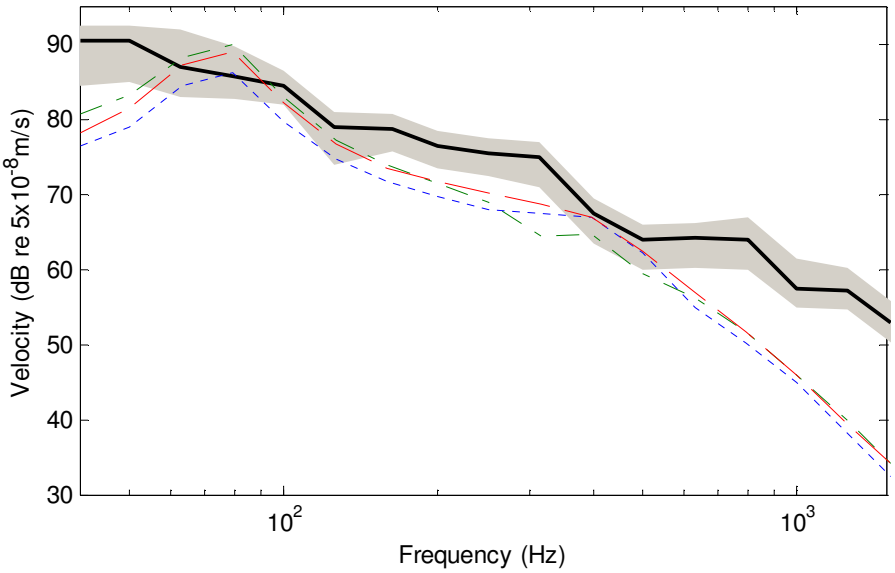

Figure 3.13. Spatially-averaged velocity on the deck of the composite bridge on the DLR shown versus frequency: ——— , measured average; ▒ , measured range; – – – – – , WFE result; – · – · – , NORBERT result; - - - - - - - - , NORBERT result using power input spectrum from WFE.

Figure 3.13 shows that the bridge deck velocity predicted using the WFE model is in reasonably close agreement with the measurements for the frequency bands from 50Hz to 630Hz. The peak in the model results at about the 80Hz band is due to the mode in which the mass of the wheel and the mass of the rail vibrate on the track stiffness. This peak is not clearly defined in the measurements. It is likely that the vehicle model is responsible for a significant part of the difference between the results of the models and the measurement in this range. For the frequency bands above 630Hz, the deck velocity given by the WFE model is 10 to 20dB lower than the measurement.

One of the NORBERT results shown in Figure 3.13 was obtained using the approach recommended by Bewes (2006) for modelling composite bridges in NORBERT. The power input to the bridge was found from the beam representation of the bridge for frequencies less than 730Hz and from the plate model for higher frequencies. The bridge velocity was calculated using the simplified SEA scheme in which the deck is set as the primary network and the beam as the secondary network. This calculation gives a similar result to the WFE model for much of the frequency range, but it is up to 4dB lower for the frequency range between 250Hz and 630Hz, and further from the measurement in this range.

It was shown in Sections 3.2.4 and 3.2.5 that there is reason to expect significant error in the NORBERT result for the power input to this composite bridge and it is expected that the WFE model represents an improved basis for this calculation. In evaluating the simplified SEA schemes proposed by Bewes for modelling composite bridges in NORBERT, it is therefore appropriate to use the power input to the bridge obtained from the WFE analysis as an input to the calculation of the component velocities in NORBERT. For the same power input to the bridge, Figure 3.13 shows that the recommended simplified SEA scheme gives lower deck velocities than the WFE analysis, by 2 to 3dB in the frequency range up to 400Hz and by typically 1.5dB in the range above 630Hz. The WFE result for deck velocity is in generally closer agreement with the measurements.

Figure 3.14 shows the spatially-averaged velocity in the side-deck of the composite bridge.

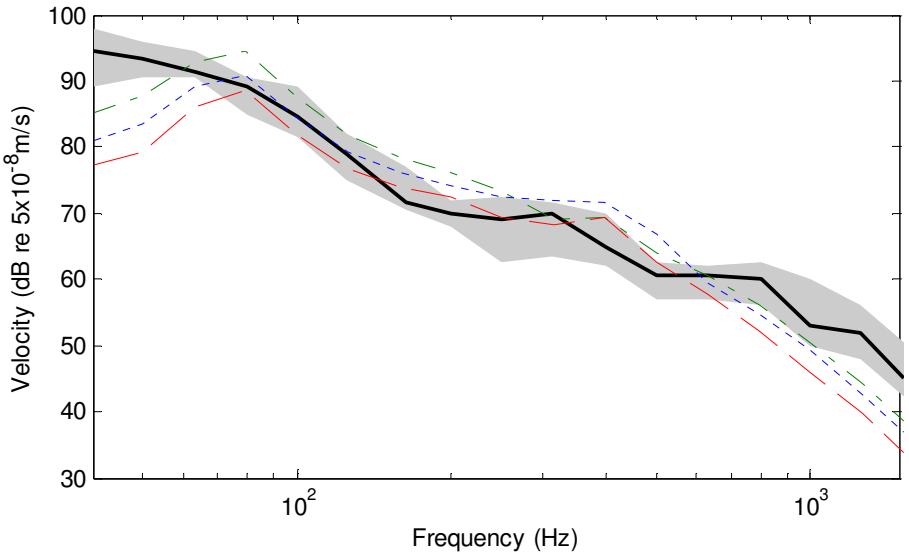

Figure 3.14. Spatially-averaged velocity on the side-deck of the composite bridge on the DLR shown versus frequency: ——— , measured average; ■ , measured range; – – – – – , WFE result; – · – · – , NORBERT result; - - - - - - - - , NORBERT result using power input spectrum from WFE.

This shows that the side-deck velocity calculated from the WFE model is comparable to the measurement in the frequency bands from 80Hz to 630Hz. For higher frequencies, the WFE result is 8 to 13dB lower than the measurement. This comparison for the side-deck velocity is similar to that for the deck velocity (Figure

3.13), but the under-prediction of the high frequency response is less severe for the side-deck than for the main deck.

The NORBERT results for the side-deck velocity, using both the power input to the bridge calculated in NORBERT and using the power input taken from the WFE model, are generally higher than the WFE result. Given the comparison shown between the results of these models for the deck velocity in Figure 3.13 above, where the WFE result was higher than the NORBERT result, this indicates that the division of energy between the deck and the side-deck in the simplified SEA calculation in NORBERT is different to that in the WFE analysis. This is studied further in Section 3.3.2 below.

Bewes (2006) identified uncertainty in the assumed wheel-rail roughness spectrum and the fastener stiffness as the most likely causes of the difference between the deck and side-deck velocity spectra predicted using NORBERT and the measurements for frequencies greater than 630Hz. The use of the WFE method for this structure does not address either of these issues.

3.3.2. Assessment of the SEA schemes proposed for the composite bridge

In this section, the WFE method has been used to calculate the spatially-averaged velocities of all the main components of the bridge, including those for which measurement data is not available. Comparison has been made to the results of the two different simplified SEA schemes studied by Bewes (2006) for modelling composite bridges using NORBERT: one in which the deck is primary network (used in Section 3.3.1 above) and one in which the beam is the primary network. These have been assessed against measurements for the deck and side-deck only in the previous work by Bewes (2006). Here they have been compared with the WFE model for prediction of the spatially-averaged velocity for all the main components of the bridge. The power input to the bridge obtained from the WFE analysis has been used as input data to the NORBERT calculations here such that the energy sharing between the bridge components in the simplified SEA schemes may be compared directly with that given by the WFE analysis.

Figure 3.15 shows the spatially-averaged velocity spectra for each of the major bridge components, obtained using the two simplified SEA schemes in NORBERT and the WFE model.

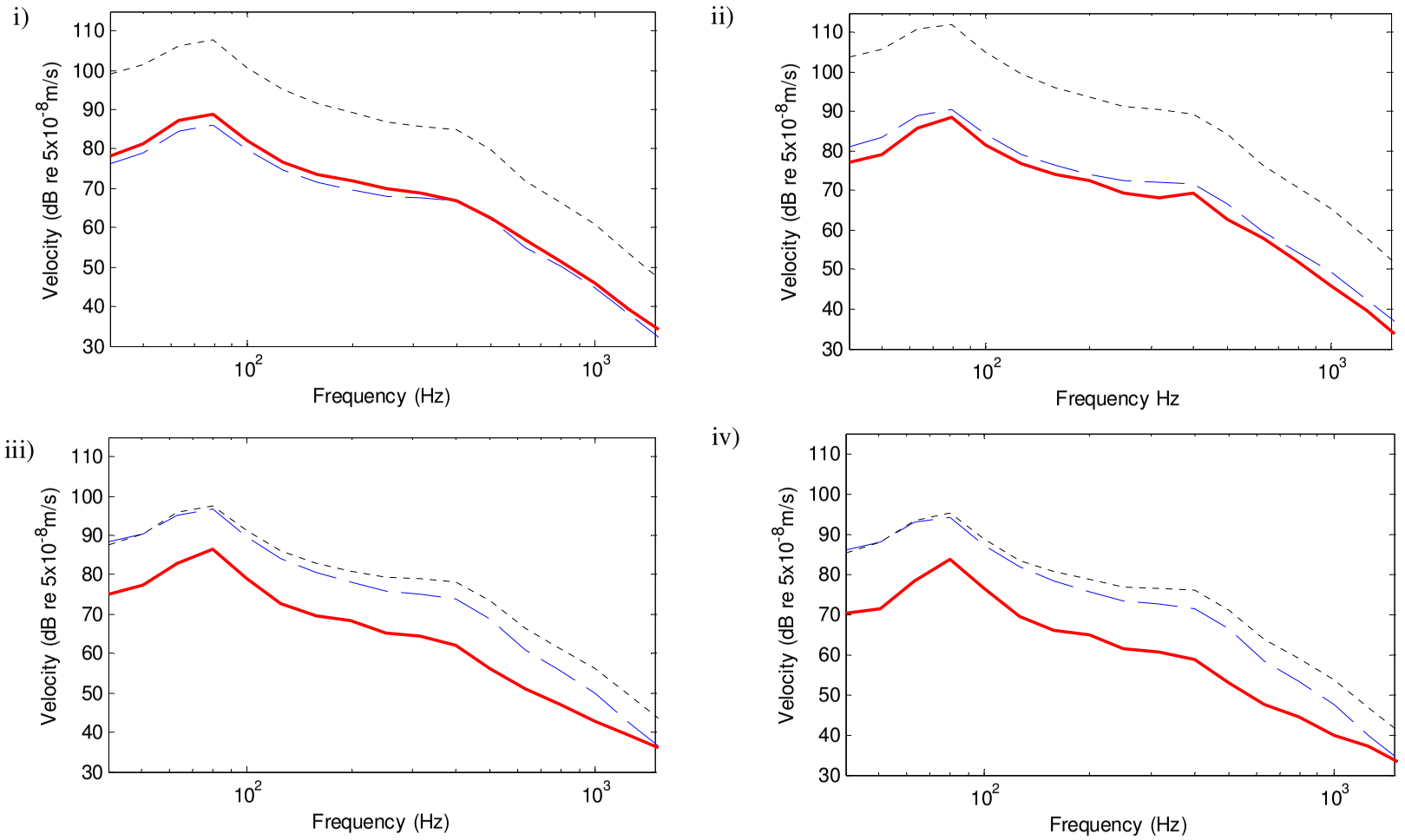

Figure 3.15. Spatially-averaged velocity of the composite bridge on the DLR shown versus frequency: ——, WFE; - - - - - -, NORBERT with beam as primary network; – – –, NORBERT with deck as primary network: i) deck, ii) side-deck, iii) web, iv) flange.

Figure 3.15 shows that the component velocities given by the simplified SEA scheme in which the beam is the primary network are much higher than those obtained from the WFE analysis or the alternative SEA-based calculation. The difference between the two simplified SEA schemes is large, up to 25dB. That with the beam as the primary network will not be discussed further in this work.

The component velocities given by the simplified SEA scheme in which the deck is the primary network compare much less closely with those obtained from the WFE model for the beam flanges and the beam webs than for the deck and side-deck in the frequency range up to 800Hz. The simplified SEA scheme gives velocities for the beam flanges and beam webs that are up to 15dB greater than those from the WFE model in this range. These two models therefore differ in the division of the input power between the concrete components (deck and side-deck) and the steel components (beam flanges and beam web). It is expected that this can be modelled more accurately using the WFE approach than a simplified SEA scheme in which the concrete and steel components are treated separately.

3.4. CONCLUSIONS

The WFE method has been used to predict the vibration response of this composite bridge on the DLR and to study the issues regarding the application of NORBERT to this type of bridge identified by Bewes (2006). The point mobility on the deck of this bridge was predicted using the WFE model and this shows that the bridge behaves as a coupled beam and plate over a significant part of the frequency range of interest. The simple structural models based on the use of either the mobility of the support beam, that of the deck or a smooth transition between these are therefore not readily applicable to this bridge.

A representation of the rail and track support was added to the WFE model of the bridge and used to calculate the power input to the bridge. The NORBERT model overestimates the power input to this composite bridge in the frequency range up to about 300Hz, relative to the WFE model. This is due to the higher mobility of the bridge in NORBERT, which is found from a beam model for the bridge in this range.

It has been shown that the WFE method can be used to predict the vibration response of the bridge under-traffic, given the excitation force at the rail as an input to the calculation. This has been found using the wheel-rail interaction model in

NORBERT. The bridge structure response is in satisfactory agreement with the measurements for the deck and side-deck made by Bewes (2006) for the frequency bands between 63Hz and 630Hz. At higher frequencies, the WFE result, like the NORBERT result, is significantly lower than the measurement. The WFE and NORBERT results for the deck and side-deck are in quite close agreement for the frequency bands above 630Hz. Bewes (2006) identified the assumed wheel-rail roughness and the rail fastener stiffness as the most likely causes of the discrepancy between NORBERT and the measurements at high frequency, and these apply equally to the results the WFE modelling.

Comparison of the spatially-averaged velocity for each major component of the bridge given by the WFE and NORBERT models indicates that the distribution of energy amongst these components is significantly different in the two models, for frequencies up to about 800Hz.

The WFE method is expected to be a more reliable means to predict the power input to this composite bridge and the sharing of this power amongst the major components of the bridge than NORBERT. This is due to the more detailed representation of the structure on which the WFE calculations are based, such that fewer simplifying assumptions are required than in using NORBERT for this type of bridge. It is therefore recommended that a WFE model should be used for predicting the vibration of a composite bridge.

4. THE DYNAMIC BEHAVIOUR OF RAILWAY BALLAST

4.1. INTRODUCTION

4.1.1. Railway ballast in bridge noise modelling

Most tracks, even on bridges, are ballasted and it is the layer of ballast that forms the connection between the track and the bridge deck. For these cases, it is therefore necessary to include a representation of the ballast layer in a model for bridge noise and vibration. This introduces additional uncertainty to the modelling task, relative to the case of directly-fastened track, because the properties of the ballast layer are the least well-defined parameters in the track model, (Jones et al., 2000).

Ballasted track is normally regarded as the low-noise option for the track form on railway bridges. This is supported by the case described by Stuber (1975). Directly-fastened track on a steel bridge was replaced by ballasted track, with a reported 12dB(A) reduction in the noise level at distance of 25m from the bridge. However, the noise survey reported by Hardy (1999) shows that bridges with ballasted track produce relatively high noise levels in some cases.

There is also disagreement with regard to a physical explanation for any noise reduction that the use of ballasted track in preference to directly-fastened track may provide. Stuber (1975) attributed this to the sound absorption properties of the ballast, Hardy (1999) identified the damping in the ballast as the primary mechanism by which ballast could reduce bridge noise and Kurzweil (1977) refers to the additional mass on the deck of a ballasted bridge. There may also be a significant difference in the dynamic stiffness of these two trackforms, and therefore also in the vibration isolation effect between the rail and the bridge. However, this discussion remains at a speculative stage, because there is a lack of reliable measurement data for the stiffness and damping properties of railway ballast.

Bridges with ballasted track have been studied using NORBERT, (Cobbing and Jones, 2008). The dynamic stiffness of the ballast was found by treating the ballast loaded in compression beneath each sleeper as an axially-loaded rod of finite length. The analytical solution for the response of such a rod was presented by Snowdon

(1963). The first longitudinal mode is expected in the ballast 'rod' within the frequency range of interest in bridge noise, such that the ballast stiffness would be frequency-dependent.

While the axially-loaded rod model provides a simple means to predict the dynamic stiffness of the ballast based on the expected physical behaviour, there is currently a lack of evidence in the literature to support this approach. Further, when this model has been used in NORBERT for bridges with ballasted track, the predicted noise and vibration levels have generally been in a lesser degree of agreement with measurement data than is normally the case for bridges with directly-fastened track.

The aim of the work presented in this chapter is to validate a simple model that can be used to describe the behaviour of a ballast layer in NORBERT against appropriate measurement data.

4.1.2. Previous work on the dynamic properties of ballast

Jones et al. (2000) measured the dynamic transfer stiffness of a ballast layer in a test section of at-grade railway track using accelerometers mounted on the sleeper and force transducers on a concrete slab beneath the ballast. Note that it is the transfer stiffness, the force transmitted to a blocked termination per unit displacement at the input side (Thompson and Verheij, 1997), which is required to calculate the vibration transmission from the rail to the bridge. A predictive model for the ballast transfer stiffness was proposed in which the ballast loaded by each sleeper was treated as a frustum of material, with sides inclined at an angle of 30 degrees to the vertical (i.e. a cone angle of 60 degrees). The level of agreement shown between the results of the model and the measurement work was not conclusive. This was attributed, at least in part, to the inability to calibrate force transducers buried under the track.

Zhai et al. (2004) studied the direct stiffness of the ballast layer on an in-service railway by embedding a protected accelerometer in the ballast to measure its acceleration during a train pass-by. A model for the ballast's direct stiffness was proposed, also based on a frustum of loaded ballast beneath each sleeper with sides inclined at an angle of 30 degrees to the vertical. The model differs from that proposed by Jones et al. (2000) in that shear stiffness and damping parameters were used to account for the effects of interaction between frustums of loaded ballast beneath adjacent sleepers, in cases where this is expected to occur. This interaction

between adjacent columns of loaded ballast was reported to have an important vibration-attenuation effect on the dynamic behaviour of the track. The transfer stiffness of the ballast was not considered in this work.

Al Shaer et al. (2008), Burrow et al. (2007), Chebli et al. (2008) have each used finite element (FE) models to study ballasted at-grade railway track, inclusive of the subgrade. However, since the sub-grade is normally less stiff than the ballast, these studies do not address the need for a model of ballasted track on a railway bridge.

Some models of railway ballast have been developed in which the ballast is modelled as a group of discrete particles, Discrete Element modelling, rather than assuming it may be treated as a homogeneous continuum of material, as in the rod, frustum and FE models. Suiker et al. (1999), Kruse and Popp (2003), Sahin and Indraratna (2006) and Saussine et al. (2006) present examples of this approach. These models have been developed to study the deterioration of ballast layers over large numbers of cycles in service. This is an important concern, due to the enormous cost of maintaining ballasted track (Saussine et al., 2006).

Suiker et al. (1999) suggest that heterogeneous effects in the ballast become more important at high frequencies, as the wavelength in the ballast becomes comparable to the grain size. Saussine et al. (2006) remark on the small depth of the ballast layer relative to the grain diameter, typically in the ratio of around ten to one, in justifying the need for this type of model. While only the case of ballast on a relatively soft sub-grade was considered, these models do provide information on the contact force network in the ballast and the settlement process. This is relevant to the study of the dynamic behaviour of ballast and would be very difficult to obtain experimentally.

The numerical model developed by Kruse and Popp (2003) was based on a two-dimensional representation of the ballast layer, with each grain modelled as a polygon with between five and eight sides. A random number generator was used to set the dimensions of these polygons within limits expected of railway ballast. This model was used to simulate pouring the ballast, laying the sleeper and a series of load cycles intended to represent the passage of a train. The settlement of the ballast during these load cycles was found to vary greatly as the simulation was re-run for the same type of ballast layer. This was attributed to the chaotic process of pouring the ballast, such that the initial conditions to differ in successive simulations, and the randomly

selected grain sizes. It was also reported that the network of contact forces between the ballast grains consists of only a small number of paths through the depth of the ballast layer. The majority of the grains are therefore not involved in the transmission of load across the ballast. The increase in stiffness of the ballast due to an applied static load was attributed, at least in part, to the formation of new contacts between the grains.

Saussine et al. (2006) also used a two dimensional discrete element model of a layer of ballast to predict its settlement. The simulation showed how the grains move relative to each other during the settlement process. A 'breathing' phenomenon was reported over a load cycle, where the grains move to areas of relatively low force intensity as the external load is reduced. The contact force network was strongest directly beneath the sleeper in all cases.

In summary, the literature review shows that the case of ballasted track on a relatively stiff foundation such as on railway bridges has received little attention. There does not appear to be a proven means for prediction of the dynamic stiffness of railway ballast, or measurement data that could be used to validate such a model.

The finite element and discrete element approaches to modelling the ballast described in the literature are not considered suitable for use in NORBERT, due to their complexity and computational demand. Relatively simple models for the ballast have therefore been considered here and tested against dynamic transfer stiffness measurements.

4.2. EXPERIMENT DESIGN

4.2.1. Approach taken to measurement of ballast stiffness

Measurements were made for the dynamic transfer stiffness of the ballast in the laboratory using a measurement rig, rather than in-situ on a railway bridge. Practical difficulties were expected in making these measurements on a railway bridge, particularly with regard to the required level of access. It was assumed in the design of the measurement rig that the effects of the moving load on ballast in railway track could be neglected, following Grassie et al. (1982).

Dynamic transfer stiffness measurements have been made for rail fasteners in previous work, normally by the 'direct' method or the 'indirect' method. The

difference between these is the means by which the force transmitted across the resilient element is determined. In the former, it is measured directly using a force transducer mounted on the output side of the resilient element under test. This requires a body on the output side that has a large stiffness and a small mass relative to that of the resilient element (Morrison et al., 2005). This does not seem practically achievable for measuring the stiffness of a quantity of ballast that is representative of that loaded by the sleeper in railway track. The indirect method of transfer stiffness measurement has therefore been adopted here, in which the transmitted force is found by measuring the acceleration of the solid body on the output side of the ballast and deriving the force by applying Newton's second law.

4.2.2. Simple model of the ballast stiffness test rig

A simple model of a rig that is suitable for making dynamic transfer stiffness measurements by the indirect method is shown below in Figure 4.1.

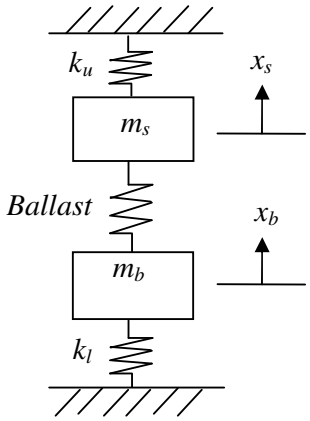

Figure 4.1. Simple model of the ballast stiffness test rig.

Figure 4.1 shows a two degree-of-freedom system, with three stiffness elements. k_u is required to isolate the upper mass from the structure used to apply a static preload to the system, simulating the effect of the wheel-load on the ballast in railway track. k_l provides isolation between the lower mass and the ground. The upper mass, m_s, will be referred to as the 'sleeper' hereafter and the lower mass, m_b, as the 'base slab'.

In the experiment, the transfer stiffness of the ballast layer is found from acceleration measurements made on the sleeper and base slab as follows,

$$k_{BT}(\omega) = \frac{F_{Trans}}{x_s - x_b} = \frac{m_b \ddot{x}_b}{x_s - x_b} \tag{4.1}$$

$$\therefore k_{BT}(\omega) = \frac{-\omega^2 m_b \ddot{x}_b}{\ddot{x}_s - \ddot{x}_b} = -\omega^2 m_b \left(\ddot{x}_s / \ddot{x}_b - 1 \right)^{-1} \qquad (4.2)$$

where F_{Trans} is the force transmitted across the ballast, x_s is the displacement of the sleeper and x_b is that of the base slab. The quantity required from the measurement work is therefore a transfer function between the acceleration of the sleeper and that of the base slab.

The factors that control the frequency range over which valid stiffness measurements can be made using this approach can be identified from the system model shown in Figure 4.1. For excitation at the sleeper by the harmonic force $f_s e^{i\omega t}$, the equations of motion are given by,

$$-\omega^2 m_S x_S + k_u x_S + k_{BP} x_s - k_{BT} x_b = f_s \qquad (4.3)$$

$$-\omega^2 m_b x_b + k_l x_b + k_{BP} x_b - k_{BT} x_s = 0 \qquad (4.4)$$

where k_{BP} is the point stiffness of the ballast and k_{BT} is the transfer stiffness of the ballast. Writing equations (4.3) and (4.4) in matrix form,

$$\begin{bmatrix} k_u + k_{BP} - \omega^2 m_s & -k_{BT} \\ -k_{BT} & k_l + k_{BP} - \omega^2 m_b \end{bmatrix} \begin{Bmatrix} x_S \\ x_b \end{Bmatrix} = \begin{Bmatrix} f_s \\ 0 \end{Bmatrix} \qquad (4.5)$$

The response of the system can be found by matrix inversion of equation (4.5). A practically realisable set of parameter values are shown in Table 4.1, together with a pre-estimate for the ballast layer stiffness.

m_s (kg)	m_b (kg)	k_u (MN/m)	k_l (MN/m)	k_{BT}, k_{BP} (MN/m)
100	1000	5	5	100

Table 4.1. Example parameter values for the simple model of the measurement rig.

No damping was included in this model. For these parameter values, the accelerance of the sleeper and the base slab are shown in Figure 4.2 below.

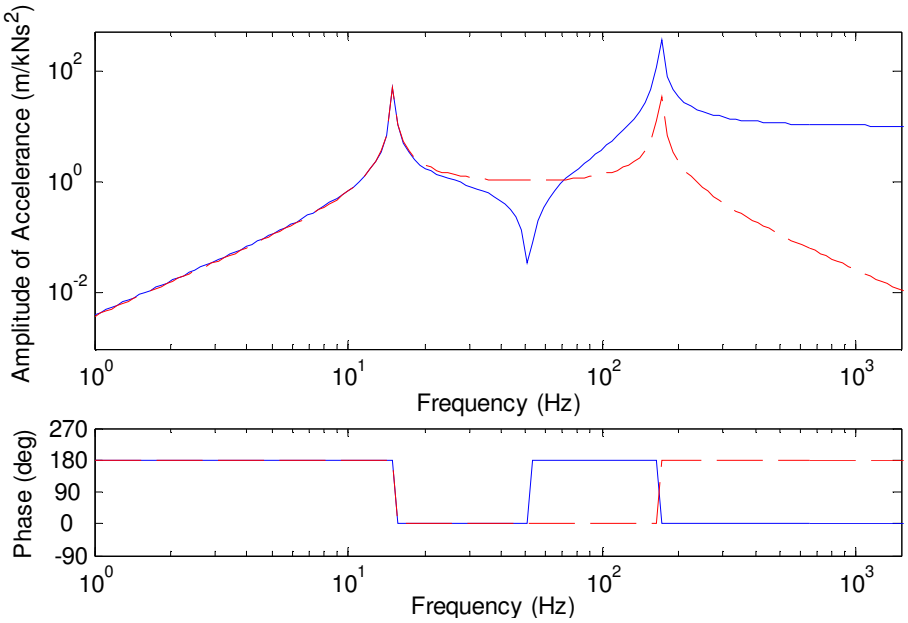

Figure 4.2. Amplitude and phase of accelerance, for excitation at the sleeper: ——— *, sleeper;* – – – – – *,base slab.*

Figure 4.2 shows the response expected of a two degree-of-freedom system with excitation at the upper mass (sleeper): a resonance of both masses at a frequency f_1, an anti-resonance of the sleeper at a frequency f_A and a second resonance of both masses at frequency f_2. From the system equations, these frequencies can be estimated as follows (Thompson et al., 1998).

$$f_1 \approx \frac{1}{2\pi}\sqrt{\frac{k_l + k_u}{m_s + m_b}} \tag{4.6}$$

$$f_A = \frac{1}{2\pi}\sqrt{\frac{k_l + k_{BP}}{m_b}} \tag{4.7}$$

$$f_2 \approx \frac{1}{2\pi}\sqrt{\frac{k_{BP}\left(m_s + m_b\right)}{m_s m_b}} \tag{4.8}$$

Figure 4.2 shows that the motion of the two masses is well-coupled up to a frequency of close to f_A. Since there is no displacement across the ballast in this part of the frequency range, its stiffness has no effect on the response of the masses. It was therefore expected that the lower limit to the frequency range for valid measurements would be close to f_A. In order to make measurements down to low frequencies,

therefore, the mass of the base slab should be large and the stiffness of the lower resilient mount small, while retaining stability of the rig.

For frequencies greater than f_A, Figure 4.2 shows that the motion of the two masses is de-coupled. The simple model indicates that valid measurements could be made up to a frequency at which the response of the base slab becomes very small, due to vibration isolation between the sleeper and base slab, such that the signal from the base slab accelerometer would be dominated by noise. Physically, however, it is the modal response of the base slab and sleeper that needs to be considered in determining the upper limit to the frequency range for valid measurements. Equation (4.2) is valid only for the frequency range in which the sleeper and base slab behave as simple masses.

4.2.3. The main components of the test rig

The measurements would ideally be made on a quantity of ballast that is representative of that loaded beneath a single monobloc railway sleeper during the passage of a train. Initial calculations showed that for a rig based on a monobloc sleeper, the internal modes of the sleeper and any practically-achievable base slab would occur from frequencies as low as 100Hz. A rig with smaller physical dimensions is therefore required in order to use equation (4.2) to determine the ballast stiffness over a range of frequencies, such that its frequency-dependence can be assessed.

It has been assumed here that the transmission of load between the sleeper and the ballast takes place in areas local to the two rail seats. This is supported by inspection of some ballasted track, the work of Kaewunruen and Remennikov (2007) and also Esveld (1988); it is common for the sleeper to be out of physical contact with the ballast in the centre-span region. It is therefore sufficient for the measurement rig to simulate the ballast loaded in compression beneath a single rail seat. On this basis, the 'sleeper' used in this work was a concrete block with a length of 600mm and a width of 285mm. These dimensions correspond to those for a one-quarter length section of an F40 monobloc sleeper.

The ballast was poured into an open-topped box, referred to as the ballast box hereafter. It was intended that the side walls of this box would not be subject to significant normal load by the ballast, for safety reasons and so that these walls do not

influence the stiffness measurements. The literature shows two different load distribution patterns in the ballast: Saussine et al (2006) report that the compressive load in the ballast is concentrated in the ballast directly beneath the sleeper, while Jones et al. (2000) and Zhai et al. (2004) assumed that the ballast load spreads downwards at an angle of 60 degrees (cone angle). The latter is a more conservative approach and has therefore been taken here in designing the rig. On the basis of this assumed load distribution and a ballast layer depth of 300mm, the length of the ballast box was set to 900mm and its width to 600mm. Measurements have been made for a deeper layer of ballast, but only for relatively low preloads, such that no significant safety risk was expected.

The length and width of the base slab follow those of the ballast box. The depth of the base slab was chosen by using a simple ANSYS FE model to predict its first few natural frequencies. Eight-noded brick elements (ANSYS element SOLID45) were used to model the base slab. No constraints were applied to this model, such that any partial constraint applied to the base slab by the ballast has been neglected.

Concrete is the only material that can provide the mass and stiffness required here at an acceptable cost. Relatively basic equipment was used to produce this concrete in the laboratory, such that the mixing and composition could not be controlled with the accuracy expected of commercially-produced concrete. The dynamic Young's modulus of this concrete was therefore subject to significant uncertainty, but it was set to a mid-range value of 30GPa (Kong and Evans, 1987) in the FE model. The density and Poisson's ratio were set to 2400kg/m^3 and 0.2 respectively.

It is expected that torsional modes of the base slab or the sleeper would not be strongly-excited in the test rig and these have therefore been ignored in this analysis. The first internal mode of the base slab of interest here is a vertical bending mode. The deformed shape of the base slab in this mode is shown in Figure 4.3.

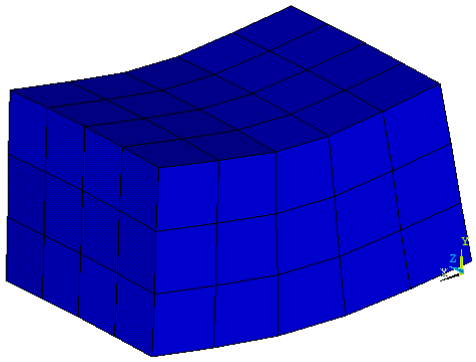

Figure 4.3. Deformed shape of the base slab in the first vertical bending mode.

The natural frequency of the mode shown in Figure 4.3 is approximately 1.5kHz when the depth of the base slab is set to 500mm. Together with the length and width dimensions given above, this represents a reasonably large concrete casting, but one that could be cast satisfactorily in the laboratory and subsequently moved into position on the lower resilient mounts. Note that the maximum overall depth of the base slab and sleeper is 800mm, limited by the ceiling height in the laboratory.

The measurement made using the accelerometer on the sleeper in the fully-assembled test rig is a point response measurement. An anti-resonance in the sleeper response must therefore follow the bounce resonance at frequency f_2 (equation (4.8)). With regard to the sleeper, it is this feature of its response that may impose the upper limit for valid stiffness measurements, rather than the first internal resonance.

The acceleration measurement on the base slab represents a transfer response. In this case, there only will be an anti-resonance between consecutive modes if the modal constants for these modes have the same sign (Ewins, 2000). The sign of the modal constant for a given mode is dependent on the relative phase of the motion at the excitation and response positions. Given that the high-frequency behaviour of the ballast was not well-understood in advance of the test work, this was difficult to predict. However, it seemed possible that if this problem occurred at a sufficiently low frequency to prevent measurements being made over an acceptable frequency range, it could be treated by moving the accelerometer on the base slab to another position.

Prediction of the sleeper anti-resonance frequencies requires a more detailed knowledge of the test rig properties, including the ballast, than was available prior to building the rig. The expected first bending resonance frequency of the sleeper was

therefore used to set the depth of the sleeper block, estimated using the same FE approach as that for the base slab. For a 300mm deep sleeper, with same material properties as those used for the base slab analysis, the first bending resonance frequency of the sleeper was estimated as 2kHz.

4.3. APPARATUS AND PROCEDURE

4.3.1. Description of the test rig

A photograph of the rig used to make the ballast stiffness measurements is shown below in Figure 4.4.

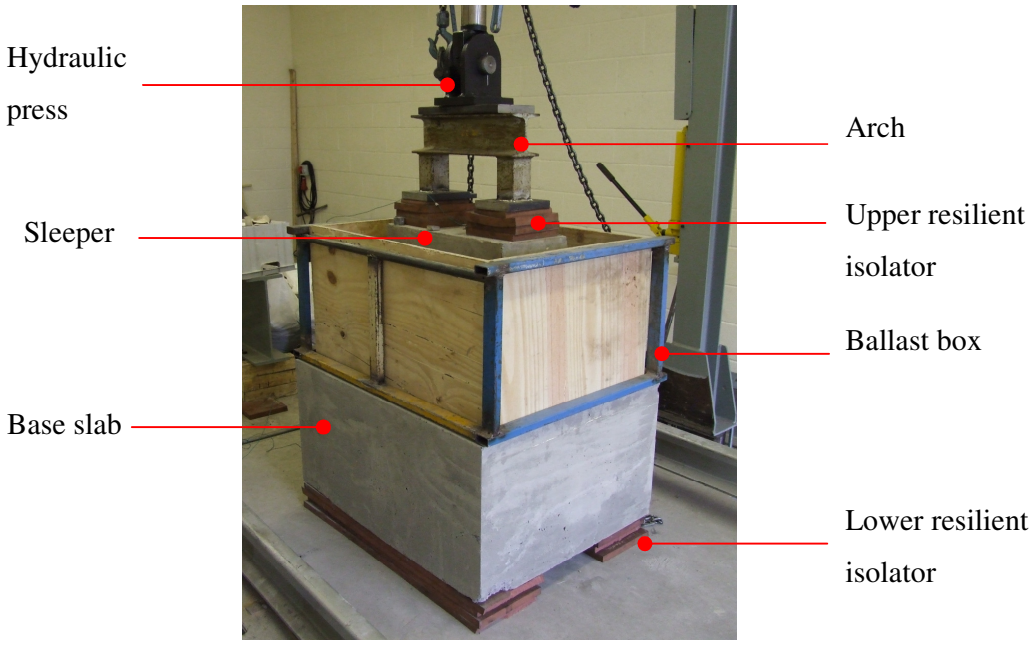

Figure 4.4. Photograph of the ballast stiffness test rig.

The upper resilient isolator shown in Figure 4.4 provides vibration isolation between the sleeper and the hydraulic press for all but very low frequencies. It consists of three layers of ballast mat material, specification DFSAH12, supplied by CDM-UK. A fabricated steel 'arch' structure was fitted between this resilient material and the hydraulic press. This allows access to the upper face of the sleeper, so that the system can be excited using the impact hammer.

The ballast box consists of a steel frame, which supports four vertical sides formed of 12mm thick plywood panels. A 1mm thick steel sheet was welded to the bottom of the steel frame. This is required to prevent the escape of ballast from beneath the steel frame of the box under preload.

Figure 4.4 shows three layers of resilient material beneath the base slab, labelled lower resilient isolator. This resilient material is also to specification CDM-DFSAH12 and provides vibration isolation between the base slab and the foundation.

The Enerpac hydraulic press shown in Figure 4.4 was supported by a steel load frame, used to apply a static preload to the system. A force gauge was fitted to the pump and this was used to determine the applied preload in each test. This gauge was checked by comparison with a calibrated load-cell. The preloads referred to in this work are subject to a maximum error of +/-2kN.

The reinforced concrete sleeper and base slab have masses of approximately 150kg and 850kg respectively.

4.3.2. Measurement method

Accelerometers were used to measure the acceleration of the sleeper and base slab at the centre of their upper faces, such that the transfer function between these can be found and used to calculate the ballast stiffness from equation (4.2). In order to avoid damage from the ballast under load, the accelerometer on the base slab was placed inside an inverted steel cup and the cable was run along the floor of the ballast box inside a stiff-walled nylon pipe. A third accelerometer was used to measure the acceleration of the impact hammer, which was converted to a force estimate. Accelerance spectra for the sleeper and base slab were found from the excitation force spectrum and used to study the behaviour of the measurement rig.

The equipment used to make these acceleration measurements is shown below in Table 4.2.

1	Kistler Accelerometer 8712A5M1 accelerometer (on base slab)
2	Kistler Accelerometer 8702B25M1 accelerometer (on sleeper)
3	Kistler Accelerometer 8702B500M1 accelerometer (on impact hammer)
4	National Instruments SCXI-1531 Accelerometer Input Module
5	National Instruments SCXI-1600 USB Data Acquisition Module
6	National Instruments SCXI-1000 Chassis for SCXI-1531 and SCXI-1600
7	Laptop computer running Pandrol LOGGER software

Table 4.2. Equipment list for acceleration measurements.

The accelerometers were calibrated by making point accelerance measurements on a known mass supported on resilient material and inspection of the spectra in the mass-controlled frequency range. Since it is the transfer function between the acceleration of the sleeper and the base slab that is required here, the accelerometers to be used on the base slab and the sleeper were calibrated simultaneously. This was repeated periodically through the test work.

The impact hammer has a mass of 0.6kg and relatively stiff plastic tip, such that strong excitation could be delivered to the sleeper for frequencies up to approximately 1.2kHz. A series of ten hammer taps were recorded in each test so that the effects of noise on the measurement signals could be reduced by averaging. The equipment described in Table 4.3 was used to record acceleration time-histories and to produce the required frequency response functions.

The ballast stiffness beneath each sleeper in railway track is a function of the contact state between the sleeper and the base slab (Wu and Thompson, 2000). Since significant variability may be expected in this contact state from one sleeper to another, the ballast stiffness would also be expected to differ between sleepers. Three sets of measurements were therefore made for each ballast layer configuration tested. The ballast was dug-out and then re-poured between each of the three measurements.

4.3.3. Test set-up procedure

The ballast was poured into the ballast box to the required depth and the top surface levelled by hand. The sleeper was then lifted into place on top of the ballast. A plumb line was used position the sleeper centrally about the axis of the press. The ballast beneath the sleeper was adjusted until the sleeper was horizontal, by ramming the ballast with a steel rod. A series of load cycles were used to simulate the initial ballast settlement process. A load of up to 100kN was applied over nine cycles, with checks made for the inclination of the sleeper every three cycles. The steel rod was again used to adjust the ballast until the sleeper was horizontal where necessary.

Point accelerance measurements were made on the upper surface of the sleeper close to each corner and mid-way along each of the longer sides. These measurements showed the behaviour of the ballast had become steady from one load application to another after the nine load cycles. A comparison between the point accelerance at symmetrically opposed locations about the centre of the sleeper upper face was used

to assess the uniformity of the support provided by the ballast to the sleeper. Rigid body 'rocking' motion of the sleeper must be avoided, as this would not fully engage the stiffness of the ballast. In some cases it was necessary to adjust the ballast further using the steel rod.

4.3.4. Types of ballast layer tested

Various ballast materials are used in different parts of the world, laid to a range of depths and the state of the grains with respect to wear is expected to change significantly over the service life of the ballast. Further, some form of liner is laid between the ballast and the bridge deck in many cases, to protect the deck from impact damage and to exclude rainwater from the bridge structure. It was therefore necessary to make measurements on a range of different ballast layers in this work, to account for the variability in behaviour expected between them. These are summarised in Table 4.3 below.

Configuration Number	Depth (mm)	Wear State	Liner
1	150	New	None
2	300	New	None
3	450	New	None
4	450	New	10mm plywood
5	300	New	Geotextile mat
6	300	Old	None

Table 4.3. Summary of the different types of ballast layer tested in this work.

The use of a liner between the ballast and the bridge deck is expected to affect the overall stiffness between the sleeper and bridge deck by two different mechanisms: the connection of the liner stiffness in series with the ballast stiffness and modification of the contact state between the ballast and the bridge deck. At present, only two types of liner are approved for use between a bridge deck and the ballast on UK mainline track. A sample of one of these liners was supplied by the manufacturer, Stirling Lloyd plc. This liner normally consists of two parts: a 2mm thick hard resin layer applied to the bridge deck in the form of a spray and a 6mm thick geotextile mat laid between the resin layer and the ballast. The hard resin layer is not expected to have a significant influence on the stiffness between the sleeper and bridge deck. Measurements were therefore made with only the geotextile mat laid beneath the

ballast. For bridges built in the past, it is common to find a layer of wood laid between the ballast and the bridge deck. Measurements were therefore made for the case of a 12mm thick plywood panel laid between the sleeper and the ballast.

Table 4.3 shows that two different types of ballast material were used in this test work, labelled 'new' and 'old'. The new ballast was supplied by Lafarge Aggregates and is typical of the granite ballast used on railways in central and eastern England. The old ballast was obtained from a ballast recycling plant in Doncaster. This ballast had been removed from mainline UK track at the end of its service life. Photographs of new and old ballast samples are shown in Figure 4.5 below.

Figure 4.5. Photographs of samples of the new ballast, left-hand pane, and old ballast, right-hand pane.

Figure 4.5 shows that the old ballast grains have edges and corners that are visibly less angular than those for the new ballast grains, due to wear action.

4.4. RESULTS AND DISCUSSION

4.4.1. Introduction

Some example measurements are considered in sub-sections 4.4.2 to 4.4.4, to illustrate the frequency range over which the valid results have been obtained, some important features of the stiffness spectra and the effects of a liner in the system. The effect of preload on the stiffness of the ballast layer is discussed in sub-section 4.4.5.

4.4.2. Example stiffness spectrum for a 150mm deep ballast layer

The dynamic transfer stiffness of the 150mm deep ballast layer is close to frequency-independent over a larger frequency range than that of the deeper ballast layers tested

in this work. It is therefore the most suitable one to study the effects that limit the valid frequency range for the measurements made on this rig.

Figure 4.6 shows the accelerance spectra of the sleeper and base slab obtained during a test for a 150mm deep layer of new ballast, under a preload of 60kN.

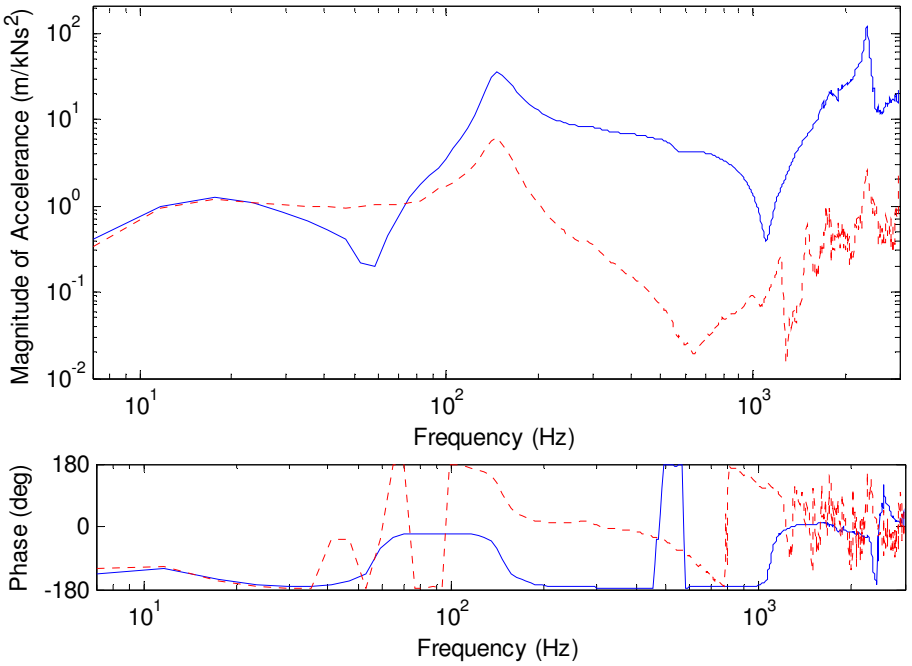

Figure 4.6. Magnitude and phase angle of accelerance, for a 150mm deep layer of new ballast, subject to a preload of 60kN, with no liner present: _____ , sleeper; - - - - - - - , base slab.

For frequencies up to 500Hz, the measured accelerance spectra are similar to those given by the simple model of the test rig presented in Section 4.2.2. The main differences between them in this range are due to the effects of damping in the physical system, which was not included in the simple model. Figure 4.6 shows that the first resonance of the system occurs at approximately 20Hz, the anti-resonance of the sleeper at 58Hz and the second resonance of the system at 145Hz.

At frequencies greater than 500Hz, the modal response of the sleeper and base slab introduce features to the accelerance spectra that are not present in the results of the simple model. Figure 4.6 shows anti-resonances of the base slab and the sleeper at 650Hz and 1.1kHz respectively. These features have a significant influence on the accelerance spectra for frequencies down to approximately 500Hz for the base slab and 800Hz for the sleeper. Note that these frequencies are dependent on the stiffness

of the ballast layer under test. It will be shown in the sections to follow that this ballast layer has a relatively low stiffness.

An internal resonance of the base slab is shown in the measurements at a frequency of 1.2kHz and of the sleeper at 2.2kHz. The base slab was designed for a first bending resonance of 1.5kHz, and the sleeper for 2kHz, as discussed in Section 4.2.3 above. The material properties achieved in casting the base slab were therefore disappointing relative to those for the sleeper.

The ballast transfer stiffness calculated from the accelerance measurements for this case using equation (4.2) is shown below in Figure 4.7. A solid line has been used to show the stiffness measurement in the valid frequency range and a dashed line has been used outside this frequency range.

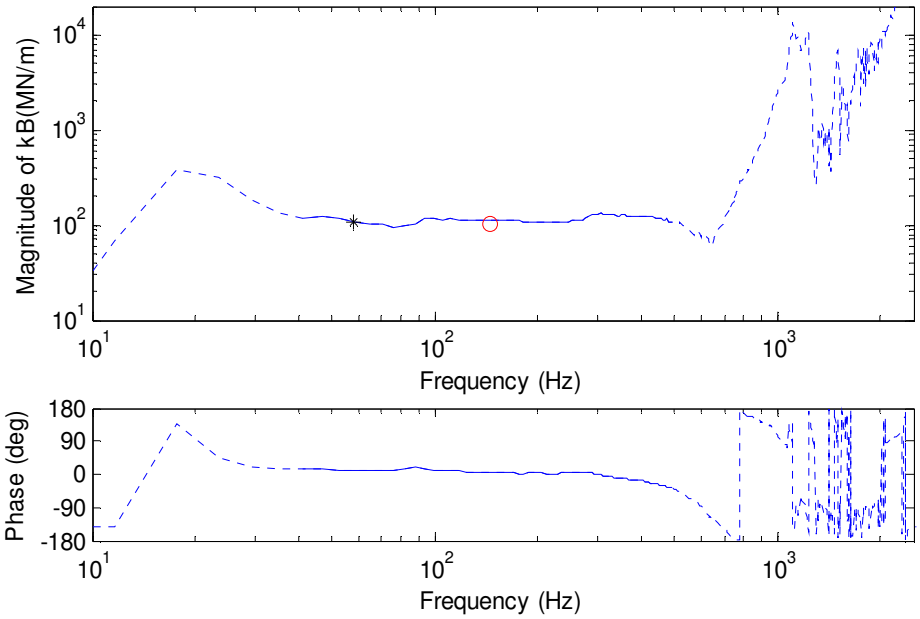

*Figure 4.7. Magnitude and phase of ballast transfer stiffness, for a 150mm deep layer of new ballast, subject to a preload of 60kN, no liner present: _____ ,measurement in valid frequency range; _ _ _ _ _ _ _, measurement outside valid frequency range; *, point stiffness given by equation (4.7); ○ , point stiffness given by equation (4.8)*

Figure 4.7 shows a stiffness magnitude of close to 100MN/m for frequencies between 40Hz and 500Hz. The phase angle is steady over much of this frequency range, at approximately 10 degrees. The estimates made for the direct stiffness of the ballast using equations (4.7) and (4.8) compare well with the measured transfer stiffness at the first anti-resonance frequency of the sleeper (f_A) and the second resonance

frequency of the system (f_2). The ballast behaves as a damped spring in this frequency range, such that the direct stiffness and the transfer stiffness should be equivalent.

The transfer stiffness found using equation (4.2) is not valid for frequencies less than about 40Hz or greater than 500Hz in this case. This is consistent with the accelerance spectra shown in Figure 4.6, which shows that the motion of the sleeper and base slab are well-coupled up to 40Hz and that the base slab only behaves as a simple mass up to approximately 500Hz. It is the anti-resonance of the base slab that imposes the upper limit for valid measurements made using this rig. While this limit is lower than had been hoped for, it is slightly higher for ballast layers with greater stiffness and it is sufficient for the frequency-dependence of the ballast stiffness to be studied for the deeper ballast layers tested here.

4.4.3. Example stiffness spectrum for a 300mm deep ballast layer

Figure 4.8 shows the transfer stiffness results obtained for a 300mm deep layer of new ballast under a preload of 20kN, with no liner present.

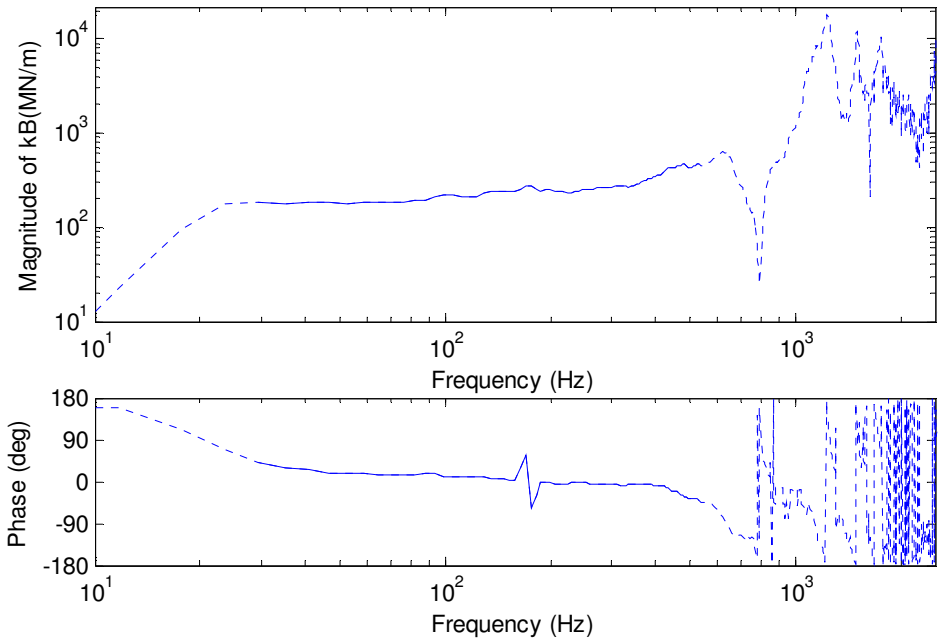

Figure 4.8. Magnitude and phase of ballast transfer stiffness, for a 300mm deep layer of new ballast, subject to a preload of 20kN, no liner present: _____ ,measurement in valid frequency range; - - - - - - - , measurement outside valid frequency range.

Figure 4.8 shows a stiffness magnitude of approximately 200MN/m and a phase angle of typically 10 to 15 degrees in the frequency range between 30Hz and 300Hz. For higher frequencies, the stiffness magnitude increases significantly with frequency, up to approximately 460MN/m at 500Hz. This is accompanied by a change in the phase angle. It has been shown in Section 4.4.2 above that the sleeper and base slab behave as simple masses in this frequency range. These features can therefore be attributed to an internal mode of the ballast layer.

4.4.4. Example stiffness spectra for a 450mm deep ballast layer

Figure 4.9 shows the transfer stiffness results obtained for a 450mm deep layer of new ballast under a preload of 10kN, with no liner present.

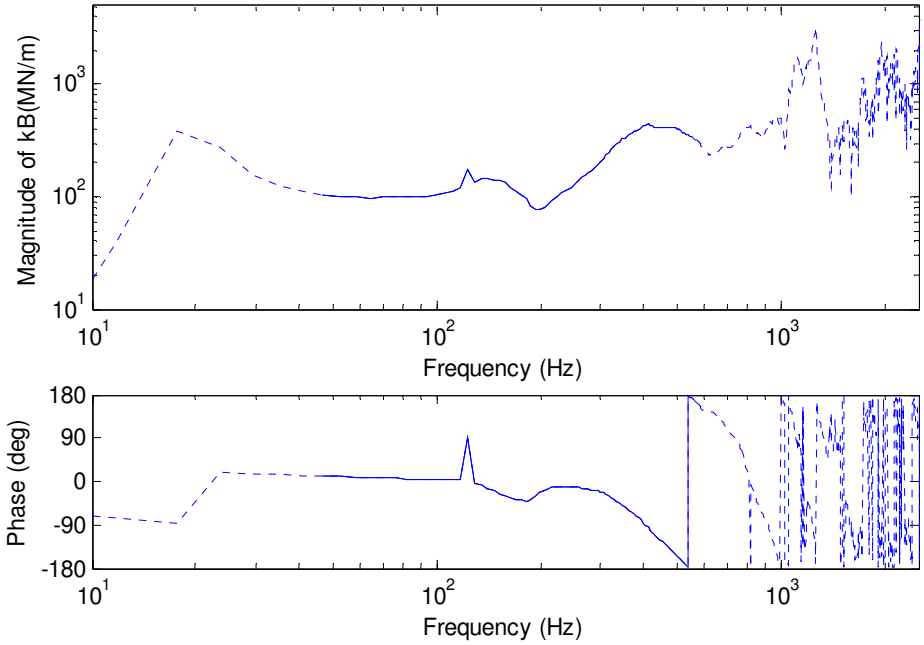

Figure 4.9. Magnitude and phase of ballast transfer stiffness, for a 450mm deep layer of new ballast, subject to a preload of 10kN, no liner present: _____ ,measurement in valid frequency range; - - - - - - - , measurement outside valid frequency range.

The measured stiffness has a magnitude of approximately 100MN/m and a phase angle of 5 to 10 degrees for frequencies between 45Hz and 100Hz. For higher frequencies, the stiffness is frequency-dependent. There is a broad peak in the magnitude spectrum at around 450Hz, together with a phase change of close to 180 degrees over the frequency range from 250Hz to 530Hz. These features are more fully-formed for this deeper ballast layer within the valid frequency range than was

the case for the 300mm deep layer and show the effects of an internal mode of the ballast more clearly.

There is also a peak in the stiffness magnitude shown in Figure 4.9 at a frequency of 150Hz, together with a small change in the phase angle. The cause of these features is not clear.

Figure 4.10 shows the transfer stiffness spectrum, for a 450mm deep ballast layer under a 10kN preload, with a 12mm thick plywood panel fitted between the sleeper and the ballast.

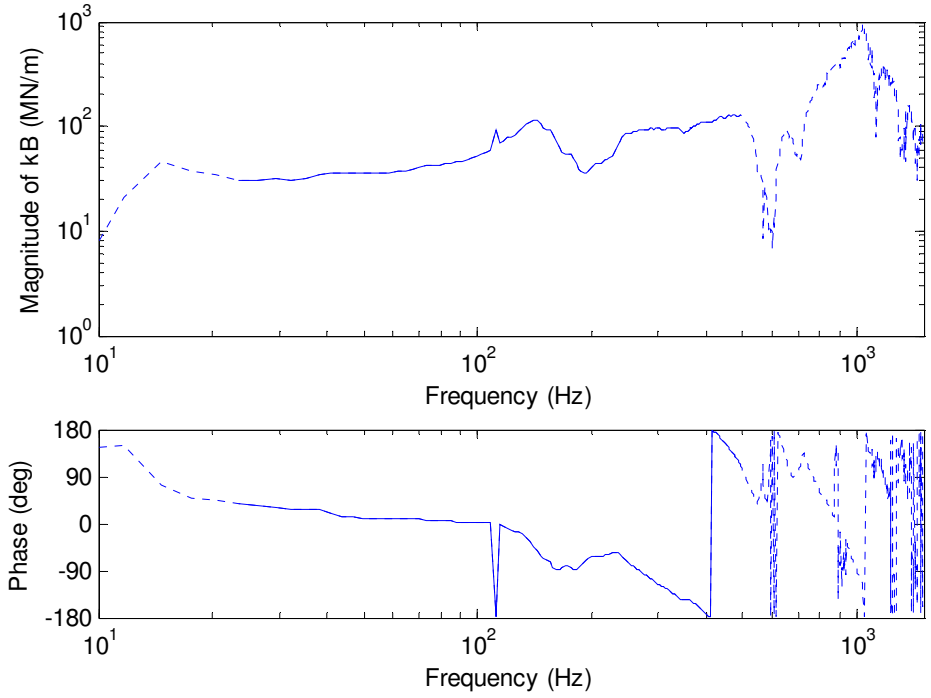

Figure 4.10. Magnitude and phase of ballast transfer stiffness, for a 450mm deep layer of new ballast, subject to a preload of 10kN, with a 12mm thick plywood panel fitted between the sleeper and ballast: _____ ,measurement in valid frequency range; - - - - - - - , measurement outside valid frequency range.

For frequencies up to 70Hz, the measured stiffness magnitude is approximately 35MN/m and its phase is about 10 degrees. Comparison with the stiffness magnitude shown in this frequency range for the 450mm deep layer of ballast without liner in Figure 4.9 shows that the effect of the 12mm plywood panel is to reduce the stiffness by a factor of around 3 in this frequency range. For frequencies between 70Hz and 250Hz, the stiffness spectra obtained with and without the plywood liner are similar in appearance.

The stiffness of the 450mm deep ballast layer with the plywood panel is approximately 100MN/m in the frequency range between 250Hz and the upper frequency limit for valid measurements (500Hz). The effect of the liner in this range is therefore to remove the peak expected due to the internal mode of the 450mm deep ballast layer, with a consequent reduction in stiffness by up to a factor of 4.

4.4.5. Effect of preload

The results presented in sub-sections 4.4.2 to 4.4.4 show that the magnitude and phase of the ballast stiffness are quite steady over the frequency range from the lower limit for valid measurements (around 40Hz) to about 100Hz. The stiffness of the various ballast layers under a range of preloads has therefore been compared at a frequency of 100Hz. Figures 4.11 i) to iii) show the transfer stiffness of the three different types of 300mm deep ballast layers tested in this work, at a frequency of 100Hz, versus preload.

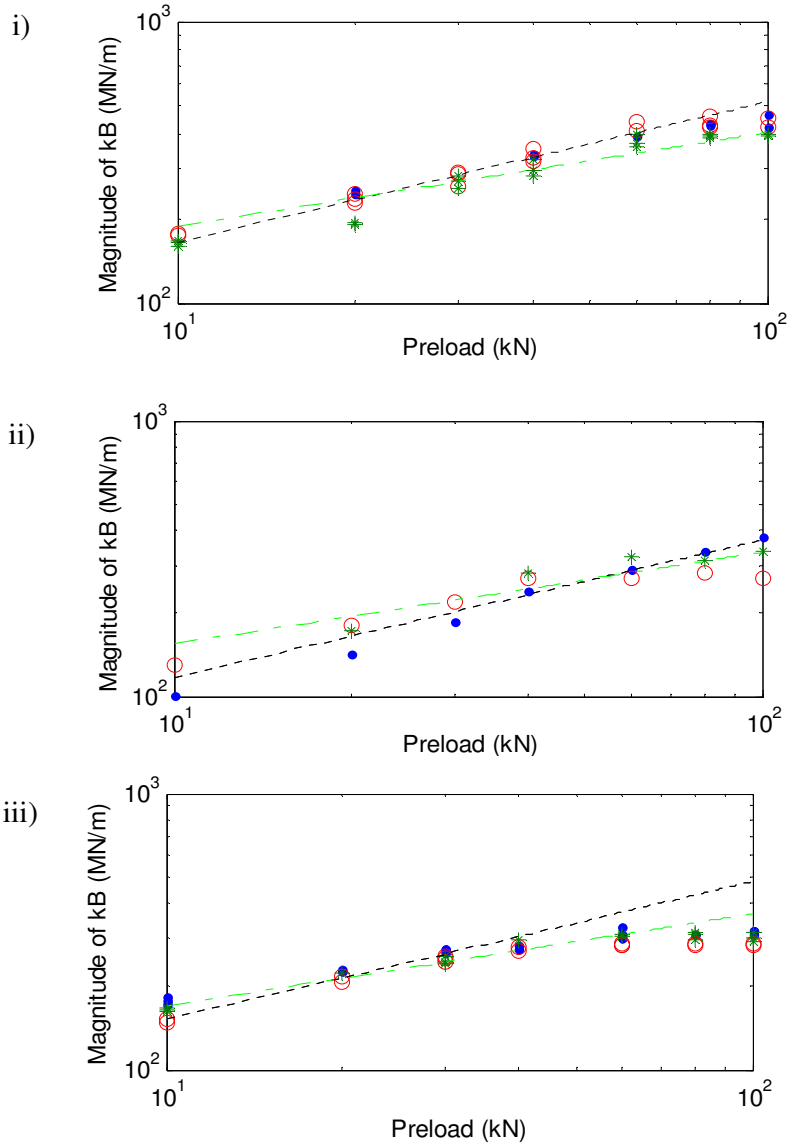

*Figure 4.11. Transfer stiffness magnitude for the 300mm deep layers of ballast, shown versus preload, at a frequency of 100Hz. i) new ballast, ii) new ballast plus geotextile mat, iii) old ballast: ● , seating 1; ○ , seating 2; * , seating 3; - - - - - - - , ½ power law; _ . _ . _ . , 1/3 power law.*

Figures 4.11 i) to iii) show that there is reasonable consistency between the results obtained for the three sleeper seatings in each case.

For the new ballast layer and also for the new ballast plus geotextile mat, the stiffness magnitude is approximately proportional to the square root of the applied preload, for preloads up to 60kN. The preload applied to the ballast per sleeper end, during a train pass-by, normally lies within this range. Jones et al. (2000) reported a similar finding

for a 300mm deep layer of new ballast. A comparison of Figures 4.11 i) and 4.11 ii) shows that the geotextile mat causes a reduction in the stiffness magnitude by approximately 25%. Thus, of the two stiffnesses in series, the stiffness of the ballast is greater than that of the geotextile.

Figure 4.11 iii) shows that the preload dependence of the 300mm deep layer of old ballast appears to follow a one-third power law more closely than a one-half power law. The former is that expected from Hertzian contact theory, for a pair of elliptical surfaces. The photographs of the new and old ballast grains presented in Figure 4.5 above show that the old ballast grains are less angular than the new ballast grains. Contact between the old ballast grains may therefore represent a significantly closer approximation to the Hertzian contact model than that between new ballast grains.

Comparing Figures 4.11 i) and 4.11 iii) shows that for high preloads, the old ballast is less stiff than the new ballast. This is contrary to the expectation that the stiffness of railway ballast would increase significantly through its service life. A primary mechanism by which this is thought to occur is the production of fine material as the ballast grains wear, such that voids between the grains become filled. This effect may not have been properly included in this test work, because fine material would have been lost as the ballast was removed from the track and during subsequent handling.

It has been shown that the ballast behaves as a damped spring over a significant range of frequencies. Assuming that the damping in the ballast layer may be modelled using a loss factor approach, the damping may be quantified as follows,

$$k^* = k_r\left(1 + i\eta\right) \tag{4.9}$$

$$\therefore tan(\theta) = \frac{\eta k_r}{k_r} = \eta \tag{4.10}$$

where k^* is the complex ballast transfer stiffness, θ is the phase angle and k_r is the real part of the ballast transfer stiffness.

Figure 4.12 shows the damping loss factor estimates made using equation (4.10) for a 300mm deep layer of new ballast, with no liner, with the geotextile liner, and also for a 300mm deep layer of old ballast, versus preload.

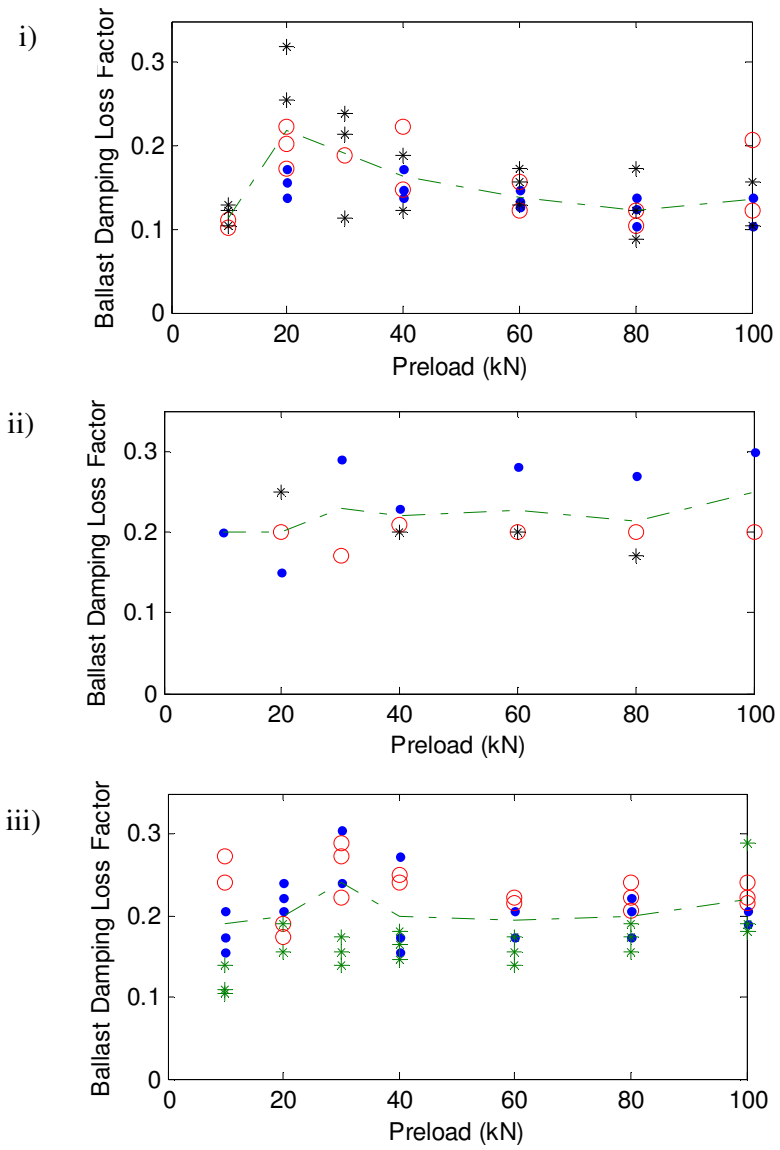

*Figure 4.12. Damping loss factor for a 300mm deep layer of ballast at frequency of 100Hz, shown versus preload. i) 300mm new ballast, ii) 300mm new ballast plus geotextile mat, iii) 300mm old ballast: ● , seating 1; ○ , seating 2; * , seating 3; _·_·_ , mean of all measurements.*

There is significant spread in the damping loss factor values obtained for different sleeper seatings and also in repeat measurements made for a single sleeper seating. For the old ballast, this variability is greater for low preloads, but this trend is less clear for new ballast. The mean damping loss factor for new ballast without a liner is typically in the range from 0.1 to 0.15, while for new ballast plus geotextile mat and for old ballast it is typically 0.2. Higher damping in the old ballast may be expected

from the less angular shape of the old grains, such that there would be greater relative motion between them and therefore more energy dissipation due to friction. The greater damping loss factor found for new ballast when the geotextile mat is present is likely to be due to energy dissipation within the mat, rather than due to any effect it may have on the settlement of and relative motion between the ballast grains.

Now consider the 450mm deep ballast layer, with and without the 12mm thick plywood liner laid between the sleeper and the ballast. Figure 4.13 shows the magnitude of the transfer stiffness versus preload.

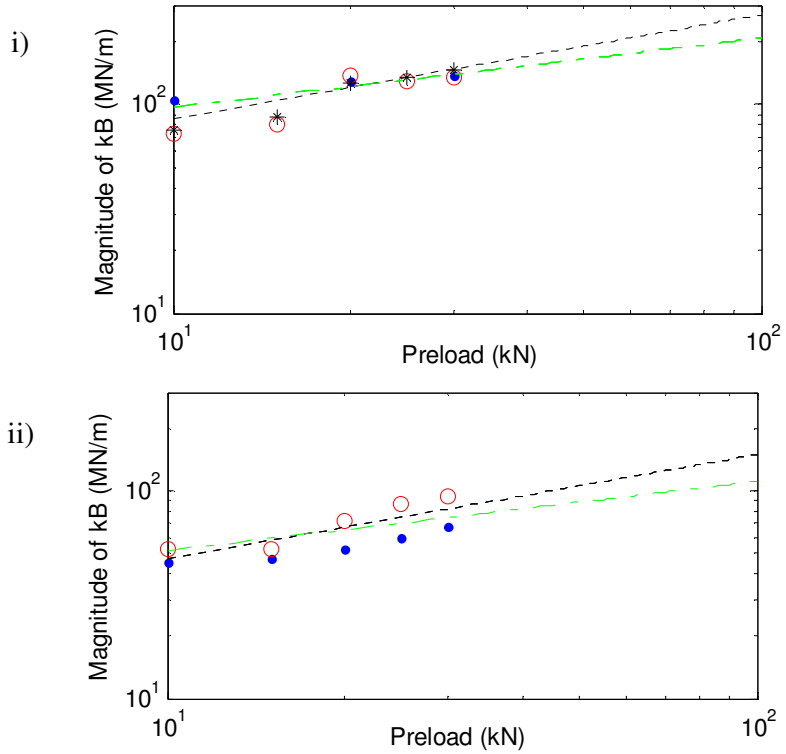

*Figure 4.13. Transfer stiffness magnitude of the 450mm deep layers of ballast, shown versus preload, i) no liner, ii) 12mm thick plywood liner: ● , seating 1; ○ , seating 2, * , seating 3, _____ , ½ power law; _ . _ . _ . _ , 1/3 power law.*

Note that it was necessary to take the results at a lower frequency than 100Hz for the plywood liner case, typically 60Hz, in order to avoid the effects of the first mode of this relatively soft ballast layer. The variability between the stiffness results obtained for the 450mm deep layers of ballast is relatively high, such that it is unclear whether their stiffness varies with preload according to a one-half or a one-third power law.

Comparing the stiffness results obtained for the 300mm and 450mm deep layers of new ballast, without liners, they differ by a factor of about two for a given preload level. The use of the plywood liner brings a further reduction in stiffness, down to approximately 60MN/m per sleeper end for a preload of 20kN. This is of the same order as that for a resilient baseplate rail fastener (Thompson, 2009).

Figure 4.14 shows the damping loss factor estimates made for the 450mm deep ballast layer with no liner present and also with the plywood liner, versus preload.

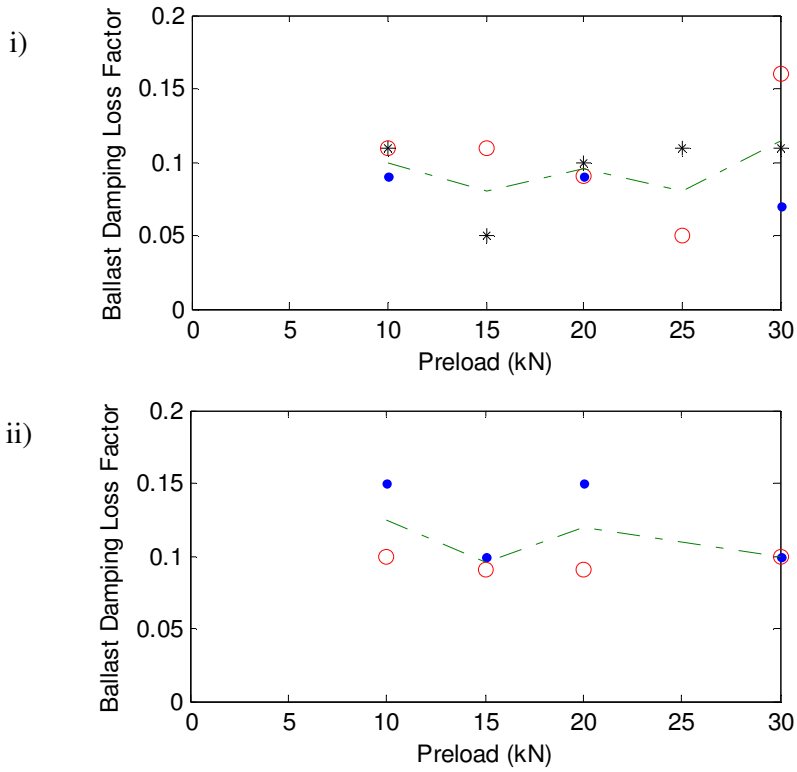

Figure 4.14. Damping loss factor for 450mm deep layer of new ballast, shown versus preload: i) no liner, ii) with 12mm thick plywood liner: ● , seating 1; ○, seating 2, _ . _ . _ . _ , mean of all measurements.

A damping loss factor of 0.1 is appropriate for the 450mm deep ballast layer over the range of preloads tested, with and also without the plywood liner. This is significantly lower than that found for the 300mm deep ballast layers.

4.4.6 Behaviour of the 150mm deep ballast layer

Figure 4.15 shows the magnitude of the transfer stiffness of the 150mm deep layer of new ballast versus preload.

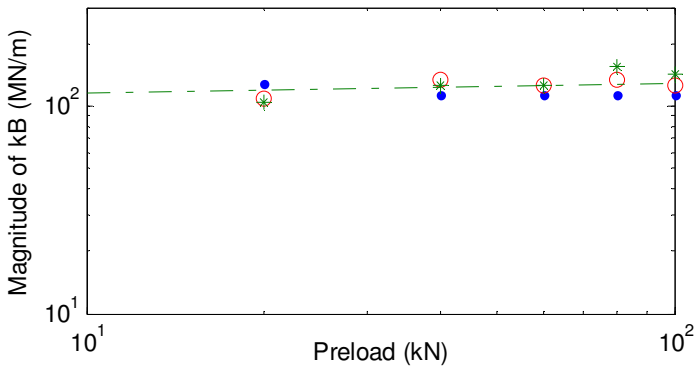

*Figure 4.15. Transfer stiffness magnitude of the 150mm deep layers of ballast, shown versus preload, at a frequency of 100Hz: ● , seating 1; ○ , seating 2, * , seating 3; _·_·_·_ , mean of all measurements.*

The transfer stiffness of the 150mm deep layer of new ballast was found to show no significant dependence on the applied preload or frequency in the range over which valid measurements have been made. The stiffness magnitude was found to lie between 100MN/m and 160MN/m in all tests, with the variability between the three sleeper seatings being responsible for almost all of this range. This stiffness is lower than that of the 300mm deep ballast layer, contrary to expectations based on models for the ballast as a continuum. It will be shown in Section 4.5 that a continuum model can be used to predict the stiffness of a 300mm and 450mm deep ballast layer reasonably well.

In many of the measurements made for the 150mm deep layer of ballast, the phase angle of the stiffness is not stable with respect to frequency over any significant part of the frequency range, such that it is not possible to estimate the damping loss factor using equation (4.10) in these cases. From those measurements that do show a stable phase angle in the low frequency range, the damping loss factors estimated from the phase angle are shown as a function of preload in Figure 4.16 below.

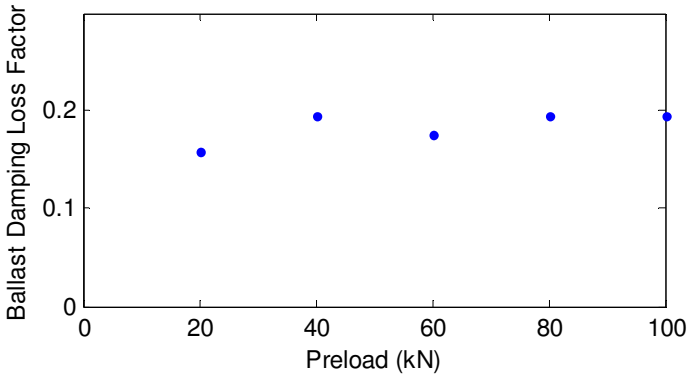

Figure 4.16. Damping loss factor for 150mm deep layer of new ballast, shown versus preload.

A damping loss factor in the range from 0.15 to 0.2 is appropriate for the 150mm deep layer of ballast.

It is proposed here that the rather different behaviour found in the test work for the 150mm deep ballast layer may be caused by a relatively restricted ballast settlement process in this layer. For most of the grains, the major dimension lies between 30mm and 50mm, but the grains are normally orientated such that the major dimension is roughly horizontal. It is therefore expected that the 150mm deep layer of ballast consists of about five adjacent grains in the vertical direction, and a 300mm deep layer of about 10 grains in the vertical direction. There may therefore be significantly more freedom for the migration of ballast grains to areas of lower force intensity during settlement of the ballast, described by Saussine et al. (2006), for the 300mm deep layer than the 150mm deep layer.

Restricted motion of the grains in the 150mm deep ballast layer would limit the formation of contacts between grains during the load cycles used to prepare each ballast layer for test and also as the preload is increased during each test. There would therefore be fewer chains of loaded grains between the sleeper and the base slab in this relatively shallow ballast layer, such that its stiffness would be low. Further, since the formation of new contacts between grains was identified as a major factor in the dependence of the ballast stiffness on preload (Kruse and Popp, 2003), restricted grain motion in the 150mm deep layer may also explain the approximately constant stiffness found over a large range of preloads in these tests.

4.5. MODELLING THE BALLAST LAYER

4.5.1. Models for the dynamic stiffness of ballast

In using NORBERT for bridges with ballasted track, the dynamic stiffness of the ballast has been calculated from an axially-loaded rod model for the ballast beneath the sleeper (Cobbing and Jones, 2008). The cross-section dimensions of this rod were set to the base dimensions of the sleeper, and its length to the depth of the ballast layer. An analytical solution for the dynamic transfer stiffness of this rod, with harmonic excitation at one end, is presented by Snowdon (1963),

$$k_B = \frac{EA\kappa}{sin(\kappa h)} \tag{4.11}$$

where h is the depth of the ballast layer and κ is the wavenumber in the rod, given by,

$$\kappa = \frac{\omega}{(E/\rho)^{1/2}} \tag{4.12}$$

Jones et al. (2000) and Zhai et al. (2004) took a slightly different approach to modelling the dynamic stiffness of the ballast, in which it is assumed that the load from the sleeper spreads downwards at an angle of 60 degrees (cone-angle) in the ballast. The transfer stiffness was calculated from the following expression for an axially-loaded circular frustum (Jones et al., 2000),

$$k_B = \frac{EA_2 n\kappa}{sin(\kappa h)} \frac{\sqrt{A_1}}{\sqrt{A_2}} \tag{4.13}$$

where A_1 is the area of the frustum at its upper face and A_2 that at its lower face. The circular frustum is specified so that the areas of its upper and lower faces are equal to those of the non-circular frustum expected in the ballast, given the base dimensions of the sleeper and a load spread angle of 60 degrees.

An alternative to the continuum models has also been considered. It may be supposed that following initial settlement of the ballast, much of the compliance of the ballast layer is local to the contact between the ballast and the containing surfaces, rather than evenly distributed through the ballast. The bulk of the ballast, which lies between the grains adjacent to the containing surfaces, may therefore be represented as a rigid mass. The ballast grains in contact with the containing surfaces above and below the

ballast may be approximated as simple stiffness elements. This will be referred to as the 'interface stiffness' model here and it is shown diagrammatically in Figure 4.17.

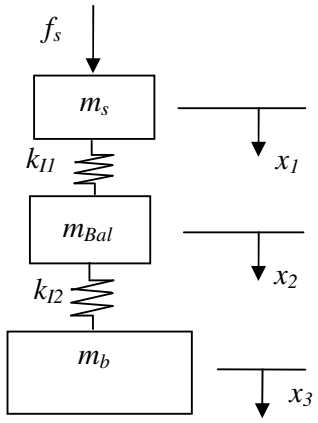

Figure 4.17. System diagram for the interface stiffness model.

k_{I1} represents the stiffness at the ballast-sleeper interface, k_{I2} represents the stiffness at the ballast-deck interface. m_{bal} represents the mass of the ballast layer, found from the volume of the prismatic rod of ballast directly beneath the sleeper and the density of the ballast. m_s is the mass of the sleeper and m_b that of the base slab.

For excitation at the sleeper by the harmonic force $f_s e^{i\omega t}$, the equations of motion for the system shown in Figure 4.17 are as follows,

$$-\omega^2 m_s x_1 + k_{I1}(x_1 - x_2) = f_s \tag{4.14}$$

$$-\omega^2 m_{Bal} x_2 + k_{I1}(x_2 - x_1) + k_{I2}(x_2 - x_3) = 0 \tag{4.15}$$

$$-\omega^2 m_b x_3 + k_{I2}(x_3 - x_2) = 0 \tag{4.16}$$

or in matrix form,

$$\begin{bmatrix} k_{I1}-\omega^2 m_s & -k_{I1} & 0 \\ -k_{I1} & k_{I1}+k_{I2}-\omega^2 m_{Bal} & -k_{I2} \\ 0 & -k_{I2} & k_{I2}-\omega^2 m_b \end{bmatrix} \begin{Bmatrix} x_s \\ x_2 \\ x_3 \end{Bmatrix} = \begin{Bmatrix} f_s \\ 0 \\ 0 \end{Bmatrix} \tag{4.17}$$

Equation (4.17) can be solved for the unknown displacements, from which the transfer stiffness is found using the indirect stiffness calculation of equation (4.2).

Each of the three models contain parameters for which values are not known. Values for the Young's modulus to be used in the rod and frustum models, and k_{I1} and k_{I2} in the interface stiffness model, were found by fitting the results of the models to the measurements for a 450mm deep layer of new ballast, under preloads of 10kN and 20kN. This fitting exercise was limited to low frequencies, where the magnitude and phase of the ballast stiffness do not vary significantly with frequency. The ability of the models to predict the frequency-dependence of the ballast stiffness at higher frequencies was assessed by comparing them to the measurements for the remainder of the frequency range in which the measurements are valid. That is, the prediction of the first resonance in the ballast was tested against the measurement data.

The ability of the three models to account for the influence of the depth of the ballast layer on its dynamic transfer stiffness was then tested by applying them to a 300mm deep layer of new ballast, for preloads of 10kN and 20kN, using the parameter values obtained for the 450mm deep layer of ballast. No attempt was made to fit the models directly to the measurements for the 300mm deep layer of ballast.

4.5.2. Modelling a 450mm deep layer of new ballast

The measured transfer stiffness for a 450mm deep layer of new ballast under a preload of 10kN is shown below in Figure 4.18, along with calculations from the three models.

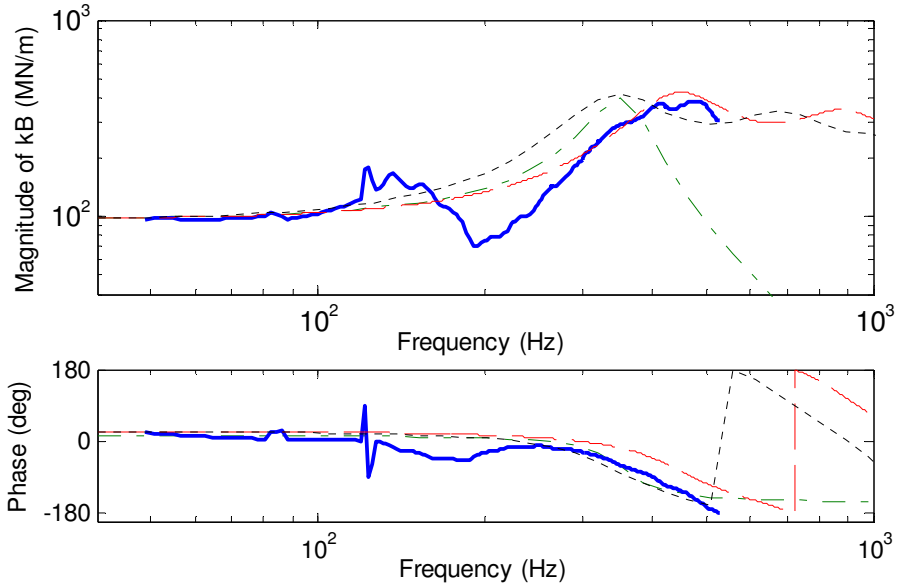

Figure 4.18. Magnitude and phase angle of the ballast transfer stiffness, for a 450mm deep layer of new ballast subject to a preload of 10kN: ——— , from measurements; – – – – – , rod model; - - - - - - - , frustum model; – · – · – , interface stiffness model.

Figure 4.18 shows best agreement between the results of the rod model and the measurements with regard to the main peak in the magnitude spectra, at about 450Hz. The frustum model predicts this main peak at a significantly lower frequency, but the maximum value and bandwidth of the peak are similar to those in the measurements. The interface stiffness model does not predict this peak in the magnitude spectrum satisfactorily. None of the models predict the feature shown in the measured result between 100Hz and 250Hz. However, this is a less significant feature than the main peak at about 450Hz.

The input data used in the rod and frustum models to produce the results shown above in Figure 4.18 above are given in Table 4.4.

	Rod	**Frustum**
Young's modulus (MN/m^2)	220	130
Material damping loss factor	0.45	0.45

Table 4.4. Input data used for the rod and frustum models of a 450mm deep ballast layer, under a preload of 10kN.

The frustum model was applied to the 450mm deep ballast layer for a load-spread angle of 40 degrees (cone angle), rather than the intended 60 degrees, limited by the dimensions of the base slab. It is clear from Figure 4.18 that the use of a larger load-spread angle would not improve the level of agreement between the frustum model and the measurements.

It was found necessary to use a material damping loss factor value in the rod and frustum models of 0.45 in order to predict the broad peak shown in the measurements at higher frequencies. This is significantly larger than that found from the phase angle of the complex stiffness at low frequencies, typically 0.1 for a 450mm deep layer (Figure 4.14). An explanation for this difference can be found in the literature. Richards and Lenzi (1984) and Kuhl and Kaiser (1952) describe the damping of granular materials in terms of a loss factor that is dependent on the amplitude of vibration. At low frequencies the energy dissipation occurs primarily within the grains, such that the damping loss factor is relatively small. For the higher amplitudes in the frequency range where the ballast layer is resonant, the loss factor becomes significantly larger due to energy dissipation by frictional forces between the grains. Much of this previous work on damping in granular materials has been done for sand, but Kuhl and Kaiser (1952) report similar behaviour for a layer of brick rubble. It is therefore expected that a frequency-dependent damping loss factor is required to model the dynamic behaviour of ballast over the frequency range of interest in bridge noise. While the measurement and modelling work described here show significant changes in the damping level with frequency, they do not provide sufficient data on which to base a precise development of the damping loss factor with frequency.

The measurements made for a 450mm deep layer of new ballast under a preload of 20kN are compared the results of the models for this case in Figure 4.19 below. Note that the parameter fitting exercise, in the low frequency range, has been repeated here for this higher preload case.

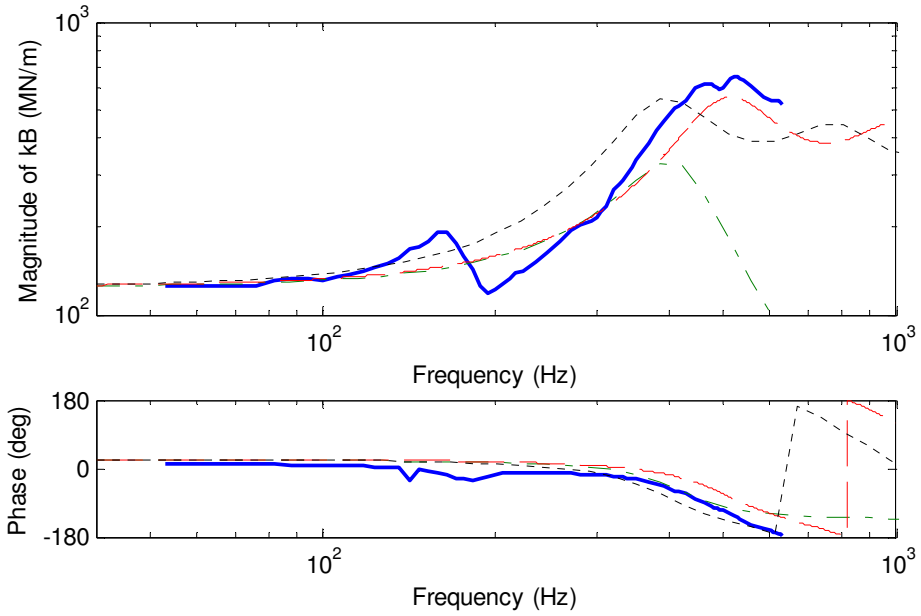

Figure 4.19. Magnitude and phase angle of the ballast transfer stiffness, for a 450mm deep layer of new ballast subject to a preload of 20kN: ——— , from measurements; – – – – – , rod model; - - - - - - - , frustum model; – . – . – , interface stiffness model.

The comparison shown between the three models and the measurement work shown in Figure 4.19 for the 20kN preload case is consistent with that shown previously for the 10kN preload case. The rod model underestimates the stiffness for the main peak at about 515Hz, but does predict the frequency of this peak correctly.

The input data used in the rod and frustum models for the 20kN preload case is shown in Table 4.5 below.

	Rod	**Frustum**
Young's modulus (MN/m^2)	285	170
Material damping loss factor	0.45	0.45

Table 4.5. Input data used for the rod and frustum models of a 450mm deep ballast layer, for preload of 20kN.

4.5.3. Modelling a 300mm deep layer of new ballast

The three models were applied to the 300mm deep layer of new ballast under preloads of 10kN and 20kN, for the same parameter values found for these preloads by fitting the models to the measurements made for the 450mm deep ballast layer in Section

4.5.2 above. Only the depth of the ballast layer was changed in the rod and frustum models, and the mass of the ballast in the interface stiffness model.

Figures 4.20 i) and ii) compare the results of the three models run for these parameter values with the measurements made for the 300mm deep ballast layer.

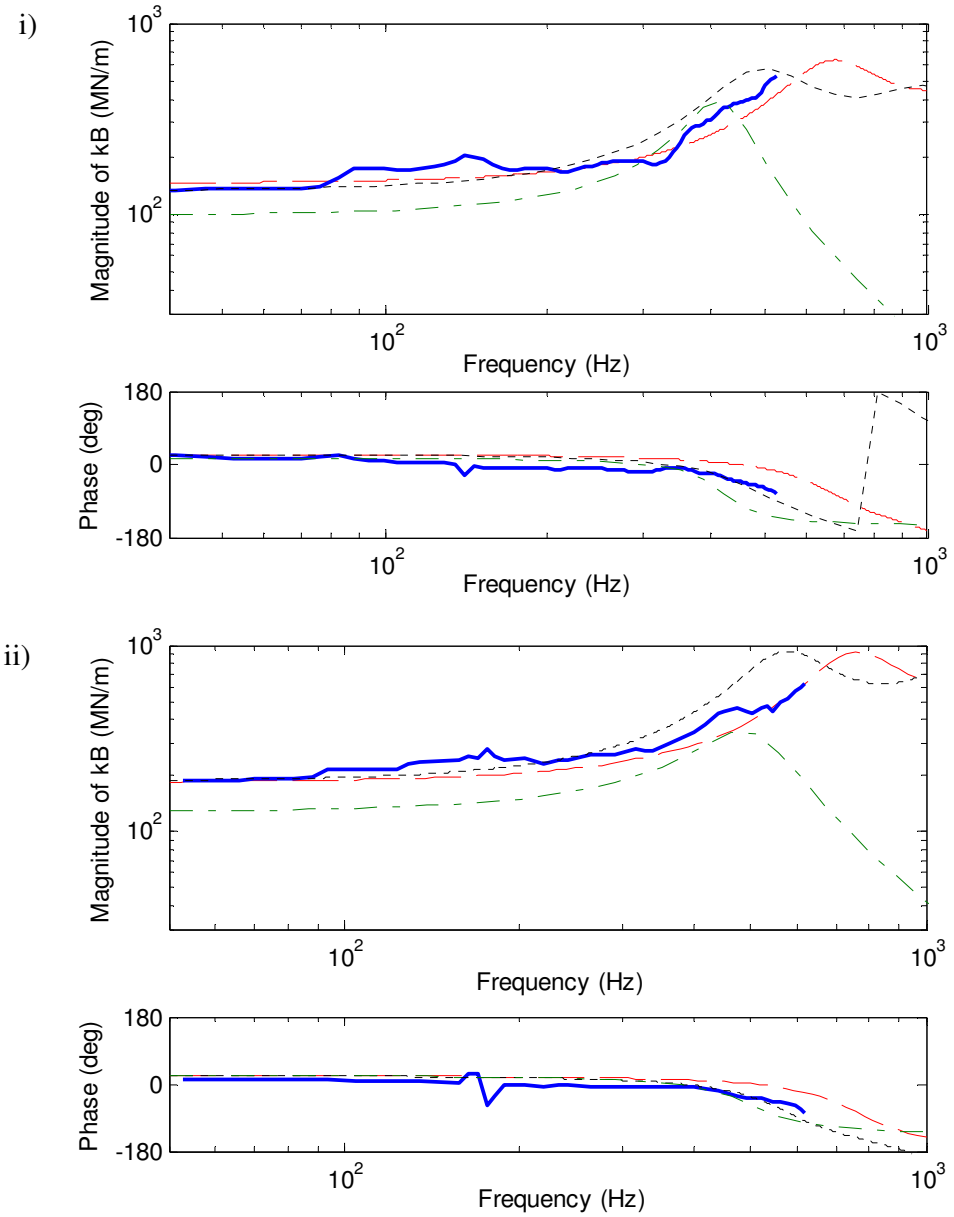

Figure 4.20. Magnitude and phase angle of the ballast transfer stiffness, for a 300mm deep layer of new ballast, i) subject to a preload of 10kN, ii) subject to a preload of 20kN: ——— , from measurements; – – – – – , rod model; – – – – – , frustum model; – · – · – · , interface stiffness model.

Over the frequency range in which the ballast stiffness is close to frequency-independent, up to about 100Hz, the stiffness magnitude predicted using the rod and frustum models is in close agreement with the measurements. Since the Young's modulus was found by fitting to the measurements for a 450mm deep ballast layer, this indicates that the dependence of the ballast stiffness on the layer depth is accounted for satisfactorily in the rod and frustum models. The interface stiffness model indicates that the ballast stiffness is independent of the layer depth. A comparison of the stiffness magnitude at low frequencies in Figures 4.18, 4.19 and 4.20 clearly shows that this is not the case.

For frequencies greater than approximately 100Hz the stiffness of the ballast is frequency-dependent and in this range, Figure 4.20 i) shows that both the rod and frustum models are in reasonable agreement with the measurements made for the 10kN preload level. However, for the 20kN preload case, Figure 4.20 ii) shows that the rod model that is in best agreement with the measurements.

On the basis of the comparison shown between the three models and the measurements made for both the 450mm and 300mm deep ballast layers, it is concluded here that the rod model is the most suitable of these for predicting the dynamic transfer stiffness of ballast. Only the rod model has therefore been used in Section 4.5.4 below.

4.5.4. Modelling a 450mm deep layer of new ballast with a 12mm thick plywood liner

The case of a ballast layer with a resilient liner is one of practical importance and it has been studied here using the rod model for the ballast, together with a simple representation of the liner. The mass of the liner is normally small relative to that of the ballast, such that a model for this combination can be proposed in which the rod for the ballast is connected in series with a simple stiffness element that represents the liner, shown in Figure 4.21 below.

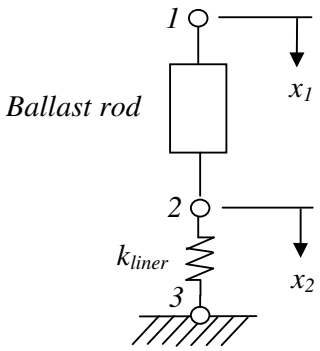

Figure 4.21. System diagram for the ballast connected in series with a liner.

The overall point and transfer stiffness of the system shown in Figure 4.21 can be obtained from the matrix equation,

$$\begin{bmatrix} k_{11} & -k_{12} \\ -k_{21} & k_{22}+k_{liner} \end{bmatrix} \begin{Bmatrix} x_1 \\ x_2 \end{Bmatrix} = \begin{Bmatrix} f_1 \\ f_2 \end{Bmatrix} \tag{4.18}$$

The displacements at nodes 1 and 2 are found by matrix inversion of equation (4.18) for a unit force applied to node 1. The two transfer stiffness terms for the ballast are assumed equal and are obtained from the rod model for the ballast (equation (4.11)). The point stiffness terms for the ballast are also found from the rod model (Snowdon, 1963),

$$k_{11} = k_{22} = \frac{EA\kappa}{tan(\kappa h)} \tag{4.19}$$

The overall point stiffness for the system at node 1 is then given by,

$$k_{point} = \frac{f_1}{x_1} \tag{4.20}$$

and the overall transfer stiffness between nodes 1 and 3 is given by,

$$k_{trans} = \frac{f_3}{x_1} = \frac{k_{liner} x_2}{x_1} \tag{4.21}$$

The measurements made for a 12mm thick plywood liner and a 450mm deep ballast layer, under a preload of 10kN, have been used to test this modelling approach. Appropriate input parameters to the rod model for new ballast and a preload of 10kN are presented in Table 4.4, but the stiffness of the plywood liner is unknown. The

model has therefore been run for three different values of liner stiffness, shown in Figure 4.22 together with the measurements for this case.

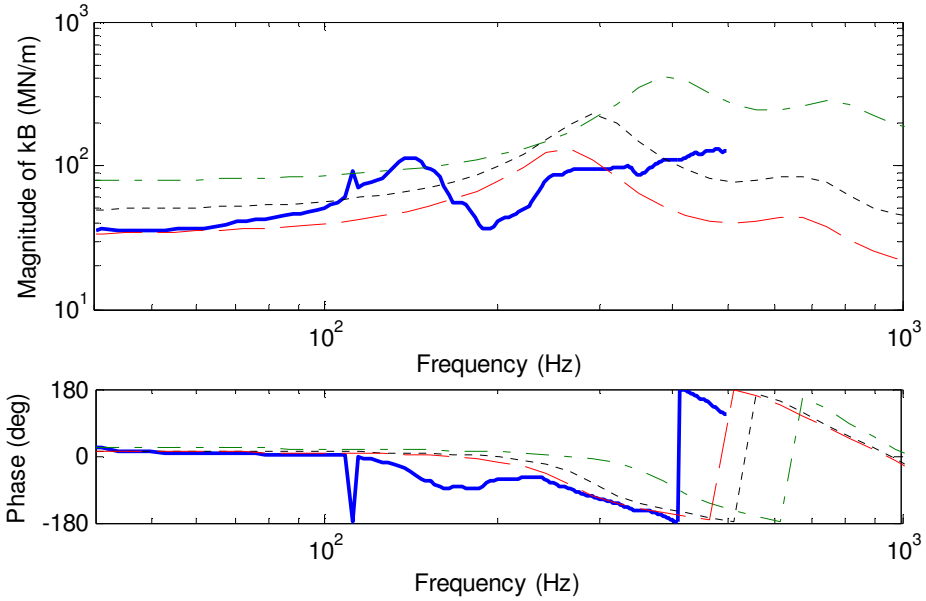

Figure 4.22. Magnitude and phase angle of the ballast transfer stiffness, for a 450mm deep layer of new ballast with 12mm thick plywood liner, subject to a preload of 10kN: ——— , from measurements; – – – – – , proposed model with 50MN/m stiffness for liner; – – – – – – – , proposed model with 100MN/m stiffness for liner; – · – · – · – , proposed model with 500MN/m stiffness for liner.

At low frequencies, the measurements show that the stiffness magnitude for the 450mm deep ballast layer with the plywood liner is typically of a factor of two smaller than that for the ballast layer alone (see Figure 4.18). The feature shown in the frequency range from 100Hz to 200Hz is very similar to that found for the ballast layer tested without a liner. For frequencies greater than about 250Hz up to the maximum measurement frequency (about 500Hz in this case), the liner has the effect of flattening the stiffness magnitude spectrum, which remains between 85MN/m and 130MN/m over this range of frequencies. The main peak in the measured stiffness magnitude in this frequency range is not found when the ballast is combined with the plywood liner. However, the phase angle measured for the combined ballast and liner case is quite similar to that for the ballast layer tested without a liner.

The stiffness magnitude spectrum obtained from the proposed model with a stiffness of 50MN/m representing the liner is in agreement with the measurements for frequencies up to about 100Hz. The model does predict a peak in the transfer

stiffness of the combined ballast and liner in the frequency range above 200Hz, due to the internal mode of the ballast layer, which is not supported by the measurement data. However, the model run with a stiffness of 50MN/m for the liner remains in reasonable agreement with the measurements up to a frequency of about 350Hz for the stiffness magnitude and over almost all of the measured frequency range for the phase angle.

In summary, the comparison made between the predicted and measured stiffness for the plywood liner and 450mm deep ballast layer shows that the proposed model is satisfactory for frequencies up to about 350Hz, but not for higher frequencies. Since the rod model has been shown to predict the behaviour of this type of ballast layer adequately when it is tested alone and that of the liner is expected be quite simple, this implies that ballast behaves differently when the liner is present. It seems likely that the interaction between the ballast and the sleeper could be substantially modified by the presence of a relatively soft liner.

4.5.5. Contact area between the ballast and the 12mm thick plywood liner

The stiffness of the plywood liner found from Figure 4.22 and the material properties of the liner can be used to estimate the total contact area between the ballast and the liner. The stiffness of the liner under a distributed load is given by,

$$K_{liner} = \frac{E_{liner} A_{contact}}{h} \tag{4.22}$$

where $A_{contact}$ is the total contact area between the ballast and the liner, E_{liner} is the Young's modulus of the liner and h is its thickness (12mm). If 12GPa is taken as an appropriate Young's modulus for the liner (Benham and Crawford, 1987) and the liner stiffness as 50MN/m, then equation equation (4.20) indicates that the total contact area is approximately 50mm^2.

A second estimate for the total contact area between the ballast and an adjacent body was made by applying inspecting the witness marks made on the liner during a single test under preloads of up to 30kN. Thirty individual marks were made on the liner and their total area was approximately 500mm^2. While this is considerably higher than the estimate obtained from equation (4.22), it is expected that a significant part of the marked area would have been produced during the initial cycles where the

majority of the ballast settlement occurs. The effective contact area during the measurements may be considerably smaller. It is therefore concluded here that the contact area between the ballast and the plywood liner is of the order of 100mm^2 and that only a small fraction of the number of ballast grains that lie within the base area of the sleeper may be in physical contact with it. Further, it is expected that the contact area between the ballast and concrete bodies such as a sleeper or bridge deck would be smaller than that between the ballast and the relatively soft plywood liner.

4.6. CONCLUSIONS

The work presented in this chapter describes a study of the dynamic behaviour of railway ballast through a programme of measurements and the use of simple models. It was found that one of these simple models is a suitable means of predicting the dynamic transfer stiffness of a 300mm or 450mm deep layer of ballast for frequencies up to approximately 600Hz. This model is based on longitudinal wave motion in a prismatic rod of ballast loaded in compression by the sleeper. There appears to be a reasonable basis for confidence in using this model for frequencies outside the range over which valid measurements have been made in this work. It is expected that this continuum approach can be used to predict the behaviour of the granular ballast material up to the frequency at which the wavelength in the ballast becomes of the same order as the grain size. Based on the properties used for modelling the ballast in this work, this implies that the rod model can be used up to a frequency of at least 2kHz.

NORBERT contains an option for modelling ballasted track using the rod model. The work reported here addresses the need for measurements to support the use of this model for ballasted track. However, the parameter values found by fitting the rod model to the measurements are different from those that have been used in previous use of NORBERT for bridges with ballasted track.

It is recommended here that a damping loss factor is used in the rod model to account for damping in the ballast. It was found that an appropriate damping loss factor for the ballast varies significantly over the frequency range for which measurements have been made. It is thought that the damping in the ballast is dependent on the amplitude of vibration in the ballast, due to energy dissipation by friction between the grains.

The measurement and modelling work described here does not provide sufficient data on which to base a precise development of the damping loss factor with frequency. It is therefore recommended that a simple two-stage approach is taken to modelling damping in railway ballast. For the frequency range in which the ballast can be described as a simple stiffness beneath the sleeper, with no internal mode effects, a relatively small damping loss factor should be used of about 0.1 to 0.2. For higher frequencies, where internal mode effects of the ballast layer are significant, a damping loss factor of about 0.45 should be used. The output of the rod model for a ballast layer of a given specification can be used to select an appropriate frequency at which to change from the low frequency damping model to the high frequency damping model.

Table 4.7 presents a summary of the data obtained in this work for 300mm and 450mm deep layers of new ballast, without liners, under preloads of 10 to 30kN.

Preload (kN)	**k_B for 300mm Ballast (MN/m)**	**k_B for 450mm Ballast (MN/m)**	**E_{rod} (MN/m^2)**
10	170	80	220
20	220	130	285
30	260	140	380

Table 4.7. Summary of the data obtained for the 300mm and 450mm deep layers of new ballast without liners, under preloads of 10kN, 20kN and 30kN.

The Young's modulus values presented in Table 4.7 can be used in the rod model (equation 4.11) to estimate the transfer stiffness of these types of ballast layer as a function of frequency. Appropriate values for the cross-sectional area and the density of the ballast rod beneath each rail seat are $0.17m^2$ and $1500kg/m^3$ respectively.

The measurements made for ballast at the end of its service life are thought to be unrepresentative of that in railway track, due to the loss of fine material when the ballast was removed from the track and during subsequent handling. This case has therefore been omitted from Table 4.7.

The 150mm ballast layer was found to behave quite differently from the deeper layers, such that the rod model does not apply to this case. However, such a shallow layer of ballast is not normally used in railway track.

The effect of two different liner materials on the transfer stiffness of the ballast layer was considered in this work. The effect of the goetextile mat was found to be quite small, but the 12mm thick plywood liner had a significant influence. It was shown that the dynamic transfer stiffness of a ballast layer with a liner could be modelled reasonably well as a series combination of the rod for the ballast and an appropriate stiffness element for the liner up to a frequency of about 350Hz.

Table 4.8 presents a summary of the data obtained for the two different types of liner tested in this work, under preloads of 10 to 30kN.

Preload (kN)	**k_{liner} for Geotextile Mat (MN/m)**	**k_{liner} for 12mm Plywood Panel (MN/m)**
10	800	50
20	800	60
30	800	70

Table 4.8. Summary of the data obtained for the two different types of liner tested in this work, under preloads of 10kN, 20kN and 30kN.

While the work presented in this chapter addresses the need for a validated means to model ballasted track on railway bridges, it does not explain the lower noise levels reported in some previous work for bridges with ballasted track than for bridges with direct fasteners. The stiffness measured for the ballast layers tested in this work can be achieved using direct fasteners. There may be some benefit with regard to bridge noise from the higher damping in the ballast, in some parts of the frequency range, but the effect of this is expected to be relatively small. It is likely therefore that the dynamic loading of the deck plates by a layer of ballast provides at least some of the measured effect.

5. THE DYNAMIC STIFFNESS OF A TWO-STAGE RESILIENT BASEPLATE

5.1. INTRODUCTION

For rail fasteners of the two-stage resilient baseplate type, those in which there is a resilient pad between the plate and the rail and also between the plate and the bridge, internal modes of the fastener may be expected in the frequency range of interest in bridge noise. This type of rail fastener will be referred to as a 'resilient baseplate' hereafter. As for the case of ballasted track considered in Chapter 4, an understanding of the modes in resilient baseplate track is required in order to predict the vibration transmission from the rail to the bridge. This need is addressed in this chapter through an experimental and modelling study of the vibration response of a resilient baseplate.

An example of a commercial resilient baseplate, Pandrol VIPA-SP, is shown in Figure 5.1 below.

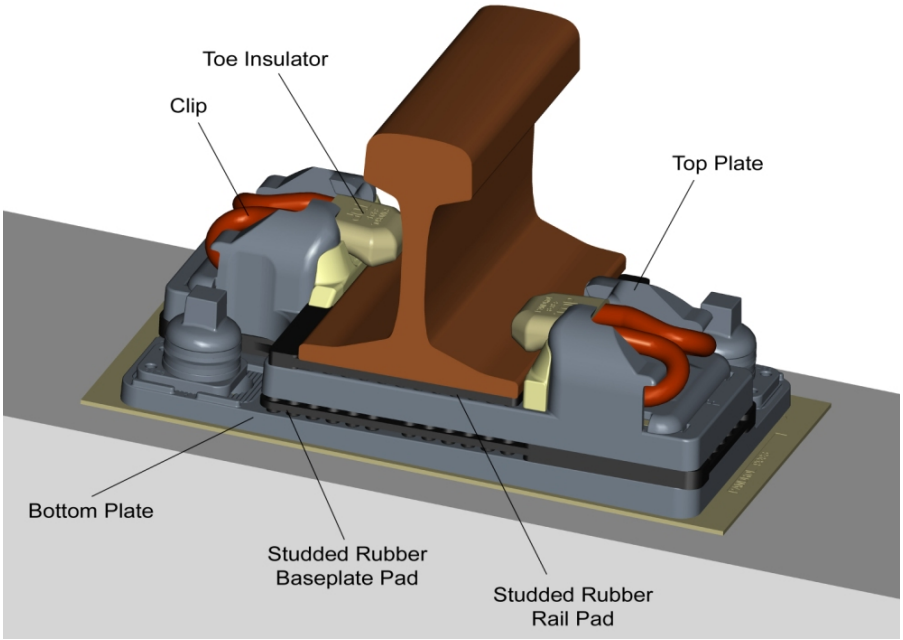

Figure 5.1. Pictorial view of a Pandrol VIPA-SP resilient baseplate (drawing courtesy of Pandrol , used with permission).

The bottom plate shown in Figure 5.1 is fixed to the bridge deck with grout, such that it is not free to vibrate. The top plate, however, is resiliently mounted between the railpad and the baseplate pad. Therefore, a mode may be expected in which the mass

of the top plate vibrates on the combined stiffness of these pads. An option is available in NORBERT to model the track as a pair of resilient layers with a distributed layer of mass between them, such that the effects of this internal mode of the baseplate assembly are accounted for. Here, this model of a resilient baseplate is referred to as the 'spring-mass-spring' model.

In some higher frequency range, modes are expected in which the top plate performs bending motion. It is not known whether or not these modes have a significant effect on the behaviour of the baseplate within the frequency range of interest for bridge noise, but this will be investigated here.

It is the vertical transfer stiffness of the resilient baseplate that is of primary interest here, because this is required in order to calculate the vibration transmission from the rail to the bridge. Reliable measurements for the transfer stiffness of a resilient baseplate assembly may be difficult to achieve. A purpose-built measurement rig would be required, and due to the time and cost involved in producing such a rig, it was decided that this should not be attempted in this project. An alternative approach has therefore been taken to determine the transfer stiffness of resilient baseplates.

Measurements have been made of the vibration response of the component parts that are expected to control that of the complete assembly: the railpad, the baseplate pad and the top plate. These measurements have been used to develop simple predictive models for the response of the assembly. Finally, these models have been evaluated against measurements of the direct stiffness, rather than the transfer stiffness, of a resilient baseplate assembly. Measurements of the direct stiffness are more straight-forward than for the transfer stiffness, because the need to measure the force or displacement at the output side of the system is avoided.

A Pandrol VIPA-SP baseplate, the 'offset shoulder' variant, is the subject of the experimental and modelling work described here. However, there are other baseplates of broadly similar design and it is intended that the outcomes of this work should be applicable to this class of rail fastener in general.

5.2. MEASUREMENT OF THE DYNAMIC TRANSFER STIFFNESS OF A RAILPAD AND A BASEPLATE PAD

5.2.1. Measurement rig and procedure

A knowledge of the stiffness of the railpad and baseplate pad under the load conditions found in railway track is required in order to create a representative model of the resilient baseplate assembly. Transfer stiffness measurements were therefore made for a railpad and a baseplate pad taken from a VIPA-SP baseplate assembly, using a similar method to that described in Chapter 4 for the ballast stiffness measurements. Both of these pads are studded natural rubber pads with an installed overall thickness of approximately 12mm.

It was necessary to use a pair of steel blocks for the pad stiffness measurements, rather than the concrete blocks used for the ballast measurements. The concrete blocks were either not sufficiently flat or too rough for the pads to be compressed uniformly over their working area. The two steel blocks used for the upper and lower masses in this work are each rectangular with dimensions of 490 x 240 x 100mm and a mass of 90kg. The first internal resonance frequency of these blocks is approximately 2.2kHz. Their dimensions are not ideal; the frequency range of measurement could be increased by using deeper blocks. However, the steel blocks used in this work were available at no cost and are adequate for measurement of the pad stiffness over a significant part of the frequency range of interest in bridge noise. A photograph of the test rig used to measure the dynamic transfer stiffness of the railpad and baseplate pad is shown in Figure 5.2.

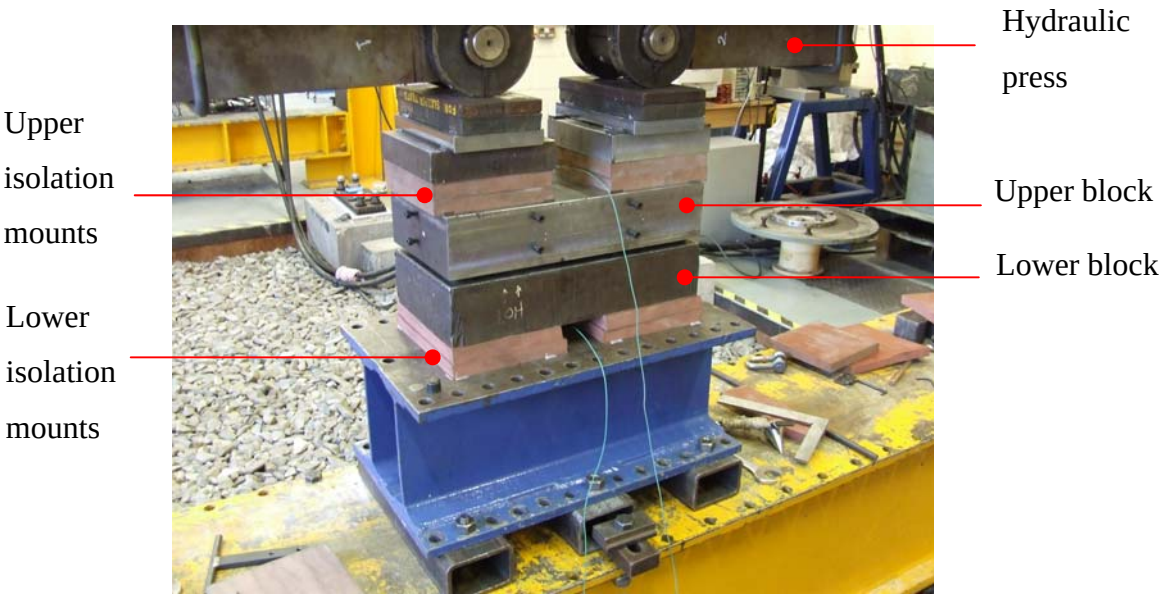

Figure 5.2. Photograph of the rig used to measure the dynamic transfer stiffness of the railpad and baseplate pad.

Figure 5.2 shows the two steel blocks mounted on soft isolation mounts, positioned beneath a hydraulic press that was used apply a preload to the system. Two Kistler 8702B25M1 accelerometers were used to measure the acceleration of the steel blocks: one mounted at the centre of the top face of the upper block and one mounted at the centre of the underside of the lower block. Two railpads were tested together, placed side-by-side between the two blocks. This was helpful with regard to the stability of the rig. A single baseplate pad was tested, because it was not possible to fit two of these larger pads between the blocks. The system was excited by striking the upper block close to the centre of its top face with a 0.6kg impact hammer. The dynamic transfer stiffness spectrum was found from the acceleration measurements using the same calculation as described in Chapter 4 for the ballast stiffness measurements (equation (4.2)).

5.2.2. Results

Results are presented here are for the expected preloads on each pad during a train pass-by on the Docklands Light Railway (DLR), for B90/B92 rolling stock. The case is relevant to the modelling work presented in the following chapter for the concrete box-section viaduct. The wheel load for the B90/B92 rolling stock with passengers on-board is approximately 33kN. The railpad is subject to an additional load from the rail clips, nominally 20kN. Assuming that about half of the train wheel load is

transmitted to the baseplate (Carlone and Thompson, 2001), due to the bending stiffness of the rail, the preload on the baseplate pad is approximately 15kN and that on the railpad is approximately 35kN.

The transfer stiffness spectrum obtained from the acceleration measurements made on a single baseplate pad under a preload of 15kN is shown below in Figure 5.3. The frequency range over which the results are valid is indicated by the use of a solid rather than a broken line.

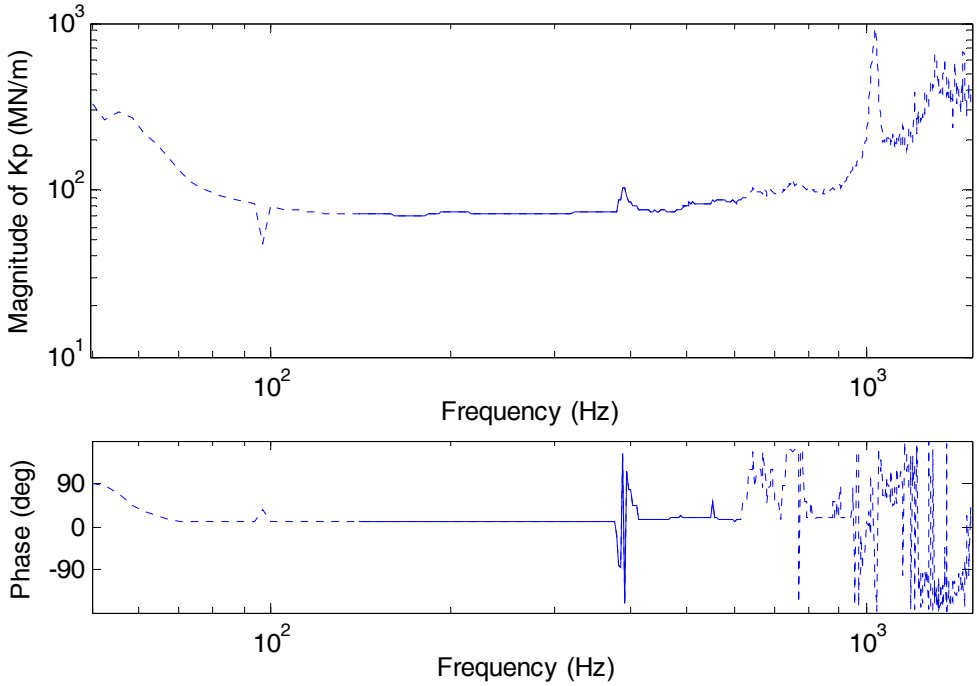

Figure 5.3. Magnitude and phase of the transfer stiffness of a single Pandrol 11247 baseplate pad shown versus frequency, for a preload of 15kN.

Figure 5.3 shows that the stiffness magnitude ranges from approximately 70MN/m at a frequency of 140Hz to 90MN/m at a frequency of 615Hz. The phase angle is stable for frequencies between 120Hz and 370Hz, at approximately 10 degrees. This corresponds to a damping loss factor of around 0.17. At high frequencies, both the magnitude and phase spectra show the effects of noise on the accelerometer signal from the lower steel block. This is due to the vibration isolation effect provided by the resilient pads between the two blocks.

The stiffness spectrum obtained from the acceleration measurements made for two railpads under a total preload of 70kN is shown below in Figure 5.4.

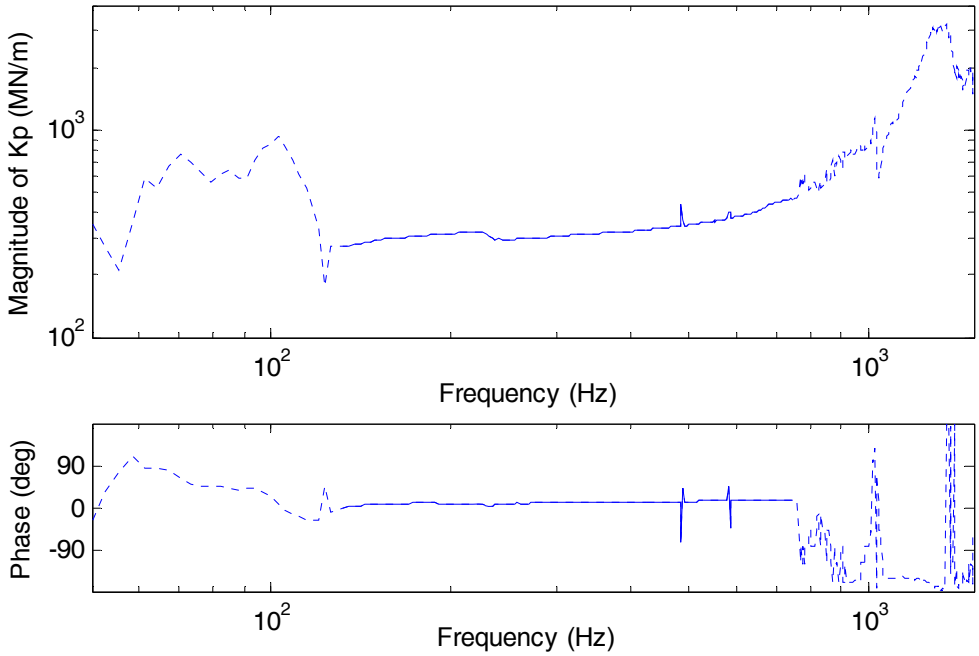

Figure 5.4. Magnitude and phase of the transfer stiffness of two Pandrol 11246 railpads combined in parallel, shown versus frequency, for a preload of 70kN.

The total stiffness magnitude for the two railpads ranges from approximately 280MN/m at a frequency of 140Hz to 450MN/m at 700Hz. The phase angle is approximately 10 degrees for much of this frequency range, corresponding to a loss factor of 0.17.

For the purposes of the modelling work presented in the sections to follow, the frequency-dependence of the railpad and baseplate pad stiffness has been ignored. The assumed values, taken from these measurements, are shown below in Table 5.1.

	Railpad	**Baseplate Pad**
Stiffness (MN/m)	160	80
Damping Loss Factor	0.17	0.17

Table 5.1. Stiffness and damping loss factor values used in the modelling work for the railpad and baseplate pad, for the loaded track condition on DLR.

5.3. THE MODES OF VIBRATION FOR A RESILENT BASEPLATE

An ANSYS FE model was used to study the modes of vibration of the Pandrol VIPA-SP resilient baseplate. The top plate has complex three-dimensional geometry, particularly around the rail clip positions (see Figure 5.1). However, for the prediction of the first few modes, it has been assumed here that this can be neglected.

Shell elements with out-of-plane displacements, ANSYS element type SHELL93, have been used to create a flat plate with the plan-view geometry of the top plate. The plate was given a thickness of 20mm, which is appropriate for much of the physical component, and the material properties for cast iron were used, as shown in Table 5.2 below.

Property	**Value**
Young's Modulus	160GPa
Density	7300kg/m^3
Poisson's ratio	0.3

Table 5.2. Material properties for the cast iron top plate.

A free vibration response analysis was run for the shell element representation of the top plate only, with no constraints applied to it. This case is equivalent to that of the top plate laid on a soft support, for all but very low frequencies. Measurements have been made for the point and transfer accelerance of the top plate in this support condition, which show two resonances in the frequency range of interest, one at 685Hz and one at 1500Hz. The resonance frequencies found in the measurements were used to check that the FE model of the top plate captures its dynamic behaviour adequately, despite the omission of some geometric detail.

The mode shape plots obtained from the FE model for the first two modes of the unconstrained top plate are shown together in Figure 5.5 below.

i) ii)

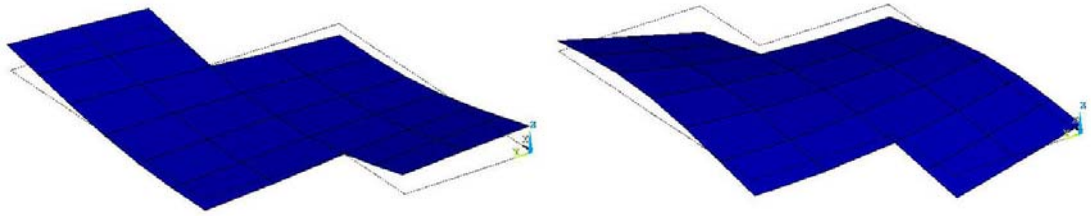

Figure 5.5. Mode shape plots obtained from the ANSYS model for the first two modes of the unconstrained top plate: i) vertical bending mode with a natural frequency of 685Hz, ii) torsional mode with a natural frequency of 1400Hz.

Figure 5.5 i) shows a vertical bending mode of the top plate, with a natural frequency of 685Hz that is in close agreement with the first resonance frequency found in the measurements made for a top plate laid on a soft support. Figure 5.5 ii) shows a

torsional mode, with a natural frequency of 1400Hz that is in satisfactory agreement with the second resonance frequency found in the measurements.

The railpad and the baseplate pad were next added to the FE model of the top plate. Both pads have a working area of approximately 210mm by 120mm, neglecting the voids between the studs. The areas of the baspelate pad that lie beneath the rail clips when the baseplate is assembled have also been ingnored here. The stiffness of these parts of the baseplate pad is not engaged unless there is significant rail-roll. Nine equally-spaced linear spring elements, ANSYS element type COMBIN14, were used to represent each of the pads. There was no damping in these elements.

A point mass of 5kg was added to the upper node of the central element in the spring array used to represent the railpad. This allows straight-forward comparison of the FE results to the experimental work described in Section 5.5. The upper nodes in this array of spring elements were constrained to move together in the vertical direction, such that they are all effectively coupled to the point mass. The nodes at the lower end of the spring elements used to represent the baseplate pad were constrained in all degrees-of-freedom, so that the fastener has a blocked termination.

The ANSYS FE model of the baseplate assembly is shown below in Figure 5.6.

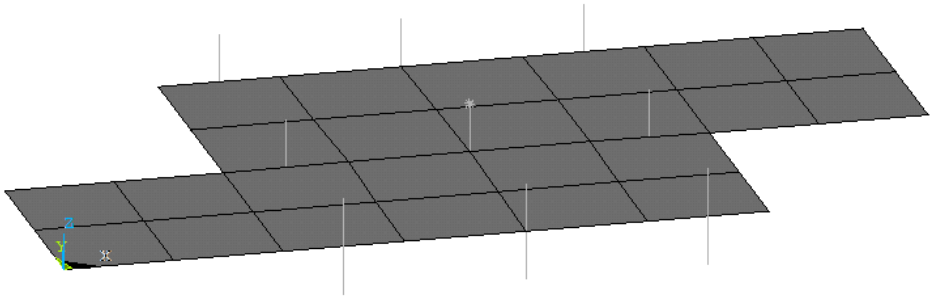

Figure 5.6. ANSYS FE model of the baseplate assembly.

A free response analysis was run for the model shown in Figure 5.6. Over the frequency range of interest here, there are three modes of the baseplate assembly that are important in the response of the baseplate to vertical excitation at the rail. These are shown in Figure 5.7.

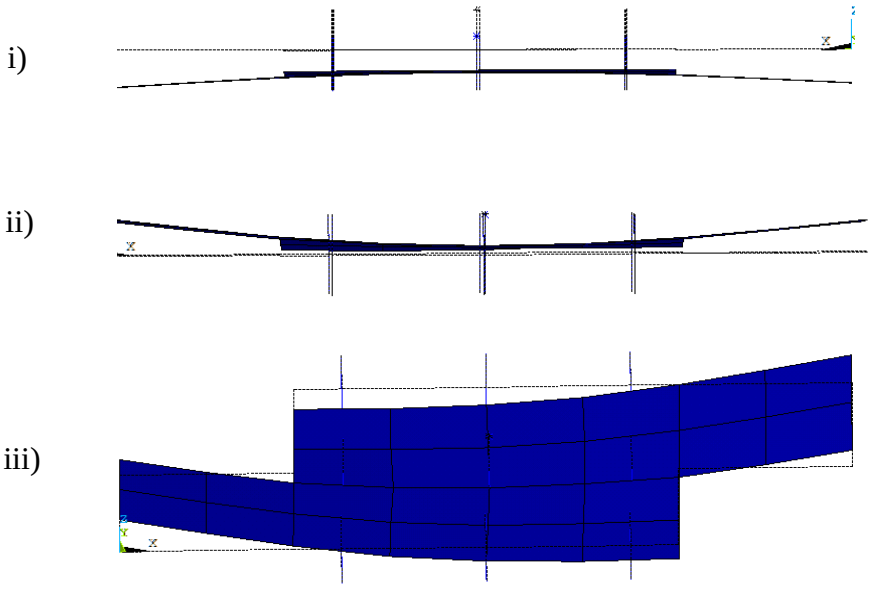

Figure 5.7. Mode shape plots for three important modes of the resilient baseplate: i) mode with a natural frequency of 350Hz, ii) mode with a natural frequency of 650Hz, iii) mode with a natural frequency of 1.2kHz.

Figure 5.7 i) shows a mode in which the combined mass of the rail and baseplate move vertically on the stiffness of the baseplate pad. There is only slight deformation of the top plate in this mode and the natural frequency can be predicted well using a lumped mass approach. In the mode shown in Figure 5.7 ii), the outer parts of the top plate move in large-amplitude motion relative to those in the central part of the top plate. This mode will be referred to as the vertical-flapping mode hereafter. The mode shown in Figure 5.7 iii) is the bending mode of the top plate. This mode occurs at a higher frequency when the top plate is combined with the railpad and baseplate pad than when it is modelled alone (Figure 5.5 i)), due to the additional stiffness of the pads.

The modes shown in Figure 5.7 indicate that it is necessary to include the bending motion in the top plate in order to model the dynamic stiffness of the resilient baseplate over the frequency range of interest in bridge noise. Further, it can be seen that the bending motion takes place almost entirely along the length of the top plate. That is the top plate performs beam-bending motion, rather than plate-bending motion in its first internal mode. This finding has been used to develop relatively simple

models of the baseplate that are appropriate for use in the prediction of bridge noise and vibration.

5.4. SIMPLE MODELS FOR A RESILENT BASEPLATE

5.4.1. Simple FE Model

The modes of vibration presented in Section 5.3 indicate that it is sufficient to use beam finite elements to represent the top plate in a model for the resilient baseplate, within the frequency range of interest in bridge noise. A relatively simple FE model has been programmed in MATLAB using six Euler beam elements (Petyt, 1990) to represent the top plate and six linear spring elements to represent the pads. It is possible to represent the Pandrol VIPA-SP baseplate adequately using an even smaller number of elements, however, but this model is used as some flexibility is required so that it can be adapted to other resilient baseplate designs.

Figure 5.8 shows the simple FE model of the resilient baseplate schematically.

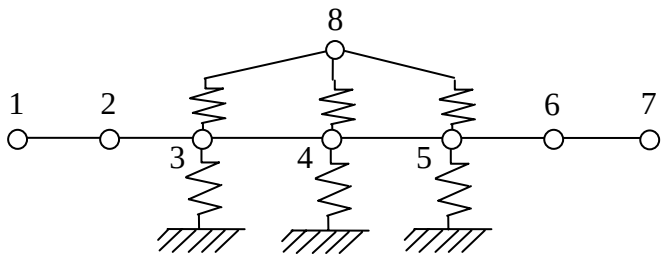

Figure 5.8. Simple FE model of the resilient baseplate and section of rail: ○, nodes.

Each of the nodes shown in Figure 5.8, with the exception of node 8, has two degrees-of-freedom, one for vertical displacement and one for rotation. A point mass element may be been added to node 8, to represent the mass of a section of rail loaded into the fastener (see Section 5.5). Only vertical motion is allowed at node 8. The following dimensions were used to represent the top plate in the VIPA-SP baseplate as a beam, together with the material properties of Table 5.2.

Parameter	Value	Units
Length	360	mm
Width	200	mm
Height	20	mm

Table 5.3. Dimensions of the beam used to represent the top plate in the simple FE model of the VIPA-SP baseplate.

A free vibration response analysis for the beam defined in Table 5.3 (without springs) shows a first natural frequency in bending that is in close agreement with that found from the measurements made on the top plate laid on a resilient support and the analysis presented in Section 5.3 above.

A damping loss factor of 0.1 was assigned to the beam, required in order to obtain results that are in satisfactory agreement with those from the measurements made for the baseplate assembly (Section 5.5). This accounts for the energy dissipated at joints and areas where there is relative motion between the component parts in the assembly. The springs also have damping loss factors of 0.17 as listed in Table 5.1.

A forced response analysis was obtained from the simple FE model for harmonic excitation of unit amplitude at node 8. The overall transfer stiffness of the system is given by,

$$k_T = \frac{\sum_{n=1}^{N} k_{BPn} x_{TPn}}{x_{N8}} \qquad (5.1)$$

where k_{BPn} is the transfer stiffness of each element used to represent the baseplate pad, x_{TPn} is the displacement at the upper node of these elements and x_{N8} is the displacement at node 8.

The direct stiffness at node 8 is given by,

$$k_{D\_N8} = \frac{F}{x_{N8}} \qquad (5.2)$$

where F is the force applied to node 8.

The transfer stiffness and the direct stiffness of the baseplate given by equations (5.1) and (5.2), for excitation but no mass at node 8, are shown in Figure 5.9 below.

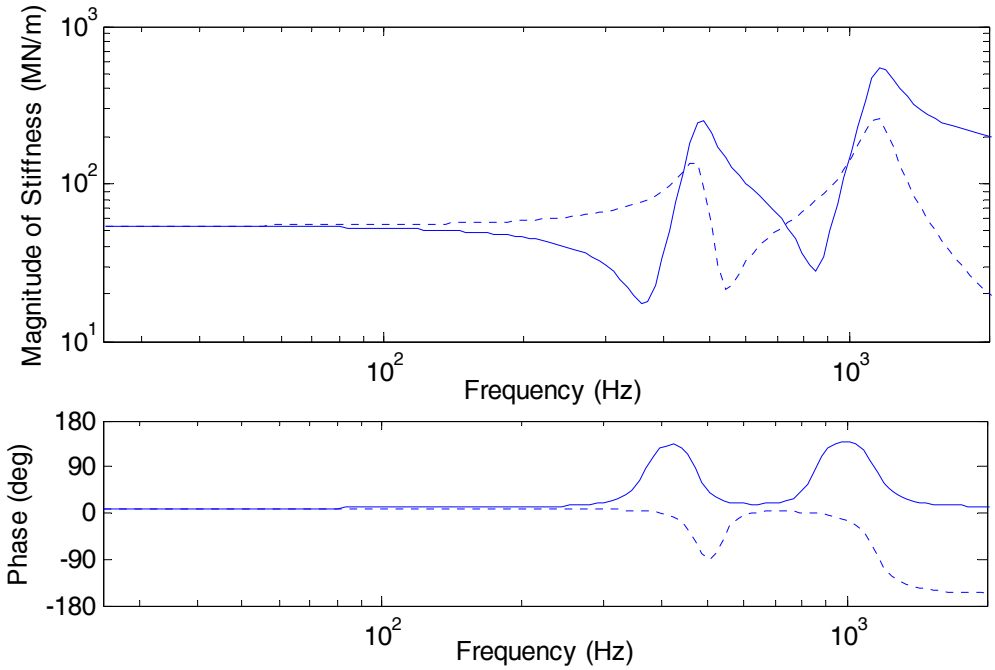

Figure 5.9. Magnitude and phase of the baseplate stiffness obtained from the simple FE model, for excitation but no mass at node 8, shown versus frequency: ——— *, direct stiffness;* - - - - - - - - *, transfer stiffness.*

In the frequency range up to about 200Hz the magnitude of the direct and transfer stiffness are both approximately 53MN/m, that expected of the railpad stiffness connected in series with the baseplate pad stiffness. There is a minimum in the magnitude of the direct stiffness at about 360Hz, due to the first mode of the system (see Figure 5.7 i)) and also at about 850Hz due to the second mode of the system (see Figure 5.7 ii)). The magnitude spectra for the direct and transfer stiffness show peaks at about 480Hz and 1150Hz, these are due to the anti-resonances in the response at node 8.

The minimum in the transfer stiffness magnitude at a frequency of about 560Hz occurs due to cancellation between the forces applied by the three springs (in the lower set) to the foundation. The outer two springs are compressed when the centre spring is stretched, and visa versa. The summation of the spring forces made in the numerator of equation (5.1) therefore has a minimum value at this frequency. This behaviour is expected physically, but will take place continuously over the area of the baseplate pad rather than from the summation of the just three spring forces.

5.4.2. Spring-mass-spring model

The approach used to model resilient baseplate track in NORBERT has also been considered here. This is shown for the case of a single baseplate and section of rail in Figure 5.10 below.

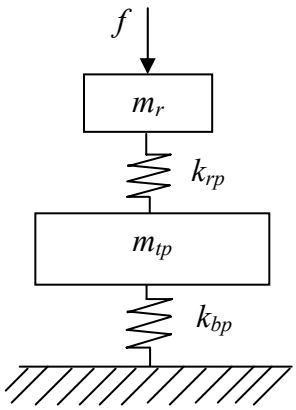

Figure 5.10. Spring-mass-spring model of the resilient baseplate and rail section.

In this figure, m_r is the mass of the rail section, k_{rp} the stiffness of the railpad, m_{tp} the mass of the top plate and k_{bp} the stiffness of the baseplate pad. The equations of motion for this system can be derived for an analytical solution. Alternatively, the simple FE model described above in Section 5.4.1 can be made to behave as a spring-mass-spring system, by setting the Young's modulus of the top plate to a very large value, such that the top plate behaves as a lumped mass over the frequency range of interest. Note that the mass of the top plate is approximately 11kg.

The transfer stiffness and the direct stiffness of this system, with m_r set to zero, are shown in Figure 5.11 below.

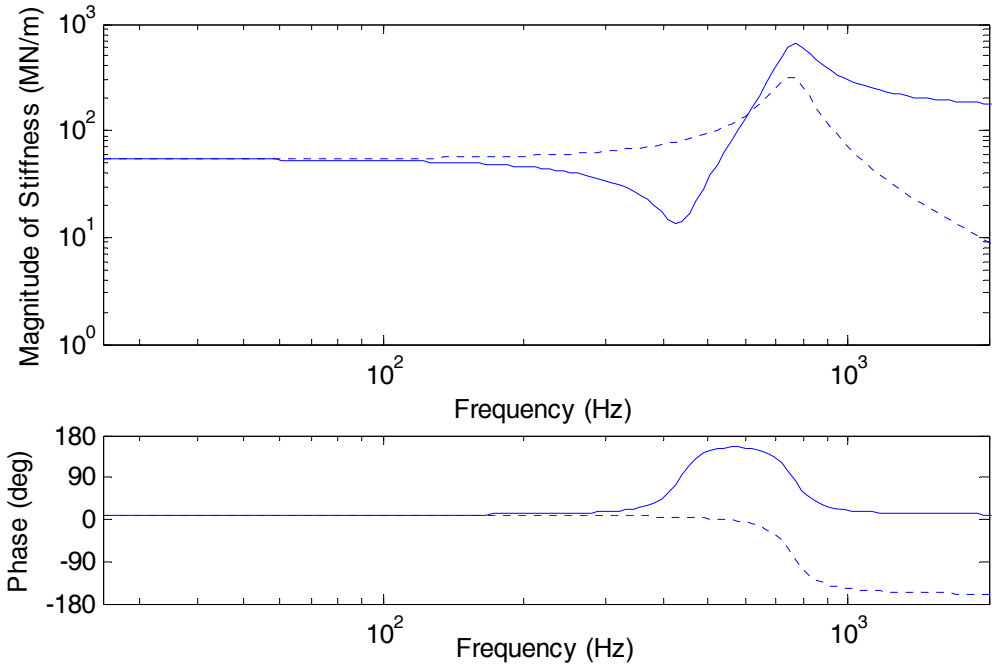

Figure 5.11. Magnitude and phase of the baseplate stiffness obtained from the spring-mass-spring model, shown versus frequency: _____ , direct stiffness; - - - - - - - - , transfer stiffness.

The stiffness spectra given by the spring-mass-spring model are of the expected form: a single minimum in the magnitude of the direct stiffness due to the first mode of the system and a peak in the magnitude of both the direct and transfer stiffness due to the first anti-resonance of the system. Note that the minimum in the direct stiffness magnitude associated with the first mode occurs at a different frequency for the spring-mass-spring system than for the simple FE model. This is due to the effect of bending motion in the top plate on the engagement of the stiffness of the baseplate pad.

5.5. THE DIRECT STIFFNESS OF A RESILIENT BASEPLATE

5.5.1. Direct stiffness measurements on a baseplate assembly

As described in Section 5.1 above, direct stiffness measurements have been used as a basis for an assessment of the proposed models for the baseplate assembly, due to the difficulties expected in making transfer stiffness measurements for such a baseplate assembly. It is assumed here that a model shown to predict the direct stiffness of the baseplate is also a reliable means to determine its transfer stiffness.

The measurements were made on a complete Pandrol VIPA-SP assembly with a 250mm length section of aluminium rail loaded into the clips. An aluminium rail was

used in order to minimise the effects of the inertia forces associated with the mass of the rail on the point response at the rail head for high frequencies. The aluminium rail section has a mass of 5kg and it is known to behave as a lumped mass up to a frequency of at least 1.2kHz.

The resilient baseplate, rail section and the arrangement used to apply a preload to the system is shown in Figure 5.12 below.

Figure 5.12. Photograph of the Pandrol VIPA-SP baseplate, rail section and the arrangement used to apply a preload to the system.

Figure 5.12 shows a clamping arrangement that consists of four threaded rods, nuts to allow adjustment of the preload and two cross-beams that transmit the load to a pair of load cells. The load cells were mounted on a 20mm thickness layer of resilient material, which provides vibration isolation between the clamping arrangement and the system under test. The upper surface of the load cells has a domed shape, which promotes vertical loading of the rail. The load cells were connected to appropriate instrumentation, such that a known preload could be applied to each end of the rail.

5.5.2. Assessment of the models against direct stiffness measurements

Figure 5.13 shows the direct stiffness measured at the rail using the test rig described above, for an applied preload of 15kN. The results of the simple FE model and the spring-mass-spring model are also shown.

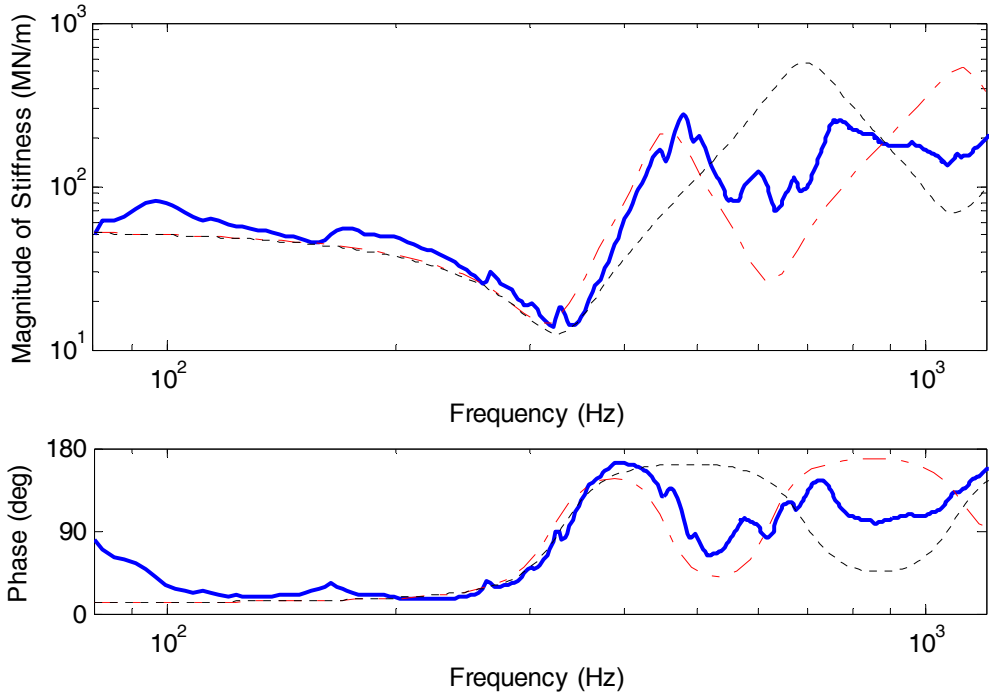

Figure 5.13. Magnitude and phase of direct stiffness at the railhead shown versus frequency, for a preload of 15kN: ——— , measurement; - - - - - - - - , spring-mass-spring model; _ . _ . _ . _ , simple FE model.

The measured stiffness spectrum shown in Figure 5.13 has the expected form up to a frequency of approximately 550Hz: the minimum in the stiffness magnitude at about 330Hz due to the first mode of the system and the peak at about 450Hz due to the first anti-resonance in the response of the rail. For frequencies greater than 550Hz the measured stiffness does not show the structure of clearly-separated modes that was expected. It is not clear whether this is due to the behaviour of the baseplate or that of the measurement rig.

The direct stiffness at the railhead given by the simple FE model is in satisfactory agreement with the measurement up to a frequency of approximately 550Hz, for both the magnitude and phase. The spring-mass-spring model fails to predict the response of the baseplate beyond the first natural frequency of the system (330Hz), which is the mode in which the combined mass of the rail and top plate move on the stiffness of the baseplate pad.

It was found that the direct stiffness measured at the railhead had the expected form over a much greater frequency range when the system was subject to a smaller preload. One such case of practical interest here is that for an unloaded BS80A rail supported by Pandrol VIPA-SP baseplates set at 0.75m intervals. When no train

wheel-load is present, the external preload on the baseplates of this track is due to the mass of the rail in one span, approximately 0.3kN. The total preload on the railpad is therefore 20.3kN and that on the baseplate pad is 0.4kN (external preload plus load due to top plate mass). Appropriate stiffness values for the pads under these load conditions, obtained from measurements, are shown below in Table 5.4.

	Railpad	**Baseplate Pad**
Stiffness (MN/m)	80	15
Damping Loss Factor	0.17	0.17

Table 5.4. Stiffness and damping loss factor values used in the modelling work for the railpad and baseplate pad, for the unloaded track condition on DLR.

Figure 5.14 shows the direct stiffness at the railhead for an external preload of 0.3kN, obtained by measurement and from the two predictive models.

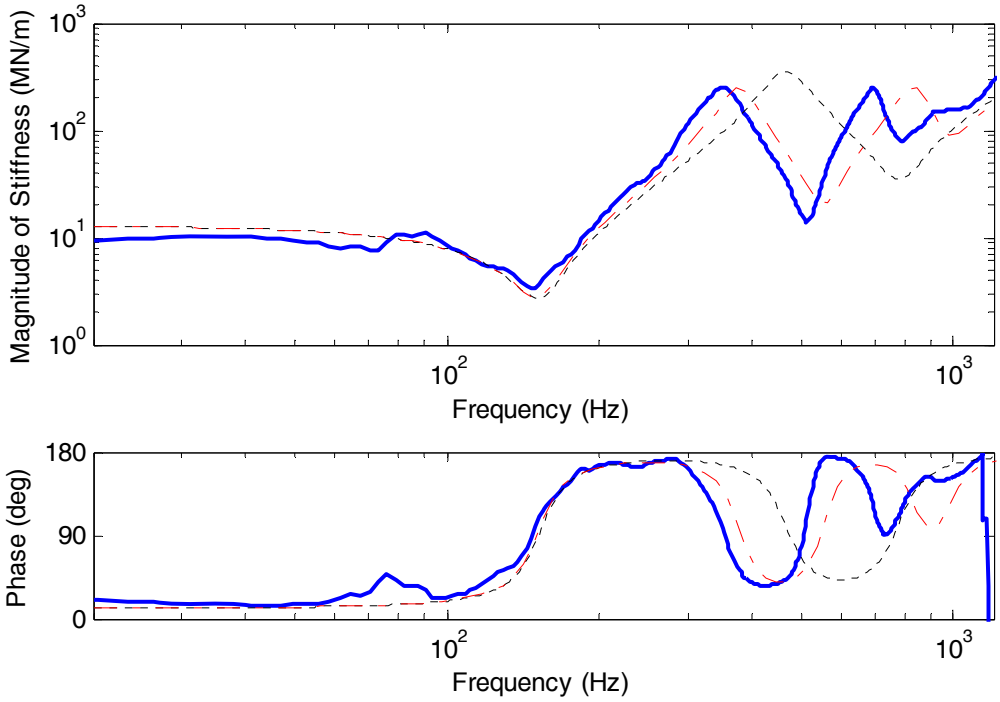

Figure 5.14. Magnitude and phase of direct stiffness at the rail head shown versus frequency, for an external preload of 0.3kN: ——— , measurement; - - - - - - - - , spring-mass-spring model; _ . _ . _ . _ , simple FE model.

The measured direct stiffness spectrum has the expected form over the frequency range of interest here. There are three minima, at about 150Hz, 515Hz and 800Hz. These correspond to the three types of mode described in Section 5.3, but with different natural frequencies due to the lower preload level considered here. Anti-

resonances in the response give rise to two peaks in the stiffness spectrum, at 350Hz and 700Hz. For frequencies greater than 1kHz, the response is dominated by the inertia of the rail.

The simple FE model predicts a stiffness spectrum that has a similar structure to the measurements. While the predicted spectrum contains all the main features of the measurement, there are some differences in the frequencies at which these occur. Specifically, the frequencies at which the second peak in the direct stiffness spectrum occurs and the minimum that follows (due to the first internal mode of the top plate) are over-predicted by up to 20%.

The FE model predicts the first bending resonance frequency of the top plate in the free-free support condition (no railpad or baseplate pad) correctly. It is therefore likely to be the modelling of the partial constraints provided by the railpad and baseplate pad to the top plate that is responsible for the difference between the results of the simple FE model and the measurements. This may be a limitation of the highly simplified representation of the baseplates geometry on which this model is based.

There are larger differences between the results of the spring-mass-spring model and the measurement. There is an order of magnitude difference between the dynamic stiffness predicted using this model and the measurement for frequencies close to 500Hz.

5.6. INTERNAL MODES OF THE STUDDED PADS

Internal modes of the studded railpad and baseplate pad are expected in some frequency range. Two different types of mode can be envisaged: that due to the plane part of the pad moving as a mass on the stiffness of the studs and that due to longitudinal wave motion in the thickness dimension of the pad. An assessment is made here of the need to include these modes in a predictive model for the transfer stiffness of a resilient baseplate, by using models to estimate the frequencies at which the internal modes of the pads occur. This is necessary because the pad stiffness measurements described in Section 5.5 are valid for only part of the frequency range of interest in bridge noise. A baseplate pad under a preload of approximately 0.4kN will be considered here, which corresponds to the case of unloaded track, the practical condition in which an internal mode of the baseplate pad will occur at the lowest

frequency. The first internal mode of the railpad will occur at a higher frequency, because it is under additional preload from the rail clips.

Figure 5.15 shows a simple model of a studded pad that can be used study the mode in which the plane part of the pad vibrates as a mass on the stiffness of the studs.

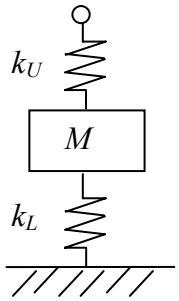

Figure 5.15. Spring-mass-spring model for the baseplate pad.

k_U and k_L represent the combined stiffness of all the upper and lower studs in the pad respectively. m represents the mass of the plane part of the pad. In this simple analysis, it is assumed that the resilience in the pad is concentrated in the studs and that all the mass lies in the plane part of the pad. k_u and k_l are therefore equal to twice the overall stiffness of the pad, and m is equal to the mass of the pad. For the baseplate pad subject to a preload of 0.4kN, the overall stiffness of the pad has been measured as approximately 15MN/m and its mass as 0.65kg. The natural frequency of the mode in which the mass of the plane part of the pad vibrates on the combined stiffness of the studs is therefore given by,

$$f_{bounce} = \frac{1}{2\pi}\sqrt{\frac{k_U + k_L}{m}} = 1.5kHz \qquad (5.3)$$

The result given by equation (5.3) represents a lower bound estimate for the natural frequency of the first internal mode of the baseplate pad, because it is for the lowest preload of practical interest and because of the assumptions made regarding the distribution of the stiffness and mass in the pad. This result indicates that it is not necessary to consider this type of mode in modelling bridge noise, but that it may be of interest in modelling rolling noise, due to the effect it is expected to have on decay rates in the rail for frequencies between 1 and 2kHz.

The longitudinal modes of vibration in the thickness dimension of the pad have been studied using an axially-loaded rod model. It has been assumed that only the zones of the plane part of the pad that lie directly beneath a stud are involved in the

transmission of load across the pad. The same material properties can then be used for the plane part of the pad and for the studs, such that a single rod can be used to model the pad. The density of the rubber material used to manufacture the baseplate pad is approximately 1300kg/m^3 in the uncompressed condition.

The cross-sectional area of the baseplate pad that is involved in load transmission is a function of the preload applied to the pad. For very low preloads, it is the total cross-sectional area of all the studs, and for high preloads it tends to the total area of the plane part of the pad as the studs deform to fill the voids between them. The axially-loaded rod model was run for both cases. The value used for the Young's modulus in each case was chosen by fitting the result of the model at low frequency to the measured stiffness of the baseplate pad in the unloaded condition. When run with these values for Young's modulus, the axially-loaded rod model predicts the first longitudinal mode of the pad at approximately 5kHz. This type of mode of the pads can therefore be disregarded in modelling bridge noise and rolling noise.

5.7. CONCLUSIONS

A combined experimental and modelling study of the dynamic stiffness of a resilient baseplate has been described in this chapter. For the Pandrol VIPA-SP baseplate, it has been shown that beam-bending motion in the top plate has an important effect on its response to vertical excitation at the rail. A simple FE model has been developed to predict the response of a resilient baseplate, inclusive of bending in the top plate.

Comparison with measurements made for the direct stiffness of a VIPA-SP baseplate attached to a short section of rail for an external preload of approximately 0.3kN shows that the simple FE model proposed here should be used in preference to the spring-mass-spring model available in NORBERT. For higher preloads, the simple FE model works well up to approximately 550Hz, above which the measurement does not show the expected form. It is not clear whether this is due to a problem in the measurement setup at these high preload levels, or if the behaviour of the system changes significantly as the preload is increased.

As noted in Section 5.1, there is a range of resilient baseplate designs in-service on railway track. The primary design parameters that vary amongst these baseplates are the length of the top plate and the stiffness of the railpad. The Pandrol VIPA-SP is a compact design, with a relatively soft railpad. Using the simple FE model it is found

that an increase in the length of the top plate from 360mm to 500mm, that for a long baseplate, has the effect of reducing the frequencies at which the main features of the stiffness spectrum significantly. However, use of a relatively stiff railpad is expected to move the natural frequency for the beam-bending mode of the top plate to frequencies outside the range of interest in bridge noise, even for a 500mm long top plate.

The stiffness spectra given by the spring-mass-spring model differ considerably from the measurements (and the simple FE model). When the baseplate length and the railpad stiffness are increased from their values for the VIPA-SP baseplate, the differences between spring-mass-spring and simple FE models remain, indicating that the spring-mass-spring model is not realistic enough.

The approach proposed here for modelling the Pandrol VIPA-SP resilient baseplates is assessed further in the following chapter, where it is applied to the case of continuous baseplate track on a viaduct.

6. APPLICATION OF THE MODELS TO A CONCRETE BOX-SECTION VIADUCT

6.1. INTRODUCTION

Bridges and viaducts of the concrete box-section type are considered in this chapter with regard to the prediction of noise and vibration. Previously, Bewes (2006) studied a viaduct of this type close to Chep Lap Kok airport in Hong Kong. Measurements were made for the vibration on the viaduct deck under traffic and these were compared with predictions made using NORBERT. Bewes found the predicted deck vibration to be significantly lower than the measurement in the higher frequency bands. One area of uncertainty is the damping loss factor that is appropriate for a concrete box-section. For a damping loss factor of 0.1, the work of Bewes shows that the NORBERT prediction is at least 10dB lower than the measurement for frequencies greater than 400Hz.

The main difficulty in using NORBERT for a concrete box-section viaduct is due to the complex cross-section geometry of these structures. Figure 6.1 shows the cross-section of the viaduct studied in the previous work by Bewes (2006).

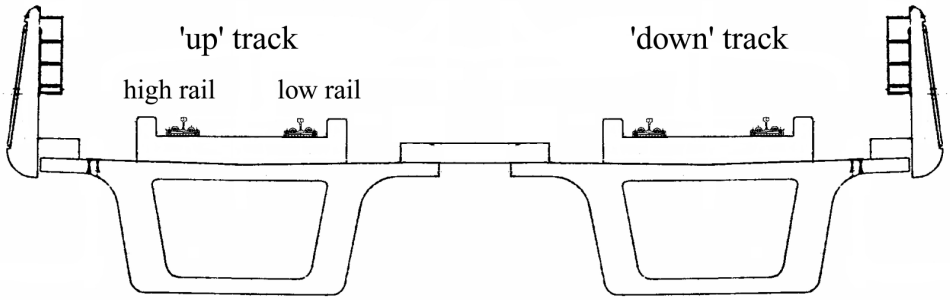

Figure 6.1. Cross-sectional view of the concrete box-section viaduct close to Chep Lap Kok airport in Hong Kong (Bewes (2006).

The viaduct shown in Figure 6.1 is less amenable to the approximation for mobility used in NORBERT than the structures studied in previous chapters, as it is difficult to express in terms of beams and plates. Below the rail decoupling frequency, Bewes (2006) used an I-section beam in the coupled beam model, with the dimensions of the beam web set to those of a single box web. The width of the beam flanges were set to the mean of those of the box flange and the viaduct deck. The thickness of the flanges

was set to that of the box flange. For frequencies greater than the decoupling frequency, either the I-section beam model or a plate model with a thickness equal to the local deck thickness around the rail seats was used to calculate the power input to the viaduct. The switch between the beam model and the plate model was made at the frequency for which the distance between the rail and the box web is equal to one-quarter of a bending wavelength in the deck.

In this work, a new set of measurements has been made for a concrete box-section viaduct on the Docklands Light Railway (DLR), with particular attention paid to the need to characterise its vibration response. In addition to the measurement of vibration under-traffic, point and transfer response measurements have been made on the viaduct deck. These measurements have been used as a basis for an evaluation of the approach proposed by Bewes (2006) to the calculation of the input power for this type of structure. The use of point and transfer mobilities in this evaluation means that the effects of uncertainty in the wheel-rail roughness and the properties of the track structure are avoided. Together with the availability of the WFE method, these new measurements allow a more detailed study of the behaviour of concrete box-section viaducts with respect to vibration than was possible in previous work.

6.2. MEASUREMENTS ON THE VIADUCT

6.2.1. The viaduct and test site

The measurements were made on a concrete box-section viaduct between Pontoon Dock and West Silvertown stations on the Bank to King George V Dock line of the DLR. A photograph is shown in Figure 6.2.

Figure 6.2. A photograph of the concrete box-section viaduct under study, taken from the platform on Pontoon Dock station, looking toward West Silvertown station.

The twin-track viaduct is made up of 37m length spans between the support pillars. The measurements were made between way markers 05096 and 05097, marked 'Test site' in Figure 6.2. This site was chosen because there is very little lateral curvature or vertical gradient in this part of the viaduct and because it is at approximately mid-span between the vertical support pillars. These are desirable conditions for use of the NORBERT and WFE models.

The rail section and rolling stock are the same as for the concrete-steel composite bridge described in Chapter 3. The rails are directly fastened to the deck of the concrete box-section viaduct using Pandrol VIPA-SP resilient baseplates, set at 0.75m intervals.

The location of the viaduct, in a busy area of London and close to roads and London City airport means that it is not possible to obtain useful measurements for the noise levels associated with a train pass-by on this viaduct.

6.2.2. Point and transfer response measurements

Point and transfer response measurements were made on the viaduct deck and rail using an instrumented hammer on 15th and 16th April 2008, before trains began running for the day. Trial measurements on large concrete castings showed that it would be necessary to use two different hammers in order to excite the structure sufficiently over the frequency range of interest, one with a mass of 3.3kg and one

with a mass of 0.6kg. The larger of these hammers provided excitation with a cut-off at a frequency of 200Hz, while the other had a cut-off of 1.25kHz. The results obtained using these two different hammers were checked for satisfactory agreement in the frequency range over which both are expected to deliver sufficient energy to the viaduct structure, approximately 100Hz to 200Hz. They have been plotted in the frequency range up to 200Hz for the large hammer tests and up to 1.25kHz for the small hammer tests.

The point response measurements were made at four different positions across the right-hand side of the viaduct. These positions are shown below in Figure 6.3.

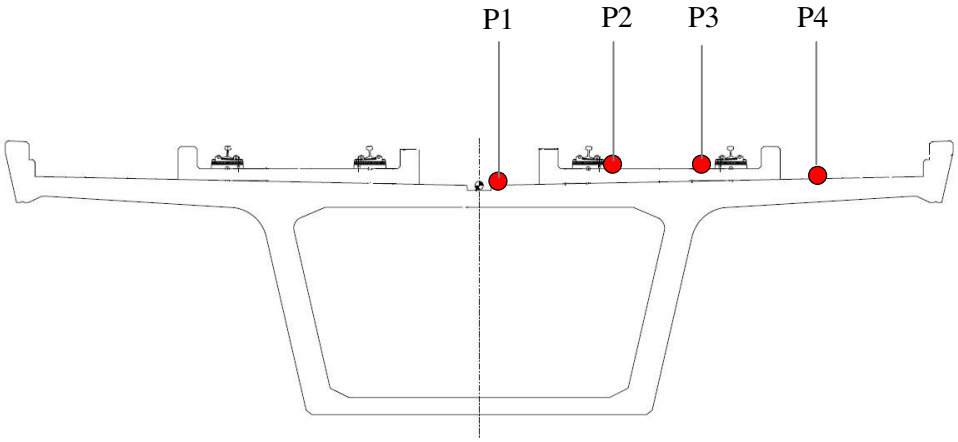

Figure 6.3. Cross-sectional view of the concrete box-section viaduct (courtesy of Halcrow Group Ltd), showing the four positions on the deck at which point response measurements were made.

Position P1 is at a lateral distance of approximately 0.25m from the viaduct centre-line. Positions P2 and P3 are close to the inner and outer rails, at approximately 1.2m and 2.6m from the viaduct centre-line respectively. Position P4 is at lateral distance of approximately 3.6m from the viaduct centre-line. Note that there is a walk-way formed by loosely-mounted bricks on top of the viaduct deck, to the outside of position P4, which is not shown in Figure 6.3. This walk-way is not expected to make a significant contribution to the mass or stiffness of the structure. It has therefore been omitted from the WFE model of the viaduct.

Transfer accelerance measurements were made along a line parallel to the viaduct centre-line, passing through position P3. The excitation position was moved along this line in increments equal to half the baseplate spacing for the first ten measurements and in increments equal to the baseplate spacing (0.75m) subsequently.

The accelerometer position remained fixed. Measurements were made for a maximum distance of 7.5m between the excitation and response positions, above which the response signal became heavily-contaminated by noise. Due to the limited time available, transfer response measurements were made using only the 0.6kg hammer. The minimum frequency for which these measurements are valid is approximately 100Hz.

Point and transfer accelerance measurements were also made at the head of the outer rail on the viaduct, for the vertical direction only. These measurements have been used to asses the track model developed in Chapter 6 for resilient baseplate track. The rate of decay of vibration in the rail is the quantity of primary interest here and the method for its calculation proposed by Jones et al. (2006) has been followed.

6.2.3. Vibration measurements under-traffic

Measurements were also made of the vibration of the viaduct deck and rail under-traffic on 16th April 2008. Acceleration measurements were made at two locations on the deck and one location on each rail, summarised below in Table 6.1.

Measurement	Location	Orientation
Inside rail	Centre of rail foot, mid-span	Vertical
Outside rail	Centre of rail foot, mid-span	Vertical
Viaduct deck	Position P2	Vertical
Viaduct deck	Position P3	Vertical

Table 6.1. Positions of the accelerometers used to measure vibration under traffic.

The accelerometers were attached to the viaduct at a single cross-section of the viaduct at mid-span between adjacent baseplates. Recordings were made for a total of 29 trains.

6.3. MODELLING THE CONCRETE BOX-SECTION VIADUCT

The application of NORBERT and the WFE method to the concrete box-section viaduct is described in this section. These two different modelling approaches have been used to predict the vibration response of the viaduct and the rail. The results of this modelling work are compared with the measurements made on the viaduct in Section 6.4.

6.3.1. Use of NORBERT for the concrete box-section viaduct

The approach proposed by Bewes (2006) for defining an I-section beam and a plate to represent a concrete box-section viaduct in NORBERT was described in Section 6.1. This approach has been followed here and an appropriate set of input parameters for this viaduct is shown below in Table 6.2.

Thickness of beam web (m)	0.3
Depth of beam web (m)	2
Thickness of beam flanges (m)	0.18
Width of beam flanges (m)	3
Thickness of deck plate (m)	0.38
Distance between the rail and beam web (m)	0.6

Table 6.2. Input parameters for the I-section beam and plate used to represent the concrete box-section viaduct in NORBERT.

The distance between the rail and the beam web shown in Table 6.2 is for the outer rail position, because the modelling work for vibration under-traffic presented in Section 6.4 is for excitation at the outer rail. Note also that the finite length coupled beam model has been used here to calculate the power input to the viaduct, for frequencies less than the decoupling frequency. The lengths of the beams used to model the structure at low frequencies were set to the span lengths of the viaduct (37m).

The material properties used to model the concrete viaduct in both NORBERT and WFE are summarised in Table 6.3 below.

Property	**Value**
Young's Modulus	40GPa
Density	2400kg/m^3
Poisson's ratio	0.2

Table 6.3. Material properties used to model the concrete box-section viaduct.

As described in Chapter 3, the Young's modulus of concrete is strongly dependent on the mixture composition. The company responsible for the construction of this viaduct, Halcrow Group Limited, took samples of the concrete used to cast the viaduct sections and measured the compressive strength of these as approximately 60kN/mm^2

after a suitable setting time. The dynamic Young's modulus given in Table 6.3 was chosen from the compressive strength measurement and reference to (Kong and Evans, 1987). Standard design values have been used for the density and Poisson's ratio, which are less sensitive to the mixture composition.

A frequency-independent damping loss factor of 0.1 has been chosen for the viaduct, based on the comparison made between the transfer accelerance measurements and corresponding results of the WFE modelling work presented in Section 6.4.1.

Two different approaches have been taken to the application of the SEA method in NORBERT for this viaduct: a relatively detailed SEA network and a relatively simple one. In the former, the geometry of the viaduct has been reproduced quite fully, such that the geometry of the plate assembly corresponds closely with the physical dimensions of the viaduct. In the relatively simple SEA network, a smaller number of plates are used, but these have larger physical dimensions. The minimum number of modes over a given frequency band in a single subsystem is therefore greater for the simple SEA network. Consequently, it may be expected that this network can be used to predict the response of the structure reliably down to lower frequencies than the more detailed SEA network. The two SEA networks are shown in Figure 6.4 below.

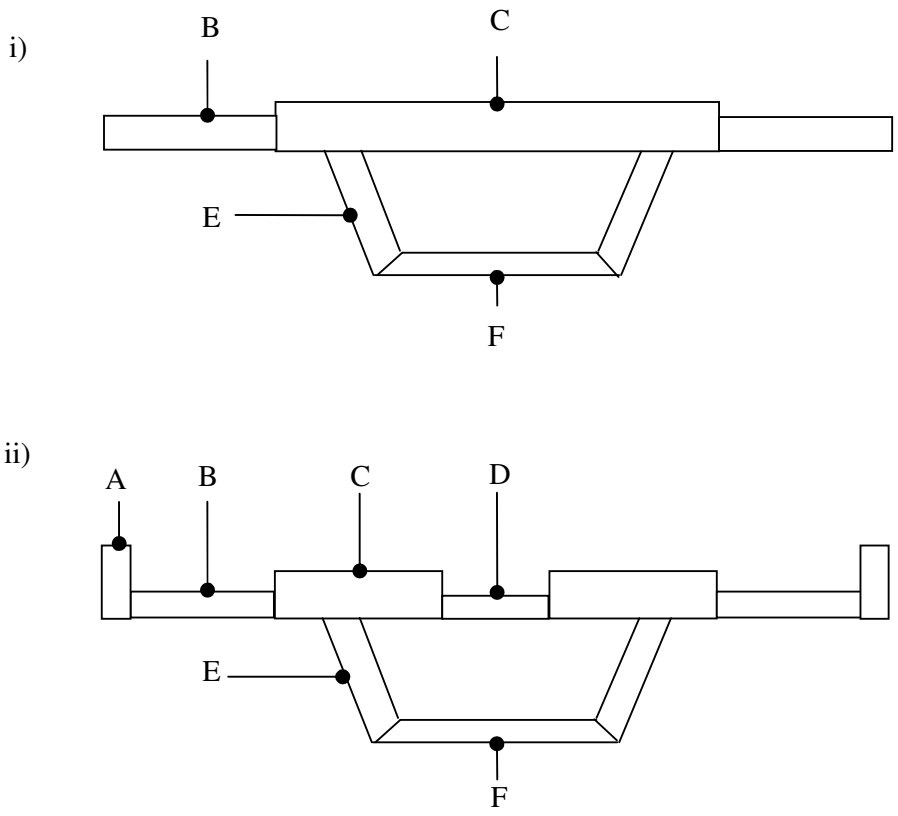

Figure 6.4. SEA representation of the concrete box-section viaduct in NORBERT: i) simple SEA network; ii) detailed SEA network.

The cross-section dimensions and the number of plates for both the simple and the detailed SEA networks are given in Table 6.4 below.

i)

	Name	Thickness (m)	Width (m)	Number
B	Side-deck	0.22	2.0	2
C	Main deck	0.38	6.0	1
E	Web	0.3	2.2	2
F	Bottom flange	0.18	3.0	1

ii)

	Name	Thickness (m)	Width (m)	Number
A	Parapet	0.25	0.65	2
B	Side-deck	0.22	1.7	2
C	Main deck	0.38	2.5	2
D	Centre-deck	0.22	1.0	1
E	Web	0.3	2.2	2
F	Bottom flange	0.18	3.0	1

Table 6.4. Specification of the plates in, i) simple SEA network, ii) detailed SEA network.

The modal density in each of the plates described in Table 6.4 can be estimated from (Cremer and Heckl, 1988),

$$n(\omega) = \frac{\kappa_B^2 A}{4\pi\omega} = \frac{A}{3.6 c_L h} \qquad (6.1)$$

where A is the surface area of the plate, κ_B is the free bending wavenumber of the plate, h is its thickness and c_L is the longitudinal wave speed in concrete. Application of equation (6.1) to the plates defined above shows that the minimum modal density in a single plate in the detailed SEA network is a factor of three smaller than that in the simple SEA network: at 0.006 modes per rad/s and 0.018 modes per rad/s respectively. However, these modal density values indicate that the number of modes expected in a single plate over any one-third octave frequency band in the range of interest is less than one for either of these SEA networks. This shows that the internal modes of the individual subsystems occur only for relatively high frequencies. The total number of modes in a given frequency band for all the plates in the SEA network may therefore be a more appropriate basis for assessment of the frequency range for

which SEA can be applied to the structure (Lyon, 1975). For both SEA networks considered here, the total number of modes of the viaduct expected in the 40Hz one-third octave band is around 5. On this basis, it expected that both of the networks shown in Figure 6.4 are suitable for use in predicting the vibration response of the viaduct over the frequency range for which measurements have been made.

The resilient baseplate track structure on this viaduct was modelled as a continuous resilient layer between the rail and the viaduct with a stiffness per unit length of $70MN/m^2$ and a damping loss factor of 0.2. These values are based on the low-frequency results of the laboratory measurements made for the VIPA-SP baseplates under a preload of 15kN presented in Chapter 5. This preload level is appropriate for the baseplates subject to the wheel-load from DLR rolling stock, as discussed in Chapter 5.

The average speed at which the trains passed the test site was found to be approximately 50km/h from inspection of the measured time series and the axle spacing for the rolling stock. The maximum train speed found from the measurements was 53km/h and the minimum speed was 44km/h.

6.3.2. Use of the WFE method for the concrete box-section viaduct

The results of the WFE modelling work will be compared with the point and transfer response measurements that are valid up to approximately 1.2kHz. It is therefore appropriate to specify the WFE model for this same frequency range. The maximum section thickness of the viaduct is 380mm, occurring in the viaduct deck. The point mobility results given by thick and thin infinite plate theory for a 380mm thick concrete plate at a frequency of 1.2kHz differ by less than 10%. Plate elements, with cubic shape functions, have therefore been used for the WFE analysis of this viaduct. Simple analytical models were used to determine appropriate element lengths for each part of the structure, together with the requirement for at least three of these plate elements per wavelength in the frequency range of interest.

Figure 6.5 shows the nodes of the WFE model for half of the concrete box-section viaduct. Symmetric and anti-symmetric boundary conditions have been applied to the nodes on the viaduct centre-line, and used to recover the solution for the full viaduct structure.

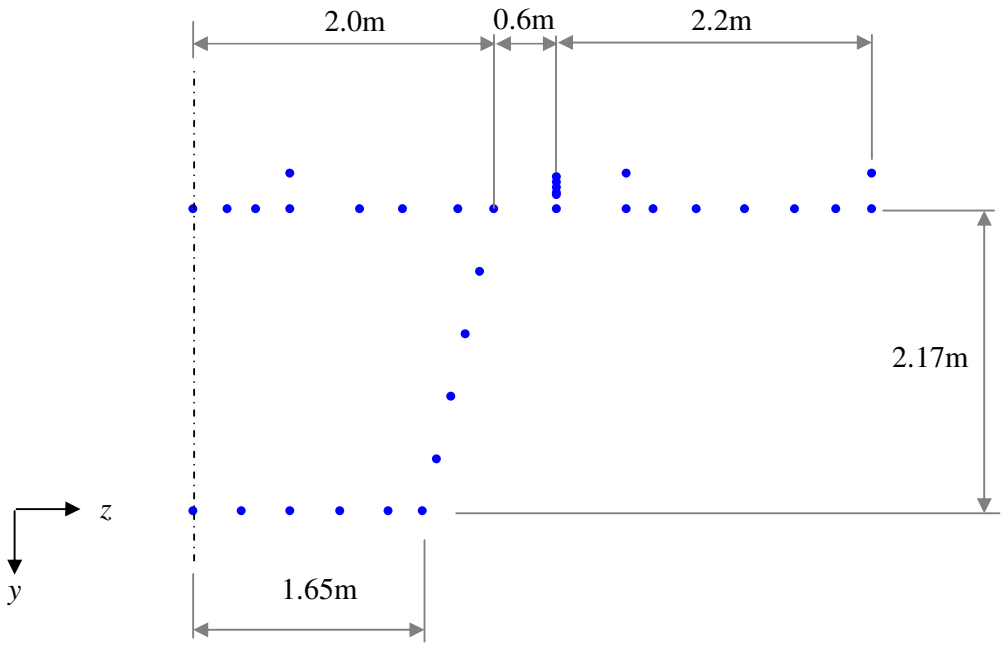

Figure 6.5. Node positions in the WFE model for half of the concrete box-section viaduct, showing the outer rail and track support.

In the WFE model shown in Figure 6.5, a single plate element represents the track structure as a continuous resilient layer between the rail and the viaduct deck. The properties of this plate element were chosen to give the same frequency-independent track stiffness per unit length and damping loss factor as described for the NORBERT model in Section 6.3.1. Above this are four plate elements representing the rail, following the method used to represent this same type of rail in Chapter 3.

In a second stage of the WFE modelling work for this viaduct, a more detailed representation of the Pandrol VIPA-SP baseplate track was used to account for the expected frequency-dependent stiffness of this track. The approach taken to modelling a single baseplate in the preceding chapter using FE was extended to the case of the track on this viaduct using WFE. The WFE model of the track is shown in Figure 6.6 below.

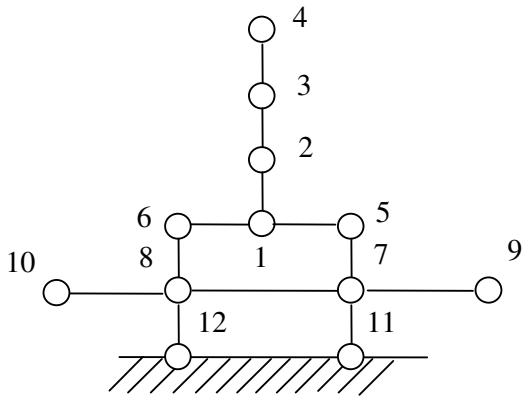

Figure 6.6. WFE model of a resilient baseplate: ○, nodes.

Nodes 1 to 6 in Figure 6.6 define the rail, in which the rail foot is now represented by two horizontally-orientated elements. There are two vertical plate elements for the railpad, three horizontal plate elements for the top plate and two vertical plate elements for the baseplate pad. The nodes at the lower end of the baseplate pad are common to elements in the viaduct deck. Fewer nodes have been used in the WFE model of this track than were used in the FE model of a single baseplate in Chapter 5, because the WFE model was intended for use in this specific case, rather than as a model for resilient baseplates in general.

All the plate elements used to represent the track support were assigned orthotropic material properties. The elastic moduli were set to very low values in all but the vertical direction, to minimise the effects of wave motion along the length of the track support, which does not occur physically because this support is not continuous. The properties of the elements used to represent the railpad and baseplate pad were chosen to give a continuous stiffness equivalent to the stiffness of these pads as presented in the preceding chapter, by dividing by the baseplate spacing, 0.75.

The top plate was defined in WFE as a plate strip with a width of 360mm and thickness of 20mm, again following the work presented in Chapter 6. In order for this plate strip to have a continuous mass per unit length equivalent to that of the discrete baseplates set at 0.75m intervals, it was necessary to assign these elements a density of 2100kg/m^3. This property change affects the onset of bending in the top plate, such that it was also necessary to change the Young's modulus to 38GPa in order to predict

the first bending mode of the unconstrained top plate in agreement with the measurement made for the top plate laid on a soft support, described in Chapter 5.

6.3.3. Free vibration analysis

As for the bridges studied in previous chapters, the WFE model of the concrete box-section viaduct was first used to study its free vibration response. The dispersion relations obtained from solution of the eigenvalue problem for a prescribed set of purely real wavenumbers are identified for the case of zero damping in Figure 6.7 below. A number of dispersion curves calculated from simple beam and plate theory are also shown in Figure 6.7 in order to aid interpretation of the waveforms in the viaduct.

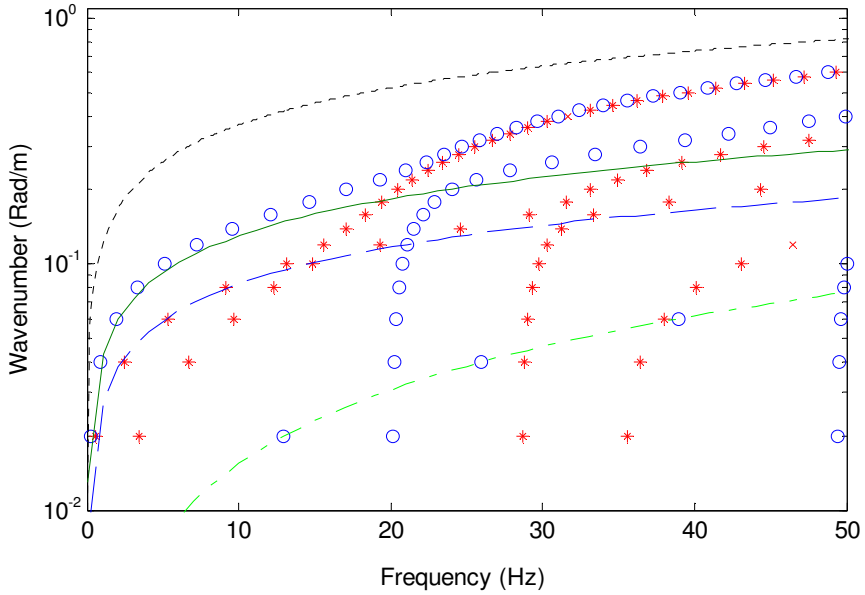

*Figure 6.7. Purely-real wavenumber shown versus frequency for the case of zero damping in the concrete box-section viaduct: ○ ,WFE for symmetric case; * , WFE for anti-symmetric case; _ _ _ _ _ _ _ , infinite thin plate model (380mm thickness); _____ , Euler beam model (vertical bending); _ _ _ _ _ , Euler beam model (lateral bending); _ . _ . _ . _ , longitudinal wave in concrete.*

Those waves in the structure with a zero cut-on frequency can be identified from a comparison of the WFE solution with the curves obtained from the analytical models at low frequencies. The Euler beam results have been obtained using the section properties of the equivalent I-section beam proposed by Bewes (2006). The WFE solutions corresponding to the vertical beam bending wave, the lateral beam bending wave and the longitudinal wave can be identified. The WFE solutions for the

torsional wave are those for the anti-symmetric case that show a zero cut-on frequency (not the lateral bending wave). The Euler beam result for the vertical beam bending wave departs from the corresponding WFE solution for frequencies greater than approximately 20Hz. At this frequency, the first non-zero frequency wave cut-on occurs in the WFE solution. For higher frequencies, the highest wavenumbers from the WFE model tend toward the results obtained by the thin infinite plate bending model.

For further identification of the modes, Figure 6.8 shows the mode shapes for the symmetric waves in the viaduct at frequencies of 1Hz, 25Hz, and 50Hz.

Frequency of 1Hz

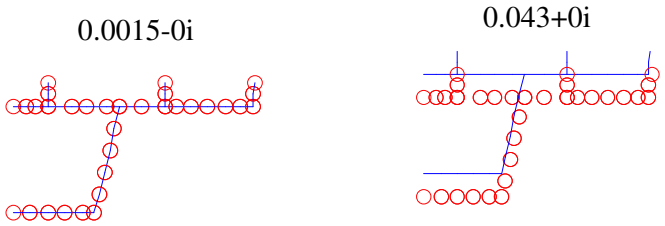

Frequency of 25Hz

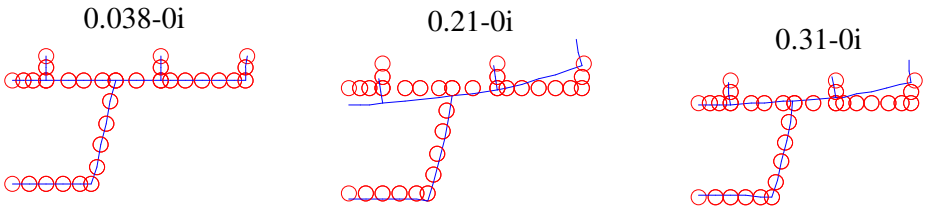

Frequency of 50Hz

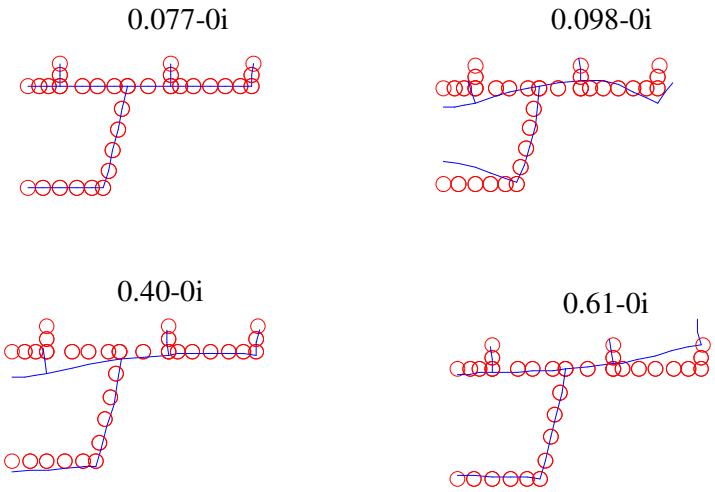

Figure 6.8. Mode shape plots and corresponding wavenumbers for the symmetric modes of the concrete box-section viaduct about the centre-line. Caption above each plot shows wavenumber (rad/m): o, original node position; _____ ,deformed shape.

At 1Hz, there is a longitudinal mode and a vertical beam bending mode with no deformation of the cross-section. At the two higher frequencies shown, the viaduct does not behave as a beam and there is significant deformation of the cross-section in all modes except the longitudinal mode. Plate bending motion in the viaduct deck appears to dominate the response in these modes.

Figure 6.9 shows the mode shapes for the anti-symmetric waves in the viaduct at frequencies of 1Hz, 25Hz, and 50Hz.

Frequency of 1Hz

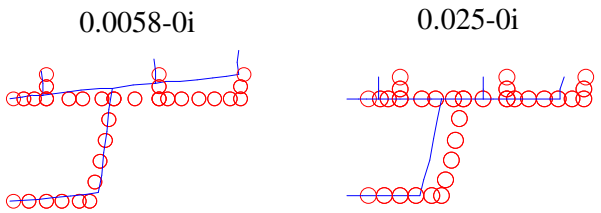

Frequency of 25Hz:

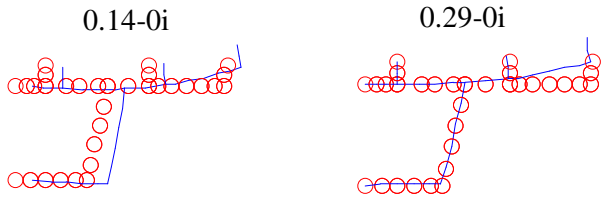

Frequency of 50Hz

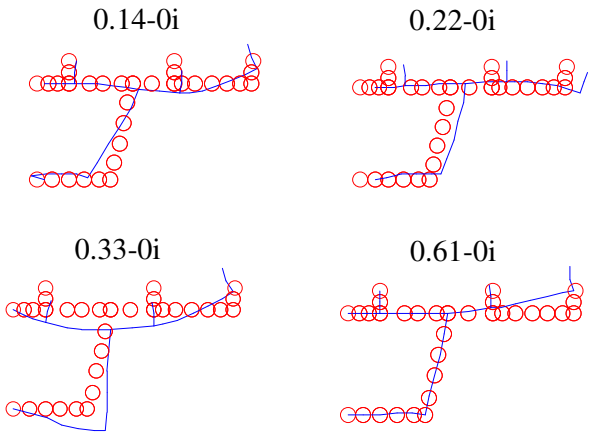

Figure 6.9. Mode shape plots and corresponding wavenumbers for the anti-symmetric modes of the concrete box-section viaduct about the centre-line. Caption above each plot shows wavenumber (rad/m): o , original node position; _____ *, deformed shape.*

At 1Hz the two modes shown in Figure 6.9 are the torsional and lateral beam bending modes. At both 25Hz and 50Hz, there is again significant deformation of the cross-section, with bending motion in the viaduct deck for all modes.

The dispersion and mode shape diagrams presented in Figures 6.7 to 6.9 show the behaviour of the viaduct at low frequencies. As for the concrete-steel composite bridge under study in Chapter 3, it is possible to plot the dispersion results clearly over a much larger range of frequencies by selecting only the waves with relatively large amplitudes for a given excitation position. Waves with an amplitude (magnitude of the complex amplitude) greater than 75% of the largest amplitude at a given frequency are referred to here as 'very high power waves', those with an amplitude between 50% and 75% of the maximum amplitude as 'high power waves' and those with between 25% and 50% of the maximum amplitude as 'medium power waves'. Note that the term 'power' is used loosely here as the relative wave amplitudes are only an approximate indicator of the relative powers transmitted to the waves.

Figure 6.10 shows the dispersion relations for the high-energy content waves when the viaduct is excited at position P3 on the deck, from the symmetric case WFE solution, together with the results of appropriate analytical models.

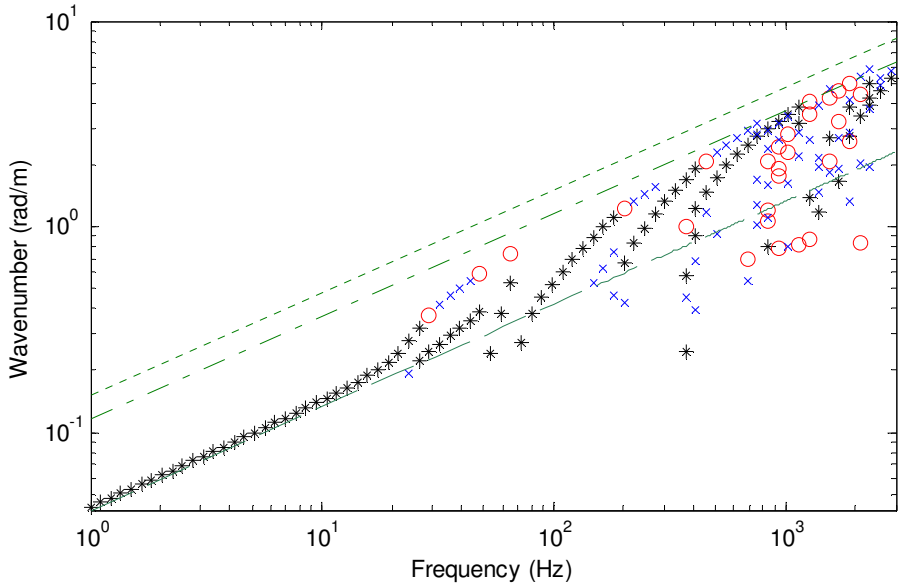

*Figure 6.10. Purely-real wavenumber shown versus frequency for the case of zero damping in the concrete box-section viaduct and excitation at position P3, symmetric case WFE solution: * , WFE result for very high power waves; × , WFE result for high power waves; ○ , WFE result for medium power waves; _ _ _ _ , Euler beam model (vertical bending); _ . _ . _ , infinite thin plate model (380mm thickness); - - - - - - - - , infinite thin plate model (220mm thickness).*

Figure 6.10 shows that for frequencies greater than approximately 500Hz, much of the vibration power input to the viaduct at position P3 on the deck is transmitted to the plate bending waves in the part of the deck which has a thickness of 380mm. For frequencies less than 20Hz, the majority of the input power is transmitted to the vertical beam bending wave of the viaduct. For frequencies between 20Hz and 500Hz, the dispersion results obtained from the WFE model indicate that much of the input power is transmitted to waves with dispersion properties that lie between those of the beam and plate bending waves.

Figure 6.11 shows the dispersion relations for the important waves in the viaduct for excitation at position P4 on the deck, where the local deck thickness is 220mm, from the symmetric case WFE solution.

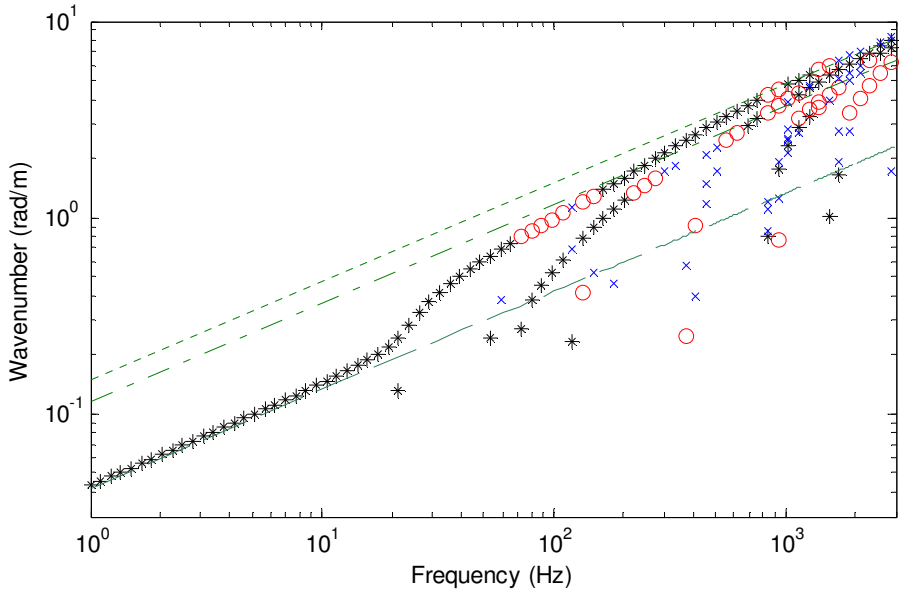

*Figure 6.11. Purely-real wavenumber shown against frequency for the case of zero damping in the concrete box-section viaduct and excitation at position P4, symmetric case WFE solution: * , WFE result for very high power waves; × , WFE result for high power waves; ○, WFE result for medium power waves; _ _ _ _ , Euler beam model (vertical bending); _ . _ . _ . , infinite thin plate model (380mm thickness); _ _ _ _ _ _ _ _ , infinite thin plate model (220mm thickness).*

The dispersion relations shown for selected waves at position P4 show broadly similar behaviour to that discussed previously for position P3. The differences between them occur at higher frequencies and are due to the lower local deck thickness around position P4. While the response shows a transition between beam bending and plate

bending waves in the local deck thickness from about 20Hz to 500Hz, as for position P3, there appears to be an additional stage in this transition for position P4. In the range from about 100Hz to 300Hz, Figure 6.11 shows that a significant part of the input power to the bridge is transmitted to waves which have dispersion characteristics that approximate to those for plate bending waves in the thickest part of the deck (380mm), rather than the local deck thickness (220mm).

In summary, the free vibration response analysis presented in this section provides a physical understanding of how this structure behaves in response to vertical excitation on the deck. The majority of the power input to concrete box section viaduct is transmitted to beam bending waves for frequencies less than 20Hz and to plate bending motion in the deck, local to the input point, above about 500Hz. Between these ranges, the input power is transmitted to waves with dispersion properties that lie between those of the beam and plate bending waves. For position P4, where the deck thickness is relatively low, power transmission to waves with dispersion characteristics similar to those for plate bending waves in the thicker parts of the deck seems to be important in the frequency range between about 100Hz and 300Hz.

6.4. COMPARISON OF THE MODELS WITH THE MEASUREMENTS

6.4.1. Transfer response on the viaduct deck

In this section the measured transfer accelerance on the viaduct deck is compared with that predicted using the WFE model. This is of interest here because it can be used to determine an appropriate damping loss factor for use in modelling the viaduct. In order to aid the comparison of the measured and predicted transfer accelerances, the following normalisation has been used,

$$A_{Norm}(x,\omega) = \frac{\left|A_t(x,\omega)\right|}{\left|A_p(\omega)\right|} \tag{6.2}$$

where, A_t is the transfer accelerance and A_p is the point accelerance.

Figures 6.12 to 6.14 (for different frequency bands) show the normalised transfer accelerance as a function of distance between the excitation and response positions on the viaduct deck, obtained from the measurements and from the WFE analysis. The WFE results are plotted for different values of damping loss factor (η_{bridge}).

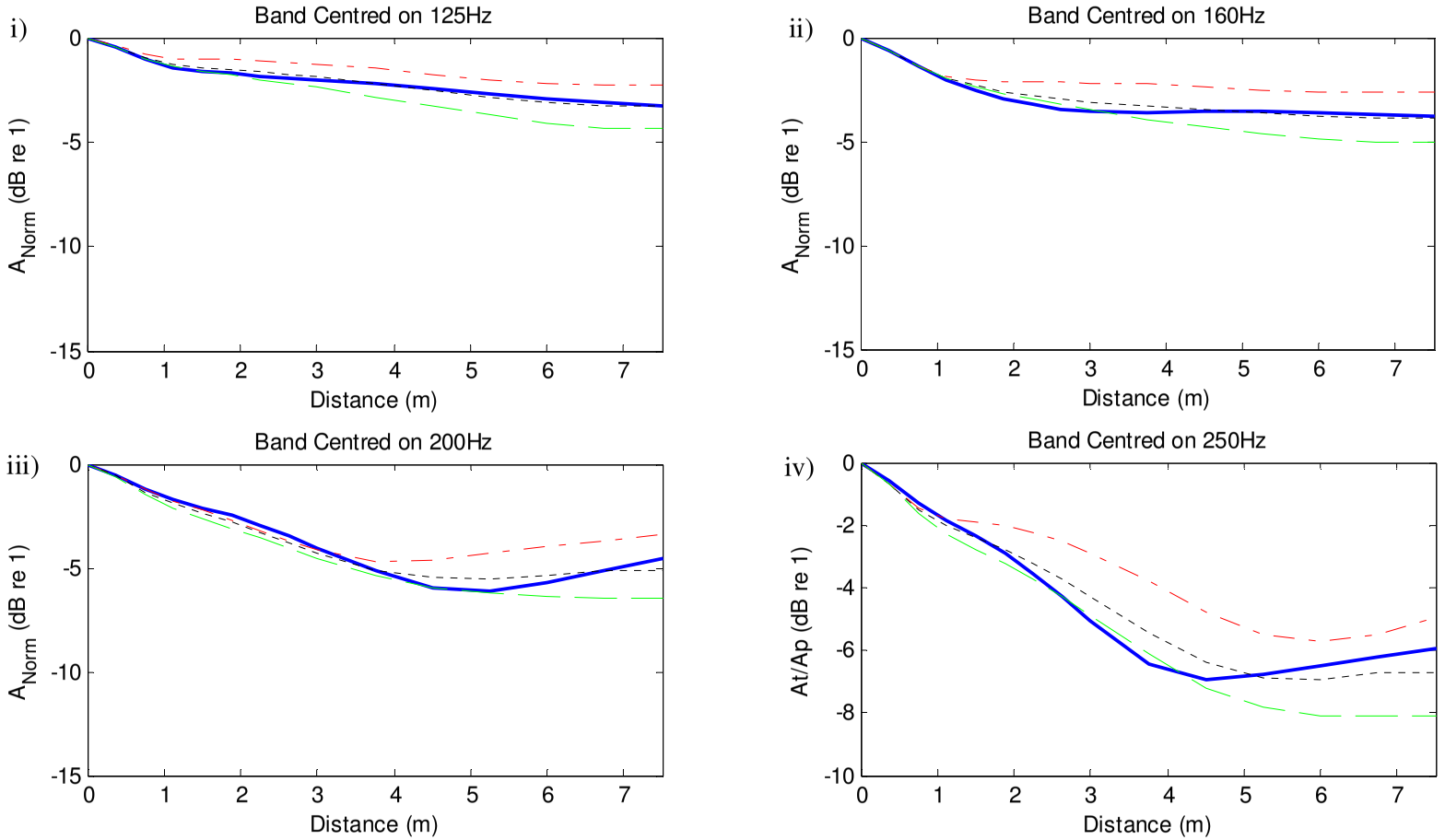

Figure 6 .12. Normalised accelerance ($|At/Ap|$) shown versus distance between excitation and response position:

———— , *measurement;* –·–·– , *WFE result for* η_{bridge}*= 0.05;* - - - - - - - , *WFE result for* η_{bridge}*= 0.1;*

– – – – , *WFE result for* η_{bridge}*= 0.2.*

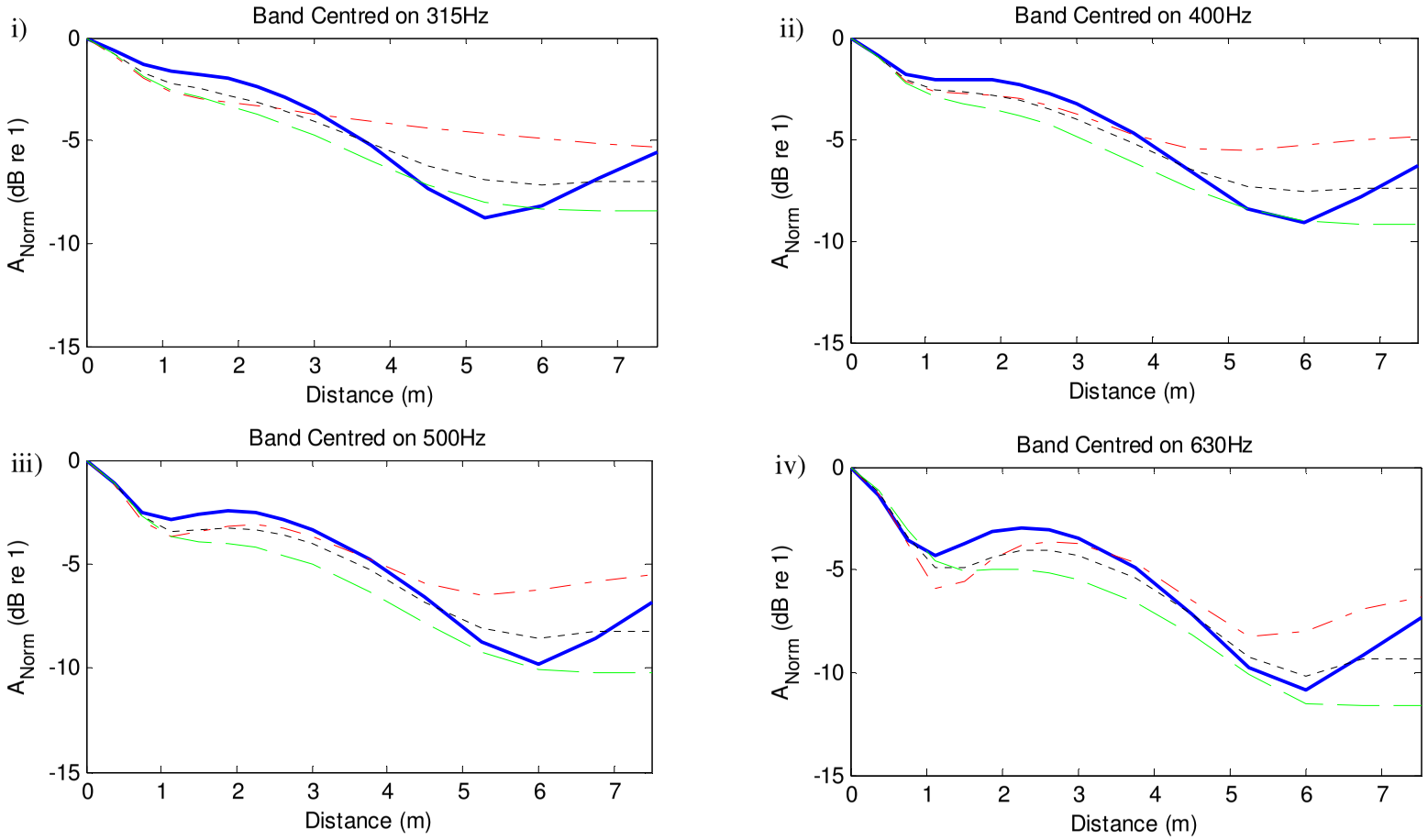

Figure 6.13. Normalised accelerance ($|At/Ap|$) shown versus distance between excitation and response position: ——— *, measurement;* –·–·– *, WFE result for* η_{bridge} *= 0.05;* - - - - - - - *, WFE result for* η_{bridge} *= 0.1;* – – – – *, WFE result for* η_{bridge} *= 0.2.*

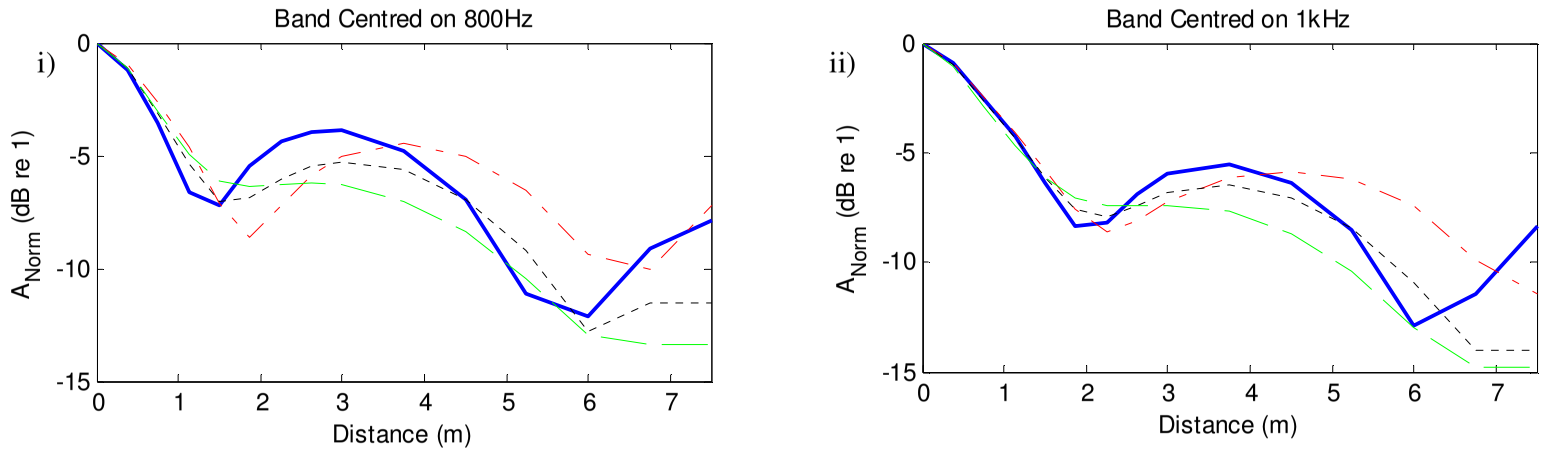

Figure 6.14. Normalised accelerance ($|At/Ap|$) shown versus distance between excitation and response position: ——— *, measurement;* –·–·– *, WFE result for* η_{bridge} *= 0.05;* - - - - - - - *, WFE result for* η_{bridge} *= 0.1;* – – – – *, WFE result for* η_{bridge} *= 0.2.*

Figures 6.12 to 6.14 show a relatively high rate of decay over a distance of approximately 1m from the excitation position, in all frequency bands. This is due to the near-field waves in the viaduct. The average decay rate over the 7.5m length of viaduct for which measurements were made increases from approximately 0.4dB/m in the 125Hz frequency band to 1.4dB/m in the 1kHz band. These values are consistent with those reported for the rate of decay of vibration in railway bridges in previous work (Hardy, 1999).

In many cases the measured response magnitude does not decrease uniformly with distance and may even increase again. This behaviour is also present in the results of the WFE analysis. For the higher frequency bands, the variation in response magnitude with distance tends towards an oscillatory appearance. This is not due to the modal response of the viaduct structure, because the WFE model is based on an infinite structure. It is due instead to the modulation produced when two waves with similar amplitude, but slightly different wavenumber are combined.

Considering all frequency bands, the agreement between the model and the measurements shown in Figures 6.12 to 6.14 is best, when a damping loss factor of 0.1 is used. This value is larger than the *material* damping loss factor for concrete, typically in the range from 0.01 to 0.05 (Beranek, 1971). This indicates that there is energy dissipation in the structure due to mechanisms other than material damping. There may be significant energy dissipation due to friction in the structure at internal joints and at connections with fixtures such as the handrail and brick walkway (see Figure 6.2). These mechanisms of energy dissipation cannot be included in the WFE model directly, but their effect is incorporated via the empirical 'structural damping loss factor' of 0.1. This has been used in all the WFE modelling work presented in the sub-sections to follow and also in the bridge noise model.

6.4.2. Point response on the viaduct deck

In this section, the measured point mobility at each position on the viaduct deck, P1 to P4, is compared with the corresponding result from the WFE model and from the NORBERT model for mobility.

The point response measurements were made using two different impact hammers, described in Section 6.2.2. Example coherence spectra for the measurements made with these hammers are shown in Figure 6.15 below.

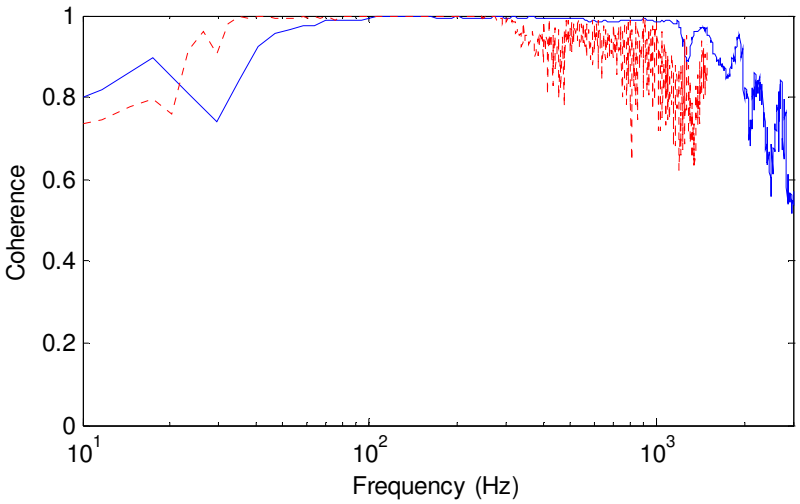

Figure 6.15. Example coherence spectra for measurements made with the two different impact hammers:_____ , 0.6kg hammer; - - - - - - - - , 3.3kg hammer.

The coherence for the 3.3kg impact hammer is satisfactory for frequencies between about 30Hz and 300Hz. That for the 0.6kg hammer is close to unity for frequencies between about 100Hz and 1200Hz. Based on this is and a comparison of the excitation spectrum produced using each of these hammers, the point mobility results have been plotted between 30Hz and 200Hz for the 3.3kg hammer tests and between 200Hz and 1200Hz for the 0.6kg hammer tests.

The WFE model was run for input and excitation at each of the four positions on the deck, P1 to P4. In NORBERT, appropriate values of plate thickness and the lateral distance to the web of the box-section have been used for each of these positions on the deck. The specification of the beam used to represent the viaduct remains as shown in Table 6.2.

Figures 6.16 to 6.19 show the real part and phase of the point mobility at positions P1 to P4 on the viaduct deck. Note that the real part of the mobility, rather than the magnitude, has been plotted here because this is directly related to the vibrational power input to the viaduct.

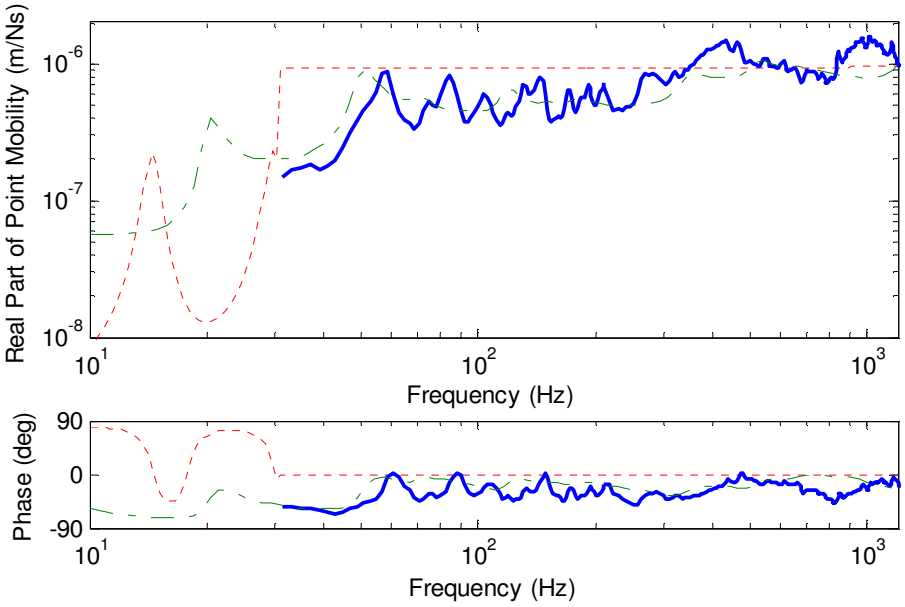

Figure 6.16. Real part and phase of point mobility on the concrete box-section viaduct deck at position P1: ——— , measurement; - - - - - - - - , from NORBERT; _·_·_·_ , from WFE model.

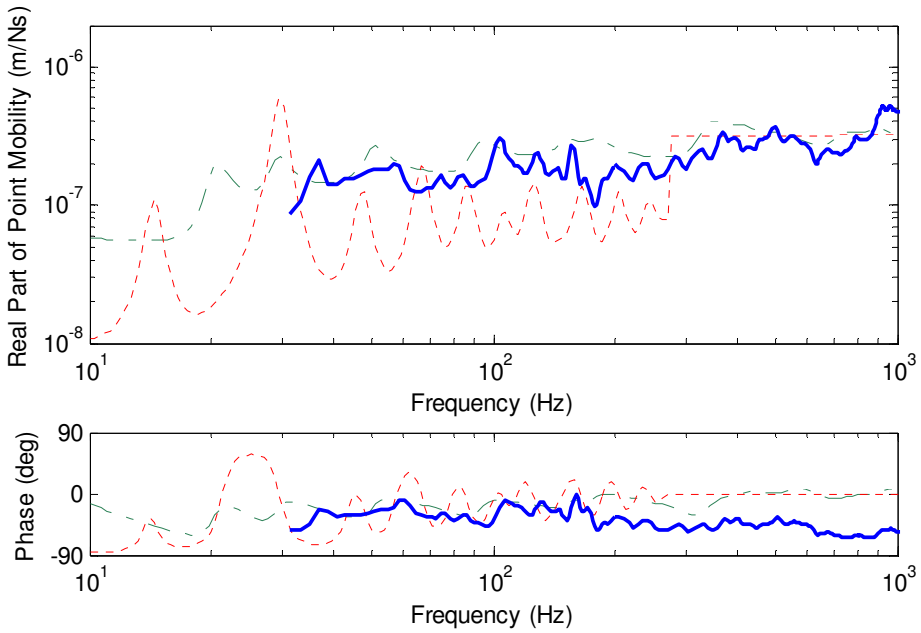

Figure 6.17. Real part and phase of point mobility on the concrete box-section viaduct deck at position P2: ——— , measurement; - - - - - - - - , from NORBERT; _·_·_·_ , from WFE model.

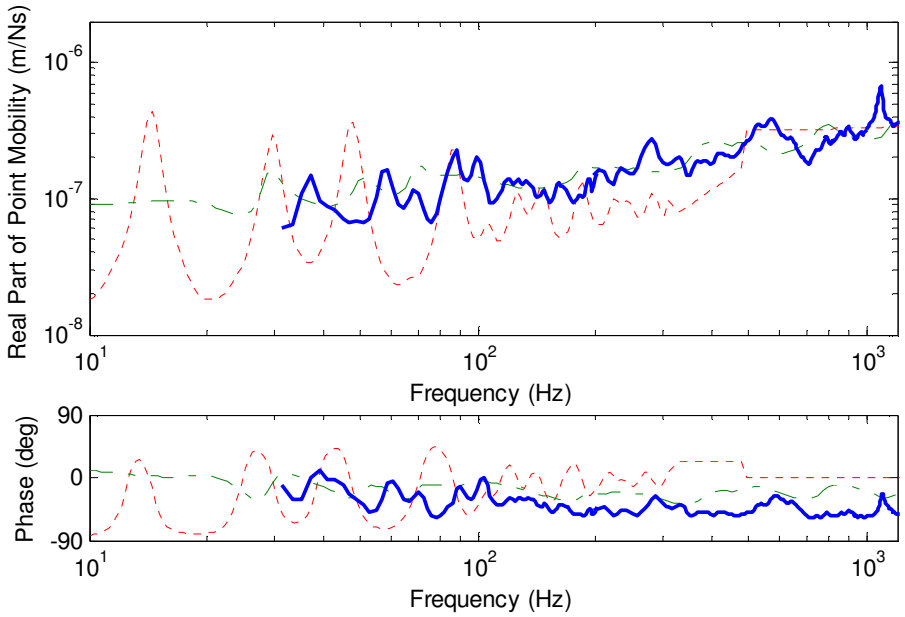

Figure 6.18. Real part and phase of point mobility on the concrete box-section viaduct deck at position P3: ——— , measurement; - - - - - - - - , from NORBERT; _·_·_·_ , from WFE model.

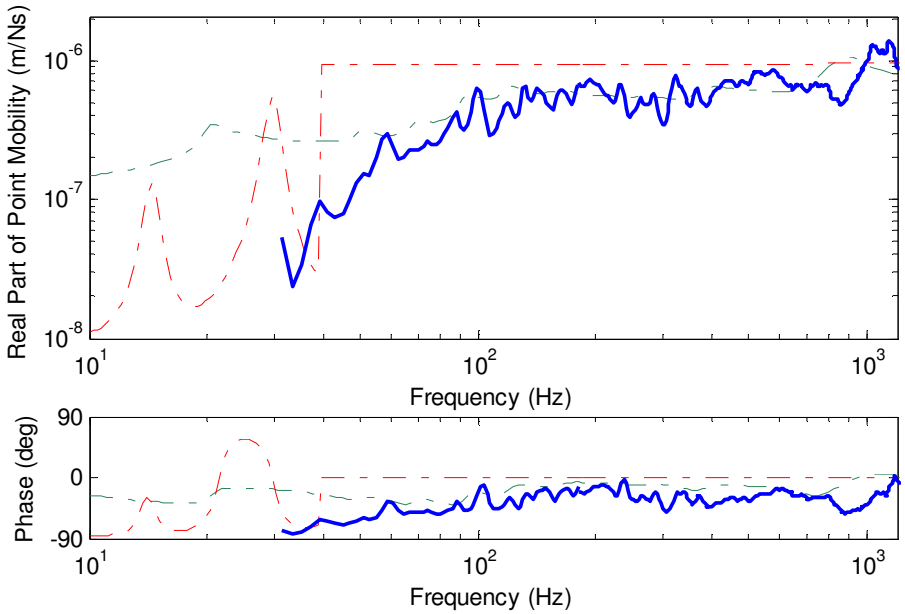

Figure 6.19. Real part and phase of point mobility on the concrete box-section viaduct deck at position P4: ——— , measurement; - - - - - - - - , from NORBERT; _·_·_·_ , from WFE model.

The spectra for the real part of the measured mobility consist of reasonably well-separated peaks at low frequencies, typically up to about 100Hz. These are due to the modes of the structure, both along its length and within the cross-section. At higher

frequencies, the modal overlap becomes larger and the response tends to that of an infinite structure.

Comparing the measured mobility spectra first with those predicted using NORBERT, it is clear that the finite length Timoshenko beam model does not predict the response of the structure correctly. The predicted real part mobility spectra show peaks that do not correspond to those in the measurements and the model results are generally lower than the measurements. At position P3 for example, the beam model is used in the frequency range up to about 500Hz and in this range the predicted real part of point mobility is typically a factor of 2 lower than the measurement. This may be expected from the results of the WFE free vibration response analysis presented in Section 6.3.3, which shows that this viaduct behaves as a beam only for frequencies up to about 20Hz. For frequencies between about 20Hz and 500Hz, the dispersion diagram of Figure 6.10 shows that the much of the power input to the viaduct at position P3 is transmitted to waves that have dispersion properties that lie between those of the beam bending and plate bending waves in the frequency range from 20Hz to 500Hz. Since the mobility of the deck plate is significantly larger than that of the beam representation of the viaduct used in NORBERT, use of the beam model leads to an underestimate for the point mobility in this frequency range.

The switch from the beam mobility model to the plate mobility model in NORBERT introduces a large step-change to the predicted mobility spectra, which is not shown in the measurements. Further, the measurements do not show a transition between the mobility of a beam and that of an appropriate plate, of the kind proposed for all-steel bridges in Chapter 2. Rather, the response of the concrete box-section viaduct at positions P2 and P3 is that of a reinforced plate over a significant part of the frequency range of interest. This is shown less clearly for the other positions on the deck, where the plate model is mainly used in NORBERT, due to the greater distance between these positions and the box webs.

The NORBERT model for mobility is in agreement with the measurements in a frequency-average sense at positions P2 and P3 over the frequency where the plate model is used. For positions P1 and P4, where the deck thickness is lower, the use of the plate model in NORBERT leads to an overestimate for the point mobility by a factor of about 2 in the frequency range up to 250Hz at P1 and up to 1kHz for P4.

The WFE results are generally in close agreement with the measurements, in a frequency-average sense. The combined beam and plate bending behaviour that is important for positions P2 and P3 is accounted for. The mobility at position P1 in the range up to about 250Hz and P4 in the range up to 1kHz are also predicted correctly using the WFE method. In these cases, the mobility on the deck is lower than that of a plate with the local section thickness, due to the restraint provided by the relatively thick parts of the deck. This is supported by the dispersion diagram of Figure 6.11, which shows that a significant part of the power input to the viaduct at position P4 is transmitted to waves that have dispersion properties similar to those for bending waves in thickest part of the deck. This occurs in a frequency range determined by the bending wavelength in the local deck thickness and the lateral distance between the position on the deck of interest and the part of the deck with greater thickness.

In summary, the results presented in this section show that the WFE method is a suitable approach to predicting the point mobility of a concrete box-section viaduct. It offers a clear benefit over the NORBERT model for mobility, particularly for cases such as at position P3, where the response of the viaduct is neither that of an equivalent beam or a plate in the frequency range from about 20Hz to 500Hz.

6.4.3. Decay rates in the rail

The rate of decay of vibration in the rail is an important measure of the acoustic performance of the track. The WFE representation of the resilient baseplate track on this viaduct described in Section 6.3.2 has been used predict the decay rate in the rail. This is compared here with decay rates obtained from the transfer accelerance measurements made on the rail. This represents a more complete assessment of the model proposed for resilient baseplate track than that described in Chapter 5, in which only a single baseplate was considered. The procedure proposed by Jones et al. (2006) for the calculation of the decay rate in the rail has been adopted here, for both the measured data and the WFE prediction.

It is the case of unloaded track that is of interest here, in order to compare with the decay rates found from the measurements made on the unloaded rail. The properties of the elements used for the railpad and baseplate pad were therefore chosen to give a continuous stiffness equivalent to the case of unloaded VIPA-SP baseplates set 0.75m apart. It was found from initial modelling work that the decay rates predicted using

this track model are sensitive to the value used for the railpad stiffness. It is therefore necessary to study the transfer stiffness measurement made during the course of the laboratory test work described in Chapter 5 for a preload level appropriate to the case of unloaded track.

Figure 6.20 shows the transfer stiffness spectrum obtained for two of these railpads combined in parallel under a total preload of 40kN.

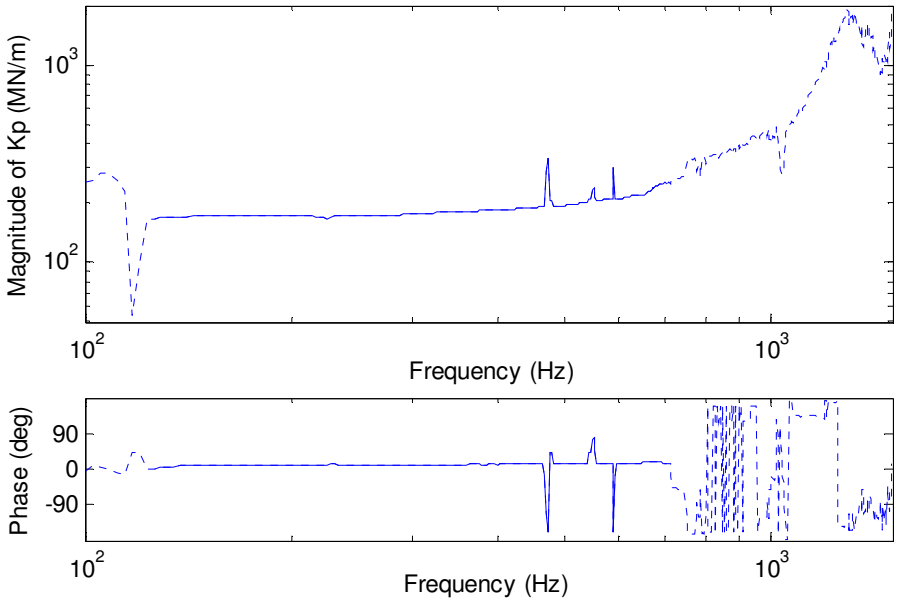

Figure 6.20. Magnitude and phase of the transfer stiffness of two Pandrol 11246 railpads combined in parallel, shown versus frequency, for a preload of 40kN.

The measurement data is valid for frequencies up to about 700Hz. Railpad stiffness values for a single railpad under a preload of 20kN, approximately that for railpads on unloaded DLR track, have been found from Figure 6.20 at frequencies of 150Hz and 500Hz. It will be shown that the 1.25kHz one-third octave frequency band is of particular importance in the decay rate spectrum for the rail. A value for the railpad stiffness at a frequency of 1.25kHz has therefore been extrapolated from the development of the transfer stiffness shown in the measurements up to 700Hz.

The railpad stiffness values used in the WFE analysis to predict the decay rates in the rail are shown in Table 6.5 together with the corresponding equivalent continuous stiffness values.

Frequency (Hz)	Railpad Stiffness (MN/m)	Equivalent continuous stiffness (MN/m/m)
150	80	107
500	100	133
1250	200	267

Table 6.5. Stiffness data for the railpad used in the WFE prediction of decay rates in the rail.

A baseplate pad stiffness of 15MN/m was used throughout the decay rate prediction work. The stiffness of the baseplate pad shows much less frequency-dependence than the railpad and this has therefore been neglected.

The decay rates in the rail obtained from the transfer accelerance measurements and those predicted using the WFE model, for the three different railpad stiffness values, are shown in Figure 6.21 below.

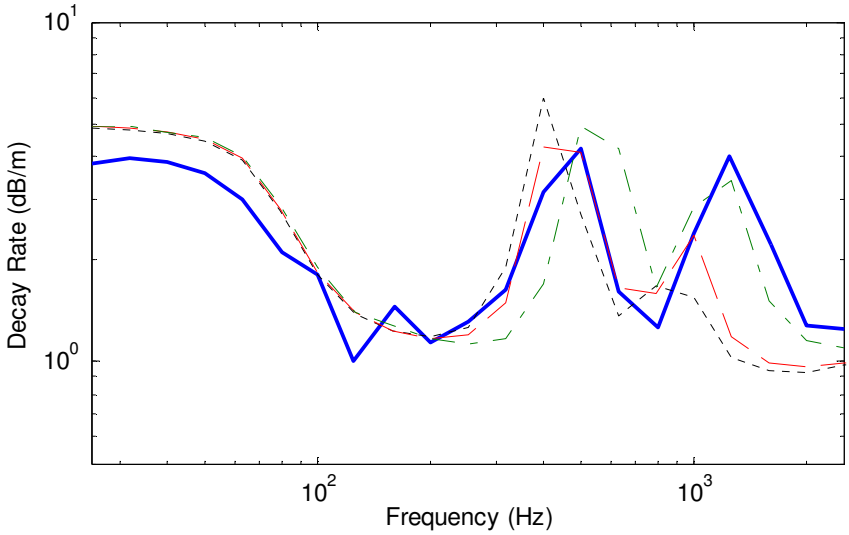

Figure 6.21. Decay rate in the unloaded rail: ——— , measured; - - - - - - - , WFE with railpad stiffness of 80MN/m; – – – – – , WFE with railpad stiffness of 100MN/m; – · – · – · – , WFE with railpad stiffness of 200MN/m.

Figure 6.21 shows a relatively high measured decay rate for the frequency bands up to 63Hz and also in the 500Hz and 1.25kHz bands, typically 4dB/m. In the lower frequency bands, this is due to the strong coupling between the motion of the rail and the viaduct. Around 63Hz, the resonance of the rail on the stiffness of the baseplate occurs and above this frequency the rail is decoupled from the bridge. The measured decay rate of vibration in the rail therefore drops to between 1dB/m and 1.5dB/m. It

is expected that the high rates of decay in the 500Hz and 1.25kHz bands are due to the vertical flapping mode and the bending of the top plate mode respectively, described in Chapter 5.

The decay rates predicted using the WFE model for the three different values of railpad stiffness are similar up to the 315Hz band and in satisfactory agreement with the measurements in these bands. For higher frequencies, the decay rates predicted using the three stiffness values are quite different. The result obtained for a railpad stiffness of 100MN/m, appropriate for a frequency of 500Hz, is in close agreement with the measurement in this part of the frequency range, where the first peak is shown. Similarly, it is the WFE result obtained with the railpad stiffness expected at high frequencies that is in closest agreement with the measurement around the peak in the 1.25kHz band.

The WFE track model can be modified so that the bending motion in the top plate is omitted from the analysis, by setting a very large Young's modulus for the top plate. The track model is then of the spring-mass-spring form used previously in the bridge noise model for this type of track. Figure 6.22 shows the decay rates obtained using this track model in the WFE analysis, together with the previous WFE result (where bending in the top plate is accounted for) and the measured decay rate. Both WFE models were run for the railpad stiffness expected at a frequency of 500Hz.

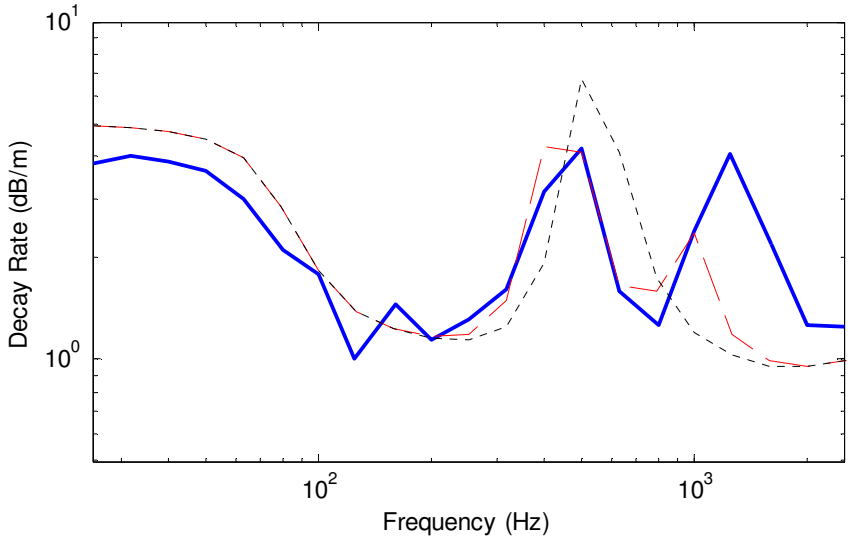

Figure 6.22. Decay rate in the unloaded rail: ——— , measured; – – – – – , WFE with proposed track model; - - - - - - - - , WFE with spring-mass-spring track model.

Figure 6.22 shows that the spring-mass-spring track model can be used to predict the peak centred on the 500Hz band reasonably well, but that the peak in the 1.25kHz band is omitted. This was expected as the spring-mass-spring model does not contain the resonance in this band. The track model proposed here offers a small benefit over the spring-mass-spring model in the prediction of the first peak in the decay rate curve and the ability to account for the second peak if a frequency-dependent railpad stiffness is used in the model.

6.4.4. Vibration of the viaduct under-traffic

Figure 6.23 shows the measured average deck velocity at position P3 on the viaduct deck, together with the spatially-averaged velocity at this position in the cross-section obtained from the WFE analysis using both the constant stiffness track model and the track model proposed in this work. Note that the spatial average of the WFE result has been taken along the length of the structure only and that an equivalent result is not available from NORBERT, because the SEA calculation only gives spatial averages for whole sub-systems.

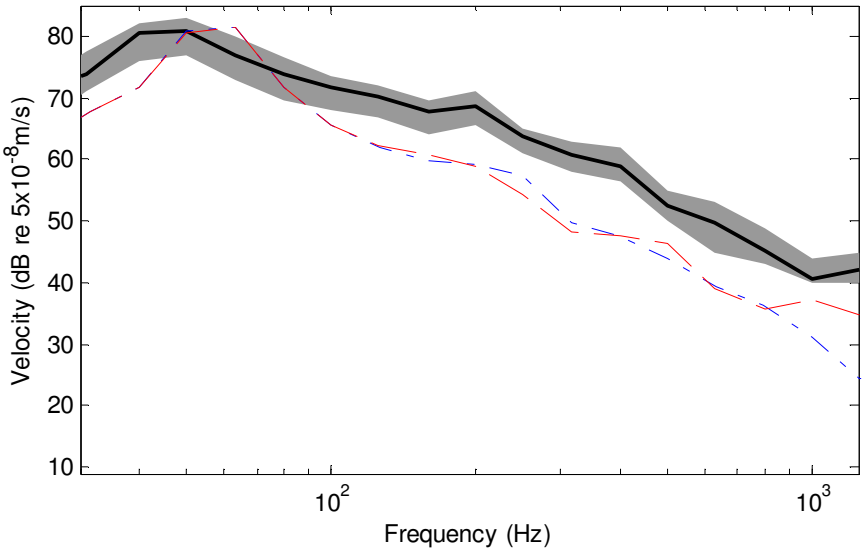

Figure 6.23. Spatially-averaged velocity at position P3 on the deck of the concrete box-section viaduct shown versus frequency: ——— , measured average; ▒ , measured range; – · – · – , WFE result for constant track stiffness; – – – – , WFE result with proposed track model.

The spectra obtained from the WFE analysis have a broadly similar shape to the measurement for the frequency bands above 80Hz, but the deck velocity is under-

predicted throughout this range by typically 6dB, or a factor of 2. The main peak in the measured velocity spectrum occurs at a slightly lower frequency than that in the results of the WFE analysis. The modelling of the resilient wheel is likely to be responsible for a significant part of this difference.

The results obtained using the two different track models in WFE are similar for the frequency bands up to 200Hz. For the higher frequency bands, where the effects of the baseplate resonances are significant, the two WFE results are different. However, that obtained using the proposed track model is only in significantly closer agreement with the measurements in the 1kHz and 1.25kHz frequency bands.

The SEA calculation in NORBERT gives the spatially-averaged velocity in each sub-system. Corresponding results can be found from the WFE analysis, by averaging over all the nodes in each subsystem, but not from the measurements, because of the limited number of measurement positions. The results of the WFE model (with the constant stiffness track model) and NORBERT have therefore been compared here, for selected parts of the structure, shown in Figure 6.24 below.

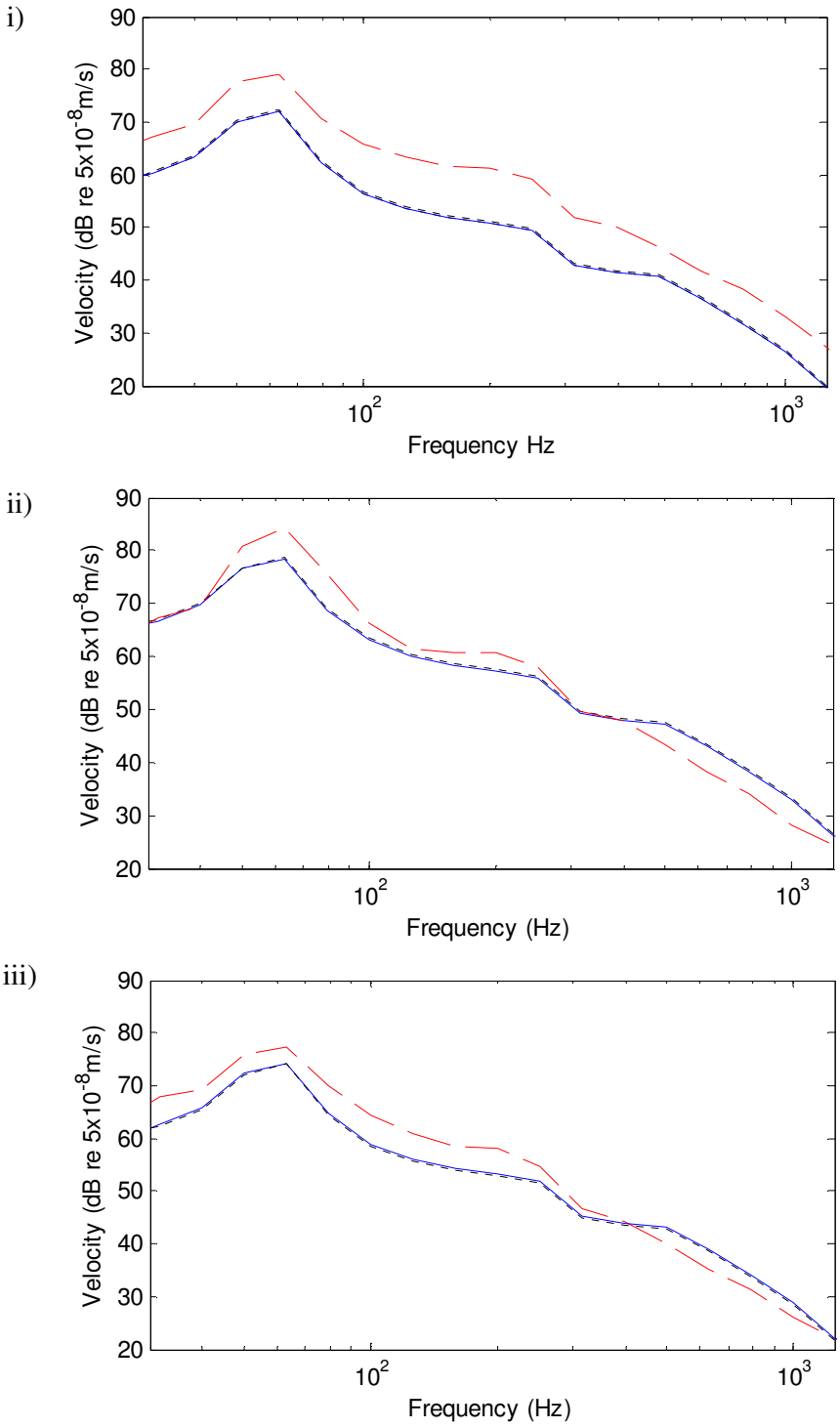

Figure 6.24. Spatially-averaged velocity for three subsystems in the concrete box-section viaduct shown versus frequency, i) main deck, ii) side-deck iii) bottom flange: _ _ _ _ _ , WFE (constant track stiffness); _____ , NORBERT simple SEA model; ..... , NORBERT detailed SEA model.

Figure 6.24 i) shows that the velocity on the main deck given by the WFE analysis is typically 10dB greater than that from the NORBERT models in the frequency bands up to 400Hz, and about 4dB greater in the higher frequency bands. Since the WFE result for deck velocity was shown to be lower than the measurement made on the viaduct deck, NORBERT is therefore in greater error relative to the deck velocity measurement than WFE. Note also that the effect of the two different approaches taken to the SEA modelling in NORBERT is very small over the frequency range shown for the deck, the side-deck and the bottom flange.

It was shown in Figure 6.18 that the structural model in NORBERT underestimates the real part of the point mobility at position P3 by a factor of 2 for frequencies up to about 500Hz, relative to both WFE and the measurements. This accounts for a 3dB difference between the deck velocity under-traffic given by the NORBERT and WFE models in this frequency range. Note that this beam representation of the bridge is used in the calculation for the power input to the bridge based on the mobility of the bridge and also that on the coupled beam model of the rail and bridge. For frequencies greater than about 500Hz, the input point mobility at position P3 in the WFE and NORBERT models is similar. The difference in the deck velocity given by the WFE and NORBERT models in this range is therefore due to the division of the input power between the components of the viaduct in these two different types of model.

There is a significant difference between the results of the WFE and NORBERT models for the velocity of the side-deck and the bottom flange of the box-section. When the lower power input to the bridge in NORBERT for the frequency range up to about 500Hz is accounted for, it is clear that the simplified SEA scheme in NORBERT predicts greater energy transfer from the deck to the components remote from the power input point than the WFE model. This indicates that the assumption of equipartition of energy, on which the simplified SEA scheme in NORBERT is based, does not hold for this structure. The lower energy transmission from the deck to the other viaduct components predicted by the WFE analysis than given by equipartition of energy indicates that the energy dissipation within the subsystems is significant relative to the energy transmitted between them. This is reasonable given the relatively high damping loss factor used to model this structure, 0.1. A more

complex SEA scheme, including coupling loss factors, would be required to account for this behaviour.

6.5. CONCLUSIONS

This chapter presents the most detailed study of a railway bridge structure of all those described in this work. A new set of measurements has been made and this allows particular attention to be paid to characterisation of the vibration response of the bridge structure, free from the influence of the track and the rolling stock. Two of the main areas of uncertainty in modelling this type of structure that were identified in the previous work by Bewes (2006) can therefore be addressed here: the structural model used to predict the power input to the viaduct and the damping level in the structure.

Point mobility measurements were made at four positions on the viaduct deck over a frequency range from 30Hz to 1.2kHz. For a significant part of this frequency range, the viaduct behaves as a reinforced plate for excitation at the rail seat positions. It has been demonstrated that the WFE method is a satisfactory means to predict this complex behaviour. However, the simple structural models in NORBERT underestimate the power input to the viaduct by a factor of about 2 over a significant part of the frequency range of interest. The WFE method has also been shown to predict the transfer response of this viaduct correctly over the frequency range from 100Hz to 1kHz, using a damping loss factor of 0.1.

The vibration under-traffic predicted using the WFE and NORBERT models differ significantly. Further, it is the WFE result that is in closer agreement with the measurements made on the viaduct deck. Part of this difference between the models is due to the lower mobility representation of the bridge in NORBERT for frequencies up to about 500Hz and part is due to the energy sharing between the major components of the structure. There is less energy transfer from the main deck, where the energy input to the viaduct from the track occurs, to other the other components in the structure according to the WFE analysis than the simplified SEA calculation in NORBERT (based on equipartition).

The approach developed in Chapter 5 for modelling the resilient baseplate track used on this viaduct was included in the WFE analysis. The comparison made between the decay rates in the unloaded rail shows that the proposed track model does offer an advantage over the spring-mass-spring approach used previously in NORBERT. This

is expected to have an important effect on the rolling noise prediction for baseplate track (on bridges or otherwise). It is also shown that the frequency dependence of the railpad stiffness is significant in predicting the correct decay rates in the rail.

However, the proposed track model seems to be of limited benefit in modelling vibration of the viaduct under-traffic. The WFE model underestimates the deck vibration in all frequency bands, typically by about 6dB, using both the proposed track model and the constant stiffness track model. The reasons for this difference are unclear. The structural model of the viaduct has been shown to be reliable from comparison to the measurements for point and transfer accelerance. Further, the decay rate analysis for the rail presented in Section 6.4.3 indicates that the track on this viaduct is modelled reasonably well in WFE, albeit for the unloaded rather than the loaded track case. It is therefore likely that the modelling of the excitation at the wheel-rail interface is responsible for a significant part of the difference between the results of the models and the measurements for vibration under-traffic.

The resilient wheels on the DLR rolling stock introduce additional difficulty to modelling the excitation at the wheel-rail interface. While a reasonably complete set of data is available for this wheel, it not known if the simple model of this wheel presented in Section 3.3.1 (Chapter 3) is an adequate means to predict its dynamic behaviour over the frequency range required here. Further, it is expected that the methods available for estimating the wheel-rail roughness levels from rail vibration measurements may not be valid when the rolling stock has resilient wheels. The suitability of the assumed wheel-rail roughness level for modelling this case is therefore unknown.

7. SUMMARY OF CONCLUSIONS AND RECOMMENDATIONS FOR FUTURE WORK

7.1. OVERVIEW

A theoretical model for the prediction of noise from railway bridges is required for use in making environmental impact assessments for new infrastructure projects, to guide noise control programmes for existing bridges and also the design of low-noise bridge and track structures. Such a model, NORBERT, was developed and used for these purposes prior to the start of this EngD project. Some aspects of this model have been identified as worthy of further study, mainly in the work of Bewes (2006). The aim of the work described in this thesis is to test these parts of the NORBERT model further and to develop improved calculation methods where required.

An advanced finite element (FE) analysis technique was used in much of this work, Wavenumber Finite Elements (WFE), in order to calculate the power flow from the rail to the bridge structure and to calculate the vibration response of the bridge. The method assumes an infinite 'extruded' geometry of the bridge. For bridges that have geometry of this kind, WFE represents a more computationally efficient modelling approach than conventional FE methods. WFE is particularly useful in that the behaviour of the structure can be understood in terms of its propagating wave modes.

A total of five major issues were addressed and the findings of the work for each of these are summarised in Sections 7.2 to 7.6 below. Recommendations for future work are made in Section 7.7.

7.2. MOBILITY MODEL FOR STEEL BRIDGES

The NORBERT model for mobility is based on expressions for the mobility of idealised bridge components; a beam and a plate. A switch between the beam and plate models is made for bridges where the track supports are not positioned directly over the longitudinal beams. However, this was found to be an over-simplification which leads to step changes in the bridge response at certain frequencies for some bridges.

Three different models were used to study the mobility of a coupled beam and plate, intended to represent a steel bridge. All these models show that a transition is required between the mobility of the beam and that of the plate as the input force is

moved away from the support beam. An empirical means to predict this transition was found by fitting to the results of one of the models for the coupled beam and plate, that based on the WFE method. It has been demonstrated that this empirical transition offers a clear improvement over the switch mobility model for mobility.

In the frequency range where the motion of the rail and the bridge is well-coupled, the input power to the bridge is found in NORBERT using the coupled beam model, rather than from the mobility of the bridge. The empirical transition proposed in this work is not compatible with the coupled beam model, which requires that the bridge is modelled as a beam. The modelling work presented in Chapter 2 indicates that the transition between beam and plate behaviour may occur for typical steel bridges over a significant part of the frequency range in which the motion of the rail and the bridge is well-coupled. A more complex model for the rail, track support structure and the bridge than that in NORBERT would be required in order to account for a transition between beam and plate behaviour of the bridge in these cases.

7.3. MODELLING THE VIBRATION RESPONSE OF CONCRETE-STEEL COMPOSITE BRIDGES

The behaviour of concrete-steel composite bridges is quite different from that of steel bridges. The type of mobility model used for steel bridges is not applicable to composite bridges because the mobility of the deck is normally comparable to the mobility of the support beam in a composite bridge. Further, the simplified SEA scheme in NORBERT is not valid for a composite bridge (Janssens and Thompson, 1996). The WFE method was used study these two issues in modelling the vibration response of composite bridges.

A WFE analysis of the composite bridge on the DLR was used to show that the response of this type of bridge is that of a reinforced plate over a significant part of the frequency range of interest. The simple structural models in NORBERT are therefore not readily applicable to this type of bridge and nor is the empirical transition developed for steel bridges. The power input to the bridge and the vibration response under-traffic were calculated from a WFE model of the rail, the track support structure and the bridge. It was found that the approach recommended by Bewes (2006) for modelling composite bridges using NORBERT leads to an overestimate for the power input to the bridge in the frequency range up to about

300Hz. This is due to the difficulty in using the simple structural models in NORBERT for this type of bridge.

The two simplified SEA schemes proposed by Bewes (2006) for modelling composite bridges in NORBERT predict different energy sharing between the major components of the bridge than the WFE model for frequencies up to about 800Hz. The results of the WFE model for vibration under-traffic are in slightly closer agreement with the measurements made by Bewes (2006) for the DLR composite bridge than the NORBERT results obtained using the preferred simplified SEA scheme for composite bridges, that with the deck as the primary SEA network. However, the under-prediction of the response in the 800Hz frequency band and above remains.

7.4. THE DYNAMIC BEHAVIOUR OF RAILWAY BALLAST

The dynamic behaviour of railway ballast has been studied through a programme of measurements and modelling work, that addresses the need for a means to model ballasted track on bridges that is supported by measurement data. A model based on longitudinal wave motion in a prismatic rod of ballast loaded in compression by the sleeper has been shown to predict the dynamic transfer stiffness of a 300mm or 450mm deep layer of ballast for frequencies up to approximately 600Hz, the maximum measurement frequency. It is expected that the model can be used up to higher frequencies. The case of a ballast layer on a bridge with a resilient liner was found to be more difficult to model. The rod model for the ballast combined in series with a simple stiffness element for the liner was shown to be in reasonable agreement with the measurements up to about 350Hz.

The damping loss factor for the ballast was estimated from the phase of the measured transfer stiffness at low frequencies where the ballast acts as a simple stiffness and at higher frequencies by comparing the first peak in the measured transfer stiffness spectrum with that predicted using the rod model. The ballast is more heavily damped in the higher frequency range, consistent with previous work for the damping in granular materials, (Richards and Lenzi, 1984) and (Kuhl and Kaiser, 1952). For modelling the damping in ballasted track on bridges, it is recommended that a damping loss factor of 0.1 to 0.2 is used for the frequency range in which the ballast behaves as a simple stiffness beneath the sleeper. In the frequency range where the

internal mode effects of the ballast layer are significant, a damping loss factor of about 0.45 should be used.

The measurements made for a sample of ballast at the end of its service life are not expected to be representative of that for ballast in railway track, due to the loss of the fine material during removal of the ballast from the track and subsequent handling.

The dynamic properties of ballast found in this work do not explain the lower noise levels reported in some previous work for bridges with ballasted track than for bridges with direct fasteners. It is likely therefore that the dynamic loading of the deck plates by a layer of ballast provides at least some of the measured effect.

7.5. THE DYNAMIC BEHAVIOUR OF A TWO-STAGE RESILIENT BASEPLATE

The high-frequency dynamic behaviour of a two-stage resilient baseplate is not well-known. A combined measurement and FE modelling study has therefore been conducted for a Pandrol VIPA-SP baseplate rail fastener. It is shown that beam-bending motion in the top plate has an important effect on the dynamic stiffness of this baseplate. A simple FE model has been developed, which accounts for the effects of bending in the top plate on the direct and transfer stiffness. Measurements for the direct stiffness of a VIPA-SP baseplate loaded with a short section of rail show that this simple FE model is a more accurate means to predict the behaviour of this baseplate than the spring-mass-spring model used previously in NORBERT. It is expected that the simple FE model is applicable to other types of two-stage resilient baseplate.

7.6. MODELLING THE VIBRATION RESPONSE OF A CONCRETE BOX-SECTION VIADUCT

A new set of measurements were made in this work on a concrete box-section viaduct on the DLR, with a particular emphasis on characterising the vibration response of the bridge structure. It is shown that the WFE method is a suitable means to predict the point response on the viaduct deck, by comparison with the measurements. The response of this viaduct at the rail seat positions is that of a reinforced plate over much of the frequency range of interest. As for the concrete-steel composite bridge, this behaviour cannot be accounted for satisfactorily using the simple structural models in NORBERT. The WFE method has also been shown to predict the transfer

response of this viaduct correctly over the frequency range from about 100Hz to 1kHz, for a damping loss factor of 0.1.

The use of the simple structural models in NORBERT for the concrete box-section viaduct introduces a significant error to the calculation for the power input to the viaduct. This is responsible for part of the difference shown between the vibration under-traffic predicted using the WFE and NORBERT models. The WFE method also predicts different energy sharing between the major components of the structure than the simplified SEA scheme in NORBERT. While the WFE result for the velocity on the viaduct deck under-traffic is typically a factor of two smaller than the measurement, the NORBERT result is in significantly greater error relative to the measurement.

The measurements made on the concrete box-section viaduct have been used as a further basis for evaluating the approach proposed for modelling two-stage resilient baseplate rail fasteners. This was incorporated in the WFE model of the rail, track support structure and the concrete box-section viaduct. It is shown that the decay rates in the rail obtained using the proposed track model are in closer agreement with the measurements than those given by the spring-mass-spring model used for this track form in previous NORBERT modelling work. This is expected to have an important effect on the rolling noise prediction for baseplate track. However, the inclusion of bending motion in the top plate in the WFE model has only a small effect on the predicted viaduct vibration.

7.7. RECOMMENDATIONS FOR FUTURE WORK

7.7.1. Recommendations for bridge modelling

A WFE model of the rail, the track and the bridge offers some important advantages over NORBERT in modelling concrete-steel composite and concrete box-section bridges in which the cross-section properties are constant along the span length. It is therefore recommended that the WFE approach is used to model these types of bridge structure in future work. It is expected that a plate element WFE model is suitable for bridges over the frequency range of interest in bridge noise, unless they have unusually large thickness concrete construction. A WFE calculation for bridge vibration under-traffic typically takes 2 to 3 hours to run, such that it is suitable for use as a design tool.

WFE should also be considered for use in modelling steel bridges in which the longitudinal support beams are offset from the track supports. The empirical transition model for mobility proposed in this work for use in NORBERT is applicable only to the frequency range where the motion of the bridge is decoupled from that of the rail. A WFE model should be used in cases where the transition between beam and plate behaviour needs to be accounted for in the frequency range below the decoupling frequency.

Steel bridges with track supports that are positioned directly over the longitudinal support beams have not been studied in this work. However, it is expected that NORBERT is the most suitable means to model these bridges. NORBERT should also be used for bridges that do not have constant cross-section properties along the span length.

The models developed in this work for ballasted track and two-stage resilient baseplate track should be used in future bridge modelling work, in NORBERT or in a WFE model as appropriate. The input data obtained in this work for the ballast model can be used in future work to model ballast layers of similar specification. For the resilient baseplates, it is expected that the input data presented in this work is applicable only to Pandrol VIPA-SP baseplates. Specific input data for the dimensions of the top plate and the stiffness of the pads would be required in order to apply this model to a different type of baseplate.

7.7.2. Recommendations for research work

It is recommended here that a major part of future work for the development of bridge noise and vibration models should be the acquisition of comprehensive sets of measurement data to be used for further validation of the two models used in this work, NORBERT and WFE. Ideally, measurements would be made for the vibration of all the major components of the structure under-traffic, the point and transfer response on the bridge deck and the wheel and rail roughness levels. Practically, such a measurement campaign would be difficult to arrange (or fund) and therefore only part of this measurement data was available during the present work. However, it may be possible to obtain more complete sets of data in the future, for a range of different types of bridge.

Rail roughness measurements can be made for a range of wavelengths appropriate to modelling bridge noise using a portable trolley fitted with an accelerometer, see Thompson (2009) for details. One of the important sources of uncertainty in the modelling work for vibration under-traffic can therefore be eliminated, but at the significant cost of hiring this specialist equipment. It may also be possible to make measurements for the vibration under-traffic of all the major components of a bridge in the future. This could be used to test the division of the input power amongst the major components of the bridge in the models.

The modelling of the resilient wheels on the DLR rolling stock is a further source of uncertainty in the modelling work presented here. In the absence of suitable measurement data, it is not clear how adequately the simple model of a resilient wheel used in this work represents its dynamic behaviour. Rolling stock with resilient wheels is widely-used on light urban railways, which represent an important application for the bridge models, because they usually include elevated sections of track and are often in noise-sensitive areas. It is therefore recommended here that the dynamic behaviour of resilient wheels should be studied in future work.

A useful extension could be made to the ballast stiffness measurements made in this work if the case of ballast at a late stage of its service life, including the fine material produced by wear action, could be tested in some way. It is recommended here that point response measurements are made on sleepers in ballasted track, for ballast at various stages of its life, such that the effect of wear on the stiffness of the ballast can be quantified. Measurements of this kind would only provide information on the direct stiffness of the ballast at low frequencies, but this may be sufficient to determine how the transfer stiffness results obtained in this work for new ballast should be adjusted for the effects of wear.

It is recommended here that the next step in the development of modelling approaches for bridges with ballasted track should be to quantify the effect of the dynamic loading of the deck plates by a layer of ballast on their vibration response. It is expected that this effect is significant, particularly for a steel bridge, and that it may explain the lower noise levels reported in previous work for bridges with ballasted track than those with directly-fastened track. It is recommended here that this is studied experimentally, rather than through FE or other modelling work. This is

because a modelling study would require detailed material property data for the ballast and this is not available.

While it is expected that the WFE models for the concrete-steel composite bridge and the concrete box-section viaduct represent reasonably complete models of these structures, there may be scope to develop improved models using existing structural modelling methods. For example, it is possible to perform a WFE analysis for a finite length representation of the bridge structure with idealised boundary conditions, rather than for an infinite length structure representation. The modes of the bridge span could then be included in the analysis. The point and transfer response measurements made on the concrete box-section viaduct in this work indicate that the effects of these modes are relatively small. However, for bridges with shorter spans, or with lower damping, the benefits of a finite length bridge model may be significant. In addition to WFE analysis of finite length structures, it may also be useful to apply advanced structural modelling methods based on periodic structure theory to bridges. Specifically, this type of model may be appropriate for studying the effect of cross-beams on the vibration response of a bridge.

8. REFERENCES

Al Shaer, A., Duhamel, D., Sab, K., Foret, G. and Schmitt, L. 2008. *Journal of Sound and Vibration*, **316**, 211-233. Experimental Settlement and Dynamic Behaviour of a Portion of Ballasted Railway Track Under High Speed Trains.

Ban, Y. and Miyamoto, T. 1975. *Journal of Sound and Vibration*, **43**, 273-280. Noise Control of High-Speed Railways.

Behr, W. 2005. *Proceedings of the 5th International Conference on Computation of Shell and Spatial Structures, Salzburg*. Calculation of the Sound Radiation of a Railway Bridge.

Benham, P.P. and Crawford, R.J. 1987. *Mechanics of Engineering Materials*. Pearson Education Limited.

Beranek, L.L. and Ver, I.L. 1992. *Noise and Vibration Control Engineering*. John Wiley and Sons, New York.

Bewes, O. 2006. *Engineering Doctorate Thesis*, University of Southampton. The Calculation of Noise from Railway Bridges and Viaducts.

Brennan, M.J. and Ferguson, N.S. 2004. *Vibration Control*, in Advanced Applications in Acoustics, Noise and Vibration. Fahy, F.J. and Walker, J.G. (eds). Spon Press, London.

British Standard BS EN 13450. 2002. *Aggregates for Railway Ballast.*

Burrow, M.P.N., Chan, A. H. C. and Shein, A. 2008. *Proceedings of the Institution of Civil Engineers – Geotechnical Engineering*, **160**, 169-177. Deflectometer-Based Analysis of Ballasted Railway Tracks.

Calculation of Railway Noise. 1995. *Department of Transport*. HMSO, London.

Carlone, L. and Thompson, D.J. 2001. *ISVR Technical Memorandum*, 873. Vibrations of a Rail Coupled to a Foundation Beam through a Series of Discrete Elastic Supports.

Chebli, H., Clouteau, D. and Schmitt, L. 2008. *Soil Dynamics and Earthquake Engineering*, **28**, 118-131. Dynamic Response of High-Speed Ballasted Railway Tracks: 3D Periodic Model and In-Situ-Measurements.

Cobbing, C. and Jones, C.J.C. 2007. *Proceedings of the 9th International Workshop on Railway Noise, Munich* (eds Schulte-Werning et al.), Springer, 179 – 185, Minimising Noise from Viaducts in the Borough area of London for the Thameslink Programme.

Cremer, L., Heckl, M., Ungar, E.E. 1988. *Structure-Borne Sound.* Springer Verlag, 2nd Edition.

Crockett, A.R. and Pyke, J.R. 2000. *Journal of Sound and Vibration,* ***293,*** 883-897. Viaduct Design for Minimization of Direct and Structure-Radiated Train Noise.

Dings, P.C. and Dittrich, M.G. 1996. *Journal of Sound and Vibration,* **193**, 103-112. Roughness on Dutch Railway Wheels and Rails.

Directive 2001/16/EC on the Interoperability of the Trans-European Conventional Rail System. 2001. The European Parliament and Council. *Official Journal of the European Communities*, **L110**.

Directive 2002/49/EC Relating to the Assessment and Management of Environmental Noise. 2002. The European Parliament and Council. *Official Journal of the European Communities*, **L189**/12.

Esveld, C. 1989. *Modern Railway Track.* MRT Productions.

Ewins, D. J. 2000. *Modal Testing: Theory and Practice II*, Research Studies Press Ltd.

European Environment Agency. 2009. *EEA Report* No. 3/2009. Transport at a Cross-Roads.

Future Noise Policy, 1996, EU Green Paper (COM(96) 540), available from: http://ec.europa.eu/environment/noise/greenpap.htm (accessed 31st August 2009).

Fields, J.M. and Walker, J.G. 1982. *Journal of Sound and Vibration,* **81**(1), 51-80. Comparing the Relationships Between Noise Level and Annoyance in Different Surveys: A Railway Noise vs. Aircraft and Road Traffic Comparison.

Fitzgerald, B.M. 1996. *Journal of Sound and Vibration,* **193**(1), 377-385. The Development and Implementation of Noise Control Measures on an Urban Railway.

Gavric, L. 1994. *Journal of Sound and Vibration.* **173**(1), 113-124. Finite Element Computation of Dispersion Properties of Thin-Walled Waveguides.

Grassie, S.L., Gregory, R.W., Harrison, D. and Johnson, K.L. 1982. *Journal of Mechanical Engineering Science,* **24**(2), 77-90. The Dynamic Response of Railway Track to High Frequency Vertical Excitation.

Hanel, J.J. and Seeger, T. 1978. Der Stahlbrau, **47** (12), 353-361. Schalldämpfungsgrossversuch an Zwei Stählemen Eisenbahn-Hohlkastenbrüken (Full Scale Tests of Sound Damping on Two Steel Railway Box Girder Bridges).

Hardy, A.E.J. 1997 *Report RR-SPS-97-012 of AEAT Rail Ltd.* Draft Proposal for Noise Measurement Standard for ERRI Committee C163. Published through European Rail Research Institute.

Hardy, A.E.J. 1999. *Proc. Inst. Mech. Eng., Part F,* **213** (3)**,** 161-172. Noise from Railway Bridges.

Harrison, M.F., Thompson, D.J. and Jones, C.J.C. 2000. *Proc. Inst. Mech. Eng., Part F,* **214** (3), 125-134. The Calculation of Noise from Railway Viaducts and Bridges.

Herron, D.C. 2008. *Pandrol Report 85114-32*. Bridge Noise Study and Rail Fastener Selection - Basarab Bridge, Bucharest.

Janssens, M.H.A. and Thompson, D.J. 1996. *Journal of Sound and Vibration,* **193**(1), 295-305. A Calculation Model for the Noise from Steel Railway Bridges.

Japanese National Railways. 1973. *Shinkansen noise.*

Japanese National Railways. 1975. *Shinkansen noise – Report II,* (Supplement).

Jones, C.J.C. and Thompson, D.J. 2003. *Journal of Sound and Vibration,* **267**(3), 509 – 522. Extended Validation of a Theoretical Model for Railway Rolling Noise using Novel Wheel and Track Designs.

Jones, C.J.C., Thompson, D.J. and Diehl, R.J. 2006. *Journal of Sound and Vibration,* **293**(1), 475-484. The Use of Decay rates to Analyse the Performance of Railway Track in Rolling Noise Generation.

Kaewunruen, S. and Remennikov, A.M. 2007. *Proc. Inst. of Mech. Engrs., Part F: J.Rail and Rapid Transport,* **221**, 495-507. Investigation of Free Vibrations of Voided Concrete Sleepers in Railway Track System.

Karassalo, I. 1994. *Journal of Sound and Vibration*. **172**(5), 671-688. Exact Finite Elements for Wave Propagation in Range-Independent Fluid-Solid Media.

Kong, F.K. and Evans, R.H. 1982. *Reinforced and Pre-Stressed Concrete*. Spon Press.

Kruse, H. and Popp, K. 2003. *Lecture Notes in Applied Mechanics Vol. 6 - System Dynamics and Long-Term Behaviour of Railway Vehciles, Track and Subgrade*, 275-294, Springer.

Kuhl, W. and Kaiser, H. 1952. *Acustica*. **2**, 179 - 188. Absorption of Structure-Borne Noise Sound in Building Materials Without and With Sand-Filled Cavities.

Kurzweil, L.G. 1977. *Journal of Sound and Vibration,* **51**, 419 – 439. Prediction and Control of Noise from Railway Bridges and Tracked Transit Elevated structures.

Lyon, R.H. 1975. *Statistical Energy Analysis of Dynamical Systems: Theory and Applications*. The MIT Press, Cambridge, Massachusetts.

Lyon, R.H. and Dejong, R.G. 1995. *Theory and Application of Statistical Energy Analysis*, 2nd edition. Butterworth-Heinemann.

Mead, D.J. 1998. *Passive Vibration Control*. John Wiley and Sons.

Miedema, H.M.E. and Vos, H. 1998. *Journal of the Acoustical Society of America* **104**, 3432-3445. Exposure-Response Relationships for Transportation Noise.

Morrison, C., Wang, A. and Bewes, O. 2005. *Journal of Low Frequency Noise, Vibration and Active Control*, **24**(2), 107-116. Methods for Measuring the Dynamic Stiffness of Resilient Rail Fastenings for Low Frequency Vibration Isolation of Railways, Their Problems and Possible Solutions.

Nilsson, C-M. 2004. *Doctoral Thesis*, KTH, Stockholm. Waveguide Finite Elements Applied on a Car Tyre.

Oderbrant , T. 1996. *Journal of Sound and Vibration*, **193**(1), 227-233. Noise from Steel Railway Bridges: A Systematic Investigation Method for Sound Reduction.

ORE 1966 Report No. D105/RP1. *Noise Abatement on Bridges: Noise Developments in Steel Railway Bridges.*

ORE 1971 Report No. D105/RP3. *Noise Abatement on Bridges: Final Report.*

Ouelaa, N., Rezaiguia, A. and Laulagnet, B. 2005. *Applied Acoustics*, **67**, 461-475. Vibro-Acoustic Modelling of a Railway Bridge Crossed by a Train.

Petyt, M., 1990. *Introduction to Finite Element Vibration Analysis*, Cambridge University Press.

Poisson, F. and Margiocchi, F. 2006. *Journal of Sound and Vibration*, **51**(3), 944-952. The Use of Dynamic Dampers on the Rail to Reduce the Noise of Steel Railway Bridges.

Remington, P.J. and Wittig, L.E. 1985. *Journal of the Acoustical Society of America*, **78**(6), 2017-2033. Prediction of the Effectiveness of Noise Control Treatments in Urban Rail Elevated Structures.

Remington, P.J. and Wittig, L.E. 1987. *Journal of the Acoutiscal Society of America*, **81**, 1805-1823. Wheel/Rail Rolling Noise, I: Theoretical Analysis.

Richards , E.J., and Lenzi, A. 1984. *Journal of Sound and Vibration*, **97**(4), 549-586, On the Prediction of Impact Noise, VII: The Structural Damping of Machinery.

Sahin, M.A. and Indraratna, B. 2006. *Can. Geotech. J.* **43**, 1144-1152. Modelling the Mechanical Behaviour of Railway Ballast using Artificial Neural Networks.

Saussine, G., Cholet, C., Gautier, P.E, Dubois, F., Bohatier, C. and Moreau, J.J. 2006. *Comput. Methods Appl. Engrg, **195**, 2841-2859*. Modelling Ballast Behaviour Under Dynamic Loading. Part 1: a 2D Polygonal Discrete Element Method Approach.

Shield, B., Roberts, J. and Vuillermoz, M. 1989. *Applied Acoustics*, **26**, 305-315. Noise on the Docklands Light Railway.

Skurdrzyk, E. 1980. *Journal of the Acoustical Society of America, **67**, 1105-1135.* The Mean-Value Method of Predicting the Dynamic Response of Complex Vibrators.

Snowdon, J.C. 1963. *Vibration and Shock in Damped Mechanical Systems*, John Wiley and Sons Inc., New York.

Thompson, D.J. 1992. *TNO Report*, TPD-HAG-RPT-92-0069. An Analytical Model for the Vibration Isolation for a Rail Mounted on a Bridge.

Thompson, D.J. 1993. *Journal of Sound and Vibration*, **161**, 387-400. Wheel-Rail Noise Generation, Part I: Introduction and Interaction Model.

Thompson, D.J., Hemsworth, B and Vincent, N. 1996. *Journal of Sound and Vibration*, **193**(1), 123-135. Experimental Validation of the TWINS Prediction Program for Rolling Noise, Part 1: Description of the Model and Method.

Thompson, D.J., Fodiman, P. and Mahe, H. 1996. *Journal of Sound and Vibration*, **193**(1), 137-147. Experimental Validation of the TWINS Prediction Program for Rolling Noise, Part 2: Results.

Thompson, D.J. and Verheij, J.W. 1997. *Applied Acoustics*. vol. **52**, 1-17. The Dynamic Behaviour of Rail Fasteners at High Frequencies.

Thompson, D.J., van Vliet W.J. and Verheij, J.W. 1998. *Journal of Sound and Vibration*, **213**(1), 169-188. Developments of the Indirect Method for Measuring the High Frequency Dynamic Stiffness of Resilient Elements.

Thompson, D.J. and Jones, C.J.C. 2000. *Journal of Sound and Vibration*, **231**(3), 519-536. A Review of the Modelling of Wheel-Rail Noise Generation.

Thompson, D.J., Jones, C.J.C., Bewes, O.G. 2005. *ISVR Contract Report*, CR 05.12. NORBERT – Software for Predicting the Noise of Railway Bridges and Elevated Structures. Version 2.0.

Thompson, D.J. 2009. *Railway Noise and Vibration – Mechanisms, Modelling and Means of Control.* Elsevier Ltd.

Transport and Works Act. 1992, HMSO, London.

Vincent, N., Bouvet, P., Thompson, D.J. and Gautier, P.E. 1996. *Journal of Sound and Vibration*, **193**(1), 161-171. Theoretical Optimisation of Track Components to Reduce Rolling Noise.

Walker, J. G., Ferguson, N.S and Smith, M.G. 1996. *Journal of Sound and Vibration*, **193**(1), 307-314. An Investigation of Noise from Trains on Bridges.

Wang, A., Cox, S.J., Gosling, D. and Prudhoe, J.E.W. 2000. *Journal of Sound and Vibration*, **231**(3), 907-911. Railway Bridge Noise Control With Resilient Baseplates.

Wang, A., Bewes, O.J., Cox, S.J. and Jones, C.J.C. 2007. *9th International Workshop on Railway Noise*. Measurement and Modelling of Noise from the Arsta Bridge in Stockholm. Proceedings of the 9th International Workshop on Railway Noise, Munich, 4 - 8 Sept. 2007, (Eds Schulte-Werning *et al.*), Springer, Berlin,

Wu, T.X. and Thompson, D.J. 2000. *Acta Acustica united with Acustica*, **86** (2), 313-321. The Influence of Random Sleeper Spacing and Ballast Stiffness on the Vibration Behaviour of Railway Track.

Yoo, J.W., Thompson, D.J. and Ferguson, N.S. 2004. *ISVR Memorandum* No: **944**. Structural Analysis of a Four-Beam and Plate Coupled Structure using a Modal Method and an Approximate Wave Method.

Zhai , W.M., Wang, K.Y. and Lin, J.H. 2004. *Journal of Sound and Vibration* , **270**, 673-683. Modelling and Experiment of Railway Ballast Vibrations.

APPENDIX A – ANALYTICAL MODEL FOR THE RESPONSE OF AN INFINITE PLATE AND BEAM

A.1. INTRODUCTION

Yoo (2004) developed a model for the response of an infinite beam coupled to a plate of infinite length, but finite width. A very similar approach can be used to model a plate that is of infinite width and length, coupled to an infinite beam. This is described here and has been used in Section 2.3 of the thesis.

The cross-section of the infinite plate and beam system is shown in Figure A.1 below, together with the waves expected in the structure.

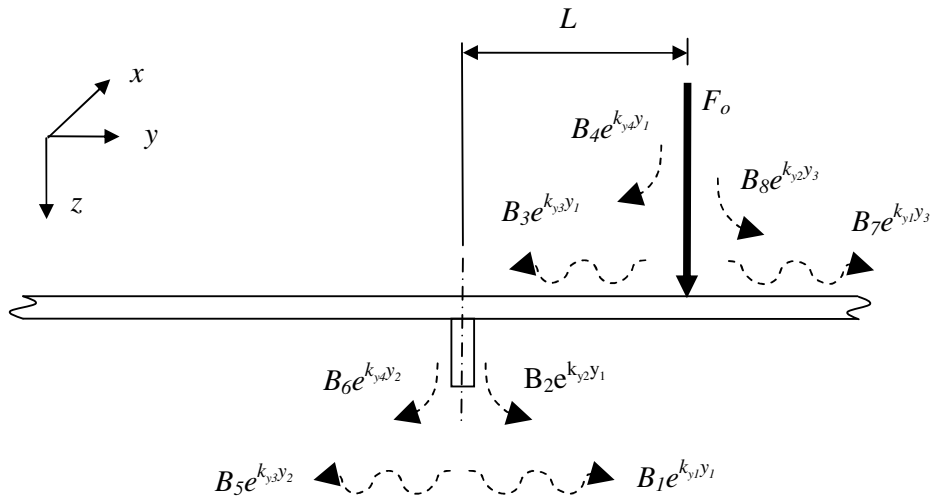

Figure A.1. Infinite beam and infinite plate system shown in cross-section together with the expected waves.

Figure A.1 shows an external point force of magnitude F_o applied to the plate, at a lateral distance L from the beam. Harmonic forcing and motion of the structure are assumed at a frequency ω. Eight waves are shown by a symbol that indicates either a propagating or a near-field wave is expected. The time dependency terms, $e^{i\omega t}$, have been omitted from both the waves and the external forcing term in Figure A.1. The structure will be considered in three sections, where a local coordinate system is used for each section as follows.

Section P1, for $0 < y < L$. Local coordinate is y_1, where $y_1 = y$.

Section P2, for $-\infty < y < 0$. Local coordinate is y_2, where $y_2 = y$.

Section P3, for $L < y < \infty$. Local coordinate is y_3, where $y_3 = y - L$.

Figure A.2 shows the structure divided into these sections, so that the internal shear forces per unit distance in the x direction (f), acting between the sections, can be idntified.

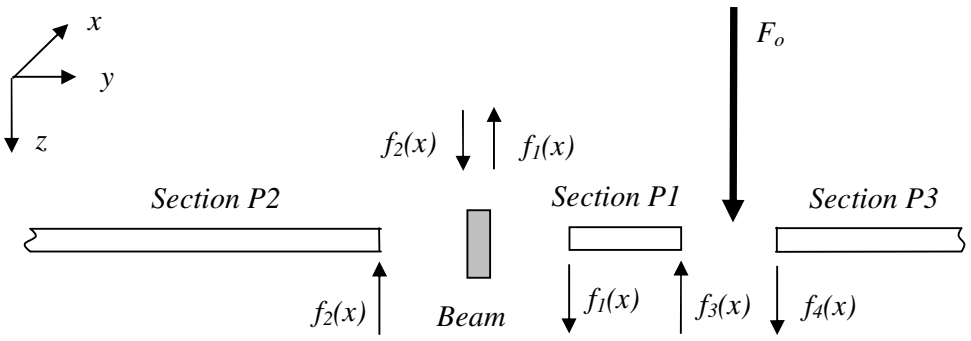

Figure A.2. Infinite beam and infinite plate system shown divided into three sections.

The external point force applied at location $x = x_0, y = L$ can be represented in the spatial domain using the delta function as $F_0\delta(x - x_0)\delta(y - L)$.

No external force is shown applied to the beam in Figure A.2, it is only the shear forces in the plate that excite the beam. Assuming that the beam behaves as an Euler beam, its equation of motion is given by,

$$D_b \frac{d^4 w_b(x)}{dx^4} - m'_b \omega^2 w_b(x) = f_2(x) - f_1(x) \tag{A.1}$$

where D_b is the flexural rigidity of the beam, m'_b is the mass per unit length of the beam and $w_b(x)$ is the vertical (z direction) displacement of the beam. A Fourier transform can be applied to find the displacement of the beam in wavenumber domain as follows,

$$W_b(\kappa_x) = \int_{-\infty}^{\infty} w_b(x) e^{-i\kappa_x x} dx \tag{A.2}$$

The spatial derivatives of the displacement and the shear forces in the plate can be transformed in a similar manner. For example, the first spatial derivative of the displacement is transformed as follows,

$$\int_{-\infty}^{\infty} \frac{dw_b(x)}{dx} e^{-i\kappa_x x} dx = i\kappa_x W_b(\kappa_x) \tag{A.3}$$

Equation (A.1) can therefore be expressed in the wavenumber domain as,

$$D_b \kappa_x{}^4 W_b(\kappa_x) - m'_b\, \omega^2 W_b(\kappa_x) = f_2(\kappa_x) - f_1(\kappa_x) \tag{A.4}$$

The equation of motion for the thin plate, if it was free from both the applied external force and the forces applied by the beam would be given by,

$$D_p\left(\frac{\partial^4 w_p(x,y)}{\partial x} + 2\frac{\partial^4 w_p(x,y)}{\partial x^2 \partial y^2} + \frac{\partial w_p(x,y)}{\partial y^4}\right) - m_p{}''\omega^2 w_p(x,y) = 0 \tag{A.5}$$

where D_p is the flexural rigidity of the plate, m''_p is the mass per unit area of the plate and $w_p(x)$ is the out-of-plane displacement of the plate. This can be expressed in the wavenumber domain by using Fourier transforms,

$$D_p\left(\kappa_x^4 W_p(\kappa_x, y) - 2\kappa_x^2 \frac{\partial^2 W_p(\kappa_x, y)}{\partial y^2} + \frac{\partial^4 W_p(\kappa_x, y)}{\partial y^4}\right) - m_p{}''\omega^2 W_p(\kappa_x, y) = 0 \tag{A.6}$$

For harmonic motion, a solution for the displacement of the plate in equation (A.6) would be expected of the form,

$$W_p(\kappa_x, y) = Be^{k_y y} \tag{A.7}$$

Substituting equation (A.7) into (A.6),

$$D_p\left(\kappa_x^4 Be^{k_y y} - 2\kappa_x^2 k_y^2 Be^{k_y y} + k_y^4 Be^{k_y y}\right) - m_p{}''\omega^2 Be^{k_y y} = 0 \tag{A.8}$$

$$\therefore \left(\kappa_x^4 - 2\kappa_x^2 k_y^2 + k_y^4\right) - \frac{m_p{}''\omega^2}{D_p} = 0 \tag{A.9}$$

where $\sqrt[4]{\frac{m_p{}''\omega^2}{D_p}} = \kappa_p$ is the free plate wavenumber. k_y and κ_x can be related to the free plate wavenumber as follows,

$$\left(\kappa_x^4 - 2\kappa_x^2 k_y^2 + k_y^4\right) - \kappa_p^4 = 0 \tag{A.10}$$

$$\left(\kappa_x^2 - k_y^2\right) = \pm\kappa_p{}^2 \tag{A.11}$$

Solutions for k_y can be found from equation (A.11). Waves travelling in the positive *y* direction, should have a negative real part wavenumber, the negative square root is therefore taken for these waves. The '$\pm$' signs in equations (A.11) provide two negative-real part solutions,

$$k_y = -\sqrt{\kappa_x^2 - \kappa_p^2} = k_{y1} \tag{A.12}$$

$$k_y = -\sqrt{\kappa_x^2 + \kappa_p^2} = k_{y2} \tag{A.13}$$

For $\left|\kappa_x^2\right| < \left|\kappa_p^2\right|$, the solution for k_{y1} from equation (A.12) will mean that equation (A.5) for the displacement of the plate takes the form of a complex exponential, representative of a propagating wave. For $\left|\kappa_x^2\right| < \left|\kappa_p^2\right|$, the solution for k_{y2} from equation (A.13) will mean that equation (A.5) for the displacement of the plate takes the form of an exponential decay function, representative of a near-field wave. For $\left|\kappa_x^2\right| > \left|\kappa_p^2\right|$, the solutions for both k_{y1} and k_{y2} will represent near-field waves.

For waves travelling in the negative *y* direction, positive wavenumbers are required and the positive square root is therefore taken,

$$k_y = \sqrt{\kappa_x^2 - \kappa_p^2} = k_{y3} \tag{A.14}$$

$$k_y = \sqrt{\kappa_x^2 + \kappa_p^2} = k_{y4} \tag{A.15}$$

k_{y3} gives rise to a propagating wave if $\left|\kappa_x^2\right| < \left|\kappa_p^2\right|$ and k_{y4} is associated with a near-field wave under this condition. For $\left|\kappa_x^2\right| > \left|\kappa_p^2\right|$ both k_{y3} and k_{y4} will be associated with near-field waves.

The displacement of each section of the plate can now be considered, using the local coordinate system defined above. For section P1,

$$W_{p1}(\kappa_x, y_1) = B_1 e^{k_{y1} y_1} + B_2 e^{k_{y2} y_1} + B_3 e^{k_{y3} y_1} + B_4 e^{k_{y4} y_1} \tag{A.16}$$

For section P2,

$$W_{p2}(\kappa_x, y_2) = B_5 e^{k_{y3} y_2} + B_6 e^{k_{y4} y_2} \tag{A.17}$$

For section P3,

$$W_{p3}(\kappa_x, y_3) = B_7 e^{k_{y1} y_3} + B_8 e^{k_{y2} y_3} \tag{A.18}$$

A set of equations for the response of the coupled plate and beam structure to the external force on the plate can be found by application of the boundary conditions of the problem.

Equal displacement of the beam and section P1 of the plate is required at their intersection. In spatial terms, this is for all x and for $y_1 = 0$ of section S1.

$$W_{p1}(\kappa_x, y_1)\big|_{y1=0} = W_b(\kappa_x) \tag{A.19}$$

$$\therefore B_1 + B_2 + B_3 + B_4 - W_b(\kappa_x) = 0 \tag{A.20}$$

The torsional stiffness of the deep beams used in steel railway bridges relative to the bending stiffness of the thin deck plate implies that vertical bending motion, rather than torsional motion, will be of greatest importance to the response of the structure to a vertical load. A simplifying assumption will be made here that the beam does not rotate, it moves in the vertical direction only. Under this condition, it follows that the rotation of sections P1 and P2 of the plate along $y_1 = y_2 = 0$ would also be zero.

$$\therefore \left.\frac{\partial W_{p1}(\kappa_x, y_1)}{\partial y_1}\right|_{y_1=0} = B_1 k_{y1} + B_2 k_{y2} + B_3 k_{y3} + B_4 k_{y4} = 0 \tag{A.21}$$

And,

$$\therefore \left.\frac{\partial W_{p2}(\kappa_x, y_2)}{\partial y_2}\right|_{y2=0} = B_5 k_{y3} + B_6 k_{y4} = 0 \tag{A.22}$$

A further expression can obtained by substituting into equation (A.1) for the shear forces in the plate,

$$\therefore D_p \left[\frac{\partial^3 W_{p2}(\kappa_x, y_2)}{\partial y_2^3}\right]_{y2=0} - D_p \left[\frac{\partial^3 W_{p1}(\kappa_x, y_1)}{\partial y_1^3}\right]_{y1=0} = D_b \kappa_x{}^4 W_b(\kappa_x) - m'_b\, \omega^2 W_b(\kappa_x) \tag{A.23}$$

$$\therefore D_p \left[B_5 k_{y3}^3 + B_6 k_{y4}^3\right] - D_p \left[B_1 k_{y1}^3 + B_2 k_{y2}^3 + B_3 k_{y3}^3 + B_4 k_{y4}^3\right]$$

$$- D_b \kappa_x{}^4 W_b(\kappa_x) + m'_b\, \omega^2 W_b(\kappa_x) = 0 \tag{A.24}$$

For continuity of displacement between sections p1 and p2 of the plate,

$$W_{p1}(\kappa_x, y_1)\Big|_{y1=0} = W_{p2}(\kappa_x, y_2)\Big|_{y2=0} \tag{A.25}$$

$$B_1 + B_2 + B_3 + B_4 = B_5 + B_6 \tag{A.26}$$

For continuity of displacement between sections p1 and p3 of the plate,

$$W_{p1}(\kappa_x, y_1)\Big|_{y1=L} = W_{p3}(\kappa_x, y_3)\Big|_{y3=0} \tag{A.27}$$

$$B_1 e^{\kappa_{y1} L} + B_2 e^{\kappa_{y2} L} + B_3 e^{\kappa_{y3} L} + B_4 e^{\kappa_{y4} L} = B_7 + B_8 \tag{A.28}$$

For continuity of rotational displacement between sections p1 and p3 of the plate,

$$\left.\frac{\partial W_{p1}(\kappa_x, y_1)}{\partial y_1}\right|_{y1=L} = \left.\frac{\partial W_{p3}(\kappa_x, y_3)}{\partial y_3}\right|_{y3=0} \tag{A.29}$$

$$\therefore B_1 k_{y1} e^{k_{y1} L} + B_2 k_{y2} e^{k_{y2} L} + B_3 k_{y3} e^{k_{y3} L} + B_4 k_{y4} e^{k_{y4} L} = B_7 k_{y1} + B_8 k_{y2} \tag{A.30}$$

For force equilibrium at the junction between sections p1 and p3 of the plate,

$$-F_3(\kappa_x, y_1)\Big|_{y1=L} + F_4(\kappa_x, y_3)\Big|_{y3=0} = F_0(\kappa_x) \tag{A.31}$$

$$\therefore -D_p\left[\frac{\partial^3 W_{p1}(\kappa_x, y_1)}{\partial {y_1}^3} - {\kappa_x}^2(2-\nu)\frac{\partial W_{p1}(\kappa_x, y_1)}{\partial y_1}\right]_{y1=L}$$

$$+ D_p\left[\frac{\partial^3 W_{p3}(\kappa_x, y_3)}{\partial {y_3}^3} - {\kappa_x}^2(2-\nu)\frac{\partial W_{p3}(\kappa_x, y_3)}{\partial y_3}\right]_{y3=0} = F_0(\kappa_x) \tag{A.32}$$

$$\therefore -D_p\begin{bmatrix} B_1 e^{k_{y1} L}\left(k_{y1}^3 - \kappa_x^2(2-\nu)k_{y1}\right) + B_2 e^{k_{y2} L}\left(k_{y2}^3 - \kappa_x^2(2-\nu)k_{y2}\right) \\ + B_3 e^{k_{y3} L}\left(k_{y3}^3 - \kappa_x^2(2-\nu)k_{y3}\right) + B_4 e^{k_{y4} L}\left(k_{y4}^3 - \kappa_x^2(2-\nu)k_{y4}\right) \end{bmatrix}$$

$$+ D_p\left[B_7\left(k_{y1}^3 - \kappa_x^2(2-\nu)k_{y1}\right) + B_8\left(k_{y2}^3 - \kappa_x^2(2-\nu)k_{y2}\right)\right] = F_0(\kappa_x) \tag{A.33}$$

For moment equilibrium at the junction between sections P1 and P3 of the plate,

$$M_{p1}(\kappa_x, y_1)\Big|_{y1=L} = M_{p3}(\kappa_x, y_3)\Big|_{y3=0} \tag{A.34}$$

Where the Fourier transform of the moment per unit length is given by (Yoo, 2004),

$$M_{pi}(\kappa_x, y_i)\Big| = D_p\left[\frac{\partial^2 W_p(\kappa_x, y_i)}{\partial y_i^2} - \kappa_x^2 v W_p(\kappa_x, y_i)\right] \tag{A.35}$$

In this case,

$$D_p\left[B_1 e^{k_{y1}L}\left(k_{y1}^2 - \kappa_x^2 v\right) + B_2 e^{k_{y2}L}\left(k_{y2}^2 - \kappa_x^2 v\right) + B_3 e^{k_{y3}L}\left(k_{y3}^2 - \kappa_x^2 v\right) + B_4 e^{k_{y4}L}\left(k_{y4}^2 - \kappa_x^2 v\right)\right]$$
$$- D_p\left[B_7\left(k_{y1}^2 - \kappa_x^2 v\right) + B_8\left(k_{y2}^2 - \kappa_x^2 v\right)\right] = 0 \tag{A.36}$$

Equations (A.20), (A.21), (A.22), (A.24), (A.26), (A.28), (A.30), (A.33) and (A.36) can be used to construct a dynamic stiffness matrix, which relates the amplitudes of the waves to the amplitude of the applied force as follows,

$$\mathbf{Ku} = \mathbf{F} \tag{A.37}$$

This can be done more concisely if the following terms are introduced,

$$\alpha_n = k_{yn}^3 - \kappa_x^2(2-v)k_{yn} \qquad \text{for } n = 1, 2, 3, 4 \tag{A.38}$$

And,

$$\gamma_n = k_{yn}^2 - \kappa_x^2 v \qquad \text{for } n = 1, 2, 3, 4 \tag{A.39}$$

The dynamic stiffness matrix can then be written as follows,

$$K = \begin{bmatrix}
1 & 1 & 1 & 1 & 0 & 0 & 0 & 0 & -1 \\
k_{y1} & k_{y2} & k_{y3} & k_{y4} & 0 & 0 & 0 & 0 & 0 \\
0 & 0 & 0 & 0 & k_{y3} & k_{y4} & 0 & 0 & 0 \\
-D_p k_{y1}^3 & -D_p k_{y2}^3 & -D_p k_{y3}^3 & -D_p k_{y4}^3 & D_p k_{y3}^3 & D_p k_{y4}^3 & 0 & 0 & -D_b\kappa_x^4 + m'_b\omega^2 \\
1 & 1 & 1 & 1 & -1 & -1 & 0 & 0 & 0 \\
e^{k_{y1}L} & e^{k_{y2}L} & e^{k_{y3}L} & e^{k_{y4}L} & 0 & 0 & 1 & -1 & 0 \\
k_{y1}e^{k_{y1}L} & k_{y2}e^{k_{y2}L} & k_{y3}e^{k_{y3}L} & k_{y4}e^{k_{y4}L} & 0 & 0 & -k_{y1} & -k_{y2} & 0 \\
-D_p e^{k_{y1}L}\alpha_1 & -D_p e^{k_{y2}L}\alpha_2 & -D_p e^{k_{y3}L}\alpha_3 & -D_p e^{k_{y4}L}\alpha_4 & 0 & 0 & D_p\alpha_1 & D_p\alpha_2 & 0 \\
D_p e^{k_{y1}L}\gamma_1 & D_p e^{k_{y2}L}\gamma_2 & D_p e^{k_{y3}L}\gamma_3 & D_p e^{k_{y4}L}\gamma_4 & 0 & 0 & -D_p\gamma_1 & -D_p\gamma_1 & 0
\end{bmatrix} \tag{A.40}$$

The column vector of amplitudes can be written as,

$$u = \left[B_1 \quad B_2 \quad B_3 \quad B_4 \quad B_5 \quad B_6 \quad B_7 \quad B_8 \quad W_b(\kappa_x)\right]^T \tag{A.41}$$

And the vector of force amplitudes is given by,

$$\boldsymbol{F} = \begin{bmatrix} 0 & 0 & 0 & 0 & 0 & 0 & 0 & F_0(\kappa_x) & 0 \end{bmatrix} \tag{A.42}$$

Re-arrangement of equation (A.37) allows the vector of the unknown amplitudes to be found from,

$$\mathbf{u} = \mathbf{K}^{-1}\mathbf{F} \tag{A.43}$$

The inversion of matrix $\mathbf{K}$ can be performed numerically using MATLAB. Although it is known that the dynamic stiffness matrix can be ill-conditioned when obtained in this way, the results obtained by this means appear to be satisfactory. The inverse of the dynamic stiffness matrix was therefore not obtained analytically.

The wave amplitudes together with k_y allow calculation of the displacement of the plate as a function of the *y* coordinate and κ_x. To obtain the displacement of the structure in the spatial domain, that is as a function of both the *x* and *y* coordinates, an inverse Fourier transform is required, given by,

$$w_p(x,y) = \frac{1}{2\pi}\int_{-\infty}^{\infty} W_p(\kappa_x, y) e^{i\kappa_x x} d\kappa_x \tag{A.44}$$

Point frequency response functions are sought here, rather than transfer quantities. Equation (A.44) therefore need only be evaluated at the coordinates at which the force is applied, that is $x = x_0$, $y = L$. The choice of datum in the *x* direction is arbitrary for this structure, which is infinite in this direction, so the integrand in equation (A.44) can be simplified by setting $x_0 = 0$.

$$\therefore w_p(0,L) = \frac{1}{2\pi}\int_{-\infty}^{\infty} W_p(\kappa_x, L) d\kappa_x \tag{A.45}$$

Since the displacement of sections P1 and P3 must be equal, we can find the displacement of either of these to calculate the point receptance, and from this the mobility of the structure. Considering section P1,

$$w_p(0,L) = \frac{1}{2\pi}\int_{-\infty}^{\infty} \left(B_1 e^{k_{y1}L} + B_2 e^{k_{y2}L} + B_3 e^{k_{y3}L} + B_4 e^{k_{y4}L} \right) d\kappa_x \tag{A.46}$$

APPENDIX B – THE INPUT POINT MOBILITY OF BRIDGE BEAMS

B.1. INTRODUCTION

Bewes (2006) developed sets of equations for the point mobility of both rectangular-section beams and I-section beams over the frequency range of interest in bridge noise. Here, the WFE method is applied to these beams in order to show that this method gives results that are equivalent to those from the Bewes equations and to study the in-plane modes of these beams further. Bewes (2006) reported difficulty in identifying the in-plane modes of these beams using conventional FE methods. This can be addressed using the WFE method.

B.2. A RECTANGULAR-SECTION BEAM

A rectangular-section beam with a depth equal to 1m and a thickness of 0.02m was studied by Bewes (2006) and this geometry has been retained here. The WFE representation of the beam is shown diagrammatically in Figure B.1 below.

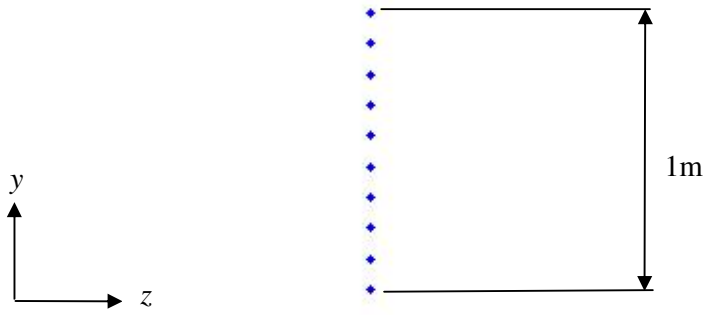

Figure B.1. Node positions in the WFE model of the rectangular cross-section beam.

In order to allow all high frequency behaviour that might occur in the range of real analyses, the WFE analyses for beams have been performed up to a frequency of 10kHz. The element length in the *y* direction was chosen based on a calculation for the minimum expected wavelength of the longitudinal wave in the depth of the beam, together with the requirement for at least three of these cubic-interpolation plate elements per wavelength. The motion of the nodes was constrained in the *z* direction, because this is not expected to be of importance in the response of the beam to forcing

in the *y* direction. Note that the material properties of steel have been used for all the beam modelling work reported here.

The matrix eigenvalue problem (equation (2.20), Section 2.4.2) was solved for a set of prescribed frequencies, in order to obtain purely real, purely imaginary and complex wavenumbers for the undamped case. For the simple geometry under consideration here, these can be shown on a single dispersion diagram, Figure B.2 below.

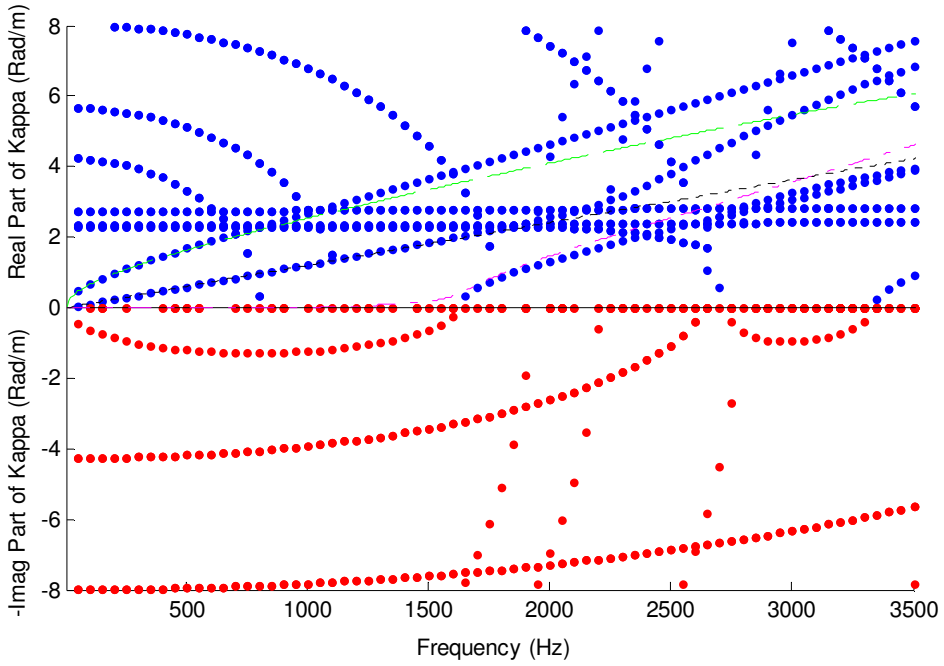

Figure B.2. Real part (positive y axis) and imaginary part (negative y axis) of wavenumber plotted against frequency: ● , real part of wavenumber from WFE; ● , imaginary part of wavenumber from WFE; _____ , longitudinal wave theory; _____ , 1st solution to Timoshenko beam equation; _____ , 2nd solution to Timoshenko beam equation.

Figure B.2 shows that there are just two propagating waves with a zero cut-on frequency for this case where the beam is not free to move in the z direction. These are a vertical bending wave and a longitudinal wave, which have wavenumbers that can be calculated using Timoshenko beam and simple longitudinal wave theory respectively, at low frequencies. The other waves which have a real part to their wavenumber at low frequency also have a significant imaginary part. The rate of decay with distance travelled for these waves is therefore large, such that their influence on the response of the beam is expected to be small. The wave that cuts-on

at a frequency of approximately 1500Hz corresponds to the second solution of the Timoshenko beam equation.

The input point mobility of the beam was calculated using the WFE method, for an applied force at the top of the beam in the *y* direction and a damping loss factor of 0.01. The results obtained are compared with those from the equations proposed by Bewes for rectangular-section beams in Figure B.3 below.

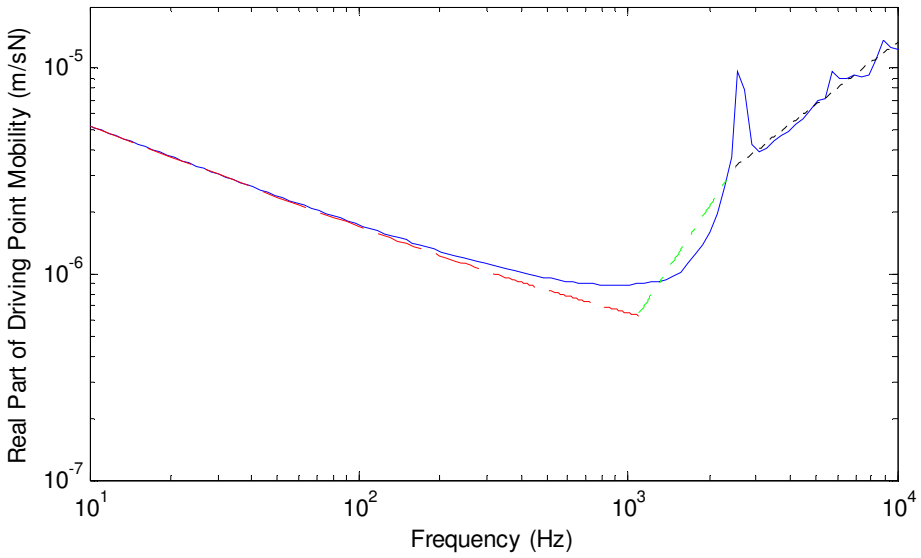

Figure B.3. Real part of input point mobility for the rectangular-section beam shown versus frequency: ——— , WFE solution; – – – – , Timoshenko beam result; –·–·– , Bewes transitional model; - - - - - - - - , edge-excited plate model.

Figure B.3 shows that the WFE mobility spectrum is in agreement with the results of the three equations proposed for modelling rectangular-section beams by Bewes (2006). A large peak is shown in the WFE mobility spectrum centred on a frequency of about 2.5kHz. This corresponds to the frequency at which the longitudinal wave in the beam has a wavelength equal to twice the depth of the beam, i.e. this is the cut-on frequency of the first in-plane wave of the beam. Figure B.3 shows smaller peaks in the WFE mobility spectrum at frequencies of approximately 5.5kHz and 9kHz, the cut-on frequencies of the second and third in-plane waves respectively. The first in-plane wave is of particular interest, because it is associated with a large increase in the mobility of the beam and may occur in the frequency range of interest in bridge noise for some bridges. However, this wave is not easily-identifiable from the dispersion diagram of Figure B.2, due to the number of propagating waves in the beam at high frequencies.

The wavenumber-frequency pairs for the first in-plane wave were identified from the forced response WFE calculation. A dispersion diagram could then be produced to show this wave clearly, in Figure B.4 below.

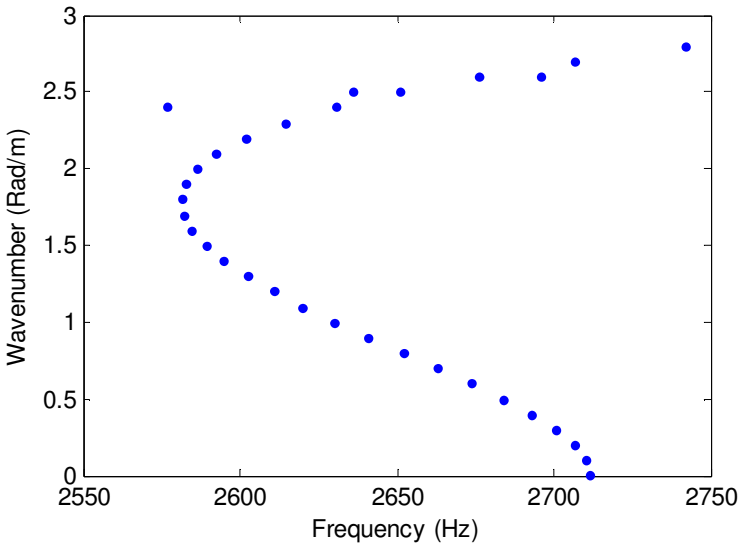

Figure B.4. Wavenumber shown versus frequency for waves with purely real wavenumbers, for a beam with zero damping: ● , WFE solution.

The wavenumber-frequency pairs for the first in-plane wave of the beam show a cut-on frequency of about 2.7kHz and a negative gradient for wavenumbers less than 2 rad/m, *i.e.* the group velocity is negative. The mode shape associated with this wave is shown in Figure B.5 below.

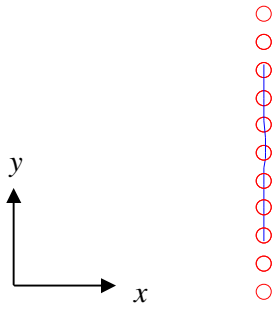

Figure B.5. Mode shape plot for the first in-plane wave of the rectangular-section beam: ○ , original node position; ——— , deformed shape.

As expected, the first in-plane mode of the beam is dominated by stretching/compression motion in the plane of the beam.

B.3. AN I-SECTION BEAM

Figure B.6 shows the cross-section geometry of an I-section beam studied by Bewes (2006) together with the WFE representation of this beam.

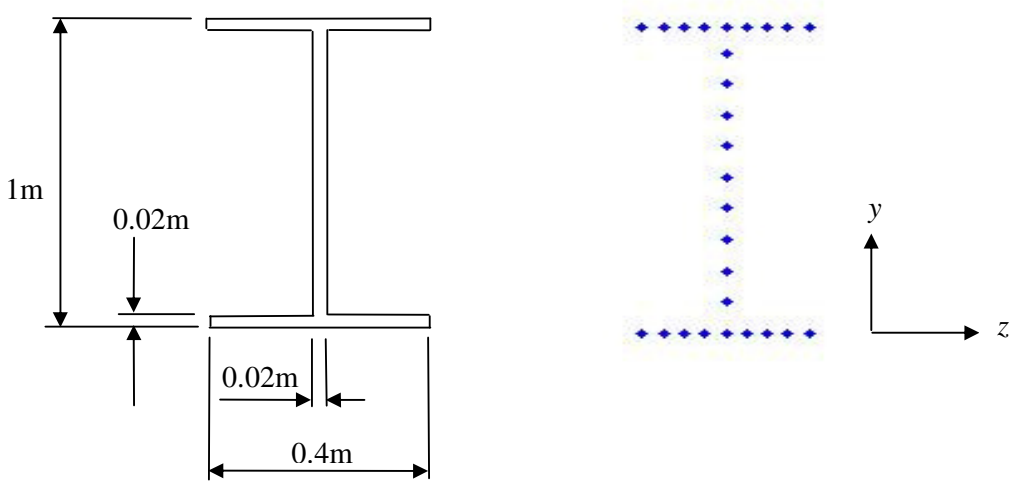

Figure B.6. Cross-section geometry and WFE representation of the I-section beam.

The element sizes have been specified based on the minimum wavelength expected in the web and flanges and the requirement for at least three elements per wavelength. The motion of the nodes in the web was constrained in the z direction.

Figure B.7 shows the dispersion diagram obtained by solution of the eigenvalue problem for unknown frequencies, given a prescribed set of real wavenumbers. The results of Timoshenko beam and longitudinal wave theory are also shown.

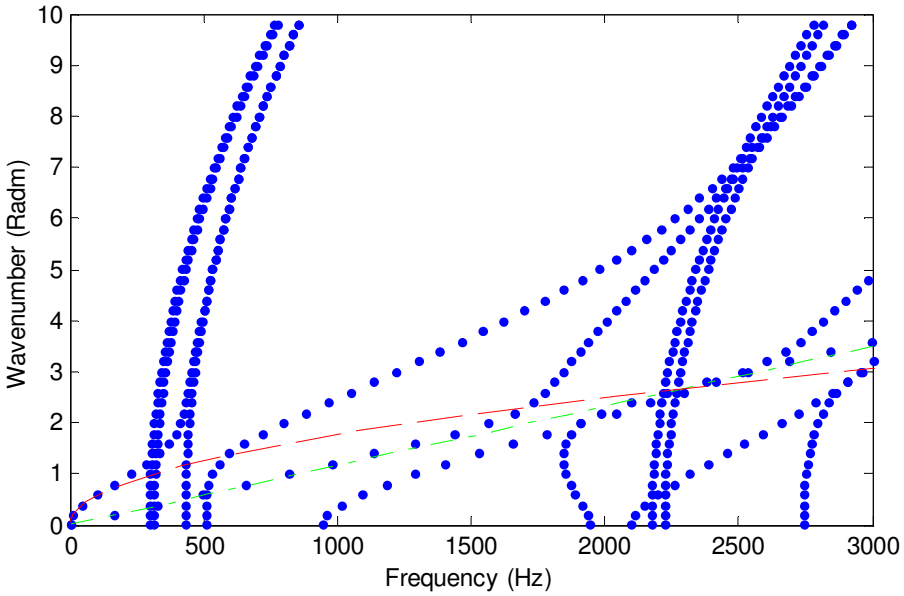

Figure B.7. Wavenumber shown versus frequency for waves with purely real wavenumbers: ● , WFE solution; – · – · – , Longitudinal wave; – – – – – , 1st solution to Timoshenko beam equation; – – – – – , 2nd solution to Timoshenko beam equation.

The first wave solution to the Timoshenko beam model is in agreement with the WFE result up to a frequency of approximately 300Hz. The second Timoshenko solution is in agreement with the WFE result up to a frequency of approximately 1800Hz.

Figure B.8 shows the input point mobility of the I-section beam found using the WFE method for an applied force in the *y* direction at the top of the beam (on the centre-line) and the Bewes equations for the mobility of an I-section beam. The damping loss factor is 0.01 in both calculations.

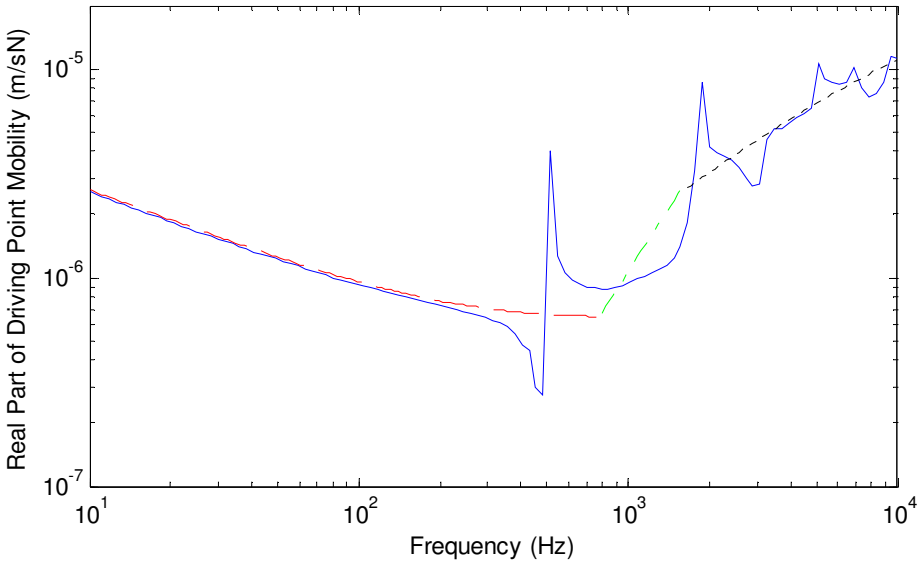

Figure B.9. Real part of input point mobility of the I-section beam plotted versus frequency: ——— , WFE solution; – – – – – , Timoshenko beam result; – – – – – , Bewes transitional model; - - - - - - - - , Bewes high frequency model.

Figure B.9 shows that the WFE mobility spectrum is in agreement with the results of the Bewes equations for the mobility of an I-section beam. There are several distinct peaks in the mobility spectrum obtained from the WFE matrices, which correspond to wave cut-on frequencies. The large peak centred on a frequency of approximately 1.8kHz is due to the first in-plane mode of the beam. The locus corresponding to this wave in the dispersion diagram of Figure B.7 can be identified and shows the negative group velocity characteristic for small wavenumbers also found for the first in-plane wave of the rectangular-section beam. The mode shape associated with this wave is shown in Figure B.10 below.

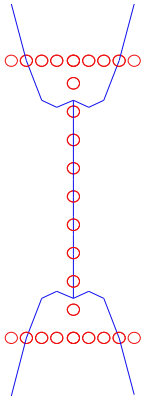

Figure B.10. Mode shape plot for the first in-plane wave of the I-section beam: ○ *, original node position;* ——— *, deformed shape.*

The first in-plane mode of the I-section beam consists of compression/extension in the web accompanied by a flapping motion in the flanges. This finding supports the approach taken to calculating the point mobility of this type of beam at high frequencies by Bewes (2006).